

VIRTUAL INFECTION MODELING FOR *ASPERGILLUS FUMIGATUS* IN
HUMAN AND MURINE ALVEOLI

Dissertation
zur Erlangung des akademischen Grades
„doctor rerum naturalium“ (Dr. rer. nat.)

vorgelegt dem Rat der Fakultät für Biowissenschaften
der Friedrich-Schiller-Universität Jena
von Marco Blickensdorf
geboren am 17.07.1989 in Jena



FRIEDRICH-SCHILLER-
UNIVERSITÄT
JENA

Gutachter

Prof. Dr. Marc Thilo Figge - Leibniz-Institut für Naturstoff-Forschung und Infektionsbiologie – Hans-Knöll-Institut Jena

Prof. Dr. Marie von Lilienfeld-Toal - AG Infektionen in der Hämatologie/Onkologie im Universitätsklinikum Jena

Prof. Dr. Matthias Gunzer - Institut für Experimentelle Immunologie und Bildung im Universitätsklinikum Essen

zusätzliche Mitglieder der Kommission zur Verteidigung am 09.02.2022:

Prof. Dr. Stefan Schuster - Professur für Bioinformatik - Matthias Schleiden Institut der Universität Jena

Prof. Dr. Steve Hoffmann - Leibniz-Institut für Alternsforschung - Fritz-Lipmann-Institut Jena

Prof. Dr. Ralf Oelmüller - Professur für Pflanzenphysiologie - Matthias Schleiden Institut der Universität Jena

CONTENTS

I	INTRODUCTION	3
1	INTRODUCTION	5
1.1	The Pathogenic Mold <i>Aspergillus fumigatus</i>	5
1.1.1	Morphology and Life Cycle	5
1.1.2	<i>A. fumigatus</i> Pathogenicity	6
1.1.3	Host-Pathogen Interactions	8
1.2	Virtual Infection Modeling & Systems Biology	10
1.2.1	Systems, Models and Simulations	11
1.2.2	The Cycle of Modeling	13
1.2.3	Virtual infection modeling of <i>A. fumigatus</i>	16
2	OBJECTIVES OF THIS THESIS	19
II	MANUSCRIPTS	21
3	OF MICE AND MEN	23
4	PORES OF KOHN IN HUMAN ALVEOLI	35
5	ASPERGILLOSIS-ON-CHIP	49
6	SPHARM SHAPE CLASSIFICATION OF MIGRATING CELLS	77
III	DISCUSSION	91
7	DISCUSSION	93
7.1	Discussion of Main Results	93
7.1.1	Modeling reveals infection dynamics in murine alveoli	93
7.1.2	Fungal burden governs infections in murine model	94
7.1.3	Pores of Kohn influence infection dynamics	96
7.1.4	Hyphal growth is affected by macrophage presence	97
7.1.5	Dynamic SPHARM captures cell migration dynamics	99
7.2	Open Issues, Perspectives and Future Work	100
7.2.1	Perspectives on experimental validation	102
7.2.2	Perspectives on model developments	103
	BIBLIOGRAPHY	107
	ACKNOWLEDGMENTS	123
	EHRENWÖRTLICHE ERKLÄRUNG	125
IV	APPENDIX	127

ABSTRACT

The filamentous pathogenic fungus *Aspergillus fumigatus* may cause severe infections in the form of invasive pulmonary aspergillosis. These infections are characterized by high mortality rates and have shown a rising incidence over the last decades. These tendencies created a strong need for research to understand the fungi's opportunistic nature, to develop efficient treatment strategies and ultimately save lives. Since the lung as primary target of *A. fumigatus* infections provides only limited accessibility for experimental studies *in vivo*, research has to incorporate alternative strategies. The field of systems biology has established a broad variety of modeling strategies to overcome the experimental limitations. Such computer models *in silico* capture essential aspects of systems including *A. fumigatus* infections, thus allowing to simulate infection dynamics in special regard of relevant parameters. Consequently, key mechanisms of infections may be detected and quantified to identify new targets for diagnostics or treatment.

The fundament of this thesis builds upon an established hybrid agent-based model of *A. fumigatus* infections. The applied model captures the scaled spatial properties of the pulmonary alveolus and allows to simulate the early phase of such infections after inhalation of the fungal conidia. The model comprises the alveolus, its epithelial surface cell layer, macrophages as migrating immune cells, a molecular diffusion model and a signal receptor differential equation model of macrophage chemotactic migration. Thus, the hybrid agent-based alveolus model enables to simulate the arms race between the invading fungus and the chasing immune cells to investigate the impact of parameters and mechanisms. The presented studies in this thesis have extended and developed this model further to focus on open questions in the understanding of *A. fumigatus* infections.

Animal models provide a valuable tool for the investigation of infections. The most widely used animal model to study aspergillosis is the murine model. Although the evolutionary link between human and murine systems is close, their pulmonary morphology and the applicable infection dosages differ. To investigate these differences and evaluate their implications for the transferability of results from experimental mice models to human infections, the hybrid agent-based alveolus model was extended to resemble the alveolar morphology of mice. The infection dynamics of both organisms were simulated and compared from a single alveolus perspective to assess how efficiently conidia can be detected depending on the morphology. Various dosages ranging from natural to experimental levels were incorporated as well as the differing number of alveoli per lung to compare the clearance efficiency in the whole lung. The simulations revealed a faster clearance of conidia in the murine alveolus. Furthermore, the clearance efficiency for both organisms decreases with increasing fungal burden of the lung. For high fungal burdens, as locally observable in the murine

model, the smaller murine alveolus is confronted with so many conidia that efficient signaling is no longer possible and clearance efficiency declines quickly, whereas the human morphology allows to clear such a fungal burden.

Immune cell migration is crucial for host defense. For a quantitative understanding of cellular migration, descriptors are needed that efficiently distinguish relevant shape changes during migration of various cells or experimental settings from random variations. In the SPHARM study, spherical harmonics (SPHARM), a 2D and 3D shape descriptor were extended by including time-resolved dynamics. The descriptive power of dynamic SPHARM for murine T cell images from various tissues acquired by 3D two-photon microscopy, as well as for synthetically generated 3D cell images was tested. A support vector machine was used to classify the T cells of different origins based on the dynamic SPHARM descriptor. An improved distinction of cellular origins by extending temporal dynamics to the SPHARM analysis could be demonstrated. This allows for a more detailed analysis of 3D images of migrating cells as well as refined *in silico* modeling of such migration processes in future.

Pores of Kohn (PoK) are a morphological feature of the mammalian lung which interconnect neighboring alveoli. Although known for a long time, their impact on immune dynamics has not yet been investigated extensively. Therefore, the hybrid agent-based alveolus model was adapted to test opposing hypotheses on immune cell trafficking and molecular diffusion through PoK during early aspergillosis. The study showed that passaging of alveolar macrophages through PoK results in a lower migration distance to the conidium and thus enables alveolar macrophages to clear infections faster. This impact, however, is small compared to other parameters, *e.g.* macrophage speed, and an efficient infection clearance is also possible without PoK passaging. The simulations revealed that PoK passaging ensures a uniform spatial distribution of macrophages on the alveolar surface and thus helps maintaining immune homeostasis.

The limited experimental accessibility of alveolar tissue limits investigations of pulmonary aspergillosis. Novel *aspergillus-on-chip* devices enable experimental investigation of alveolar tissue under enhanced precision. Confrontation assays with *A. fumigatus* conidia and macrophages under different conditions were developed to live-image cellular dynamics with confocal laser scanning microscopy. This allowed to quantitatively analyse spatial dynamics, *e.g.* hyphal growth. It was observable that the hyphae successfully penetrated the chip membrane's pores, similar to the invasive penetration during infection. The analysis reveals an increase in invasive growth during presence of macrophages. This may suggest a signal-driven growth process but also a possible evasion strategy. In addition, the analysis allows for a parameter dependent modeling of hyphal growth *in silico* under the condition of caspofungin treatment, amongst others.

ZUSAMMENFASSUNG

Der filamentöse pathogene Pilz *Aspergillus fumigatus* kann schwere Infektionen wie die invasive pulmonale Aspergillose in immungeschwächten Patienten verursachen. Verbunden mit einer hohen Mortalität und einer steigenden Inzidenz der letzten Jahrzehnte bezeugt dies die Notwendigkeit zur Erforschung seines opportunistischen Verhaltens sowie zur Entwicklung effizienter Behandlungsstrategien, um Menschenleben zu retten. Da die Lunge, als primäres Ziel von *A. fumigatus* Infektionen, nur begrenzt experimentell *in vivo* studiert werden kann, müssen alternative Strategien angewandt werden. Das Feld der Systembiologie hat ein breites Spektrum an Modellierungsstrategien etabliert, die solche Begrenzungen überwinden können. Computermodelle können *in silico* essenzielle Aspekte eines Systems, wie *A. fumigatus* Infektionen, erfassen und erlauben eine Simulation der Infektionsdynamiken unter Betrachtung der relevanten Parameter. Folglich können Schlüsselmechanismen der Infektion erkannt und quantifiziert werden, um neue Ziele für Diagnose oder Behandlung zu identifizieren.

Grundlage dieser Doktorarbeit bildet ein etabliertes agentenbasiertes Modell von *A. fumigatus* Infektionen. Das genutzte Modell erfasst die räumlichen Eigenschaften der pulmonalen Alveolen maßstabsgetreu und erlaubt, die frühe Phase der Infektion ab Inhalation der Konidien zu simulieren. Das Modell enthält die Alveole, deren Oberflächenepithel, Makrophagen als mobile Immunzellen, ein molekulares Diffusionsmodell sowie ein Signal-Rezeptor Differentialgleichungsmodell der alveolaren chemotaktischen Bewegung. Folglich erlaubt das Modell, das Wettrennen zwischen invasivem Pilz und jagenden Immunzellen zu simulieren, um den Einfluss von Parametern und Mechanismen zu untersuchen. Die präsentierten Studien dieser Arbeit haben das agentenbasierte Alveolenmodell erweitert und weiterentwickelt, um offene Fragen im Verständnis von *A. fumigatus* Infektionen zu beantworten.

Tiermodelle sind ein wertvolles Werkzeug für die Erforschung von Infektionen, wobei die Maus das etablierteste Aspergillosemodell darstellt. Trotz der nahen evolutionären Verwandtschaft unterscheiden sich sowohl die Morphologie von Mäusen und Menschen als auch die aufgenommene Infektionsdosis. Zur Untersuchung dieser Unterschiede und deren Implikationen für die Transferierbarkeit von Ergebnissen aus experimentellen Mausmodellen zu humanen Infektionen wurde das agentenbasierte Alveolenmodell erweitert und die alveolare Morphologie von Mäusen abgebildet. Die Infektionsdynamik zwischen beiden Organismen wurde auf der Ebene einzelner Alveolen simuliert und verglichen, um festzustellen, wie effizient die Konidien in Abhängigkeit von der Morphologie detektiert werden können. Weiterhin wurden die unterschiedlichen, natürlichen bis experimentellen, Infektionsdosen und die unterschiedliche Zahl von Alveolen pro Lunge mit den Ergebnissen kombiniert, um die Effizienz auf der Ebene der Lunge zu vergleichen. Die Simulationen zeigen eine schnellere Beseitigung von Konidien in der Mausalveole. Ebenso sinkt die Effizienz in beiden

Organismen mit steigender Infektionsdosis. Bei besonders hohen Dosen, wie sie lokal im experimentellen Mausmodell zu beobachten sind, ist die Mausalveole mit so vielen Konidien konfrontiert, dass eine effiziente Beseitigung nicht länger möglich ist. Die menschliche Morphologie hingegen erlaubt eine Beseitigung solcher Pilzbelastungen.

Die Bewegung von Immunzellen ist zentral für die Verteidigung des Organismus. Für ein quantitatives Verständnis von zellulärer Bewegung braucht es Marker, die zwischen relevanten Formänderungen und zufälligen Variationen unterscheiden. Die SPHARM Studie erweiterte die Kugelflächenfunktionen (SPHARM), eine Beschreibung von 3D-Oberflächenformen, durch Einbeziehung zeitlicher Dynamiken. Bilder von 3D T-Zellen aus diversen Geweben sowie synthetisch generierte Zellen dienten als Testdaten für die dynamische SPHARM Beschreibung. Eine Support Vector Machine wurde genutzt, um die T-Zellen je nach Herkunft anhand der dynamischen SPHARM Marker zu klassifizieren. Eine verbesserte Unterscheidung der T-Zellen durch Erweiterung von SPHARM um zeitliche Dynamiken ließ sich beobachten. Dies erlaubt zukünftig eine detailliertere Unterscheidung von 3D Bildern sich bewegender Zellen sowie eine verbesserte Modellierung solcher Bewegungsprozesse.

Kohnsche Poren (PoK) verbinden benachbarte Alveolen und sind morphologisch Merkmale der Lung aller. Obwohl PoK lange bekannt sind, ist ihr Einfluss auf Immundynamiken noch nicht umfassend untersucht. Aus diesem Grund wurde das agentenbasierte Alveolenmodell angepasst, um gegenüberstehende Hypothesen der Passage von Immunzellen und molekularer Diffusion durch PoK während der frühen Aspergillose zu untersuchen. Die Studie zeigte, dass die Migration von Makrophagen durch PoK zu einer kürzeren Migrationsdistanz zum Konidium führt und daher deren Beseitigung schneller möglich ist also ohne Migration durch PoK. Allerdings ist dieser Einfluss gering im Vergleich zu anderen Parametern wie beispielsweise der Geschwindigkeit der Makrophagen und eine effiziente Beseitigung der Konidien ist auch ohne Migration durch PoK möglich. Die Simulationen haben darüber hinaus gezeigt, dass Migration durch PoK eine gleichmäßige räumliche Verteilung der Makrophagen erlaubt und damit einen Beitrag zur Immunhomöostase leistet.

Die begrenzte Erreichbarkeit alveolaren Gewebes begrenzt die experimentelle Erforschung von Aspergillose. Neuartige aspergillosis-on-chip Geräte erlauben die experimentelle Untersuchung alveolaren Gewebes mit gesteigerter Realitätstreue. Ein Konfrontationstest mit *A. fumigatus* Konidien und Makrophagen unter unterschiedlichen Bedingungen wurde entwickelt, um die zellulären Dynamiken mithilfe eines Konfokalmikroskops aufzunehmen. Dies erlaubte, die Dynamiken des Hyphenwachstums quantitativ zu analysieren. Es konnte beobachtet werden, dass die Hyphen erfolgreich die Poren des Chips penetrieren, ähnlich der invasiven Penetration während einer Infektion. Die Analyse enthüllt einen verstärkt invasiven Wachstumsprozess bei Präsenz von Makrophagen. Dies suggeriert ein signalgetriebenes Hyphenwachstum aber auch eine mögliche Evasionsstrategie. Des Weiteren erlaubt die Analyse eine bedingungsabhängige Modellierung des Hyphenwachstums, beispielsweise der Präsenz von Caspofungin.

ACRONYMS

ABM agent-based model
ABPA allergic bronchopulmonary aspergillosis
AEC alveolar epithelial cells
AM alveolar macrophage
IPA invasive pulmonary aspergillosis
MIP-1 macrophage inflammatory protein 1
NET neutrophil extracellular traps
ODE ordinary differential equation
PAMP pathogen-associated molecular pattern
PMN polymorphonuclear neutrophils
PoK pore of Kohn
PRR pattern recognition receptor
SPHARM spherical harmonics

PREFACE

When I started to write the first lines of this thesis, it coincided with the lockdown of the global corona pandemic caused by the SARS-CoV-2. Suddenly, writing about infectious disease has gained a new relevance. Although right now, no one knows how this pandemic will influence the future of humanity's society, economy and research, it is a harsh reminder of something vital. Infectious diseases are a constant and global threat to each and everybody of us. It requires manifold efforts from the world's scientific community to evaluate these threats: from the understanding of mechanisms of pathogenicity, genetics and host-immune interactions to the development of efficient medication, treatment, epidemic action plans and scientific communication to the public. This is a thesis about infections of the pathogenic fungus *Aspergillus fumigatus*, not SARS-CoV-2. But as both pathogens infiltrate the lung, co-infections cannot be avoided and an increased necessity in efficient treatment of *A. fumigatus* infections can be expected. In this present these, I want to share my thoughts and research results on the deciphering of infections caused by *A. fumigatus* to contribute to a healthier future.

Jena, June 2020

Part I

INTRODUCTION

INTRODUCTION

1.1 THE PATHOGENIC MOLD *Aspergillus fumigatus*

With an estimated age of more than one billion years since their first encounter on land, long before plants and animals, the fungal kingdom has reached remarkable diversity [1–3]. Although fungal taxonomy is a fluid field under constant changes, up to 120 000 fungal species have been described until today and estimates about the total number of fungal species range up to a few millions [4–6]. The hitherto-undescribed species are difficult to reveal due to the diverse habitats of fungi: arctic regions [7], desert sands [8] or as commensals, *e.g.* in the human gastrointestinal tract [9], which makes it more difficult to discover and distinguish novel fungal species. Consequently, this rich taxonomy allows for diverse metabolic activity of fungi, which can be seen as fungi serve as a source of food and antibiotics or other bioactive compounds. The downside of this diversity is fungal infections. Around one-seventh of the world's population is assumed to suffer from fungal infection, with 150 million patients developing severe diseases, including more than 1.6 million fatal cases each year [10]. The variety of infections ranges from superficial infections of the nails, hair or skin to allergic, chronic or even invasive infections mostly caused by the genera *Candida*, *Cryptococcus*, *Pneumocystis*, *Histoplasma* and *Aspergillus* [10]. The latter may cause various severe infections and will be introduced to the reader in this chapter.

1.1.1 Morphology and Life Cycle

The diverse genus of *Aspergillus* comprises more than 300 species [11]. One of its most relevant representatives, *Aspergillus fumigatus*, was first described by Georg W. Fresenius more than 150 years ago [12]. This worldwide abundant filamentous fungus is typically detected in soil but also found in hot deserts, deep seas and even ancient Egyptian mummies [13, 14]. Its ability for the aerobic decomposition of organic molecules implicates an important ecological role as a carbon and nitrogen recycler [15].

The morphology of *A. fumigatus* is heterogeneous. Conidia, the spores of *A. fumigatus*, are spherical, dark green-blue, have a diameter ranging from 2.5 – 3 μm and a smooth to indiscernibly echinulate surface structure [16]. The high tolerance to temperature, pH and nutrient or oxygen availability allows the conidia to rest for years until moisture allows for sporulation. This induction is controlled by several pathways and regulatory genes like *Cph1* and *Efg1*, which induce activation of downstream genes and functions such as *Ume6* (hyphal growth), *Eed1* (endocytosis escape) or *Hgc1* (cell separation suppression). The conidial volume increases due to a swelling of the cell wall caused by an accumulation of important polysaccharides such as galactomannan and galactofuranose, pathogen-associated molecular pattern (PAMP), which allow for detection by host phagocytes [17]. The next phase of morphogenesis is characterized by the formation of hyphae, elongated, filamentous, branching structures that constitute the fungal mycelium. These hyphae, 2 μm in diameter, are the only way in which the fungus can actively translocate itself and possibly acquire new nutrient sources. Although our understanding of hyphal growth modulators is not yet complete, it has been shown that hyphae have high adhesive capacities and can penetrate various tissues and blood vessels [18]. The life cycle ends when the hyphae build a conidiophore, which generates a new generation of conidia. The conidiophores are also name-giving for the genus since their shape reminds one of the aspergillum in Christian liturgy. The species name *fumigatus* is derived from the Latin word for smoke 'fumus' and refers to the dark blue to green colonies of *A. fumigatus* (see Figure 1.1).

1.1.2 *A. fumigatus* Pathogenicity

Although prevalence for healthy, immunocompetent persons is low, serious diseases may be caused by *A. fumigatus* [20]. These share in common the fact that they are caused by the inhalation of *A. fumigatus* conidia, which are distributed in each part of the human lung due to their small size. The worldwide abundance of *A. fumigatus* implies that conidia are present all of the time around us and thousands are inhaled every day [21].

The allergic bronchopulmonary aspergillosis (ABPA) is a disease caused by *A. fumigatus*, typically in immunocompetent patients with preconditions, mostly asthma or cystic fibrosis [22]. The allergic overreaction of the immune system causes damage to pulmonary tissue, which, if untreated, may cause irreversible bronchiectasis or fibrosis [23]. The worldwide prevalence is estimated at up to 4 800 000 active cases per year [24]. Like ABPA, allergic aspergillus sinusitis (AAS) manifests with lower prevalence in the paranasal sinuses [25].



Figure 1.1: *A. fumigatus* colony. The dark blue to green color of the *A. fumigatus* colonies is eponymous [19].

A more severe infection, with several sub-types and 240 000 active cases per year in Europe, represents the chronic pulmonary aspergillosis (CPA) [26]. Like ABPA, it is typically diagnosed in immunocompetent patients with pre-existing conditions, mostly those with ABPA or tuberculosis. In contrast to patients with ABPA, CPA patients exhibit an *A. fumigatus* manifestation *e.g.* an aspergilloma, a fungal ball comprising of mostly hyphae, in their lung, which often has to be surgically resected [26].

The most severe type of *A. fumigatus* infection is invasive pulmonary aspergillosis (IPA). Typically found in (severely) immunocompromised patients, the fungus becomes invasive and is able to penetrate the bloodstream, followed up by sporulation and dissemination of conidia to other organs [27].

Although Arthur T. Henrici wrote in 1939 that “...*Aspergillus* infections are so rare as to be of little practical importance”, we are witnessing an emerging threat by IPA [28]. Since then there has been enormous progress in medicine, which has saved millions of lives and yielded an increasing group of immunocompromised patients, including the elderly, patients after organ transplantation or patients with preconditions as neutropenia, cancer, HIV or other chronic diseases. Consequently, Groll *et al.* could demonstrate an increase in hospital-related prevalence of invasive fungal infection from 2.2% (1978-1982) to 5.1% (1988-1992), mostly caused by *A. fumigatus* [29]. In 1996, the US was confronted with an estimated 10 190 hospitalizations related to Aspergillosis, 1 970 deaths

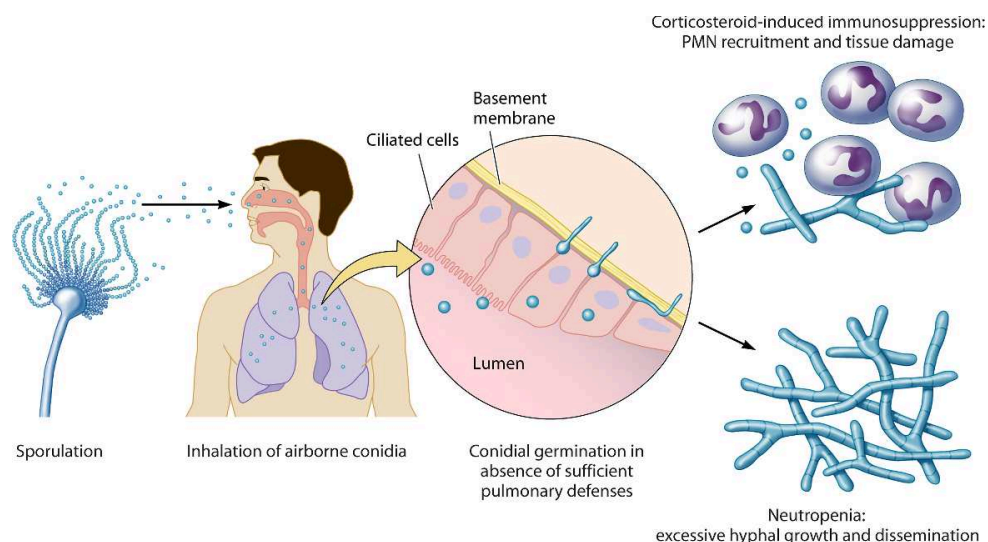


Figure 1.2: Life cycle of *A. fumigatus*. Conidiophores releasing new conidia into the environment followed up by inhalation into lung and alveoli. Conidia develop hyphae, disseminate and cause invasive aspergillosis. Adapted from [33].

and health care costs of \$ 633 million [30]. The reported annual 75 000 cases with costs of \$ 1.2 billion in 2014 show the increasing incidence and reveal, in combination with the high mortality rates of IPA between 45 % and 90 %, the need for better diagnostics and therapeutics [31, 32].

1.1.3 Host-Pathogen Interactions

Upon inhalation into the human lung, a race between the host and *A. fumigatus* is triggered (see Figure 1.2). The fungus aims to invade the host, whereas the host immune system attempts to eliminate the fungal spores. Due to the fast dynamics of *A. fumigatus* infections, from hours up to a few days, the adaptive immune system is unable to interfere in sufficient time. Therefore, the innate immune system plays a pivotal role in the *A. fumigatus* defense.

Upon contact with the alveolar epithelium, conidia trigger activation of the complement system, a system of roughly 30 proteins, which support the cellular immune response. *A. fumigatus* may activate the classical, alternative and lectin pathway, all leading to cleavage of C3, a central molecule of the complement system, whose fragments opsonize pathogens and thus allow for more efficient cellular defense [34]. However, *A. fumigatus* has developed evasive mechanisms that limit the impact of the complement system. Masking of surface antigens by cell wall DHN-melanin inhibits C3 opsonization and the acquisition of e.g. the inhibiting factor H consequently downregulate the complement system [35].

The first line of cellular defense is constituted by macrophages, patrolling leukocytes, occurring in high number in each human tissue. The macrophages

in the human lung can phagocytose *A. fumigatus* spores [36]. Recognition of PAMP is realized either by surface-bound pattern recognition receptor (PRR) as Dectin-1 or via soluble PRR such as the long pentraxin PTX₃ [37, 38]. The most prominent PAMP are the glucans on the fungal surface. The aforementioned alterations on the fungal surface during morphogenesis change the recognizability of *A. fumigatus*. The exposed β -1-3-Glucan content on the cell wall surface, as detected by macrophage surface PRR Dectin-1, is increasing from the resting to the swollen morphotype, and finally, for mature hyphae, it is masked again by exopolysaccharides, causing a peak of recognizability around the swelling phase [39]. By contrast, the α -Mannans fraction, as recognized by macrophage surface PRR Dectin-2, is smaller in the hyphal form [40]. Although the general recognition of *A. fumigatus* is essential for phagocytosis, the activation of macrophages induces different host responses. The activation of the Dectin-1 pathway, and others such as TLR2, triggers the regulation of more than 1800 genes including many pathways for chemo- and cytokines including TNF- α or the macrophage inflammatory protein 1 (MIP-1), which is an important pro-inflammatory regulator [41, 42].

The second line of cellular defense, polymorphonuclear neutrophils (PMN), is recruited to the site of infection. PMN are blood-circulating, highly efficient phagocytosing cells, which are recruited to sites of infection. Their phagolysosomes, highly reactive cell compartments, allow for an unspecific phagocytosis of many pathogens [43, 44]. Although they aim for phagocytosis of *A. fumigatus* like macrophages, PMNs play an intricate role in the immune response. They are faster and more efficient phagocytes than macrophages but only available after recruitment to the site of infection [45]. Their pro-inflammatory potential is higher than that of macrophages but may also become deleterious to lung tissue [46]. It has been shown *in vitro*, that PMN produce neutrophil extracellular traps (NET), burst fibers with fungicidal proteins that engulf pathogens, to battle *A. fumigatus* infections [47].

The third prominent cell type for understanding the host response are the epithelial cells of the human lung, since they are first to come into contact with the conidium [48]. They have been shown to internalize conidia followed by either phagocytosis or, in some cases, a continuation of germination [49, 50]. Upon contact with the conidium, pro-inflammatory cytokines and chemokines are up-regulated within epithelial cells and contribute to inflammation [51]. Nevertheless, *A. fumigatus* benefits from the interaction with epithelial cells as they provide a source of iron, known to be a crucial virulence factor [52, 53]. *A. fumigatus* releases a variety of toxins, proteases, and enzymes damaging epithelial cells [48].

1.2 VIRTUAL INFECTION MODELING & SYSTEMS BIOLOGY

While the previous section introduced *A. fumigatus* and its pathogenicity, this chapter presents the concepts of systems biology and modeling applied in this thesis. The term systems biology has undoubtedly gained an enormous popularity since its introduction into biology around 2000 [54]. Depending on the perspective, it comprises a methodological extension of biology, an interdisciplinary mix of biology, mathematics, and physics, or even an essential shift of paradigm in biology [55, 56]. Although the truth might be somewhere in between, it definitely offers a new perspective, leaving the traditional reductionism of subsetting biology in smaller, easy-to-capture entities towards a comprehensive and systematic contemplation [57]. While the traditional approach aims to find and describe puzzle parts, systems biology aims to solve the puzzle by integrating knowledge into theoretical systems.

A definition of systems biology that does not include the interplay of systems theory and validation by experiments remains incomplete. The core and undoubted strength of systems biology lies within this constant and frequent exchange between the theoretical perspective and the validating feedback from experiments. Thus, a relation between the traditional *wet lab* experiments and the systems biology *dry lab* experiments has emerged, which is nowadays often referred to as the *cycle of systems biology*. This cycle involves generating new hypotheses in the dry lab, which in return can be tested in the wet lab. This approach generates new data, allowing refinements of the dry lab analysis, starting a new cycle [58].

Three key factors can be identified as the basis for success of systems biology: data, computation and theory [59]. The traditionally low amount of data in biology has been replaced by a vast heap of data derived from genomics, proteomics, metabolomics, and other -omics during recent decades. The European Bioinformatics Institute stored around 20 petabytes in 2015 while expecting a more exponential than linear increase [60]. In parallel, technical advances have enabled increase in computational power over magnitudes during recent decades. The third factor refers to the broad theoretical fundamentals of functional systems, which originate long before 2000 [61]. In this way, established and well-examined concepts originating from mathematics, physics and systems theory have found new applications within biology.

1.2.1 Systems, Models and Simulations

Despite being extensively used, the term *system* is abstract and evades a clear definition [62]. One way to describe it, is as a set of entities connected by relations imposing a complexity exceeding the summed-up complexity of its parts. Intuitively, it is often rephrased as: *the whole is more than the sum of its parts*.

In practice, an abstract picture of the term system, which we call model, is depicted, including its essential entities and relations. Models are the tools of systems biology and aim to capture significant aspects of a system. Models and their respective designers precisely define which entities of a system are considered necessary, how they behave and interact with each other and thereby define a system's simplified abstraction. This abstraction is essential globally and locally for the model because internal and surrounding entities at some point must be simplified. This observation demonstrates the two directions that are typically applied in systems biology: top-down and bottom-up. A top-down approach tries to understand a system by starting with a general model followed by a constant increase of the level of detail. Bottom-up approaches start with a detailed model, at *e.g.* the molecular level, and aim for a constant increase of generality [63]. Determining a proper degree of abstraction is the critical process in model design.

A model is applied in the form of a simulation, *i.e.* an execution of the aforementioned definitions and relations. In this process, the input is applied to a model yielding the output: $\text{Input} \mapsto \text{Model} \mapsto \text{Output}$ [64]. Different aspects of systems can be investigated by different perspectives of this simple modeling scheme. A system's robustness can be analyzed by varying the input and comparing its variance to the output variance [65]. Redundant parts of models can be identified if an alteration or removal of a part does not affect the output. Similarly, a redundant input parameter can be identified if its variation does not change the output [54], whereas input parameters that strongly correlate to the output identify crucial parts of systems and possible therapeutic targets [66]. Biological parameters not accessible by wet lab experiments can be fitted by varying the model's input until yielding the desired output [67]. All of these examples show that models can be very powerful as they assist inspecting a wide variety of system properties.

Since the aim of a model is to elucidate specific questions, identical systems can be represented by different models depending on the question of interest. The practical differences in the resulting system-to-model relation must be considered during the design process and can be characterized by several viewpoints, which will be explained in the following.

ENTITY QUANTITY AND QUALITY Systems, especially in biology, easily exceed thousands of entities such as cells or molecules. Hence, a computationally feasible size of the entity population quickly approaches as their possible interactions grow exponentially or the necessary memory grows with the level of detail applied for each individual entity. This may demand a quantitative or qualitative simplification of the model [68]. It can be achieved by a reduction of the individual entities properties, inducing a loss of distinguishability but a gain in memory [69]. Generally, a trade-off must be made between the level of detail used to describe a model (position, speed, state, interaction ...) and the costs for *e.g.* computation or implementation with respect to the investigated question.

MODEL SCALE As each living organism is composed of cells, each biological system covers multiple scales from nanometers (molecules) to micrometers (cells) to centimeters (organs) or kilometers (habitats). Consequently, a comprehensive model must also cover multiple scales to obtain a general perspective of a biological system. Such so-called multiscale models require higher implementation efforts as they are composed of sub-models covering knowledge from different scales and therefore they must typically integrate data from different experimental origins [54, 70]. Despite the higher effort, only multiscale models allow for a comprehensive understanding of biological systems.

STOCHASTICITY The traditional reductionism in biology originates from René Descartes, who captured systems as compositions of parts that can be investigated, understood and reassembled to the whole [71]. Although Descartes' ideas were a huge success in science for a long time, they are increasingly debatable in terms of solving questions of today's biology [72]. Non-deterministic processes such as fluctuation and noise are considered to be crucial for the understanding of biological systems and must be included into the theories of biology [73, 74]. Given that the result of a stochastic process may only be interpreted in the context of repetitions, the simulation effort is much higher compared to a deterministic model. Additional difficulties arise when including stochasticity into a model. First, specifying stochastic processes is not necessarily trivial and, second, the stochastic law of huge numbers only applies to many entities that are not given for each problem.

BOUNDARY CONDITION Compulsory, every model contains some entities and their relations and excludes entities outside of the model boundary. Independently of the question of where the model boundary is placed best, it has to be defined how the model entities interact with it. The most

sparse way of including boundary conditions would be to include a fixed exchange rate of entities and or to describe an isolated system with no exchange [75]. By contrast, most biological systems of interest are not equilibrated and cannot be described as isolated, and thus require more complex model boundaries. Generally, boundary interactions should be kept restrained or, if dynamically complex, included into the model [75]. Although established boundary conditions like the Dirichlet boundary condition [76] or periodic boundary conditions [77] are typically used, their impact on the models within systems biology is rarely investigated although possibly significant [78].

GENERALITY Research in biology used to search for general laws, as could be found in *e.g.* physics. Although such laws would be beneficial, it is doubtful that this can ever be reached [79]. Although theoretically a perfect model can be generalized to investigate different questions, practically a trade-off with the realism, precision and implementation effort of the model must be made and a weighting of these constraints depends on the research focus [80].

In practice, two limiting factors must additionally be considered for the model design. First, despite today's computational resources, a simulation has to finish in a reasonable time. Although this may reach weeks or months in extreme cases, a practical limit exists and induces a limit of granularity. The second important factor to consider is the availability of data. Each parameter and mechanism included in the model originates from prior knowledge typically derived from a time- and cost-expensive wet lab experiment representing the most limiting factor in model design.

1.2.2 The Cycle of Modeling

Within the aforementioned cycle of systems biology the modeling process itself is often considered as a cyclic process. Independent of the specific modeling technique, certain steps in the model life cycle apply to most models and will be presented in the following. The answers that a model can give to a question strongly depend on the decisions made during each step of design and specific steps are better suited for model improvement than others.

MODEL DESIGN The modeling process starts with a precise definition of the problem and the open questions that are addressed. Analyzing the prob-

lem structure reveals fundamental mechanisms that should be included in the model. This identification allows for an abstraction from the system to the model resulting in a clear mathematic definition. Essential for this step is a complete overview of available data that can be used for the model [81]. Similarly, a clear definition of the model output should be made. Since a computational model can be captured as a whole, a complete output of all variables during the simulation time course is possible but not desired in most cases. Adequate model output comprises data that is relevant for the addressed problem but also critical model checkpoints that allow capturing the plausibility of the model mechanisms and detecting errors.

MODEL IMPLEMENTATION Advances in computer science have created a wide range of programming languages and software that can be applied for modeling. Therefore, the question of a proper implementation choice is not easy to answer [82]. Many software tools have been created in recent decades and allow for easy access for researchers with minimal programming experience. However, programming of self-implemented models yields the most freedom for the developer and allows for most control during the modeling process and simulation [83]. Modern programming languages have made immense advances and a proper choice is predominantly a question of the developer's preferences.

PARAMETER DEFINITION Parameters of a model may be distinguished into several types. *Fixed parameters* do not change their value during the simulation and typically originate from prior experiments, as *e.g.* body temperature [84]. For *variable parameters*, a specific value cannot be given, due to either variability of the parameter itself, as is the case for *e.g.* cell speeds, heterogeneous experimental results or no experimental accessibility at all. The variability of such data can be adequately modeled by sampling the observed heterogeneity [85]. Where this is not possible, unknown parameters can be scanned over reasonable ranges. However, this is time-consuming because the model results must be interpreted in the context of the complete scanning range. Besides, the parameter space grows exponentially and thus quickly exceeds a scannable size. In parallel, the parameter space can be reduced by combining highly correlated parameters into *derived parameters*. Although they may not directly reflect a biological entity, it allows for model simplification. Some parameters of a model must be calibrated before simulation of a model. This calibration may involve derived parameters or parameters that originate from the model design, *e.g.* the influx of an external resource at model bound-

aries. In practice, the parameter is varied over multiple simulations until an error function is minimized [86, 87].

VALIDATION & SIMULATION Validation of the model with test input data against a ground truth will ensure the model plausibility and quality [88]. If this is not given and a model fails to reproduce *e.g.* experimental results, the modeling cycle needs to be restarted at previous steps. Moreover, the model can be validated by assessing the sensitivity, *i.e.* investigating the dependence of the output on input perturbations [89]. Depending on the impact of one parameter's perturbation, key parameters of the model can be identified. In parallel, a variation of the model, *e.g.* exclusion of a mechanism, will reveal the dependencies of the model to this mechanism [64]. This approach allows identifying the importance of mechanisms and might allow excluding mechanisms with a weak influence on the outcome for simplification and a reduction of computation needs. In the same way, indispensable mechanisms might be identified to increase the understanding of the underlying biological system. Biological systems typically exhibit a homeostatic state that must be reached again after perturbations. A model's stability can be assessed by determining how efficiently this state can be reached again after perturbations [90]. All of these methods allow validating a model and ensure its quality for application but also reveal valuable insights into the modeled system itself.

When simulation results are analyzed, new hypotheses can be formulated and validated in experiments contributing to the cycle of systems biology (see Figure 1.3). In the following, the modeling cycle restarts, and the model can be refined by including new knowledge. Decisions from the first cycle must be inspected critically, resulting in either a new model design, alterations in the model structure or a higher degree of detail.

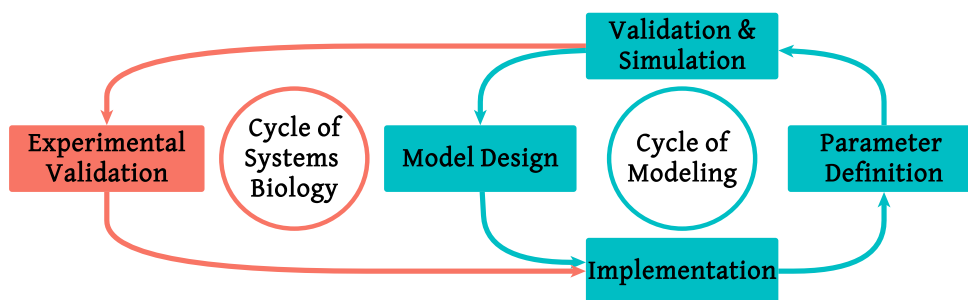


Figure 1.3: Wet lab experiments yield knowledge that can be used to design computer models in the dry lab. The circular process of modeling enables a repetitive increase in quality. Hypotheses derived from models will be validated in wet lab experiments resulting in an iteration of the whole cycle.

1.2.3 Virtual infection modeling of *A. fumigatus*

Many different models have been published in recent decades, from simple mathematical models to huge modeling frameworks [91]. Whereas certain model types show advantages and disadvantages over other types, it is difficult to make a comprehensive characterization between all design concepts. Since this thesis builds on publications where so-called agent-based models are the model type of choice, a focus is set on this type of model. Selected publications of different model designs in the context of *Aspergillus fumigatus* infections are presented first, to reflect the agent-based model's advantages and disadvantages.

1.2.3.1 Existing models of *A. fumigatus* infections

In 2015, Tanaka *et al.* presented an ordinary differential equation (ODE) model of *A. fumigatus* infections [92]. It comprises four equations of cellular and molecular entities, including thirteen parameters, of which eight were derived from literature and five were calibrated by fitting the model to experimental data. This ODE model allowed evaluating infection courses depending on the uptake dose of fungal spores or the state of PMN depletion. As a result, the relative contribution of parameters and cells on the infection outcome can be quantitatively described. This example shows the benefits of ODE models. ODEs can be explicitly defined by a clear and mathematical definition and solved by established explicit and implicit methods such as from Euler or Runge and Kutta. They can be simulated quickly by many reliable tools with little effort. ODE systems are well understood and a broad theoretical background on *e.g.* steady state, stability, or bifurcation analysis, eases application [93]. On the drawback side, ODEs assume a well-mixed system of entities without spatial confines and have no spatial dimension at all, which prohibits the investigation of spatial processes. Although this may be partly overcome by partial differential equations or the introduction of compartments into the model, it remains a significant limitation [94]. Entities of the same type cannot be distinguished and therefore do not allow for individual-based behavior within the model. Although deterministic, stochastic processes may be included with drawbacks such as higher computation needs [95]. In practice, additional disadvantages often appear as additional assumptions must be made, *e.g.* Tanaka *et al.* assume the number of available PMN to be constant.

A way of modeling that does allow for individuality is based on game theory, a mathematical concept originating from social science that has been widely applied in biology [96]. It focuses on the decision-making of model entities and

therefore allows evaluating strategies. Model mechanisms are reduced from a result-oriented perspective allowing for a low number of parameters without losing the entities' individuality. Pollmächer *et al.* [97] published a paper applying evolutionary game theory models on *A. fumigatus* infections in which the infection outcome is modeled from a conidium perspective. Each conidium follows a different strategy of *e.g.* resting or swelling, and as a result of this it triggers different responses from the immune system in a three-staged setup. Finally, the infection outcome can be compared under different strategies and parameters.

In contrast to ODE models, game theory models can capture individuality by assigning different states to entities of the same type without the need for many or mixed entities. Besides, it is much easier to incorporate spatial aspects as Pollmächer *et al.* did by extending the model by a graph-based neighborhood relation. A disadvantage of game theory models is a set of assumptions that are made on the entities' individuality. In the classical game theory, each model entity is assumed to follow logical decisions based on information that represents a general rationality in behavior [98]. Although this assumption can be made for whole organisms, it can only be made limited for cells such as the conidia of *A. fumigatus* as their behavior depends on molecular responses but not active decision-making after information evaluation. Evolutionary game theory, as used by Pollmächer *et al.*, drops the assumption of rationality in behavior and replaces it with an evolutionary fit of behavior by trial and error [99].

1.2.3.2 Agent-based Models

Models requiring a considerable level of detail can be designed as an agent-based model (ABM). This modeling concept captures each model entity – named agents – at a high individuality, which allows distinguishing between agents of the same type [100]. Thus, each aspect of a model, such as movement and interaction between agents, can be modeled at an application-dependent detail level. Consequently, the design may require much more effort as more details must be incorporated into the model and, potentially, more data is needed.

On the other hand, the description of complex systems by simulating individual agent behavior allows for a new level of model validation, which *e.g.* ODE models cannot provide. Although tools for the development of ABMs, such as Netlogo [101] and Repast [102], are available, the high level of individuality typically enforces custom code creation and requires programming skills. As this may be seen as a drawback, it prompted the publication of a diverse set of ABM in biology with a high degree of detail [103]. These custom models are even combined with models of other types where an individual agent perspective is

not needed [104]. Such hybrid models are expensive to construct in terms of time, data and money but combine the power of different modeling techniques while leaving a maximum of freedom in design choices.

The basis of this thesis is a hybrid agent-based alveolus model capturing the spatio-temporal aspects of *A. fumigatus* infections. Although the conidia of *A. fumigatus*, after inhalation, may settle in various parts of the human lung, the alveoli represent the majority of lung surface and the spot with highest incidents for lethal infections and therefore are considered to be the most prominent space of infection [105]. These alveoli are polyhedral to spherical with a diameter of approximately $120\ \mu\text{m}$ and interconnected by Pores of Kohn [106, 107]. Their surface is covered by alveolar epithelial cells (AEC) of type I and II, which secrete a layer of surfactant covering the cellular surface [108]. Single alveoli are connected to the alveolar sac by an alveolar entrance ring. Upon inhalation of a conidium and its arrival in the alveolar surfactant layer, a run against time is triggered between the fungus and the host immune system, which is lost by the host if the conidium cannot be phagocytosed by an alveolar macrophage (AM), PMN or AEC before dissemination [109–111]. The implications for model design are apparent. First, the complex polyhedral to spherical shape of alveoli must be considered in which immune cells chase to detect the conidium. Second, the low number of cells participating in this arms race does not allow *e.g.* for assumptions of well-mixed cell populations and only one successful phagocytosis would clear the threat. Consequently, cells have to be captured on a detailed and individual basis. As a result, agent-based modeling is a practical choice to simulate the complex dynamics during *A. fumigatus* infections.

OBJECTIVES OF THIS THESIS

Understanding the dynamics of host interactions during *A. fumigatus* infections is crucial to assess factors of pathogenicity and potentially develop new therapeutic targets. Understanding key factors of the immune system in a disease with rising worldwide incidence and high mortality would allow developing new strategies, improving diagnostics, allowing for purposeful treatment and ultimately saving lives.

The innate immune response as a first line of cellular defense represents a key factor in infection clearance at an early stage. Although many wet lab experiments have been conducted, a complete picture of the infection dynamics *in vivo* remains unavailable. This thesis aims to fill the picture by applying a hybrid agent-based alveolus model of *A. fumigatus* infections in the human lung. In this way, wet lab limitations can be overcome and detailed mechanisms can be analyzed quantitatively.

In wet lab experiments, animal models are often used to gather *in vivo* data of *A. fumigatus* infections. However, new findings originating from mouse models can only be transferred to humans in a limited way. The existing hybrid agent-based model was therefore adapted from humans to mice to assess differences in the infection dynamics and answer the following questions:

- Which differences in the lung morphology between human and mice are important in the context of *A. fumigatus* infection?
- How do differences on the lung morphology alter the infection dynamics?
- How comparable are typically-used infection doses in murine models to natural infections of humans?

Pores of Kohn are a morphological feature of the mammalian lung and they are assumed to have an impact on cellular dynamics in the alveoli [112]. However, partly contradicting theories exist and a comprehensive understanding of the role of Pores of Kohn is lacking [113, 114]. Especially the function as possible passageways for cells is not understood. To evaluate this role, the hybrid agent-based alveolus model was adapted to assess how different theories on Pores of Kohn would alter the infection dynamics of infections of *A. fumigatus* to answer the following questions:

- How do Pores of Kohn influence the infection clearance of *A. fumigatus* conidia?
- How do Pores of Kohn change the migration of alveolar macrophages?

Novel aspergillosis-on-a-chip devices allow for an *in vitro* accessibility of alveolar tissue to examine the dynamics of *A. fumigatus* infections. Combining these chips with 3D imaging technique allows quantifying and modeling growth mechanisms of invasive hyphae. This enables exploring the following question:

- How do hyphae grow and manage to penetrate tissue during infections of *A. fumigatus*?

Part II

MANUSCRIPTS

FORMULAR 1¹

Manuskript Nr. 1

Titel des Manuskriptes: Comparative Assessment of Aspergillosis by Virtual Infection Modeling in Murine and Human Lung

Autoren: Marco Blickensdorf, Sandra Timme, Marc Thilo Figge

Bibliographische Informationen : *Front Immunol* 2019 Feb 5;10:142. doi: 10.3389/fimmu.2019.00142.

Der Kandidat / Die Kandidatin ist

Erstautor/-in, Ko-Erstautor/-in, Korresp. Autor/-in, Koautor/-in.

Status : publiziert

Anteile (in %) der Autoren / der Autorinnen an der Publikation (anzugeben ab 20%)

Autor/-in	Konzeptionell	Datenanalyse	Experimentell	Verfassen des Manuskriptes	Bereitstellung von Material
Blickensdorf	10 %	70 %	80 %	40 %	
Timme	20 %	20 %	20 %	40 %	
Figge	70 %	10 %		20 %	100 %

Unterschrift Kandidat/-in

Unterschrift Betreuer/-in (Mitglied der Fakultät)

¹ Die Unterschriften müssen nur im separat im Dekanat einzureichenden ausgefüllten Formular im Original vorliegen. In der in die Dissertation eingebundenen Fassung dürfen die Unterschriften und Unterschriftenfelder fehlen.



Comparative Assessment of Aspergillosis by Virtual Infection Modeling in Murine and Human Lung

Marco Blickensdorf^{1,2}, Sandra Timme^{1,2} and Marc Thilo Figge^{1,2*}

¹ Research Group Applied Systems Biology, Leibniz Institute for Natural Product Research and Infection Biology-Hans Knöll Institute, Jena, Germany, ² Faculty of Biological Sciences, Friedrich Schiller University of Jena, Jena, Germany

OPEN ACCESS

Edited by:

Burkhard Ludewig,
Kantonsspital St. Gallen, Switzerland

Reviewed by:

Lalit Kumar Dubey,
Université de Lausanne, Switzerland
Joana Vitte,
Aix-Marseille Université, France

*Correspondence:

Marc Thilo Figge
thilo.figge@leibniz-hki.de

Specialty section:

This article was submitted to
Molecular Innate Immunity,
a section of the journal
Frontiers in Immunology

Received: 25 October 2018

Accepted: 17 January 2019

Published: 05 February 2019

Citation:

Blickensdorf M, Timme S and
Figge MT (2019) Comparative
Assessment of Aspergillosis by Virtual
Infection Modeling in Murine and
Human Lung. *Front. Immunol.* 10:142.
doi: 10.3389/fimmu.2019.00142

Aspergillus fumigatus is a ubiquitous opportunistic fungal pathogen that can cause severe infections in immunocompromised patients. Conidia that reach the lower respiratory tract are confronted with alveolar macrophages, which are the resident phagocytic cells, constituting the first line of defense. If not efficiently removed in time, *A. fumigatus* conidia can germinate causing severe infections associated with high mortality rates. Mice are the most extensively used model organism in research on *A. fumigatus* infections. However, in addition to structural differences in the lung physiology of mice and the human host, applied infection doses in animal experiments are typically orders of magnitude larger compared to the daily inhalation doses of humans. The influence of these factors, which must be taken into account in a quantitative comparison and knowledge transfer from mice to humans, is difficult to measure since *in vivo* live cell imaging of the infection dynamics under physiological conditions is currently not possible. In the present study, we compare *A. fumigatus* infection in mice and humans by virtual infection modeling using a hybrid agent-based model that accounts for the respective lung physiology and the impact of a wide range of infection doses on the spatial infection dynamics. Our computer simulations enable comparative quantification of *A. fumigatus* infection clearance in the two hosts to elucidate (i) the complex interplay between alveolar morphometry and the fungal burden and (ii) the dynamics of infection clearance, which for realistic fungal burdens is found to be more efficiently realized in mice compared to humans.

Keywords: virtual infection modeling, *Aspergillus fumigatus* lung infection, mouse model, human model, hybrid agent-based computer simulations

INTRODUCTION

The concept of systems biology constitutes a powerful approach to investigate biological phenomena by combining wet-lab and dry-lab investigations that mutually support and complement each other (1–3). However, systems biology of infection faces problems that can interrupt the experiment-theory-cycle of systems biology (4–6). First, since *in vivo* experiments are predominantly conducted in animals, the general transferability of findings in the context of immunology to the human system is a matter of ongoing dispute (7, 8). Secondly, even in animal experiments it may be impossible to capture the spatio-temporal dynamics of infection processes. For example, in the case for lung infection *in vivo* time-lapse imaging is challenging due

to animal breathing. In these cases, virtual infection modeling is of particular importance, since it has the potential to advance our knowledge despite the aforementioned limitations and to generate hypotheses that direct future experiments in a targeted manner (9, 10). In particular, building *in silico* models of infection on the available experimental data basis, gives rise to realistic to-scale models that can be used to compare the outcome of computer simulations for animal and human systems.

In this study, we use virtual infection modeling to investigate *Aspergillus fumigatus* lung infections. *A. fumigatus* is an environmentally wide-spread fungus that is an opportunistic pathogen causing severe infections in immunocompromised patients (11–14). The fungal conidia are small in size of 2–3 μm (12, 13) and can reach the alveoli in the lower respiratory tract of the lung. Because alveoli make up about 50% of the lung volume and also make the largest contribution to lung surface area, they are by far the most likely niche for infection (15). If not efficiently removed by the innate immune system, *A. fumigatus* can cause invasive pulmonary aspergillosis (IPA) with high mortality rates of 30–90% (11). The resident immune cells in the lung are alveolar macrophages (AM) that constitute the first line of immune defense by phagocytosing the inhaled conidia (11, 14, 16). Without efficient clearing by innate immunity, *A. fumigatus* conidia can undergo morphological changes: Upon contact to the surfactant layer, which covers the alveolar epithelial cells (AEC) (15), resting conidia can swell and after $\sim 6\text{h}$ start forming hyphae. These hyphae are able to penetrate the epithelial tissue of the alveolus and can thereby reach the bloodstream, from where they may disseminate and cause severe systemic infections (12, 13, 17). The first six hours after entrance of the conidia in the lung are therefore considered as a critical time frame, during which conidia need to be found in order to prevent damage of host tissue. This implies that the role of adaptive immunity can be neglected compared to a required rapid response by innate immunity, e.g., involving the complement system as well as phagocytic activity by AM and neutrophils. The condition of neutropenia, i.e., the considerable reduction in the absolute neutrophil count, poses a major risk factor for IPA (14, 18). Therefore, the nowadays increasing number of immunocompromised patients leads to a rising clinical prevalence, making *A. fumigatus* a relevant target for fungal infection research. Due to its complex interactions with the host immune system and its ability to adopt different morphologies, various levels of pathogenicity have to be considered in the development of effective therapy (13, 19).

Various mammalian species have been used for experimental research on *A. fumigatus* infection. Besides rats, rabbits, and guinea pigs, mice models have been used most extensively (20). It is important to note that—in order to provoke measurable numbers of interactions between pathogens and host cells—the experimentally applied infection doses typically are orders of magnitude higher compared to the natural inhalation dose for humans, which ranges between a few hundred and thousands of conidia per day (21–25). Thus, in addition to studying animal systems with host environments that are quite different from the human system, the significant differences in the applied infection doses need as well to be taken into consideration

in the knowledge transfer from animals to humans. However, little is known about the comparability and transferability of mouse infection models in wet-lab and natural *A. fumigatus* infections in human. Therefore, in this study we compare *A. fumigatus* infection in mice and humans using virtual infection modeling to account for the respective lung morphologies and study the impact of the infection doses. In passing we note that, even though daily inhalation doses will be associated with homeostatic clearance and will typically pass unnoticed, we here use throughout the more general term infection clearance involving inflammation, tissue damage and a multifactorial host response in the case of high fungal doses.

In previous studies, we already implemented an infection model for the simulation of *A. fumigatus* infection in humans. The agent-based model (ABM) was built on an extensive experimental data basis available from literature and represents a typical human alveolus in three-dimensional continuous space (26, 27). The human alveolus was composed of AEC of type I and II, as well as of Pores of Kohn (PoK) representing connections between neighboring alveoli (28, 29). Our computer simulations revealed that AM performing random walk migration are not able to reliably detect a conidium in the alveolus before the onset of germination, i.e., before 6h post infection (17, 26). This led to the hypothesis that a not yet experimentally identified chemotactic signal must exist that guides AM to the position of the conidium in the alveolus (26). The virtual infection model was then extended to explicitly incorporate chemokine secretion and diffusion by solving partial differential equations in a hybrid ABM (27). Scanning all unknown parameters within reasonable ranges, we determined those relevant for efficient pathogen clearance. For example, we found that a preferably high ratio of chemokine secretion by AEC with rate s_{AEC} over chemokine diffusion with diffusion coefficient D is required to establish a chemokine gradient that facilitates AM to detect a conidium before the onset of germination.

While these studies considered the immune response in human alveoli for daily inhalation doses of *A. fumigatus* conidia, the focus of the present study is on comparing *A. fumigatus* infections in mice and humans taking into account natural as well as experimental infection doses. Thus, we significantly adapted the agent-based virtual infection model to the to-scale morphometry of mouse alveoli. This enables generating comparative and quantitative predictions on the influence of morphological factors as well as dose-dependent effects during *A. fumigatus* infection in mice and humans.

RESULTS

Aspergillus fumigatus lung infection is commonly investigated using mouse models (20), where the pathogens can be administered in different ways (30): Intranasal deposition and intra-tracheal/intra-bronchial instillation bring the conidia directly in the nose or trachea/bronchia and are based on liquid solutions, while a more natural administration is realized in inhalation chambers with air-soluted conidia. All methods have in common that relatively high doses of $10^6 - 10^8$ conidia

are applied; however, the amount of conidia which is actually reaching the lower respiratory tract, i.e., the fungal burden in the alveoli of the mouse lung is found to be in the range of $10^3 - 10^5$ conidia (31, 32). On the other hand, it is reported that the distribution of conidia is fairly uniform only for administration by inhalation, whereas intranasal administration is accompanied with the accumulation of conidia in specific lung sections, i.e., inducing distributions with local variations in the fungal burden (33). This implies that our *in silico* experiments need to incorporate three major issues that differ from simulations of the human infection scenario: (i) implementing the differences in the morphometry of the lung for human and mouse, (ii) scanning for a larger range of infection doses, and (iii) studying the limit of high local fungal burdens due to the non-uniform distribution of conidia for administration based on liquid solutions.

As a measure of fungal clearance, we introduced an infection score $IS^{s=H,M}$, where the superscript refers to the human ($s = H$) or mouse ($s = M$) system and $IS^{s=H,M} = 0$ ($IS^{s=H,M} = 1$) implies that infections were cleared in each (none) simulations (for details see Materials and Methods section, Readout of Simulations).

Putative Morphology-Related Impact on Infection Clearance in Humans and Mice

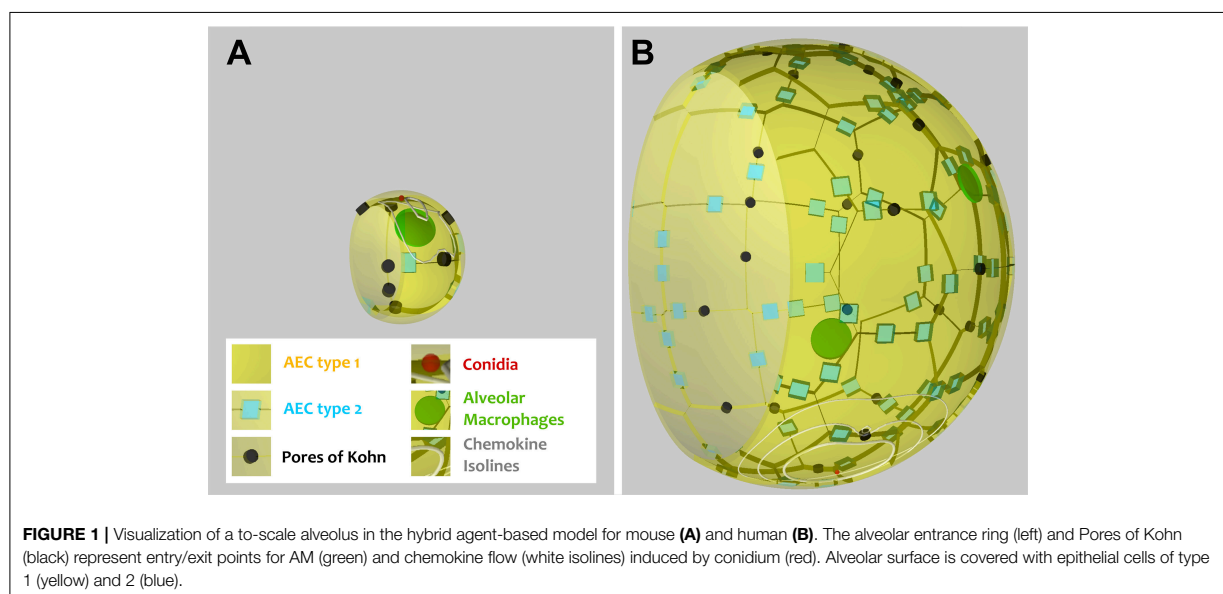
As can be seen in **Figure 1**, the alveoli for human and mouse have been implemented as to-scale models that are composed of AEC of type I and II, as well as PoK. Given the differences in the size and composition of alveoli for the two organisms (see **Table 1** and **Supplementary Table 1**), it can be expected that infections may be cleared with different efficiency. For example, the surface area of the human alveolus is about 20 times larger compared to that of the murine alveolus and the number of AM per alveolus is about 6 times higher in the human alveoli. This gives rise to a scanning area per AM, which

is about three times higher in humans suggesting that mice could cope much better with the detection of alveolar pathogens. However, the situation is complicated by the fact the number of PoK per alveolar area is higher by a factor 5.7 in the mouse alveolus, which together with the alveolar entrance ring gives rise to an increase of the relative alveolus' open boundary length by a factor 3.4 compared to the human alveolus. On the one hand, since AM can enter and leave the alveolus only across these boundaries (28, 29), this may result in a faster infection dynamics of the murine system. On the other hand, chemotactic signaling molecules can as well flow out of the alveolus via these boundaries implying that their increased length in the murine alveolus may be of disadvantage with regard to establishing an efficient chemokine gradient. Again, this argument may only be valid for a low pathogen density in the alveolus, because for high pathogen densities the induced chemokine profile may

TABLE 1 | Comparison of morphometric parameters and innate immune cells.

Parameter	Human alveolus	Mouse alveolus (references)
Radius of alveolus	116.5 μm	26.2 \pm 7.2 μm (29, 34–41)
Number of type 1 AEC	48	4 (42)
Number of type 2 AEC	84	4 \pm 2.4 (42–44)
Number of PoK	24	7 (45)
Type 1 AEC radius	27 μm	22 μm
Type 2 AEC edge length	9.34 μm	8.12 μm (42)
Number of alveoli per lung	4.8×10^8	$3.3 \pm 1.3 \times 10^6$ (34, 41)
Number of AM	2.1×10^9	$2.4 \pm 0.7 \times 10^6$ (42, 46)
Radius of AM	10.6 μm	9.5 μm (47)

The parameters of the human alveolus were taken from the literature search by Pollmächer et al. (26) and those of the mouse alveolus have been retrieved from the indicated references.



provide an ambiguous signal for AM guidance. For the same fungal burden in mice and humans, the pathogen density is much higher in the murine alveolus, due to their much lower number and smaller size. Therefore, *A. fumigatus* may be much more efficiently cleared from the human lung. Taken together, these considerations imply that the efficiency of the infection dynamics will depend on the combination of the alveolar morphometry and the fungal burden that together impact on the chemokine profile for AM migration in a way, which is impossible to quantitatively predict without performing comparative computer simulations of to-scale models.

Case of Low Fungal Burden: *A. fumigatus* Infection More Efficiently Cleared in Mice

We first consider the case of low fungal burden, which we define as the case where one *A. fumigatus* conidium per alveolus is the highest alveolar occupation number (AON) that is statistically expected to occur in the whole lung. The corresponding fungal burden can be derived from the binomial distribution (see Methods section for details) and is 2.5×10^3 in mice and 3×10^4 in humans (see Figure 2). This implies that the limit of low fungal burden covers the dose of daily inhalation for humans, but is relatively low for experimental conditions in typical mice experiments. Examples of the infection dynamics can be seen for humans and mice in Supplementary Videos 1, 2, respectively.

Our previous work on *A. fumigatus* infection in human alveoli for low fungal burden revealed that a high secretion rate s_{AEC} of chemotactic molecules combined with a low diffusion coefficient D of the chemokine is beneficial for a small infection

score IS^H in humans (27). In the present study, we screened the diffusion coefficient and the secretion rate in the regimes, respectively, $D = [20, 6 \times 10^3] \mu m^2/min$ and $s_{AEC} = [1.5 \times 10^3, 5 \times 10^5] min^{-1}$ for alveoli of mice and humans. The numerical results for the quantitative comparison between human and mouse is shown by the infection scores $IS^{H,M}$ in Figure 3A. It can be observed that, for all combinations of D and s_{AEC} , the infection score in mice is significantly smaller: $IS^M < IS^H$. Furthermore, it can be seen that the relation of a high secretion rate and a low diffusion coefficient also leads to a more efficient infection clearance in mice. The relative difference in the infection scores of the two organisms, $\Delta IS = 1 - IS^M / IS^H$, is in the range 50 – 90 %, indicating that the murine system performs always better than the human system in the limit of a low fungal burden.

Case of Low Fungal Burden: Size of Alveolus Governs Infection Dynamics

To dissect whether the infection dynamics is governed by the chemotaxis or the alveolar size, we compared the probability of directed AM migration resulting from one conidium in the alveolus of mice and humans. The chemokine concentration itself falls off with the distance from the source AEC, i.e., the AEC in contact with the conidium. In order to avoid that AM perform mostly random walk migration, the chemokine gradient (i) must not exceed a certain value to avoid saturation of AM chemokine receptors and (ii) must not fall below a certain value to provide a detectable signal. As a qualitative measure of gradient efficiency we calculated the probability that AM follow the gradient depending on the distance to the source AEC. This probability reflects the impact of the chemokine gradient on AM migration and was computed as explained in Supplementary Methods (see section on AM Migration) for optimal chemokine parameters (D_{opt}^s, s_{AECopt}^s) in the human (s=H) and mouse (s=M) system. The optimal parameters were computed from the 36 scanned parameter combinations, $\{D_1 \dots D_6\} \times \{s_{AEC1} \dots s_{AEC6}\}$, for the diffusion coefficient and the secretion rate as follows: Based on the simulation results in terms of the infection score $IS_{D_i, s_{AEC_i}}$ and the limits of its respective 95%-confidence interval, we computed the optimal diffusion coefficient as $D_{opt} = \frac{1}{\sum_i w_i} \cdot \sum_i w_i \cdot D_i$ with weights $w_i = 1 - IS_{D_i, s_{AEC_i}}$ for all those parameter combinations that had infection scores not exceeding the minimal upper limit of all confidence intervals (see Supplementary Video 3). The optimal secretion rate $\overline{s_{AECopt}^s}$ was determined in the same way yielding for the human host $\overline{D_{opt}^H} = 34 \mu m^2 min^{-1}$ and $\overline{s_{AECopt}^H} = 1.5 \times 10^4 min^{-1}$ and for the murine host $\overline{D_{opt}^M} = 61 \mu m^2 min^{-1}$ and $\overline{s_{AECopt}^M} = 4.9 \times 10^4 min^{-1}$ as the optimal parameters in the limit of low fungal burden.

The probability of directed AM migration for both host systems and for their respective optimal chemokine parameters is plotted in Figure 3B. The two curves exhibit quantitative similarity suggesting that the infection dynamics in the case of a low fungal burden is mainly governed by the size of the alveolus rather than the chemokine profile itself. Thus, in contrast to the significantly larger human alveolus, AM in the murine

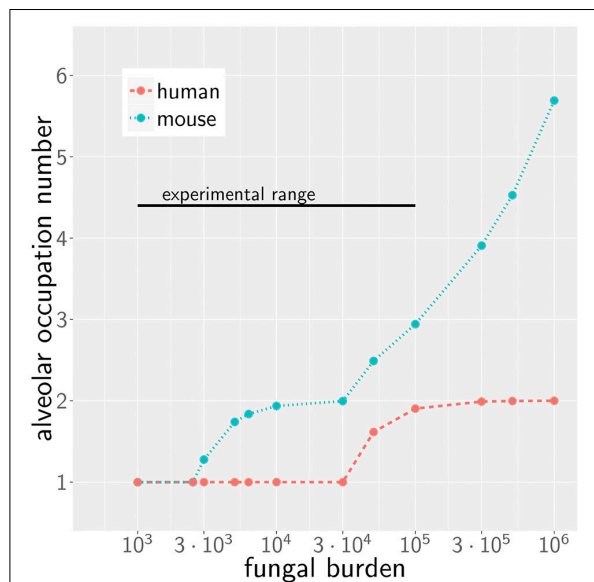
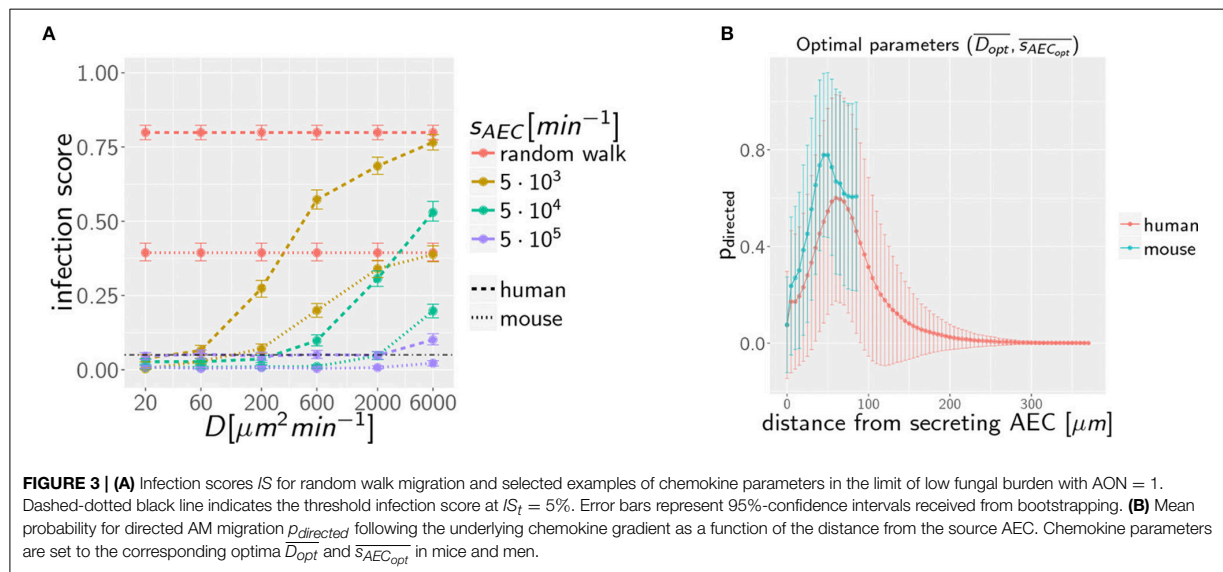


FIGURE 2 | Alveolar occupation number, the maximal expected number of present conidia per alveolus, as a function of the fungal burden in mouse (blue) and human (red). Black line represents the experimental range of fungal burden, which is reached in typical mice model experiment.



counterpart will typically perform directed migration across the entire alveolus.

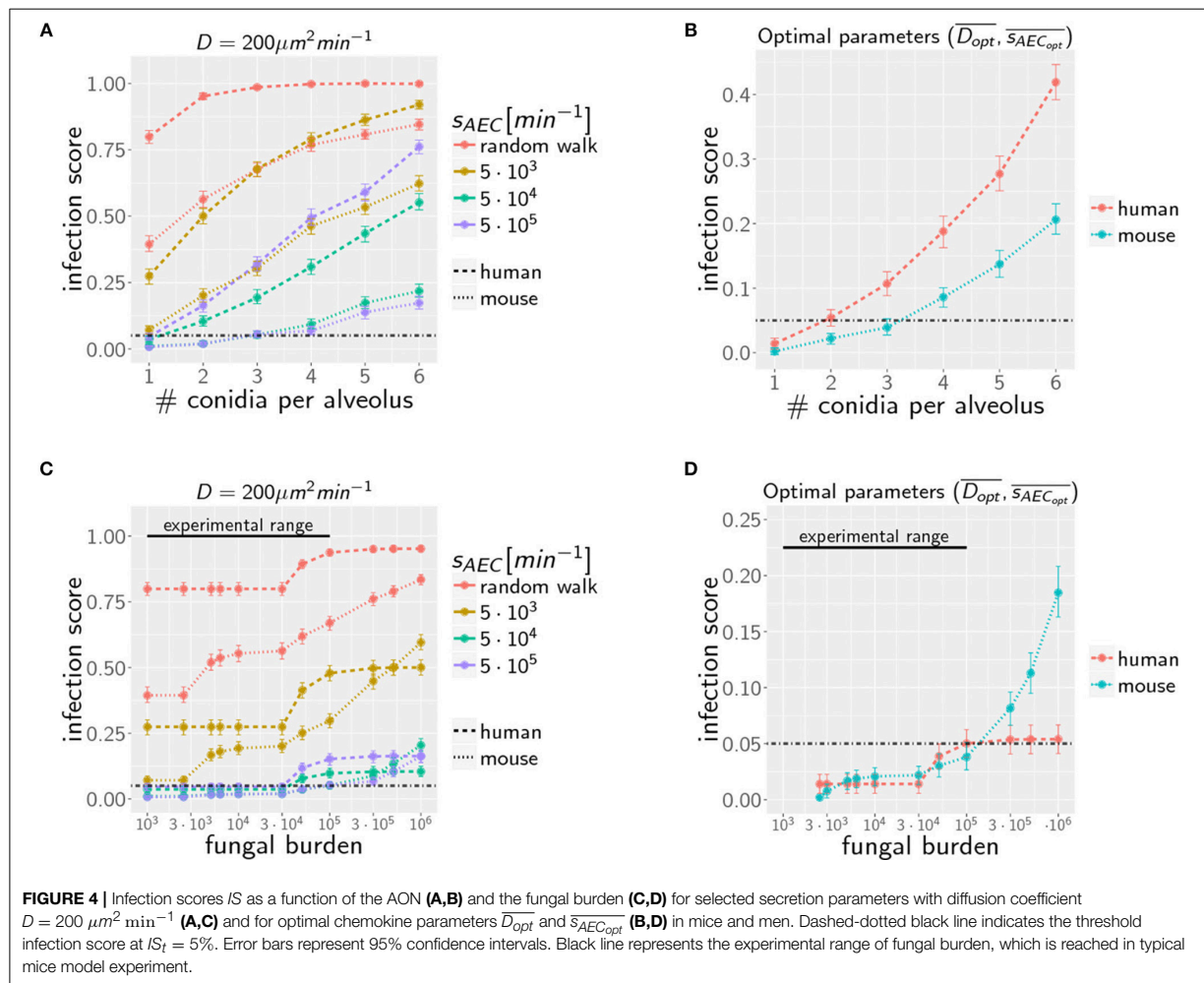
A. *fumigatus* More Efficiently Cleared in Mice for Any Alveolar Occupation Number

Increasing the AON from one to higher conidia numbers, we again performed computer simulations for various infection scenarios that differ in the parameters for chemokine secretion s_{AEC} and diffusion coefficient D . However, multiple conidia within the alveolus can lead to more complex chemokine profiles derived from the various conidia-associated AEC that are simultaneously serving as sources of chemokine secretion. In **Figure 4A** the infection scores IS obtained from 10^3 simulations are summarized for AON between one and six and for selected secretion rates s_{AEC} , while the numerical results for the full range of studied parameter values is shown for human and mouse in **Supplementary Figure 1**. Parameter regimes of efficient infection clearance in these plots resemble those previously found for one conidium in the human alveolus (27), indicating that low ratios D/s_{AEC} are as well preferred in the mouse system.

Extending the computation of optimal chemokine parameters for one conidium to larger AON enables computing for both systems the average optimal parameter set (see **Supplementary Figure 2**). We obtain for one to six conidia per alveolus the averaged optimal values $\overline{D_{opt}^H} = 26 \pm 6.6 \mu m^2 min^{-1}$ and $\overline{s_{AEC_{opt}}^H} = 1.1 \times 10^4 \pm 6 \times 10^3 min^{-1}$ for the human host and $\overline{D_{opt}^M} = 74 \pm 22.4 \mu m^2 min^{-1}$ and $\overline{s_{AEC_{opt}}^M} = 8.0 \times 10^4 \pm 4,1 \times 10^4 min^{-1}$ for the murine host. In **Figure 4B**, we show that the resulting infection score IS as a function of the AON is always significantly lower in mice compared to humans.

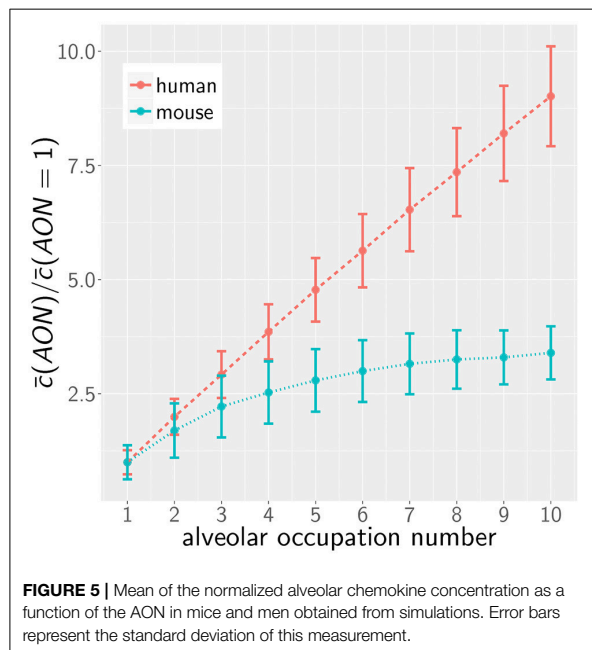
Case of High Fungal Burden: Chemokine Profile Can Deteriorate Clearance Efficiency

Due to morphometric differences between the lungs of mice and humans, the AON is not directly related to the fungal burden. This follows from our earlier statistical considerations on the highest AON that is expected to occur in the whole lung for a given fungal burden (see **Figure 2**) exhibiting a significant quantitative difference between mice and humans. Since the number of more than 10^8 alveoli in the human lung exceeds that of mice by more than two orders of magnitude, even in the case of an extremely high fungal burden with 10^6 conidia in the lung, the maximal AON for humans does not exceed two. In contrast, the same fungal burden in the lung of mice yields a maximal AON between five and six conidia in one alveolus. It thus follows that a comparison between mice and humans for the same fungal burden requires contrasting infection scenarios with different AON. Of note, our analysis focuses on the maximal AON for a given fungal burden, because it is argued that this configuration will be directly correlated with the estimated time needed to clear all occupied alveoli from the pathogen. In **Figures 4C,D** the numerical results for the infection score IS are shown for mice and humans as a function of the fungal burden, respectively, for identical chemokine parameters and for the respective optimal chemokine parameters. **Supplementary Figure 3** shows the infection score IS as a function of the fungal burden for all the scanned parameter combinations. It can be seen by the smaller infection scores in the murine host that infections are still more efficiently cleared for the entire experimentally relevant range of $10^3 - 10^5$ conidia in the lung. In **Supplementary Video 3** we indicated all combinations of chemokine parameters for which the infection score reaches values below the threshold of $IS_t = 5\%$.



However, as we have mentioned before, administration of conidia based on liquid solutions is reported to be associated with higher local fungal burdens due to a more non-uniform distribution of conidia (33). It can be seen in **Figure 2** for a uniform distribution of conidia that a high fungal burden in the range $10^5 - 10^6$ conidia per lung is associated with an AON of two in the human system, whereas this value ranges between three and six for the murine system. Consequently, for a non-uniform distribution of conidia, such high AON can be reached in the murine lung and these can result in infection scores that are much higher than for the human system with AON of two, even if the respective optimal chemokine parameters are applied (see **Figure 4B**). Our spatio-temporal computer simulations of the infection scenarios reveal that higher AON are associated with chemokine profiles that deteriorate clearance efficiency. Since the mouse alveolus contains more than 10 times fewer AEC compared to the human alveolus (see **Table 1**), multiple randomly positioned conidia will occupy most of the alveolus' AEC associated with chemokine secretion from various source AEC. First of all, this can lead to chemokine saturation that

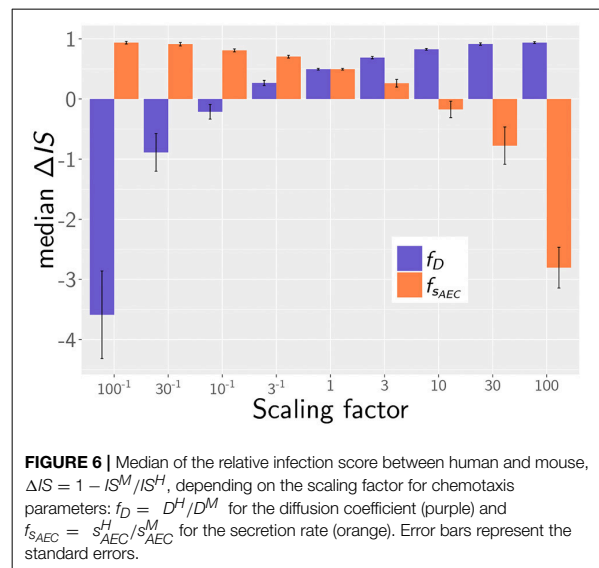
will turn directed AM migration into random walk migration. Secondly, if the number of conidia is increased further, this will not alter the chemokine gradient anymore. Consequently, AM will perform the inefficient random walk migration until a sufficient number of conidia is detected, such that AM migration becomes again dominated by the chemokine gradient. Obviously, this complex interplay between the morphometry of the alveolus and the chemokine profile will be much less pronounced for the larger human alveolus that consists of many more AEC. To validate this hypothesis, we computed the mean values of the chemokine concentration across all alveolar surface grid points in the simulations and found that significant deviations arise between the human and mouse alveolus starting at AON of four. As can be seen in **Figure 5**, for AON above four the mean concentration value in the murine alveolus does change only slightly providing no additional chemotactic guidance to AM, whereas it is still increasing in the human alveolus and can provide chemotactic guidance associated with lower infection scores IS in the human alveolus and in the limit of fungal burdens well above the typical experimental range.



Simulation Results Are Qualitatively Robust Against Variations of Model Parameters

In the quantitative comparison of infection scenarios in mice and humans, we so far assumed the same values for the model parameters. For example, we assumed that the chemokine secretion rates from human and murine alveolar epithelial cells are similar. However, it may be argued that this does not reflect the physiological reality correctly, since murine AEC are effectively about 33% smaller in area and may thus exhibit a reduced potential of chemokine secretion. Similarly, it is an open question today whether the postulated chemotactic signals in human and mice are transmitted by chemokines that are structural homologs and can therefore be expected to have similar diffusion coefficients in the surfactants of mice and humans. While these uncertainties cannot be avoided, we estimated the impact of variations in these parameters on the infection score in humans and mice. To this end, we calculated the relative infection score between the human and murine model $\Delta IS = 1 - IS^M / IS^H$, over all simulated parameter combinations in the experimental range of fungal burdens. Setting both diffusion parameters in humans and mice to identical values, the mouse shows lower relative infection scores with a median value of $\Delta IS = 0.49$.

Next, we analyzed the robustness of the infection outcome with regard to the diffusion coefficient and the secretion rate. To this end, we compared the infection scores for humans and mice for those simulated parameter combinations that obey the scaling factors $f_D = D^H / D^M$ for the diffusion coefficient and $f_{s_{AEC}} = s_{AEC}^H / s_{AEC}^M$ for the chemokine secretion rate. For example, comparing diffusion coefficients with scaling factor $f_D = 3^{-1}$ (i.e., $D^H = (20, 200, 2000) \mu m^2 / min$, $D^M = (60, 600, 6000) \mu m^2 / min$) revealed a reduction in the median



value of the relative infection score to $\Delta IS = 0.27$ over the scanned fungal burdens. This indicates that the infection score in mice is higher in > 50% of all selected parameter combinations, even if the diffusion coefficient is three times higher in the murine alveolus (see **Figure 6**). The scaling factor of the secretion rate $f_{s_{AEC}}$ has a reversed impact on the relative infection score reflecting that a high ratio s_{AEC} / D induces low infection scores (see **Figure 6**).

Taken together, our simulation results imply that our main conclusions are qualitative robust against variations in the chemotaxis parameters. As long as the associated scaling factors have values $f_D > 10^{-1}$ or $f_{s_{AEC}} < 10$, the murine system still shows better infection scores in more than half of all screened fungal burdens, even if chemotactic signaling becomes deteriorated. We therefore conclude that within these limits our simulation results are qualitatively robust against variations in the chemotaxis parameters.

DISCUSSION

In this study, we investigated clearance of *Aspergillus fumigatus* infection from the lung of mice and humans by computer simulation of the complex interplay between alveolar morphometry and fungal burden in the dynamics of infection clearance. Since *in vivo* live cell imaging of these processes in the whole lung is still not possible today, we here extended a previously developed model of IPA in humans (25, 26) to the murine alveolus. The virtual infection model represents a realistic to-scale representation that was built on detailed experimental data available on the morphometry of the alveolus in the two hosts. Furthermore, alveolar macrophages as well as chemokine secretion and diffusion were incorporated into the model and we screened the physiologically relevant parameter ranges for as small as possible infection scores IS , which represent the

percentage of simulations for which clearance of all *A. fumigatus* conidia from the lung took longer than 6 h.

One important finding of this study is that, for realistic fungal burdens comprising daily inhalation doses in humans as well as typical doses in mice experiments, infection clearance is more efficiently realized in mice compared to humans. This result holds true in the limit of low fungal burden, where at most one conidium is present in the alveolus, as well as for larger fungal burdens with a maximal number of two and three conidia, respectively, in the alveolus of humans and mice. As we observed before for the human system (27), a low ratio of chemokine diffusion over secretion, D/s_{AEC} , leads to more efficient infection clearance in the murine system. However, our simulations revealed that in the limit of low fungal burden the dominating factor of efficient infection clearance in mice is the relatively short distances between AM and conidia in the relatively small murine alveolus. On the other hand, the chemokine profile played a dominant role in the limit of high fungal burden, because for four and more conidia in the relatively small murine alveolus this is associated with a featureless chemokine profile that cannot provide sufficient guidance to AM.

A quantitative comparison revealed that distinct optimal chemokine parameters exist that ensure minimal infection scores IS in the different alveoli of the two hosts. We therefore performed simulations comparing the infection results for both identical and optimal chemokine parameters. It should be noted that, even for the same chemotactic molecule in mice and humans, differences between optimal chemokine parameters can be induced by various factors that are different in the two hosts, such as the secretion competence of AEC and the viscosity of the alveolar surfactant. In any case, the importance of a well-established chemokine gradient as well as the functional sensing by AM is reflected by the fact that conidia, which are not detected within 6 h post infection, pose the risk of germination, invasion, and systemic infection. We also studied the case of non-uniform conidia distribution in the lung leading to locally high AON in alveoli. In this limit, which is more likely realized by the administration of conidia based on liquid solutions, our calculations predict that four and more conidia per alveolus can occur, leading to infection scores that are clearly higher in mice than in humans. However, in general, clearance of uniformly distributed conidia in the lung seems to be more efficiently realized in mice than in humans and we have demonstrated that this results are qualitatively robust over a broad range of variations in the chemokine parameters. These considerations are important with regard to the comparability and transferability of mouse infection models to the human system, e.g., with regard to estimating the efficiency of new therapeutics. Virtual infection modeling in the scope of systems biology has been applied to a broad range of biological systems and pathogens, such as bacteria (48) and fungi (9, 10, 49–53), since it provides a valuable tool to investigate infection processes that are not directly accessible in experiment. Moreover, this approach can direct future experiments by identifying key factors that govern the counterplay of infection and inflammation and require most attention. It should be mentioned that our results, indicating that AM are not able to clear the infection in the limit of a high fungal burden, are in line with previous findings

based on a more phenomenological modeling approach. We applied evolutionary game theory on graphs to simulate several aspects of the immune response against *A. fumigatus* lung infection, including the complement system, phagocytosis by AM as well as recruitment and phagocytosis by neutrophils in one comprehensive model framework (54). This enabled us to reconcile the contradictory view on AM in the literature (55, 56) and predicted an infection dose-dependent switch in their function: While under low infection doses AM manage infection clearance, their role switches to a regulatory function under high infection doses by recruiting neutrophils (54).

In the future, validation of theoretical predictions needs to be addressed in experimental investigations. To date, one of the main limiting factors in understanding host response during *A. fumigatus* infections is the poor experimental accessibility and stable cultivation of alveolar tissue. However, new research approaches including organ-on-a-chip systems, which reduce the physiological complexity and bring nature closer to the simplifying virtual infection models, are promising for a better validation of e.g., alveolar epithelium properties or chemokine parameters (57–59). A lung-on-a-chip model will enable testing chemokine candidates for AM guidance, such as IL-8 that binds to the AM surface receptor CXCR2 (60). Similarly, the chemoattractant C5a is known to be activated by *A. fumigatus* conidia along the alternative pathway of the complement system (61, 62) and is able to trigger the secretion of macrophage inflammatory protein-2 and neutrophil chemoattractant-1 by AEC (63). Once chemokine parameters will have been identified and inflammatory conditions in terms of cytokine profiles will be accessible, the next step will be to extend the hybrid ABM toward neutrophil recruitment and an explicit phagocytosis model along the lines of our previous investigations based on evolutionary game theory (54). This will allow for the investigation of migration and phagocytic dynamics of AM, neutrophils and AEC in the alveolar environment during the interaction with pathogens. Furthermore, morphological changes of *A. fumigatus* including swelling and hyphae formation have a strong impact on phagocytosis of the fungus (17, 64) and can be included in such a virtual infection model. A further advancement will be in the scale-up of the alveolus to the higher organizational units of alveolar sacs for a more comprehensive simulation of infection scenarios.

MATERIALS AND METHODS

In this study, we extended our previously developed ABM of *in silico* infections by *Aspergillus fumigatus* in the human alveolus (26, 27) to the mouse alveolus in order to perform comparative analyses. The ABM is a spatio-temporal multi-scale model that simulates host-pathogen interactions on the cellular and molecular level. Thus, cells like the fungal conidia and AM are simulated as individual agents that migrate and interact in a rule-based fashion, while the chemokine secretion by AEC and the molecular diffusion of chemokines is simulated using partial differential equations. Chemokines are uniformly secreted with rate s_{AEC} at the surface of each AEC, which is associated with at least one conidium. The implementation of the ABM is described in more detail in the **Supplementary Material**, while here the

focus is on the main aspects associated with the extension to the mouse alveolus.

Morphometry of the Mouse Alveolus and Implementation

A comprehensive literature research was performed to design the virtual infection model of the mouse alveolus as realistic as possible. The most important morphology parameters are summarized and compared with the human alveolus in **Table 1**, from which other characteristics can be derived (see for examples **Supplementary Table 1**). For example, it can be seen that the radius (surface area) of a typical human alveolus is about 4.5 (20)-fold larger compared to a murine alveolus. The numbers of AEC of type 1 and 2 differ significantly in both organisms, i.e., a human alveolus contains about 12.0-fold more type 1 and 21-fold more type 2 AEC. Furthermore, the number of PoK is about 3.4 times higher in the human alveolus. A video of both model alveoli is provided in the (**Supplementary Videos 1, 2**).

Implementation of Mouse Alveolus in Virtual Infection Model

The ABM was adjusted for the implementation of the mouse alveolus with parameters as summarized in **Table 1** and **Supplementary Table 1**. This also required changes in the algorithm for cell positioning on the alveolar surface. Type 1 AEC were placed as described before around the three-quarter sphere (see **Supplementary Material** for details). Previously, type 2 AEC and PoK were placed at the borders between type 1 AEC. However, due to the larger ratio of type 2 AEC and PoK with respect to type 1 AEC in mice, the positioning of PoK and type 2 AEC had to be changed. We adjusted the position of type 2 AEC and PoK uniformly across the whole border of the type 1 AEC. While these changes in the cell positioning were required for realistic configurations of mouse alveolus morphometries, quantitative results of the ABM for the human alveolus remained within the 95%-confidence interval. Moreover, the smaller size of the mouse compared to the human alveolus required adjustment of the Delaunay-triangulated grid, on which the diffusion equation is solved (27). The number of grid points could be reduced from 10^4 in the human alveolus to only 5.1×10^2 , keeping the spatial resolution in the mouse alveolus the same as in the human system (see **Supplementary Table 1**).

Readout of the Simulations

As a measure of fungal clearance we compute for various infection scenarios the first-passage-time (FPT) of AM, i.e., the time required for migrating AM to find all conidia in a particular alveolus (26, 27). The relation between the FPT and the time point of conidia germination, which corresponds to about 6 h post conidia arrival, is obtained from repeating the simulation of each infection scenario 10^3 times. From the corresponding FPT distribution, we then compute an infection score, IS , as the percentage p of simulations with FPT above 6 h: $IS^{s=H,M} = p(FPT > 6 h)$, where the superscript refers to the human ($s = H$) or mouse ($s = M$) system and $IS^{s=H,M} = 0$ ($IS^{s=H,M} = 1$) implies that conidia were cleared in each (none) of the 10^3 simulations. The various infection scenarios correspond to scanning the parameter space in terms of AM migration, chemokine secretion,

and diffusion, as well as conidia infection doses in alveoli of mice and humans.

Comparison of Fungal Burden

For a given fungal burden δ , the conidia are distributed across all alveoli n_{alv} of the host's lung. Assuming an independent and uniform distribution of these conidia, we can describe the probability of having n_{con} conidia present in one alveolus by the Binomial distribution $B_{con}(\delta, p, n_{con})$ with probability of $p = \frac{1}{n_{alv}}$ for δ repeats. To estimate the maximal AON that is associated with a specific fungal burden, we computed n_{con} from the $1 - \frac{1}{n_{alv}}$ -quantile of the distribution $B_{con}(\delta, p, n_{con})$. The resulting number corresponds to the maximal AON that can be expected to occur in the whole lung for a specific fungal burden (see **Figure 2**). The corresponding IS was determined by linear interpolation of the results from our simulations for various AON.

DATA AVAILABILITY STATEMENT

The raw data supporting the conclusions of this manuscript will be made available by the authors, without undue reservation, to any qualified researcher.

AUTHOR CONTRIBUTIONS

MTF conceived and designed this study. MTF provided computational resources. Data processing, implementation and application of the computational algorithm were done by MB and ST. MB, ST, and MTF evaluated and analyzed the results of this study. MB, ST, and MTF drafted the manuscript and revised it critically for important intellectual content and final approval of the version to be published. MB, ST, and MTF agree to be accountable for all aspects of the work in ensuring that questions related to the accuracy or integrity of any part of the work are appropriately investigated and resolved.

FUNDING

This work was financially supported by the Deutsche Forschungsgemeinschaft (DFG) through the excellence graduate school Jena School for Microbial Communication (JSMC) the International Leibniz Research School for Microbial and Biomolecular Interactions (ILRS) and the CRC/TR124 FungiNet (project B4 to MTF).

ACKNOWLEDGMENTS

We acknowledge numerous helpful discussions with Johannes Pollmächer.

SUPPLEMENTARY MATERIAL

The Supplementary Material for this article can be found online at: <https://www.frontiersin.org/articles/10.3389/fimmu.2019.00142/full#supplementary-material>

REFERENCES

- Kitano H. Systems biology: a brief overview. *Science* (2002) 295:1662–4. doi: 10.1126/science.1069492
- Aderem A. Systems biology: its practice and challenges. *Cell* (2005) 121:511–513. doi: 10.1016/j.cell.2005.04.020
- Ideker T, Galitski T, Hood L. A new approach to decoding life: systems biology. *Annu Rev Genomics Hum Genet.* (2001) 2:343–72. doi: 10.1146/annurev.genom.2.1.343
- Horn F, Heinekamp T, Kniemeyer O, Pollmächer J, Valiante V, Brakhage AA. Systems biology of fungal infection. *Front Microbiol.* (2012) 3:108. doi: 10.3389/fmicb.2012.00108
- Medyukhina A, Timme S, Mokhtari Z, Figge MT. Image-based systems biology of infection. *Cytom Part A* (2015) 87:462–70. doi: 10.1002/cyto.a.22638
- Kreutz C, Timmer J. Systems biology: experimental design. *FEBS J.* (2009) 276:923–42. doi: 10.1111/j.1742-4658.2008.06843.x
- Bart van der Worp H, Howells DW, Sena ES, Porritt MJ, Rewell S, O'Collins V, et al. Can animal models of disease reliably inform human studies? *PLoS Med.* (2010) 7:1–8. doi: 10.1371/journal.pmed.1000245
- Mestas J, Hughes CCW. Of mice and not men: differences between mouse and human immunology. *J Immunol.* (2004) 172:2731–8. doi: 10.4049/JIMMUNOL.172.5.2731
- Hünninger K, Lehnert T, Bieber K, Martin R, Figge MT, Kurzai O. A virtual infection model quantifies innate effector mechanisms and *Candida albicans* immune escape in human blood. *PLoS Comput Biol.* (2014) 10:e1003479. doi: 10.1371/journal.pcbi.1003479
- Lehnert T, Timme S, Pollmächer J, Hünninger K, Kurzai O, Figge MT. Bottom-up modeling approach for the quantitative estimation of parameters in pathogen-host interactions. *Front Microbiol.* (2015) 6:1–15. doi: 10.3389/fmicb.2015.00608
- Brakhage AA, Bruns S, Thywissen A, Zipfel PF, Behnsen J. Interaction of phagocytes with filamentous fungi. *Curr Opin Microbiol.* (2010) 13:409–15. doi: 10.1016/j.mib.2010.04.009
- Latgé J-P. *Aspergillus fumigatus* and Aspergillosis. *Clin Microbiol Rev.* (1999) 12:310–50.
- Latgé J. The pathobiology of *Aspergillus fumigatus*. *Trends Microbiol.* (2001) 9:382–9. doi: 10.1016/S0966-842X(01)02104-7
- Dagenais TRT, Keller NP. Pathogenesis of *Aspergillus fumigatus* in invasive Aspergillosis. *Clin Microbiol Rev.* (2009) 22:447–65. doi: 10.1128/CMR.00055-08
- Weibel ER. *Morphometry of the Human Lung*. Berlin; Heidelberg: Elsevier Science (2013).
- Balloy V, Chignard M, Margalit A, Kavanagh K, Balloy V, Chignard M. The innate immune response to *Aspergillus fumigatus* at the alveolar surface. *FEMS Microbiol Rev.* (2009) 11:919–27. doi: 10.1016/j.micinf.2009.07.002
- Van De Veerdonk FL, Gresnigt MS, Romani L, Netea MG, Latgé JP. *Aspergillus fumigatus* morphology and dynamic host interactions. *Nat Rev Microbiol.* (2017) 15:661–74. doi: 10.1038/nrmicro.2017.90
- Baddley JW. Clinical risk factors for invasive aspergillosis. *Med Mycol.* (2011) 49:7–12. doi: 10.3109/13693786.2010.505204
- Latgé JP. Fungal immunology: from simple to very complex concepts. *Semin Immunopathol.* (2015) 37:81–2. doi: 10.1007/s00281-014-0474-0
- Clemons KV., Stevens DA. The contribution of animal models of aspergillosis to understanding pathogenesis, therapy and virulence. *Med Mycol.* (2005) 43:51919. doi: 10.1080/13693780500051919
- Sarfati J, Diaquin M, Debeauvais JP, Schmidt A, Lecaque D, Beauvais A, et al. A new experimental murine aspergillosis model to identify strains of *Aspergillus fumigatus* with reduced virulence. *Nippon Ishinkin Gakkai Zasshi* (2002) 43:203–13. doi: 10.3314/jjmm.43.203
- Lepak AJ, Marchillo K, Vanhecker J, Andes DR. Posaconazole pharmacodynamic target determination against wild-type and Cyp51 mutant isolates of *Aspergillus fumigatus* in an *in vivo* model of invasive pulmonary aspergillosis. *Antimicrob Agents Chemother.* (2013) 57:579–85. doi: 10.1128/AAC.01279-12
- Tang CM, Cohen J, Krausz T, Van Noorden S, Holden DW. The alkaline protease of *Aspergillus fumigatus* is not a virulence determinant in two murine models of invasive pulmonary aspergillosis. *Infect Immun.* (1993) 61:1650–6.
- Wong SSW, Rasid O, Laskaris P, Fekkar A, Cavaillon J-M, Steinbach WJ, et al. Treatment of Cyclosporin A retains host defense against invasive pulmonary aspergillosis in a non-immunosuppressive murine model by preserving the myeloid cell population. *Virulence* (2017) 8:1744–52. doi: 10.1080/21505594.2017.1339007
- Codina R, Fox RW, Lockey RE, DeMarco P, Bagg A. Typical levels of airborne fungal spores in houses without obvious moisture problems during a rainy season in Florida, USA. *J Investig Allergol Clin Immunol.* (2008) 18:156–62.
- Pollmächer J, Figge MT. Agent-based model of human alveoli predicts chemotactic signaling by epithelial cells during early *Aspergillus fumigatus* infection. *PLoS ONE* (2014) 9:e111630. doi: 10.1371/journal.pone.0111630
- Pollmächer J, Figge MT. Deciphering chemokine properties by a hybrid agent-based model of *Aspergillus fumigatus* infection in human alveoli. *Front Microbiol.* (2015) 6:503. doi: 10.3389/fmicb.2015.00503
- Peão M, Águas AP, de Sá CM, Grande NR. Morphological evidence for migration of particle-laden macrophages through the interalveolar pores of Kohn in the murine lung. *Cells Tissues Organs* (1993) 147:227–32. doi: 10.1159/000147509
- Namati E, Thiesse J, De Ryk J, McLennan G. Alveolar dynamics during respiration: are the pores of Kohn a pathway to recruitment? *Am J Respir Cell Mol Biol.* (2008) 38:572–8. doi: 10.1165/rcmb.2007-01200C
- Desoubeaux G, Cray C. Rodent models of invasive aspergillosis due to *Aspergillus fumigatus*: Still a long path toward standardization. *Front Microbiol.* (2017) 8:1–31. doi: 10.3389/fmicb.2017.00841
- Bowman JC, Abruzzo GK, Anderson JW, Flattery AM, Gill CJ, Pikounis VB, et al. Quantitative PCR assay to measure *Aspergillus fumigatus* burden in a murine model of disseminated aspergillosis: demonstration of efficacy of caspofungin acetate. *Antimicrob Agents Chemother.* (2001) 45:3474–81. doi: 10.1128/AAC.45.12.3474-3481.2001
- Sheppard DC, Marr KA, Fredricks DN, Chiang LY, Doedt T, Filler SG. Comparison of three methodologies for the determination of pulmonary fungal burden in experimental murine aspergillosis. *Clin Microbiol Infect.* (2006) 12:376–80. doi: 10.1111/j.1469-0691.2005.01349.x
- Steinbach WJ, Benjamin DK, Trasi SA, Miller JL, Schell WA, Zaas AK, et al. Value of an inhalational model of invasive aspergillosis. *Med Mycol.* (2004) 42:417–25. doi: 10.1080/13693780410001712034
- Knust J, Ochs M, Gundersen HJG, Nyengaard JR. Stereological estimates of alveolar number and size and capillary length and surface area in mice lungs. *Anat Rec.* (2009) 292:113–22. doi: 10.1002/ar.20747
- Irvin CG, Bates JHT. Measuring the lung function in the mouse: the challenge of size. *Respir Res.* (2003) 4:4. doi: 10.1186/rr199
- Stone KC, Mercer RR, Freeman BA, Chang L-Y, Crapo JD. Distribution of lung cell numbers and volumes between alveolar and nonalveolar tissue. *Am Rev Respir Dis.* (1992) 146:454–6.
- Chang S, Kwon N, Kim J, Kohmura Y, Ishikawa T, Rhee CK, et al. Synchrotron X-ray imaging of pulmonary alveoli in respiration in live intact mice. *Sci Rep.* (2015) 5:8760. doi: 10.1038/srep08760
- Faffe DS, Rocco PRM, Negri EM, Zin WA. Comparison of rat and mouse pulmonary tissue mechanical properties and histology. *J Appl Physiol.* (2002) 92:230–4. doi: 10.1152/jappphysiol.01214.2000
- Miller FJ, Mercer RR, Crapo JD. Lower respiratory tract structure of laboratory animals and humans: dosimetry implications. *Aerosol Sci Technol.* (1993) 18:257–71. doi: 10.1080/02786829308959603
- Osmanagic E, Sukstanskii AL, Quirk JD, Woods JC, Pierce RA, Conradi MS, et al. Quantitative assessment of lung microstructure in healthy mice using an MR-based ³He lung morphometry technique. *J Appl Physiol.* (2010) 109:1592–9. doi: 10.1152/jappphysiol.00736.2010
- Mercer RR, Russell ML, Crapo JD. Alveolar septal structure in different species. *J Appl Physiol.* (1994) 77:1060–6.
- Stone KC, Mercer RR, Gehr P, Stockstill B, Crapo JD. Allometric relationships of cell numbers and size in the mammalian lung. *Am J Respir Cell Mol Biol.* (1992) 6:235–43. doi: 10.1165/ajrcmb/6.2.235
- Huffman Reed JA, Rice WR, Zsengeller ZK, Wert SE, Dranoff G, Whitsett JA. GM-CSF enhances lung growth and causes alveolar type II epithelial cell hyperplasia in transgenic mice. *Am J Physiol.* (1997) 273:L715–25.
- Jung K, Schlenz H, Krasteva G, Mühlfeld C. Alveolar epithelial type II cells and their microenvironment in the Caveolin-1-deficient mouse. *Anat Rec.* (2012) 295:196–200. doi: 10.1002/ar.21543

45. Henry MM, Ranga V. A Quantitative study of the development of interalveolar pores in the postnatal mouse. *Exp Lung Res.* (1985) 9:277–87. doi: 10.3109/01902148509057528
46. van oud Alblas AB, van Furth R. Origin, Kinetics, and characteristics of pulmonary macrophages in the normal steady state. *J Exp Med.* (1979) 149:1504–18. doi: 10.1084/jem.149.6.1504
47. Haley PJ, Muggenburg BA, Weissman DN, Bice DE. Comparative morphology and morphometry of alveolar macrophages from six species. *Am J Anat.* (1991) 191:401–7. doi: 10.1002/aja.1001910407
48. Wigginton JE, Kirschner D. A model to predict cell-mediated immune regulatory mechanisms during human infection with *Mycobacterium tuberculosis*. *J Immunol.* (2001) 166:1951–67. doi: 10.4049/jimmunol.166.3.1951
49. Prauße MTE, Lehnert T, Timme S, Hünninger K, Leonhardt I, Kurzai O, et al. Predictive virtual infection modeling of fungal immune evasion in human whole blood. *Front Immunol.* (2018) 9:1–13. doi: 10.3389/fimmu.2018.00560
50. Timme S, Lehnert T, Prauße MTE, Hünninger K, Leonhardt I, Kurzai O, et al. Quantitative simulations predict treatment strategies against fungal infections in virtual neutropenic patients. *Front Immunol.* (2018) 9:1–14. doi: 10.3389/fimmu.2018.00667
51. Tokarski C, Hummert S, Mech F, Figge MT, Germerodt S, Schroeter A, et al. Agent-based modeling approach of immune defense against spores of opportunistic human pathogenic fungi. *Front Microbiol.* (2012) 3:129. doi: 10.3389/fmicb.2012.00129
52. Oremland M, Michels KR, Bettina AM, Lawrence C, Mehrad B, Laubenbacher R. A computational model of invasive aspergillosis in the lung and the role of iron. *BMC Syst Biol.* (2016) 10:34. doi: 10.1186/s12918-016-0275-2
53. Tanaka RJ, Boon NJ, Vrcelj K, Nguyen A, Vinci C, Armstrong-James D, et al. *In silico* modeling of spore inhalation reveals fungal persistence following low dose exposure. *Sci Rep.* (2015) 5:13958. doi: 10.1038/srep13958
54. Pollmächer J, Timme S, Schuster S, Brakhage AA, Zipfel PF, Figge MT. Deciphering the counterplay of *Aspergillus fumigatus* infection and host inflammation by evolutionary games on graphs. *Sci Rep.* (2016) 6:27807. doi: 10.1038/srep27807
55. Roilides E, Walsh TJ, Pizzo PA, Rubin M. Granulocyte Colony-Stimulating Factor enhances the phagocytic and bactericidal activity of normal and defective human neutrophils. *J Infect Dis.* (1991) 163:579–83. doi: 10.1093/infdis/163.3.579
56. Mircescu MM, Lipuma L, van Rooijen N, Pamer EG, Hohl TM. Essential role for neutrophils but not alveolar macrophages at early time points following *Aspergillus fumigatus* infection. *J Infect Dis.* (2009) 200:647–56. doi: 10.1086/600380
57. Huh D. A human breathing lung-on-a-chip. *Ann Am Thorac Soc.* (2015) 12:S42–4. doi: 10.1513/AnnalsATS.201410-442MG
58. Mosig AS. Organ-on-chip models: new opportunities for biomedical research. *Futur Sci. OA* (2016) 3:fsoa-2016-0038. doi: 10.4155/fsoa-2016-0038
59. Benam KH, Villenave R, Lucchesi C, Varone A, Hubeau C, Lee HH, et al. Small airway-on-a-chip enables analysis of human lung inflammation and drug responses *in vitro*. *Nat Methods* (2016) 13:151–7. doi: 10.1038/nmeth.13697
60. Miller AL, Strieter RM, Gruber AD, Ho SB, Lukacs NW. CXCR2 regulates respiratory syncytial virus-induced airway hyperreactivity and mucus overproduction. *J Immunol.* (2003) 170:3348–56. doi: 10.4049/jimmunol.170.6.3348
61. Zipfel PF, Skerka C. Complement regulators and inhibitory proteins. *Nat Rev Immunol.* (2009) 9:729–40. doi: 10.1038/nri2620
62. Kozel TR, Wilson MA, Farrell TP, Levitz SM. Activation of C3 and binding to *Aspergillus fumigatus* conidia and hyphae. *Infect Immun* (1989) 57:3412–7.
63. Riedemann NC, Guo R-F, Sarma VJ, Laudes IJ, Huber-Lang M, Warner RL, et al. Expression and function of the C5a receptor in rat alveolar epithelial cells. *J Immunol.* (2002) 168:1919–25. doi: 10.4049/jimmunol.168.4.1919
64. McCormick A, Loeffler J, Ebel F. *Aspergillus fumigatus*: contours of an opportunistic human pathogen. *Cell Microbiol.* (2010) 12:1535–43. doi: 10.1111/j.1462-5822.2010.01517.x

Conflict of Interest Statement: The authors declare that the research was conducted in the absence of any commercial or financial relationships that could be construed as a potential conflict of interest.

Copyright © 2019 Blickensdorf, Timme and Figge. This is an open-access article distributed under the terms of the Creative Commons Attribution License (CC BY). The use, distribution or reproduction in other forums is permitted, provided the original author(s) and the copyright owner(s) are credited and that the original publication in this journal is cited, in accordance with accepted academic practice. No use, distribution or reproduction is permitted which does not comply with these terms.

PORES OF KOHN IN HUMAN ALVEOLI

FORMULAR 1¹**Manuskript Nr. 2**

Titel des Manuskriptes: Hybrid Agent-Based Modeling of Aspergillus fumigatus Infection to Quantitatively Investigate the Role of Pores of Kohn in Human Alveoli

Autoren: Marco Blickensdorf, Sandra Timme, Marc Thilo Figge

Bibliographische Informationen : *Front Microbiol.* 2020 Aug 12;11:1951.doi: 10.3389/fmicb.2020.01951. eCollection 2020

Der Kandidat / Die Kandidatin ist

Erstautor/-in, Ko-Erstautor/-in, Korresp. Autor/-in, Koautor/-in.

Status : publiziert

Anteile (in %) der Autoren / der Autorinnen an der Publikation (anzugeben ab 20%)

Autor/-in	Konzeptionell	Datenanalyse	Experimentell	Verfassen des Manuskriptes	Bereitstellung von Material
Blickensdorf		80 %	80 %	80 %	
Timme					
Figge	100 %				100 %

Unterschrift Kandidat/-in

Unterschrift Betreuer/-in (Mitglied der Fakultät)

¹ Die Unterschriften müssen nur im separat im Dekanat einzureichenden ausgefüllten Formular im Original vorliegen. In der in die Dissertation eingebundenen Fassung dürfen die Unterschriften und Unterschriftenfelder fehlen.



Hybrid Agent-Based Modeling of *Aspergillus fumigatus* Infection to Quantitatively Investigate the Role of Pores of Kohn in Human Alveoli

Marco Blickensdorf^{1,2}, Sandra Timme¹ and Marc Thilo Figge^{1,2*}

¹ Research Group Applied Systems Biology, Leibniz Institute for Natural Product Research and Infection Biology – Hans Knöll Institute, Jena, Germany, ² Faculty of Biological Sciences, Institute of Microbiology, Friedrich Schiller University Jena, Jena, Germany

OPEN ACCESS

Edited by:

Esteban A. Hernandez-Vargas,
Frankfurt Institute for Advanced
Studies, Germany

Reviewed by:

Margherita Bertuzzi,
University of Manchester,
United Kingdom
Roberta Gaziano,
University of Rome Tor Vergata, Italy

*Correspondence:

Marc Thilo Figge
thilo.figge@leibniz-hki.de;
thilo.figge@hki-jena.de

Specialty section:

This article was submitted to
Systems Microbiology,
a section of the journal
Frontiers in Microbiology

Received: 19 May 2020

Accepted: 24 July 2020

Published: 12 August 2020

Citation:

Blickensdorf M, Timme S and
Figge MT (2020) Hybrid Agent-Based
Modeling of *Aspergillus fumigatus*
Infection to Quantitatively Investigate
the Role of Pores of Kohn in Human
Alveoli. *Front. Microbiol.* 11:1951.
doi: 10.3389/fmicb.2020.01951

The healthy state of an organism is constantly threatened by external cues. Due to the daily inhalation of hundreds of particles and pathogens, the immune system needs to constantly accomplish the task of pathogen clearance in order to maintain this healthy state. However, infection dynamics are highly influenced by the peculiar anatomy of the human lung. Lung alveoli that are packed in alveolar sacs are interconnected by so called Pores of Kohn. Mainly due to the lack of *in vivo* methods, the role of Pores of Kohn in the mammalian lung is still under debate and partly contradicting hypotheses remain to be investigated. Although it was shown by electron microscopy that Pores of Kohn may serve as passageways for immune cells, their impact on the infection dynamics in the lung is still unknown under *in vivo* conditions. In the present study, we apply a hybrid agent-based infection model to quantitatively compare three different scenarios and discuss the importance of Pores of Kohn during infections of *Aspergillus fumigatus*. *A. fumigatus* is an airborne opportunistic fungus with rising incidences causing severe infections in immunocompromised patients that are associated with high mortality rates. Our hybrid agent-based model incorporates immune cell dynamics of alveolar macrophages – the resident phagocytes in the lung – as well as molecular dynamics of diffusing chemokines that attract alveolar macrophages to the site of infection. Consequently, this model allows a quantitative comparison of three different scenarios and to study the importance of Pores of Kohn. This enables us to demonstrate how passaging of alveolar macrophages and chemokine diffusion affect *A. fumigatus* infection dynamics. We show that Pores of Kohn alter important infection clearance mechanisms, such as the spatial distribution of macrophages and the effect of chemokine signaling. However, despite these differences, a lack of passageways for alveolar macrophages does not impede infection clearance only to a minor extent. Furthermore, we quantify the importance of recruited macrophages in comparison to resident macrophages.

Keywords: virtual infection modeling, *Aspergillus fumigatus* lung infection, Pores of Kohn, human model, hybrid agent-based computer simulations

INTRODUCTION

External cues constantly threaten the healthy state of organisms. Due to the daily inhalation of hundreds of particles and pathogens the immune system needs to constantly accomplish the task of pathogen clearance in the lung in order to maintain and restore a healthy state. However, infection dynamics are highly influenced by the peculiar anatomy of the human lung. In 1893, Kohn described inter-alveolar pores in a pneumonia patient for the first time (Kohn, 1893). In the following years, Oertel was the first to point out that these pores, nowadays known as Pores of Kohn (PoK), may open and close due to pressure changes during respiration (Oertel, 1919). Although PoK were considered to possibly contribute to infection processes (Adams and Livingstone, 1931), the scientific community lacked evidence for this until Cordingley (1972) characterized PoK using electron microscopy. In this work, alveolar macrophages (AM) – i.e., resident phagocytes in the lung – were observed inside a PoK supporting the postulated role of PoK as inter-alveolar cellular communication channels. Furthermore, a low number of PoK, as occurs in infants, increases the risk of atelectasis, whereas an increase in the number or size of PoK, as seen in older individuals or as caused by smoking, is associated with a higher risk of emphysema (Wright, 2001; Rennard et al., 2006; Guillerman, 2010; Yoshikawa et al., 2016). Today, the important role of PoK for ventilation is widely accepted (Namati et al., 2008), although the exact function of PoK in the lung is still not fully understood and experimental evidence supports partially contradicting hypotheses. If PoK are regulators of air pressure and thus open and close at a typical human respiration rate of approximately 3–5 s (Barrett et al., 2012), how can they serve as entry/exit points for immune cells, such as AM, which migrate at a much lower pace? How do PoK allow for collateral ventilation when covered with surfactant (Oldham and Moss, 1989)? In case AM are indeed routinely migrating between neighboring alveoli through PoK, how does this affect the dynamics of infection processes?

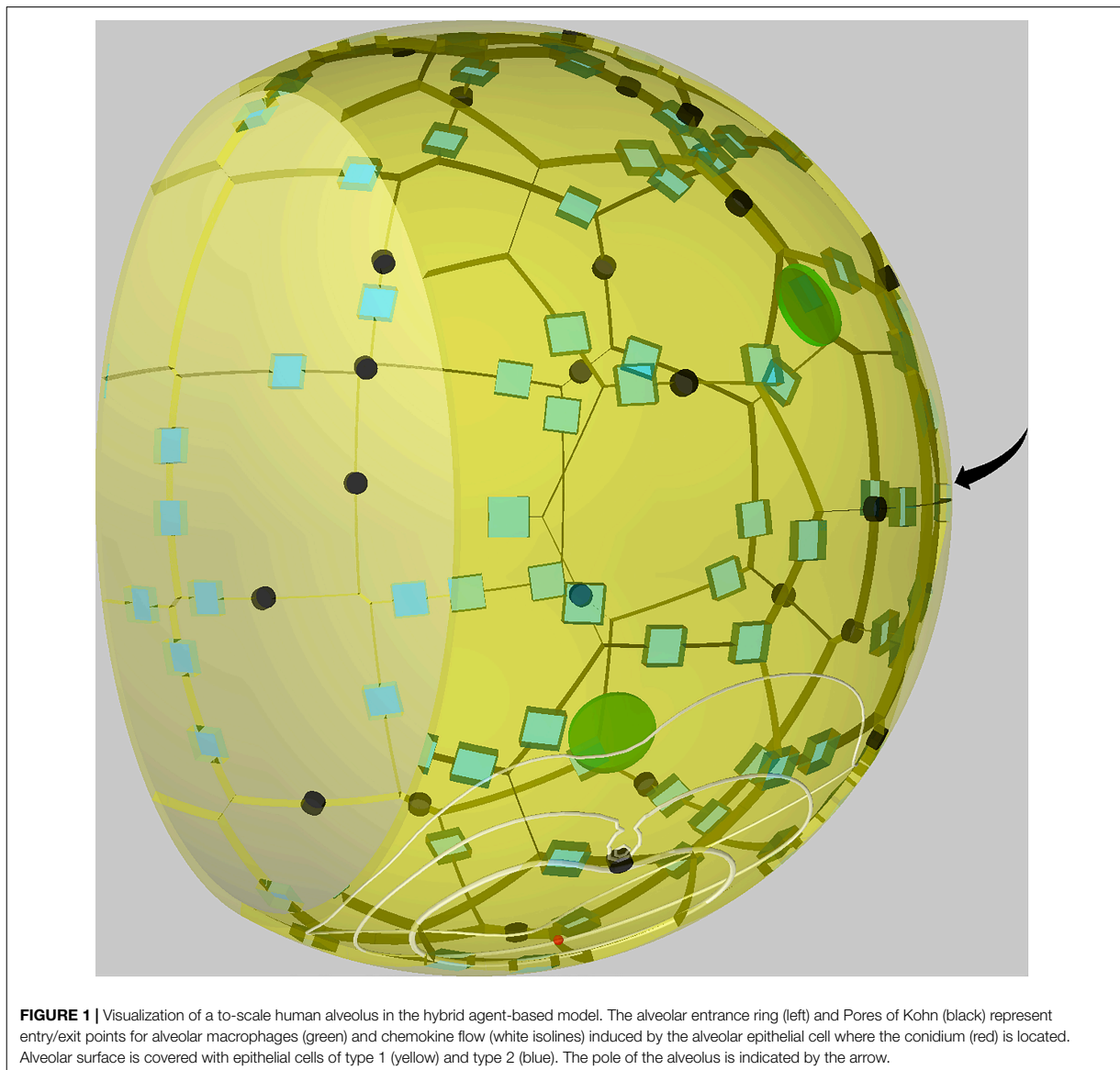
In this study, we want to investigate the function of PoK during *Aspergillus fumigatus* infection in the human lung. *A. fumigatus* is a human pathogenic mold, which can cause severe infections in immunocompromised patients (Latgé, 1999, 2001; Brakhage et al., 2010). The small conidia of *A. fumigatus*, which are 2–3 μm in size, are able to overcome the various filter mechanisms, such as the cilia and the mucous layer (Bustamante-Marin and Ostrowski, 2017), of the respiratory tract and most probable reach the alveoli, which constitute the majority of the lung surface (Weibel, 1963; Latgé, 1999; Brakhage et al., 2010). Once the conidia are embedded in the surfactant, which covers the alveolar epithelial cells (AEC), they begin to swell and a complex host-pathogen response is initiated (Behnsen et al., 2008; Margalit and Kavanagh, 2015). It can be assumed that shortly after arrival of a conidium in the alveolus, the complement system within the surfactant layer will be activated. This will be sensed by the AEC on which the conidium is located and will lead to their secretion of chemokines. Thus, complement activation and AEC chemokine secretion provide a first line of defense recruiting AM for conidia uptake (Pollmächer and Figge, 2014;

Margalit and Kavanagh, 2015). If not cleared within the first 6 h (Baltussen et al., 2018), *A. fumigatus* conidia develop hyphae, which in turn may invade the bloodstream, causing dissemination and severe infections (Van De Veerdonk et al., 2017). Therefore, *A. fumigatus* represents an interesting target to study the role of PoK during infection. Although methods for studying pulmonary tissue, such as electron microscopy, confocal laser endomicroscopy (Danilevskaia et al., 2015), *ex vivo* techniques (Hocke et al., 2017) or the emerging lung-on-chip models (Mosig, 2017) do exist, it is not yet possible to capture the full cellular and molecular dynamics during infection in alveoli in living organisms. A systems biology approach allows to address questions that cannot be answered by traditional wet-lab experiments (Horn et al., 2012; Medyukhina et al., 2015; Deinhardt-Emmer et al., 2020; Schicke et al., 2020). Especially for complex infection processes, where cellular and molecular as well as temporal and spatial dynamics may be of importance for in-depth understanding of host-pathogen interactions, virtual modeling provides a valuable tool. This has been demonstrated by established models based on ordinary differential equations (ODE) (Hancioglu et al., 2007; Voit, 2014) or partial differential equations (PDE) (Hao et al., 2015; Sharp et al., 2015) as well as state based models (Lehnert et al., 2015; Prauße et al., 2018; Sreekantapuram et al., 2020). In processes where resolution of individual cells is of importance, as in the case of *A. fumigatus* infection, agent-based models are most promising to fully capture the spatio-temporal infection dynamics (Tokarski et al., 2012; Lehnert et al., 2015; Timme et al., 2018). Therefore, we here applied a previously developed hybrid agent-based virtual infection model (Pollmächer and Figge, 2014, 2015; Blickensdorf et al., 2019), which incorporates the immune cell dynamics of alveolar macrophages as well as the molecular dynamics of diffusing chemokines that are secreted by AEC and attract alveolar macrophages to the site of infection. In this way, it enables the comparison and quantification of possible functions of PoK. Therefore, we setup three different model scenarios where PoK serve as passage points for (i) AM and chemokines referring to the hypothesis of AM passaging through PoK from Oertel (1919) and Cordingley (1972) (ii) chemokines but not AM and (iii) neither AM nor chemokines as postulated by Namati et al. (2008).

MATERIALS AND METHODS

Existing Modeling Framework

In order to investigate the role of PoK in human alveoli and, in particular, their impact on the migration and detection dynamics of AM during *A. fumigatus* infections, we performed simulations with a previously developed hybrid agent-based modeling framework (Pollmächer and Figge, 2014, 2015). This model approximates the shape of an alveolus by a sphere (see **Figure 1**) that is cut at 3/4 of its diameter forming an alveolar entrance ring, which represents its connection within an alveolar sac of the human lung. The alveolus is composed of AEC of type 1, which are placed equidistant over the surface using a Voronoi tessellation, and of type 2, placed along the edges of type 1 AEC.



PoK that represent connections between neighboring alveoli are positioned in the same way. Parameters of e.g. cell size and numbers were obtained from an in-depth literature search and can be found in **Table 1**.

Our previous studies used an agent-based framework showing that a passive movement of conidia by respiration does not delimit infection clearance, whereas a higher speed and/or persistence time of AM improves detection of *A. fumigatus* conidia. However, for reasonable parameter ranges the infection was not cleared in more than 20% of the simulations (Pollmächer and Figge, 2014). Therefore the model was extended by chemokine secretion in a hybrid agent-based model. An investigation of the chemokine parameters revealed, that a high

ratio of secretion rate to diffusion coefficient facilitates AM to detect the conidium much faster (Pollmächer and Figge, 2015).

In the current study we applied this model to infections of *A. fumigatus*, whose conidia can reach an alveolus and, if not phagocytosed, swell and develop hyphae that can invade the bloodstream leading to severe infections with high mortalities of up to 90% (Dagenais and Keller, 2009). To simulate this infection scenario, we placed a single conidium into the virtual alveolus at a random position. This is justified by the large number of alveoli per human lung, making the case of one conidium per alveolus the most probable infection scenario (Pollmächer and Figge, 2014). The number of AM inside one alveolus is binomially distributed according to the number of alveoli n_{Alv}

TABLE 1 | Default model parameters.

Parameter	Description	Value
n_{AM}	Number of AM per human lung	2.1×10^9 (Wallace et al., 1992)
n_{Alv}	Number of alveoli per human lung	4.8×10^8 (Ochs et al., 2004)
r_{AM}	Radius of AM	$10.6 \mu\text{m}$ (Krombach et al., 1997)
n_{AEC1}	Number of alveolar epithelial cells type 1 per alveolus	39–45 (estimation)
n_{AEC2}	Number of alveolar epithelial cells type 2 per alveolus	74–84 (estimation)
n_{PoK}	Number of pores of Kohn per alveolus	24 (Kawakami and Takizawa, 1987) (estimation)
r_{PoK}	Radius of pores of Kohn	$2.00 \mu\text{m}$ (Kawakami and Takizawa, 1987)
$r_{Alveolus}$	Radius of an alveolus	$116.5 \mu\text{m}$ (Balásházy et al., 2008)

and the number of AM in the human lung n_{AM} and yield a mean number of 4.38 AM (Wallace et al., 1992). We infer from this distribution $B_{AM} = (n_{AM}, p, k) = \binom{n_{AM}}{k} p^k (1-p)^{n_{AM}-k}$ the initial number of AM inside the alveolus at simulation start with $p = \frac{1}{n_{Alv}}$. AM perform a biased persistent random walk with persistence time of $t_p = 1$ min and a speed of $v = 4 \mu\text{m}/\text{min}$. AM may leave the system if they, by chance, cross the border of the alveolus at either the alveolar entrance ring or at a PoK. To maintain a constant average number of AM in the alveolus, new AM are inserted at the model boundary after an exponentially distributed waiting time of $t = 1/\lambda_{in} \ln(\frac{1}{u})$ with u uniformly distributed in $[0, 1)$ and input rate λ_{in} , which has to be calibrated for each AM speed, persistence time and model boundary in the healthy state i.e., without present pathogens.

The hybrid agent-based model also comprises chemokine signaling released by the AEC where the conidium is located. The chemokine diffuses at the inner alveolar surface forming a chemokine gradient that guides the AM toward the chemokine-secreting AEC on which the conidium is located. To simulate chemokine signaling we included a reaction-diffusion model based on PDE in the agent-based framework of the alveolus. The equation $\frac{\delta c(\vec{r}, t)}{\delta t} = D \delta c(\vec{r}, t) + S(\vec{r}, t) - Q(\vec{r}, t)$ incorporates chemokine secretion by the source term S and chemokine diffusion with diffusion coefficient D for chemokine concentration $c(\vec{r}, t)$ at point \vec{r} and time point t . Chemokines are secreted over the whole surface of the pathogen-associated AEC with constant secretion rate s_{AEC} . The chemokine uptake by AM with term Q is realized with a spherical adaption of the receptor ligand-model of Guo et al. and Guo and Tay (Riedemann et al., 2002; Guo et al., 2008), in which chemokine may be bound to AM surface receptors. This allows AM to sense the chemokine gradient, during a persistence time t_p , to obtain a weighted cumulative gradient. AM change their direction biased with a probability to follow the gradient, which is proportional to the receptor differences along the weighted cumulative gradient after t_p . Hence, AM are able to sense the chemokine gradient and adapt their migration behavior accordingly after expiration of the persistence time. The boundaries of this system, i.e., the alveolar entrance ring and the PoK, form sinks allowing for chemokine outflow. Furthermore, the presence of chemokines in the system affects the probability of an AM to enter the alveolus at a certain boundary position. The higher the chemokine concentration

at this position is, the higher is the probability that a new AM enters the alveolus at this site. The diffusion equation is solved by an implementation of the finite difference method for unstructured grids (Sukumar, 2003). As grid a near-equidistant Voronoi tessellation was created as a solution of the Thomson Problem (Thomson, 1904) by use of an algorithm implemented by MacWilliam and Cecka (2013).

Finally, in order to evaluate the infection outcome of a simulation we compute the infection score IS , which we define as the fraction of 1000 simulations, in which the conidium was not detected by AM within the first 6 h, i.e., the typical time needed for *A. fumigatus* to swell and start developing hyphae (Pollmächer et al., 2016).

Study Setup to Investigate the Role of PoK

In this study we want to investigate the impact of PoK on the infection dynamics in human alveoli. In order to do so, we setup three types of infection scenarios (see **Supplementary Videos 1–3**). The first setup represents the situation, in which PoK serve as entrance and exit points for AM and for the flow of chemokines through PoK. This setup corresponds to the standard model used in our earlier studies and we here refer to it as PoK+/+ model. It reflects the hypothesis that immune cells use PoK as migration channels between neighboring alveoli. However, since it is not experimentally verified *in vivo* that AM do indeed migrate through PoK, we setup a second model, which we refer to as PoK+/- model. In this scenario chemokines can still flow through PoK, while AM do not enter or exit through PoK. Furthermore, in the third setup neither AM can migrate through the PoK nor chemokine can flow out at PoK. Thus, we refer to this scenario as PoK-/- model. However, since conidia do not migrate actively and it is rather unlikely that they are located directly on a PoK when entering the alveoli, we do not consider passing of conidia through PoK in our model. In our study, we will quantitatively compare these three scenarios by computer simulations.

The models PoK+/- and PoK-/- have system boundaries that are decreased relative to the PoK+/+ model. This is associated with a decreased probability of AM leaving the alveolus during the course of the infection scenario. Thus, we adapted the respective AM input rate λ_{in} for the three different scenarios. As found previously, timely *A. fumigatus* clearance in the human alveolus is determined mostly by the chemokine parameters

(Pollmächer and Figge, 2015). In particular, we showed that the most important chemokine parameters are the secretion rate s_{AEC} and the diffusion coefficient D (Pollmächer and Figge, 2015). Since the physiological values for these parameters could not yet be measured in experiment, we scan for a broad range of physiologically reasonable values in our computer simulations. It is generally observed that the combination of a high value of s_{AEC} and a low value of D is beneficial for the fast conidium detection by AM. In contrast, if the ratio of s_{AEC}/D is too low, chemotactic signaling loses its unique function of guidance and AM are unable to find the conidium within 6 h, as is the case for a search by random walk (Pollmächer and Figge, 2014, 2015).

RESULTS

In the present study we investigated the impact of PoK on the infection dynamics during *A. fumigatus* lung infection. In order to do this, we constructed three different models that account for different properties of PoK, such as entry and exit points for AM as well as chemokine outflow. These three models are (i) the PoK+/+ model, where AM can enter and exit through PoK and chemokines can flow out at PoK, (ii) the PoK+/- model, where AM cannot enter and exit through PoK but chemokines can flow out at PoK, and (iii) the PoK-/- model, where PoK serve neither as migration channels for AM nor as sinks for chemokine outflow (see **Supplementary Videos 1–3**). However, we assume that, if AM are able to migrate through PoK, also the much smaller chemokine molecules can diffuse through them. Therefore, we do not consider a scenario, where PoK serve as migration channels for AM while chemokine outflow is not possible.

It may be expected that, since the recruitment of AM through the homogeneously distributed PoK everywhere in an alveolus allows for shorter AM migration distances in the PoK+/+ model, this model yields significantly lower infection scores compared to the models PoK+/- and PoK-/. In the latter models, AM enter the alveolus exclusively via its entrance ring, which may be associated with longer migration distances toward the conidium and thus extended search times. In addition, in the PoK-/- model chemokine diffusion might be affected in two different ways: First, the overall chemokine concentration in the alveolus will be higher compared to the PoK+/+ and PoK+/- model, because chemokines cannot flow out at PoK. As shown previously, a high secretion is beneficial for infection clearance by AM (Pollmächer and Figge, 2015), thus less chemokine outflow and therefore a higher chemokine concentration might also be beneficial for AM searching a conidium. Secondly, PoK provide a sink for the chemokine and thus locally distort the chemokine profile around the PoK, which may guide AM away from PoK following the locally distorted gradient. Once the distance to the PoK has increased, AM get re-directed toward the conidium. Thus, it may be expected that the absence of distortions in the chemokine profile, as in the PoK-/- model where chemokines do not flow out of PoK, could have an additional positive effect on infection clearance.

The Results section is structured as follows: In Section “Reduced Length of Alveolar Boundary Alters Spatial

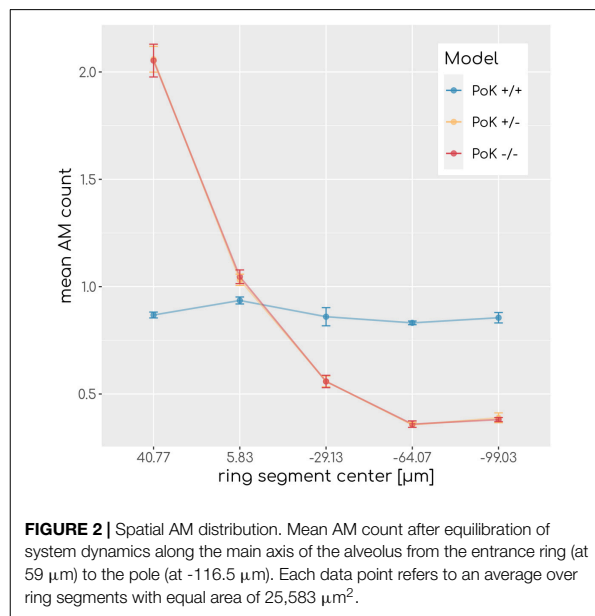
Equilibrium Distribution of AM,” we analyze the calibration of the AM input parameter for each model scenario and the spatial redistribution of AM resulting from the different conditions in the three scenarios. Next, in Section “PoK+/+ Shows Highest Infection Clearance Compared to PoK+/- and PoK-/-” we investigate the infection clearance in the three scenarios for various chemokine parameters and how this depends on the position of the conidium in the alveolus. Moreover, we analyze the contribution of AM recruitment to infection clearance in comparison with resident AM that are present in the alveolus from the start of the simulation. In Section “Presence of PoK Prevents Chemokine Accumulation,” we first compare the optimal chemokine parameters that we identify for each of the three scenarios. Secondly, we study the effect of chemokine accumulation that is observed for the PoK-/- model. Thirdly, we assess the impact of the different chemokine profiles of the three scenarios on the migration pattern of AM. Finally, in Section “Accumulation of AM Limited in Presence of PoK Passageways” we investigate the effect of AM accumulation that is observed during the simulations and is caused by the chemokine secretion by AEC. We analyze this accumulation under comparable conditions for all three model scenarios with the conidium being placed at the pole of the alveolus.

Reduced Length of Alveolar Boundary Alters Spatial Equilibrium Distribution of AM

In the PoK+/- and PoK-/- model, where AM only enter/exit the alveolus at the alveolar entrance ring but not at PoK, the length of the system boundary is effectively shorter in comparison to the PoK+/+ model, the re-calibration of the AM input rate λ_{in} in the absence of infection (for details see “Materials and Methods” section) was found to be associated with an altered spatial equilibrium redistribution of AM at the inner surface of the alveolus. To be more specific, the initial random spatial distribution of AM over the alveolar surface in the PoK+/+ model was altered into a spatial equilibrium distribution for the PoK+/- and the PoK-/- model, where AM appear accumulated at the alveolar entrance ring (see **Figure 2**). Interestingly, due to the absence of any conidia in the human alveolus during the calibration of λ_{in} (see section “Existing Modeling Framework”), this is a direct consequence of excluding PoK as part of the system boundary, where AM can leave and enter the alveolus; thus, turning the alveolus into a spatial dead end for randomly migrating AM in the PoK+/- and the PoK-/- model.

PoK+/+ Shows Highest Infection Clearance Compared to PoK+/- and PoK-/-

As measure for infection clearance we determine for each simulation the time point of first contact between an AM and the randomly positioned conidium in the alveolus; this defines the so-called first passage time (*FPT*). The infection score *IS* is given by the fraction simulations with $FPT > 6 h$, i.e., the number of 1000 simulations, where AM were unable



to clear the conidium within 6 h after entrance in the alveolus. This time duration corresponds to the typical time frame until germination of the conidium starts and the fungus becomes invasive; i.e., $IS = 0$ corresponds to infection clearance in all and $IS = 1$ corresponds to an infection clearance in no simulation within the first 6 h of infection duration. For comparison of the three different infection models we performed simulations of *A. fumigatus* infections by placing one conidium at a random position in the alveolus and by repeating this scenario for various sets of chemokine parameters. In particular, we screened the secretion rate for values $s_{AEC} = \{1500, 5000, 15,000, 50,000, 150,000, 500,000\} \text{ min}^{-1}$ and the diffusion coefficient over the range of values $D = \{20, 60, 200, 600, 2000, 6000\} \mu\text{m}^2 \text{ min}^{-1}$. This range of values is motivated by estimations for chemokine diffusion in lung surfactant and in water (see **Supplementary Material Section 1.2**).

An analysis of the infection score over all scanned parameters of chemokine signaling revealed that low values with $IS \sim 0.01$ equivalent to clearance of the infection can be achieved for all three models, albeit for different optimal chemokine parameters. For a deeper understanding of the differences between the models, we compared the *FPT* distributions of the three models by a survival analysis using a log-rank test for each combination of chemokine parameters (see **Supplementary Material Section 1.1**). This analysis revealed that for 17 out of 36 parameter combinations significant differences between the models exist (see **Figure 3**) showing that infection clearance is affected by the function of PoK. In addition, the absolute value of the relative difference between the respective infection scores are above 0.5 for 28% of all scanned chemokine parameters showing that the function of PoK induces a substantial difference for infection clearance.

To understand how PoK may influence the infection score, we studied in retrospect those AM that successfully detected a conidium ($AM_{success}$) in relation with their starting point in the alveolus. An AM may either be present in the alveolus from the start of the simulation ($AM_{resident}$) or may have entered the alveolus during the simulation ($AM_{recruited}$), either through a PoK or via the alveolar entrance ring depending on the considered PoK model. We calculated the resident ratio of AM, $r_{resident} = AM_{resident}/AM_{success}$, yielding that the mean value for $r_{resident}$ over all simulated chemokine parameters shows only small differences between the models ($r_{resident}(\text{PoK}+/+) = 0.61 \pm 0.04$, $r_{resident}(\text{PoK}+/-) = 0.58 \pm 0.03$, $r_{resident}(\text{PoK}-/-) = 0.56 \pm 0.06$) indicating that the slight majority of conidia are found by AM, which were not recruited to the alveolus but were initially present in the alveolus. In approximately 40% of the infection scenarios the conidium was found by an AM that was recruited during the infection duration of 6 h. In the PoK+/+ model recruitment of ($AM_{success}$) is realized by 54% through a PoK and by 46% via the alveolar entrance ring (see **Supplementary Figures S1–S3**). Since recruitment through a PoK is not possible in the PoK+/- and PoK-/- model, the small differences in the infection score compared to the PoK+/+ model suggest, that recruitment through the alveolar entrance ring is adequately replacing the missing passing through PoK. We expect this effect to be dependent on the precise position of the conidium in the alveolus, i.e., the larger the distance of the conidium from the alveolar entrance ring is, the more beneficial the presence of PoK will be in the PoK+/+ model. To test this hypothesis we split the alveolar surface into five ring segments of equal area from the entrance ring to the pole of the alveolus and computed the *IS* individually for each of these segments. This analysis revealed that the infection score in the PoK+/- model and the PoK-/- model is smallest when the conidium is located in the proximity of the alveolar entrance ring and increases for locations with higher distances from the entrance ring, whereas for the PoK+/+ model the infection score remains fairly independent of the location of the conidium in the alveolus (see **Figure 4**).

Presence of PoK Prevents Chemokine Accumulation

Our in-depth screening of the chemokine parameters for the lowest infection scores reveals that these are achieved for diffusion coefficient $D = 60 \mu\text{m}^2 \text{ min}^{-1}$ and secretion rate $s_{AEC} = 50,000 \text{ min}^{-1}$ in the case of the PoK+/+ and the PoK+/- model whereas for the PoK-/- model the optimal chemokine parameters are shifted toward $D = 20 \mu\text{m}^2 \text{ min}^{-1}$ and $s_{AEC} = 5000 \text{ min}^{-1}$. These findings reflect that in the PoK-/- model the chemokine dynamics is affected in two ways: First, in this model chemokine outflow is, in contrast to the PoK+/+ and PoK+/- models, prohibited and this leads to a higher accumulation of chemokines in the alveolus. Second, compared to the PoK+/+ and the PoK+/- models with PoK forming a sink for chemokines associated with a distortion of the chemokine gradient, in the PoK-/- model the

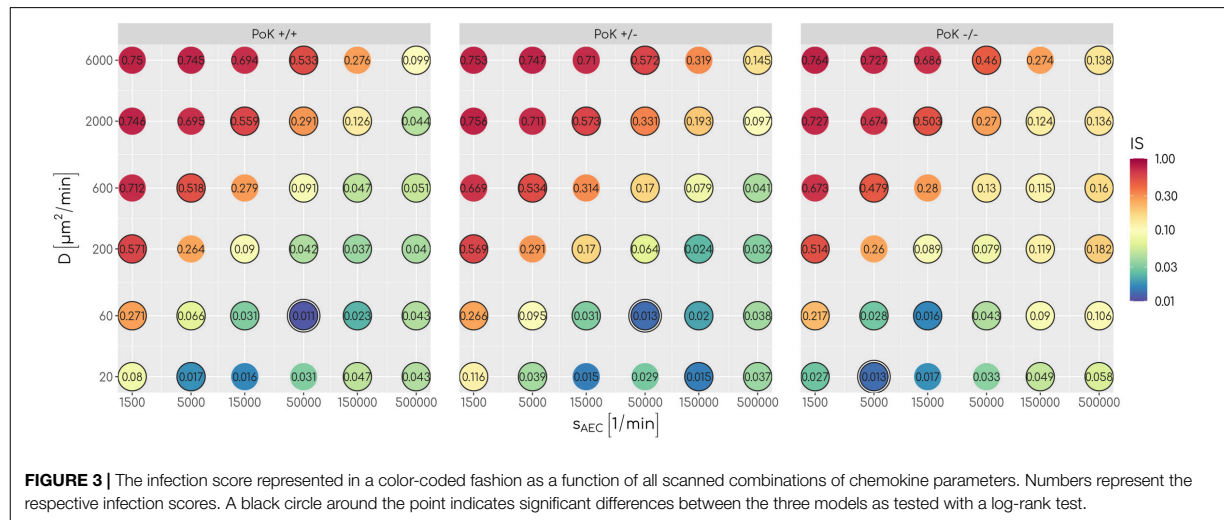


FIGURE 3 | The infection score represented in a color-coded fashion as a function of all scanned combinations of chemokine parameters. Numbers represent the respective infection scores. A black circle around the point indicates significant differences between the three models as tested with a log-rank test.

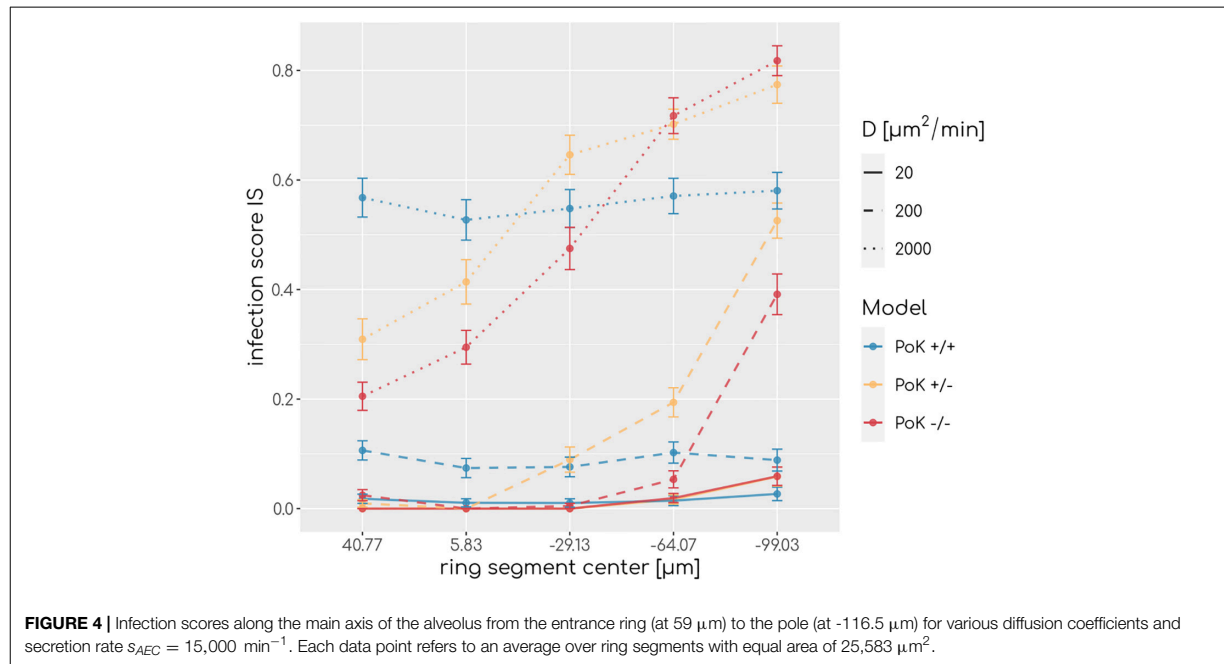
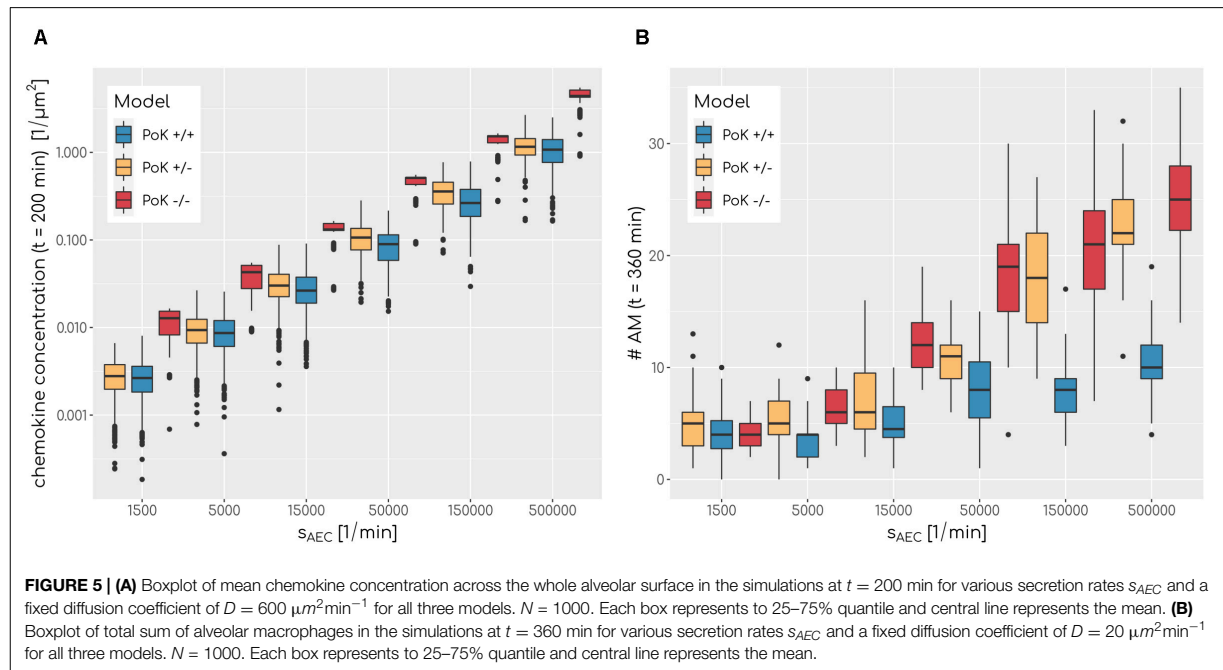


FIGURE 4 | Infection scores along the main axis of the alveolus from the entrance ring (at 59 μm) to the pole (at -116.5 μm) for various diffusion coefficients and secretion rate $s_{AEC} = 15,000 \text{ min}^{-1}$. Each data point refers to an average over ring segments with equal area of $25,583 \text{ μm}^2$.

chemokine gradient is more homogeneous and this may alter the migration patterns of AM into a migration behavior that is more directed. We analyzed the mean chemokine concentration across the whole alveolar surface after a simulation time of $t = 200 \text{ min}$. The difference in the mean chemokine concentration between the PoK+/+ model and the PoK-/- model yields on average a factor 4.4 for all secretion rates. This indicates that chemokines do indeed accumulate (see **Figure 5A**). It also explains the shift of the minimal infection score in the chemokine parameter space toward a lower secretion rate for the PoK-/- model compared to the other models, since the chemokine

accumulation partly supersedes the secretion. Interestingly, also the PoK+/- model shows a slightly increased amount of chemokine in the alveolus compared to the PoK+/+ model, although the chemokine outflow of the models through PoK is identical. However, we find that this is caused by the chemokine uptake of AM with their distinguished spatial distribution in the PoK+/- and PoK+/+ models. Since in the PoK+/- model AM are initially distributed closer to the entrance ring (see **Figure 2**), where chemokine concentration is low, the chemokine uptake by AM is reduced compared to the PoK+/+ model (see **Supplementary Figure S4**).



Next, we investigated the question if changes in the chemokine profile affect the migration behavior of AM in a measurable way. To this end, we analyzed the cell tracks of all successful $AM_{success}$ using established cell track analysis methods by computing the asphericity ratio A and the confinement ratio C of cell tracks (Mokhtari et al., 2013). The asphericity ratio is computed by the ratio of the longest and shortest axes of the enclosing ellipse for a track of N time points. The confinement ratio $C = \frac{1}{N^2} \sum_{m,n} \frac{l(m,n)}{d(m,n)}$ for a track of time-ordered points $t_1 \dots t_N$ is computed by the mean ratio of track length $l(m, n) = \sum_{i=m}^{n-1} d(i, i + 1)$ to the Euclidian distance $d(m, n)$ of track points m and n with $m, n \in [1, N]$. These two measures quantify the straightness of a track on a continuous scale with $A, C \in [0, 1]$, where values of 1 are indicative for perfectly straight tracks, while spatially confined tracks are scored with values close to 0. Since these measures are affected by the track length, we calculated the A and C for each track as a function of the track length (see Figure 6). To test for differences we applied a local regression (LOESS) analysis, which revealed that all three models show highly similar asphericity and confinement ratios with each fit being within the others fits' standard error (see Figure 6). Thus, this analysis predicts no differences in the migration patterns of successful AM for the three PoK models.

Accumulation of AM Limited in Presence of PoK Passageways

The chemokine-mediated recruitment of AM is naturally associated with their accumulation in the alveolus, because it is

unlikely that AM following the chemokine gradient will leave the alveolus before the infection is cleared. Our simulations allow for a comparative analysis of the time-dependent increase in the AM number for the three PoK models. This analysis confirmed that AM accumulate in a way that depends on the exact chemokine parameters. In Figure 5B it can be seen that a higher secretion rate s_{AEC} is associated with higher accumulation of AM. For e.g., optimal chemokine parameters ($D = 60 \mu m^2 min^{-1}$, $s_{AEC} = 50,000 min^{-1}$) the mean number of AM in the PoK+/+ model increases up to 177% compared to random walk migration of AM; this increase is even higher with up to 254% and 413%, respectively, for the PoK+/- and PoK-/- model. This accumulation is due to AM recruitment by the chemokine gradient, which depends on the model scenarios. Since AM are attracted toward the conidium, they tend to stay in the alveolus instead of leaving the alveolus by migrating against the gradient. Interestingly within the range of AM numbers observed in our simulations, accumulation of AM is only weakly correlated with lowering the infection score, i.e., we found a Pearson correlation coefficient of -0.41 (see Supplementary Figure S5A). A massive recruitment of AM toward a single alveolus within the pulmonary tissue might increase the risk for unresolved infections in other alveoli keeping in mind that the lung is constantly exposed to various pathogens simultaneously. Therefore, high levels of AM accumulation in a specific alveolus should be generally avoided to keep the immune system in a state of flexible responsiveness.

To understand why AM accumulation occurs, it is important to put the chemokine secretion induced at the conidium site into perspective. Since the evolving chemokine profile is strongly influenced by the random position of the conidium

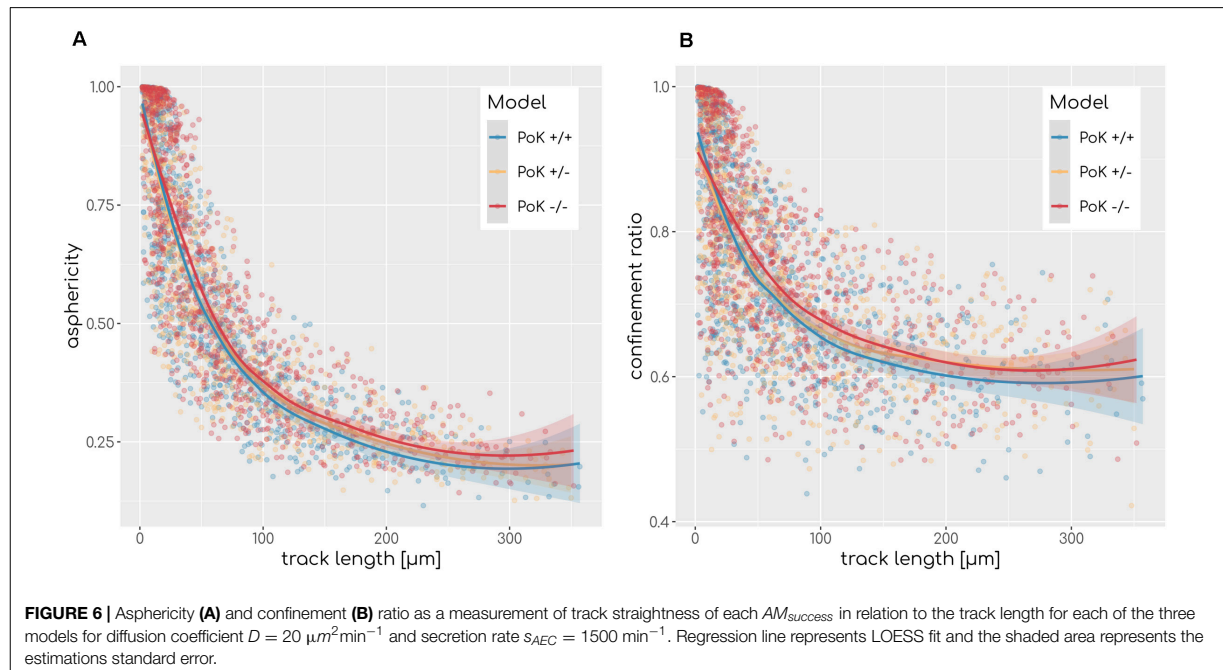


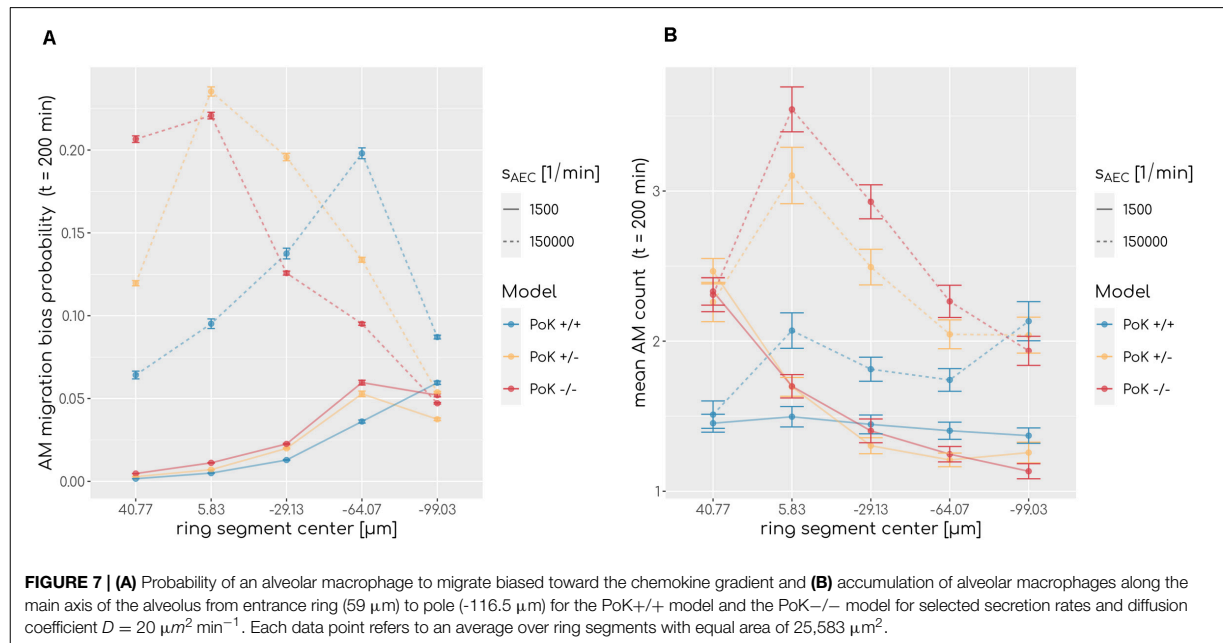
FIGURE 6 | Asphericity (A) and confinement (B) ratio as a measurement of track straightness of each $AM_{success}$ in relation to the track length for each of the three models for diffusion coefficient $D = 20 \mu m^2 min^{-1}$ and secretion rate $s_{AEC} = 1500 min^{-1}$. Regression line represents LOESS fit and the shaded area represents the estimations standard error.

in the alveolus, we decided to make the three different models comparable by locating the conidium at a fixed position in each simulation. This position was chosen to be at the pole of the alveolus, i.e., at the symmetry point of the alveolus with largest distance to the entrance ring (see **Figure 1**). The induced chemokine profile attains highest concentration values at the pole and lowest values at the alveolar entrance ring; thus, the concentration gradient has its steepest slope in between depending on the applied chemokine parameters, i.e., the diffusion coefficient and the secretion rate. While at the point of steepest slope AM follow the chemokine gradient with highest probability, they tend to switch to predominantly random walk migration close to the pole and the entrance ring (see **Figure 7A**). We observed in our simulations that the higher the chemokine secretion rate, the closer is the point of steepest slope shifted to the entrance ring. As a result, AM entering the alveolus quickly migrate to this region and will most likely remain there. As a consequence, AM are less likely to leave the alveolus or detect the conidium at the pole position (see **Figure 7B**). This effect due to the chemokine accumulation is observed in all three models, but is most pronounced in the PoK-/- model and explains the increased AM numbers (see **Supplementary Figure S6**). While increased AM numbers may be thought to be associated with a lower infection score, the quantitative evaluation of our computer simulations revealed this correlation to be only weak, independent whether the conidium was positioned randomly or at the pole (see **Supplementary Figures S5, S7**). For a more detailed comparison between the random conidium positioning model and the setup with a conidium fixed at the alveolus pole we refer to the **Supplementary Material Section 1.3**.

DISCUSSION

In the present study, we investigated the impact of Pores of Kohn (PoK) on the clearance of *Aspergillus fumigatus* infections in the human lung. To this end, we performed computer simulations based on an established hybrid agent-based virtual infection model (Pollmächer and Figge, 2014, 2015; Blickensdorf et al., 2019). This framework represents a realistic, spatio-temporal three-dimensional model that was carefully designed based on available experimental data from literature on the human alveolus. It incorporates alveolar macrophages (AM) and chemokine signaling released by AEC to allow screening for physiologically relevant signaling parameters as well as to quantitatively investigate infection clearance. We developed three model setups to investigate how infection clearance would be affected by passaging of AM or chemokines through PoK: the PoK+/+ model, which allows for chemokine and AM exchange, the PoK+/- model, which does allow only for chemokine exchange, and the PoK-/- model, which does not allow for chemokine and AM exchange.

We could show that, over the scanned range of chemokine parameters significant differences in the infection clearance between the models exist. However, the impact of PoK on the spatio-temporal infection dynamics has only a small effect size: The absolute differences in the infection scores that were computed from our simulations are smaller than 0.05 for 72% of all comparisons. This suggests that infection clearance can be comparably well achieved within the PoK+/+ model as well as the PoK-/- and PoK+/- models. We conclude that AM recruitment through PoK plays only a minor role with regard to infection clearance. However, we found that the PoK+/+ model



suggests that infection clearance is independent of the position of the conidium, whereas in the PoK+/+ and the PoK-/- model conidia detection was more efficiently realized close to the alveolar entrance ring than at the alveolus pole (see **Figure 4**). Thus, a conidium at the pole would impose a higher infection risk for the host if AM could not migrate through PoK. Although the assumption of a uniform random distribution of the conidium position after inhalation is reasonable, a spatial distribution of conidium positions that is biased in some way may affect the infection score in favor of one model. For example, Xi and Talaat (2019) suggest that conidia reside in close proximity to the alveolar entrance ring, where the PoK+/+ and PoK-/- models have a detection advantage, since all AM enter through the alveolar entrance ring leading to a higher density of AM in this region (see **Figure 4**). Our simulations also showed that, without pathogens present in the alveolus, AM migration through PoK allowed for a uniform distribution of AM on the alveolar surface, whereas prohibited AM migration through PoK leads to an accumulation of AM in the proximity of the entrance ring.

Besides differences in the infection score between the three models, our simulations revealed that other dynamics are affected by different properties of PoK. In the PoK-/- model the prohibited outflow of chemokine through PoK causes an accumulation of chemokines. As a consequence, the lowest infection score is achieved at a different chemokine parameter regime with a lower secretion rate s_{AEC} compared to the PoK+/+ and PoK+/- models. Since the true secretion rate still needs to be determined experimentally, it could indeed be possible that the PoK-/- model outperforms the other two models in terms of infection clearance. Furthermore, our simulations demonstrate the effect of AM accumulation caused by chemokine signaling and show its dependency on the properties of PoK. Although this

effect is dependent on the secretion rate s_{AEC} and the diffusion coefficient D and can be observed in all three models, relatively high AM accumulation was present in the PoK+/- and even stronger in the PoK-/- model. This AM accumulation effect imposes a higher risk for undetected pathogens. AM that are recruited to a site of infection may be effectively missing in other alveoli of the lung. The lung is an organ, which is constantly confronted with various pathogens simultaneously, implying that the AM availability is a crucial factor for a fast response of the immune defense. An unnecessarily excessive recruitment of AM, therefore, may be disadvantageous for the host and PoK that allow for AM passage can play an important role in this regulation.

One of the most recent and detailed studies on the function of PoK in the human lung discusses the behavior of alveoli during inflation (Namati et al., 2008). Namati et al. (2008) further developed a hypothesis according to which alveoli are changing their shape in reaction to air pressure changes and combined it with the hypothesis that alveoli are consecutively inflated and thus regulate the air pressure. A key role in this mechanism would be played by PoK, which might open and close due to these pressure changes. As a result, AM would have to squeeze through closing and opening PoK. The latter processes would happen fast according to the typical human breathing frequency of 12–18 min^{-1} (Barrett et al., 2012). A typical AM speed of 4 $\mu\text{m} \text{min}^{-1}$ suggests that for migrating through a PoK of a few micrometers in length, AM would need in the order of 1 min for PoK passage (Glasgow et al., 1989). Thus, AM passage through PoK would be interrupted by frequent closing and opening of PoK. One option to combine both hypotheses of AM passing through PoK and frequent PoK opening would be that AM migration is air-flow assisted due to the associated high changes

in the air pressure in PoK, as suggested by Namati et al. (2008) A similar argumentation can be found by Oldham and Moss (1989) arguing that the opening of a PoK due to inhalation may result in bursting of the surfactant layer. An AM residing at such a spot may thus be accelerated and “pushed” through a PoK. While Peão et al. (1993) as well as Bastacky and Goerke (1992) present images of AM within PoK, the quantitative analysis of the infection clearance in the three different virtual infection scenarios allows for the statement that AM passaging is not necessary for low infection scores but imposes the positive effect of homogeneous AM distributions in the alveolus.

In the future, our understanding of the role of PoK may be deepened by systems biology approaches that take into account aspects of the mechanics of alveolar ventilation as well as other immune cell types involved in the host-pathogen interaction between humans and *A. fumigatus*. In particular, Bozza et al. (2002) observed that dendritic cells (DCs) are as well involved in the immune response against *A. fumigatus* during the first hours post-infection: DCs were shown to (i) internalize conidia and hyphae (ii) discriminate between the different forms regarding cytokine production, (iii) undergo functional maturation upon migration to draining lymph nodes and spleens, and (iv) instruct local and peripheral T-helper cell reactivity against *A. fumigatus*. Furthermore, it is known that polymorphonuclear neutrophils, which may be recruited by AM from the blood stream (Pollmächer et al., 2016), are involved in the immune response during pulmonary aspergillosis and provide an arsenal of immune effector mechanisms against *A. fumigatus* (Brakhage et al., 2010). In this context, it will be important to investigate the system dynamics as a function of the number of immune cells that are estimated to be resident in or recruited to the alveolus. Additionally it has been demonstrated that AEC are able to ingest and phagocytose conidia (Oshero, 2012). Furthermore, the hybrid agent-based framework can be applied to also simulate hyphal growth of the fungus at later time points and invasion into the blood vessels. However, modeling such complex mechanisms requires a firm experimental data basis, which might be provided by imaging

experiments that can nowadays be realized using lung-on-chip models (Mosig, 2017; Deinhardt-Emmer et al., 2020; Schicke et al., 2020).

DATA AVAILABILITY STATEMENT

The raw data supporting the conclusions of this article will be made available by the authors, without undue reservation, to any qualified researcher.

AUTHOR CONTRIBUTIONS

MF conceived and designed this study and provided computational resources. MB did the data processing, implementation and application of the computational algorithm. MB, ST, and MF evaluated and analyzed the results of this study, drafted the manuscript, revised it critically for important intellectual content and final approval of the version to be published, and agreed to be accountable for all aspects of the work in ensuring that questions related to the accuracy or integrity of any part of the work are appropriately investigated and resolved. All authors contributed to the article and approved the submitted version.

FUNDING

This work was financially supported by the International Leibniz Research School for Microbial and Biomolecular Interactions (ILRS) and by the Deutsche Forschungsgemeinschaft (DFG) through the CRC/TR124 FungiNet (project B4 to MF).

SUPPLEMENTARY MATERIAL

The Supplementary Material for this article can be found online at: <https://www.frontiersin.org/articles/10.3389/fmicb.2020.01951/full#supplementary-material>

REFERENCES

- Adams, W. E., and Livingstone, H. M. (1931). Obstructive pulmonary atelectasis. *Arch. Surg.* 23:500. doi: 10.1001/archsurg.1931.01160090145005
- Balász, I., Hofmann, W., Farkas, Á., and Madas, B. G. (2008). Three-dimensional model for aerosol transport and deposition in expanding and contracting alveoli. *Inhal. Toxicol.* 20, 611–621. doi: 10.1080/08958370801915291
- Baltussen, T. J. H., Coolen, J. P. M., Zoll, J., Verweij, P. E., and Melchers, W. J. G. (2018). Gene co-expression analysis identifies gene clusters associated with isotropic and polarized growth in *Aspergillus fumigatus* conidia. *Fungal Genet. Biol.* 116, 62–72. doi: 10.1016/j.fgb.2018.04.013
- Barrett, K., Barman, S., Boitano, S., and Brooks, H. (2012). *Ganong's Review of Medical Physiology*, 24th Edn. New York, NY: McGraw-Hill.
- Bastacky, J., and Goerke, J. (1992). Pores of Kohn are filled in normal lungs: low-temperature scanning electron microscopy. *J. Appl. Physiol.* 73, 88–95. doi: 10.1152/jappl.1992.73.1.88
- Behnsen, J., Hartmann, A., Schmalzer, J., Gehrke, A., Brakhage, A. A., and Zipfel, P. F. (2008). The opportunistic human pathogenic fungus *Aspergillus fumigatus* evades the host complement system. *Infect Immun.* 76, 820–827. doi: 10.1128/iai.01037-07
- Blickensdorf, M., Timme, S., and Figge, M. T. (2019). Comparative assessment of aspergillosis by virtual infection modeling in murine and human lung. *Front. Immunol.* 10:142. doi: 10.3389/fimmu.2019.00142
- Bozza, S., Gaziano, R., Spreca, A., Bacci, A., Montagnoli, C., di Francesco, P., et al. (2002). Dendritic cells transport conidia and hyphae of *Aspergillus fumigatus* from the airways to the draining lymph nodes and initiate disparate Th responses to the fungus. *J. Immunol.* 168, 1362–1371. doi: 10.4049/jimmunol.168.3.1362
- Brakhage, A. A., Bruns, S., Thywissen, A., Zipfel, P. F., and Behnsen, J. (2010). Interaction of phagocytes with filamentous fungi. *Curr. Opin. Microbiol.* 13, 409–415. doi: 10.1016/j.mib.2010.04.009
- Bustamante-Marin, X. M., and Ostrowski, L. E. (2017). Cilia and mucociliary clearance. *Cold Spring Harb. Perspect. Biol.* 9: a028241.

- Cordingley, J. L. (1972). Pores of Kohn. *Thorax* 27, 433–441. doi: 10.1136/thx.27.4.433
- Dagenais, T. R. T., and Keller, N. P. (2009). Pathogenesis of *Aspergillus fumigatus* in invasive Aspergillosis. *Clin. Microbiol. Rev.* 22, 447–465. doi: 10.1128/cmr.00055-08
- Danilevskaia, O., Averyanov, A., Lesnyak, V., Chernyaev, A., and Sorokina, A. (2015). Confocal laser endomicroscopy for diagnosis and monitoring of pulmonary alveolar proteinosis. *J. Bronchol. Interv. Pulmonol.* 22, 33–40. doi: 10.1097/lbr.0000000000000126
- Deinhardt-Emmer, S., Rennert, K., Schicke, E., Cseresnyés, Z., Windolph, M., Nietzsche, S., et al. (2020). Co-infection with *Staphylococcus aureus* after primary influenza virus infection leads to damage of the endothelium in a human alveolus-on-a-chip model. *Biofabrication* 12:025012. doi: 10.1088/1758-5090/ab7073
- Glasgow, J. E., Farrell, B. E., Fisher, E. S., Lauffenburger, D. A., and Daniele, R. P. (1989). The motile response of alveolar macrophages. An experimental study using single-cell and cell population approaches. *Am. Rev. Respir. Dis.* 139, 320–329. doi: 10.1164/ajrccm/139.2.320
- Guillerman, R. P. (2010). Imaging of childhood interstitial lung disease. *Pediatric Allergy Immunol. Pulmonol.* 23, 43–68.
- Guo, Z., Sloot, P. M. A., and Tay, J. C. (2008). A hybrid agent-based approach for modeling microbiological systems. *J. Theor. Biol.* 255, 163–175. doi: 10.1016/j.jtbi.2008.08.008
- Hancioglu, B., Swigon, D., and Clermont, G. (2007). A dynamical model of human immune response to influenza A virus infection. *J. Theor. Biol.* 246, 70–86. doi: 10.1016/j.jtbi.2006.12.015
- Hao, W., Marsh, C., and Friedman, A. (2015). A mathematical model of idiopathic pulmonary fibrosis. *PLoS One* 10:e0135097. doi: 10.1371/journal.pone.0135097
- Hocke, A. C., Suttrop, N., and Hippenstiel, S. (2017). Human lung ex vivo infection models. *Cell Tissue Res.* 367, 511–524. doi: 10.1007/s00441-016-2546-z
- Horn, F., Heinekamp, T., Kniemeyer, O., Pollmächer, J., Valiante, V., and Brakhage, A. A. (2012). Systems biology of fungal infection. *Front. Microbiol.* 3:108. doi: 10.3389/fmicb.2012.00108
- Kawakami, M., and Takizawa, T. (1987). Distribution of pores within alveoli in the human lung. *J. Appl. Physiol.* 63, 1866–1870. doi: 10.1152/jappl.1987.63.5.1866
- Kohn, H. N. (1893). Zur Histologie der indurirenden fibrinösen Pneumonie. *Munch Med Wschr.* 40:42.
- Krombach, F., Münzing, S., Allmeling, A. M., Gerlach, J. T., Behr, J., and Dörger, M. (1997). Cell size of alveolar macrophages: an interspecies comparison. *Environ. Health Perspect.* 105(Suppl. 5), 1261–1263. doi: 10.1289/ehp.9710551261
- Latgé, J. (2001). The pathobiology of *Aspergillus fumigatus*. *Trends Microbiol.* 9, 382–389. doi: 10.1016/s0966-842x(01)02104-7
- Latgé, J.-P. (1999). *Aspergillus fumigatus* and Aspergillosis. *Clin. Microbiol. Rev.* 12, 310–350.
- Lehnert, T., Timme, S., Pollmächer, J., Hünninger, K., Kurzai, O., and Figge, M. T. (2015). Bottom-up modeling approach for the quantitative estimation of parameters in pathogen-host interactions. *Front. Microbiol.* 6:608. doi: 10.3389/fmicb.2015.00608
- MacWilliam, T., and Cecka, C. (2013). “CrowdCL: web-based volunteer computing with WebCL,” in *Proceedings of the 2013 IEEE High Performance Extreme Computing Conference, HPEC*; Waltham, MA, Waltham, MA, 1–6.
- Margalit, A., and Kavanagh, K. (2015). The innate immune response to *Aspergillus fumigatus* at the alveolar surface. *FEMS Microbiol. Rev.* 39, 670–687.
- Medyukhina, A., Timme, S., Mokhtari, Z., and Figge, M. T. (2015). Image-based systems biology of infection. *Cytom Part A* 87, 462–470. doi: 10.1002/cyto.a.22638
- Mokhtari, Z., Mech, F., Zitzmann, C., Hasenberg, M., Gunzer, M., and Figge, M. T. (2013). Automated characterization and parameter-free classification of Cell tracks based on local migration behavior. *PLoS One* 8:e80808. doi: 10.1371/journal.pone.0080808
- Mosig, A. S. (2017). Organ-on-chip models: new opportunities for biomedical research. *Future Sci. OA* 3:FSO130.
- Namati, E., Thiesse, J., De Ryk, J., and McLennan, G. (2008). Alveolar dynamics during respiration: are the pores of Kohn a pathway to recruitment? *Am. J. Respir. Cell. Mol. Biol.* 38, 572–578. doi: 10.1165/rcmb.2007-0120oc
- Ochs, M., Nyengaard, J. R., Jung, A., Knudsen, L., Voigt, M., Wahlers, T., et al. (2004). The number of alveoli in the human lung. *Am. J. Respir. Crit. Care Med.* 169, 120–124. doi: 10.1164/rccm.200308-1107oc
- Oertel, L. (1919). Ober die Alveolarporen in den Säugetierlungen. S-B Heidelberg Akad Wiss, math-nat Ki Abt B Biol Wiss. Heidelberg: Thorax.
- Oldham, M. J., and Moss, O. R. (1989). Pores of Kohn: forgotten alveolar structures and potential source of aerosols in exhaled breath. *J. Breath Res.* 139, 320–329.
- Oshero, N. (2012). Interaction of the pathogenic mold *Aspergillus fumigatus* with lung epithelial cells. *Front. Microbiol.* 3:346. doi: 10.3389/fmicb.2012.00346
- Peão, M., Águas, A. P., de Sá, C. M., and Grande, N. R. (1993). Morphological evidence for migration of particle-laden macrophages through the interalveolar pores of Kohn in the murine lung. *Cells Tissues Organs.* 147, 227–232. doi: 10.1159/000147509
- Pollmächer, J., and Figge, M. T. (2014). Agent-based model of human alveoli predicts chemotactic signaling by epithelial cells during early *Aspergillus fumigatus* infection. *PLoS One* 9:e111630. doi: 10.1371/journal.pone.0111630
- Pollmächer, J., and Figge, M. T. (2015). Deciphering chemokine properties by a hybrid agent-based model of *Aspergillus fumigatus* infection in human alveoli. *Front. Microbiol.* 6:503. doi: 10.3389/fmicb.2015.00503
- Pollmächer, J., Timme, S., Schuster, S., Brakhage, A. A., Zipfel, P. F., and Figge, M. T. (2016). Deciphering the counterplay of *Aspergillus fumigatus* infection and host inflammation by evolutionary games on graphs. *Sci. Rep.* 6:27807.
- Prause, M. T. E., Lehnert, T., Timme, S., Hünninger, K., Leonhardt, I., Kurzai, O., et al. (2018). Predictive virtual infection modeling of fungal immune evasion in human whole blood. *Front. Immunol.* 9:560. doi: 10.3389/fimmu.2018.00560
- Rennard, S. I., Togo, S., and Holz, O. (2006). Cigarette smoke inhibits alveolar repair: a mechanism for the development of emphysema. *Proc. Am. Thor. Soc.* 3, 703–708. doi: 10.1513/pats.200605-121sf
- Riedemann, N. C., Guo, R.-F., Sarma, V. J., Laudes, I. J., Huber-Lang, M., Warner, R. L., et al. (2002). Expression and function of the C5a receptor in rat alveolar epithelial cells. *J. Immunol.* 168, 1919–1925. doi: 10.4049/jimmunol.168.4.1919
- Schicke, E., Cseresnyés, Z., Rennert, K., Vau, V., Haupt, K. F., Hornung, F., et al. (2020). *Staphylococcus aureus* lung infection results in down-regulation of surfactant protein-A mainly caused by pro-inflammatory macrophages. *Microorganisms* 8:577. doi: 10.3390/microorganisms8040577
- Sharp, K., Crampin, E., and Sneyd, J. (2015). A spatial model of fluid recycling in the airways of the lung. *J. Theor. Biol.* 382, 198–215. doi: 10.1016/j.jtbi.2015.06.050
- Sreekantapuram, S., Lehnert, T., Prause, M. T. E., Berndt, A., Berens, C., Figge, M. T., et al. (2020). Dynamic interplay of host and pathogens in an avian whole blood model. *Front. Immunol.* 11:500. doi: 10.3389/fimmu.2020.00500
- Sukumar, N. (2003). Voronoi cell finite difference method for the diffusion operator on arbitrary unstructured grids. *Int. J. Numer. Methods Eng.* 57, 1–34. doi: 10.1002/nme.664
- Thomson, J. J. (1904). XXIV. On the structure of the atom: an investigation of the stability and periods of oscillation of a number of corpuscles arranged at equal intervals around the circumference of a circle; with application of the results to the theory of atomic structure. *London Edinburgh Dublin Philos. Mag. J. Sci.* 7, 237–265. doi: 10.1080/14786440409463107
- Timme, S., Lehnert, T., Prause, M. T. E., Hünninger, K., Leonhardt, I., Kurzai, O., et al. (2018). Quantitative simulations predict treatment strategies against fungal infections in virtual neutropenic patients. *Front. Immunol.* 9:667. doi: 10.3389/fimmu.2018.00667
- Tokarski, C., Hummert, S., Mech, F., Figge, M. T., Germerodt, S., Schroeter, A., et al. (2012). Agent-based modeling approach of immune defense against spores of opportunistic human pathogenic fungi. *Front. Microbiol.* 3:129. doi: 10.3389/fmicb.2012.00129
- Van De Veerdonk, F. L., Gresnigt, M. S., Romani, L., Netea, M. G., and Latgé, J. P. (2017). *Aspergillus fumigatus* morphology and dynamic host interactions. *Nat. Rev. Microbiol.* 15, 661–674. doi: 10.1038/nrmicro.2017.90
- Voit, E. O. (2014). Mesoscopic modeling as a starting point for computational analyses of cystic fibrosis as a systemic disease. *Biochim. Biophys. Acta Proteomics* 1844(1 PtB), 258–270. doi: 10.1016/j.bbapap.2013.03.023
- Wallace, W. A. H., Gillooly, M., and Lamb, D. (1992). Intra-alveolar macrophage numbers in current smokers and non-smokers: a morphometric study of tissue sections. *Thorax* 47, 437–440. doi: 10.1136/thx.47.6.437

- Weibel, E. R. (1963). *Morphometry of the Human Lung*, 1st Edn. Berlin Heidelberg: Springer, 164.
- Wright, J. L. (2001). The importance of ultramicroscopic emphysema in cigarette smoke-induced lung disease. *Lung* 179, 71–81. doi: 10.1007/s004080000048
- Xi, J., and Talaat, M. (2019). Nanoparticle deposition in rhythmically moving acinar models with interalveolar septal apertures. *Nanomaterials* 9:E1126.
- Yoshikawa, A., Sato, S., Tanaka, T., Hashisako, M., Kashima, Y., Tsuchiya, T., et al. (2016). Breakdown of lung framework and an increase in pores of kohn as initial events of emphysema and a cause of reduction in diffusing capacity. *Int. J. COPD* 11, 2287–2294. doi: 10.2147/copd.s114281

Conflict of Interest: The authors declare that the research was conducted in the absence of any commercial or financial relationships that could be construed as a potential conflict of interest.

Copyright © 2020 Blickensdorf, Timme and Figge. This is an open-access article distributed under the terms of the Creative Commons Attribution License (CC BY). The use, distribution or reproduction in other forums is permitted, provided the original author(s) and the copyright owner(s) are credited and that the original publication in this journal is cited, in accordance with accepted academic practice. No use, distribution or reproduction is permitted which does not comply with these terms.

ASPERGILLOSIS-ON-CHIP

FORMULAR 1¹**Manuskript Nr. 3**

Titel des Manuskriptes: Invasive aspergillosis-on-chip: A quantitative treatment study of human *Aspergillus fumigatus* infection

Autoren: Hoang, M.T.N., Cseresnyés, Z., Hartung, S., Blickensdorf, M., Saffer, C., Rennert, K., Mosig, A.S., von Lilienfeld-Toal, M., Figge, M.T.

Bibliographische Informationen : Submitted to *Biomaterials*

Der Kandidat / Die Kandidatin ist

Erstautor/-in, Ko-Erstautor/-in, Korresp. Autor/-in, Koautor/-in.

Status : Submitted to *Biomaterials*

Anteile (in %) der Autoren / der Autorinnen an der Publikation (anzugeben ab 20%)

Autor/-in	Konzeptionell	Datenanalyse	Experimentell	Verfassen des Manuskriptes	Bereitstellung von Material
Hoang			60 %		
Cseresnyés		40 %			
Hartung			30 %		
Blickensdorf		30 %			
Saffer					
Rennert					
Mosig	33 %				33 %
Lilienfeld-Toal	33 %				33 %
Figge	33 %	20 %			33 %

Unterschrift Kandidat/-in

Unterschrift Betreuer/-in (Mitglied der Fakultät)

¹ Die Unterschriften müssen nur im separat im Dekanat einzureichenden ausgefüllten Formular im Original vorliegen. In der in die Dissertation eingebundenen Fassung dürfen die Unterschriften und Unterschriftenfelder fehlen.

Manuscript

Invasive aspergillosis-on-chip: A quantitative treatment study of human *Aspergillus fumigatus* infection

Hoang, M.T.N.^{1,2,*}, Cseresnyés, Z.^{3*}, Hartung, S.^{1,2,*}, Blickensdorf, M.³, Saffer, C.³, Rennert, K.⁴, Mosig, A.S.^{5,6}, von Lilienfeld-Toal, M.^{1,2,#,+}, Figge, M.T.^{3,7,#,+}

1 Infections in Hematology and Oncology, Leibniz Institute for Natural Product Research and Infection Biology, Jena, Germany

2 Department for Hematology and Medical Oncology, Jena University Hospital, Jena, Germany

3 Applied Systems Biology, Leibniz Institute for Natural Product Research and Infection Biology, Jena, Germany

4 Dynamic42 GmbH, Jena, Germany

5 INSPIRE, Center for Sepsis Control and Care, Jena University Hospital, Jena, Germany

6 Institute of Biochemistry II, Jena University Hospital, Jena, Germany

7 Institute of Microbiology, Faculty of Biological Sciences, Friedrich Schiller University Jena, Jena, Germany

*,# authors contributed equally

+ corresponding authors:

Marie.von_Lilienfeld-Toal@med.uni-jena.de,

thilo.figge@leibniz-hki.de

Abbreviations

3D three-dimensional

ALI air-liquid interface

C confinement ratio

CFW Calcofluor White

COPD chronic obstructive pulmonary disease

eGFP enhanced green fluorescent protein

FITC fluorescein isothiocyanate

GM-CSF granulocyte-monocyte colony stimulating factor

HUVEC human umbilical vein endothelial cells

IAC invasive aspergillosis-on-chip

I(P)A invasive (pulmonary) aspergillosis

IL Interleukin

MEC minimal effective concentration

MIC minimal inhibitory concentration

M ϕ Macrophages

MOI multiplicity of infection

SP-A surfactant protein A

RT room temperature

vWF von Willebrand factor

Abstract

Invasive pulmonary aspergillosis is associated with a high mortality rate and poses a direct threat to immunocompromised patients. Here, we present the invasive aspergillosis-on-chip (IAC) model to investigate *Aspergillus fumigatus* infection *in vitro*. The model allows the study of the lateral growth and the invasive behaviour of fungal hyphae from the endothelium into the epithelial cell layer in an alveolus-on-chip model. We established an algorithm-based analysis pipeline for three-dimensional confocal microscopy images to visualize and quantify fungal morphology, including hyphal growth and branching. Human macrophages in the IAC model partially inhibited the growth of the fungus, contributed to the release of proinflammatory cytokines (IL-1, IL-6, TNF) and chemokines (IL-8 and MCP-1) associated with an increased number of invasive hyphae. Similar to *in vivo*, the application of the fungistatic drug caspofungin limited the fungal growth and resulted in morphological changes of the hyphal tree previously described in other studies. The IAC infection model allows the identification and characterization of cellular infection targets and *in vitro* testing of antifungal drugs in clinically relevant concentrations. It thus represents a promising tool to broaden the understanding of pathogenicity and pathophysiology of invasive aspergillosis.

Keywords

invasive aspergillosis, *Aspergillus fumigatus*, alveolus-on-chip, microphysiological system, image analysis, caspofungin

Introduction

Invasive pulmonary aspergillosis (IPA) is a life-threatening condition with high mortality rates that attacks immunocompromised human hosts, such as recipients of hematopoietic stem cells or solid organ transplants [1]. In healthy humans, alveolar macrophages guard the lung alveoli by recognizing and engulfing small pathogens, including asexual spores (conidia) of the filamentous fungus *Aspergillus fumigatus*. In the absence of proper protection mechanisms, the conidia are not removed. Still, they can give rise to filamentous bodies (hyphae), resulting in an infection characterized by lung tissue destruction and, eventually, the invasion of blood vessels [2].

Research on IPA *in vitro* is commonly executed in confrontation assays of fungal conidia and the immune cells of interest, e.g. neutrophils or macrophages, positioned in a dish providing static conditions [3-6]. More sophisticated cell culture models based on transwell inserts allow the establishment of an air-liquid interface (ALI), where lung epithelial cells reside at an air phase instead of being submerged [7-9]. While this model already gives valuable insight into epithelial-related infection processes, it does not consider the contribution of endothelial cells in the course of infection. In other studies, A549 lung adenocarcinoma epithelial cells were co-cultured with pulmonary artery endothelial cells [10, 11]. However, as the infection and subculture of the cell layers were performed under submerged and static conditions, the contribution of biophysical parameters such as ALI and flow have not been studied.

In addition, there are several mouse models of IPA available for *in vivo* research [12]. Due to the physiological differences between mice and men regarding the morphometry of the lung [13] and the immune cell composition, these animal models cannot recapitulate all aspects of the human disease [14, 15]. One way to avoid animal experiments yet move towards *in vivo*-like conditions are organ on chip-models which have been used to mimic the physiology and pathophysiology of several organs, including the human lung [16-19]. Chip models were successfully utilised to investigate mechanisms of lung diseases such as chronic obstructive pulmonary disease (COPD) [16, 19], as well as for studying the mechanism of *Staphylococcus aureus* and influenza A superinfection [20, 21].

We here leveraged a model of the human alveolus to study infection with *A. fumigatus* which we refer to as invasive aspergillosis-on-chip (IAC) model. The model creates an ALI composed of an alveolar epithelial cell layer co-cultured with macrophages covered by an endothelial lining in a three-dimensional perfused microenvironment, recreating essential microanatomical features of the human alveolus [20]. Combining microscopic imaging in the IAC model and advanced image analysis, we provide for the first time a proof-of-principle for detailed and reliable quantification of pathomechanistical events such as hyphae formation and branching during *A. fumigatus* infection in an alveolus model. Further, we demonstrate the translational potential of the IAC model in antifungal drug testing by characterizing the fungistatic drug caspofungin efficiently interfering with hyphae formation already at therapeutically relevant minimal inhibitory concentrations.

Results

Fungal infection of the lung-on-chip model captures stages of invasive aspergillosis

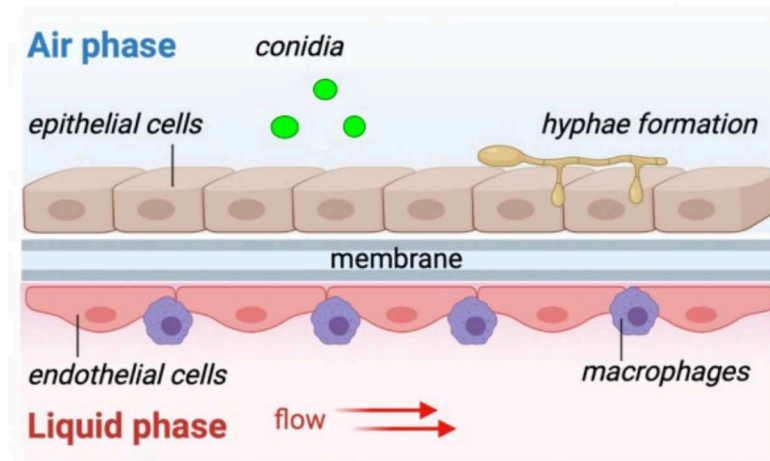


Figure 1: Invasive aspergillosis-on-chip (IAC) model. The human alveolus model contains human endothelial cells in a perfused compartment separated by a porous PET membrane from human lung epithelial cells at an air-liquid interface. Infection was performed by addition of *A. fumigatus* FITC-labelled resting conidia to epithelial cells for 90 minutes. After removal of conidia, perfused incubation overnight resulted in hyphal growth.

FITC: fluorescein isothiocyanate

Inhaled conidia from *A. fumigatus* are sufficiently small ($\sim 2 \mu\text{m}$) to reach the human alveoli [22]. To investigate if conidia can establish an IPA-like phenotype in the alveolus model, the epithelial cell layer was temporarily infected with resting fluorescein isothiocyanate (FITC)-labelled *A. fumigatus* conidia under static conditions. Overnight incubation under perfusion of the endothelial cell layer following infection gave rise to hyphal growth (Fig. 1). Most hyphae grew on the surface of the epithelial side in a long, septated, and branched manner causing limited damage to the epithelial cell layer (Fig. 2A). Moreover, we detected invasive fungal growth from the epithelial into the endothelial side of the alveolus model, accompanied by focal destruction of the confluent endothelial layer. On average, 32 conidia per image ($6 \times 10^{-4}/\mu\text{m}^2$) were found on the epithelial side, whilst this number was much lower on the endothelial side with only two conidia per image (Fig. 2B).

To prove that hyphae detected at the endothelial layer originated from the epithelial layer, an *A. fumigatus* mutant strain was used that constitutively expressed a GnoA-eGFP fusion protein [23]. This enabled us to monitor and quantify hyphal growth by microscopic imaging. We observed that single hyphal branches originating from conidia at the epithelial side grow through the epithelial cell layer, passing the membrane's pores to reach the endothelial cell layer, where they further elongated (Fig. 2C and Supplementary video 1).

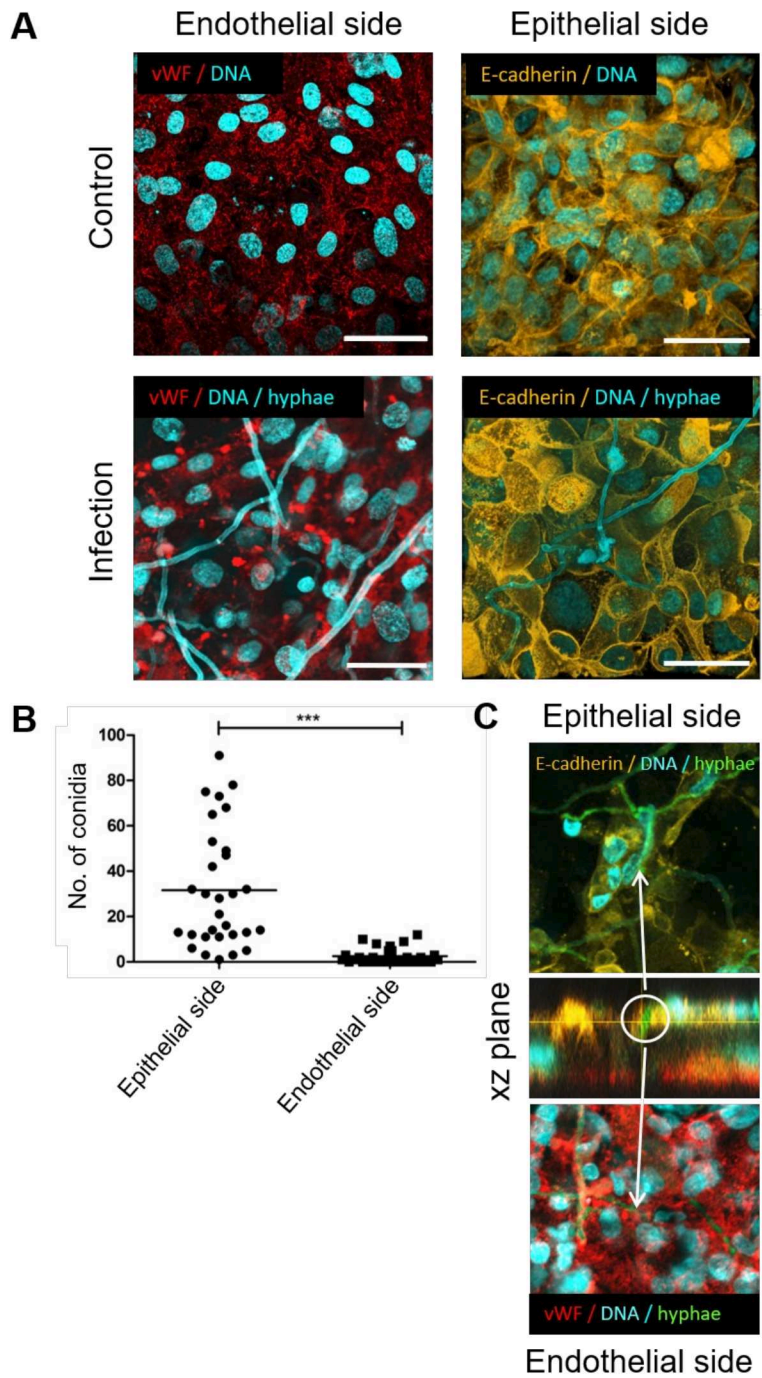


Figure 2: Fungal growth in the IAC model. A) Epithelial cells stained by E-cadherin (orange) and endothelial cells stained by von Willebrand factor (vWF, red) in not infected controls and *A. fumigatus* infected alveolus models. Hyphae stained by Calcofluor white (CFW) in blue (long filaments). Nuclei stained by Hoechst 33258 in blue (elliptic circles). Scale bars = 50µm. B) Conidial counts were high on the epithelium but usually no conidia were found in the endothelium. Mean is indicated by a line. Unpaired two-tailed t-test. *** p<0.001. C) Invasive hyphal growth from the epithelial side (E-cadherin, orange, top) to the endothelial side (vWF, red, bottom) shown by constitutively eGFP-positive *A. fumigatus* mutant (green). Hypha growing vertically through both layers (white circle, middle) with points of penetration indicated by white arrows.

To account for the presence of alveolar macrophages in the human lung, monocytes isolated from human peripheral blood were differentiated *in situ* by GM-CSF at the epithelial side of the alveolus, giving rise to mature macrophages expressing CD68 (Supplementary fig. 1). To verify macrophage functionality, live-cell imaging was used to track Cell Tracker™ Orange-labelled macrophages and FITC-labelled one-hour-swollen conidia for 13.5 hours (Supplementary video 2). We observed a non-uniform movement of macrophages: While some cells remained nearly stationary, we also observed targeted movement of other cells towards FITC-labelled conidia that were subsequently taken up. This indicates that macrophages were alive and functional in clearing conidia in the tissue model. Nonetheless, some conidia germinated and the first outgrowths were observed after four hours (five hours total swelling time). Elongating further, hyphal filaments were visible after six hours of live cell imaging and eventually pierced epithelial and endothelial cells as well as macrophages.

Advanced image analysis enables quantification of fungal growth parameters

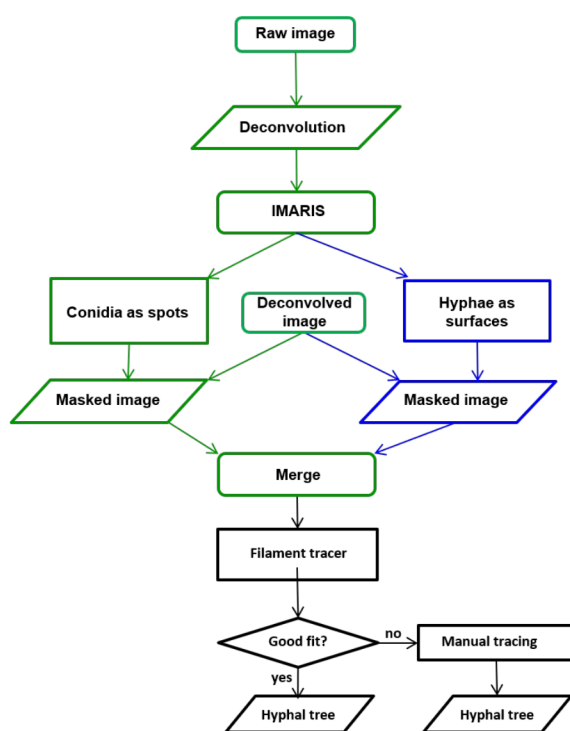


Figure 3: Advanced image analysis of *A. fumigatus* growth by reconstruction of fungal structures using IMARIS.

One of the main goals of this study was to establish a bioimage analysis approach to obtain a 3D *in silico* model of the hyphal network allowing objective quantification of fungal growth (Fig. 3). To this end, tiled 3D confocal laser scanning images were recorded. The raw images were deconvolved during processing, followed by reconstruction of the membrane pores, the conidia, and the fungal hyphae in the IAC model. Labelled hyphae were reconstructed as filaments, using FITC-labelled conidia that served as seed points for the detection algorithm, marking the origins of hyphae. Tracking of fungal hyphae was accomplished by the "Filament Tracer algorithm" as provided by the software IMARIS. However, automated tracking alone could not correctly identify and follow the hyphae from their associated conidia. Therefore,

the image data were curated by manual correction where it was necessary. The reconstructed hyphae were then used to characterize fungal growth dynamics regarding the hyphal length and the number of branches. Since hyphae develop branches with sub-branches, these hierarchical structures were quantified in branching levels (Supplementary fig. 2).

Without macrophages interfering with fungal growth, *A. fumigatus* formed long, up to 2000 μm , hyphae (Fig. 4A) with a mean length of $427 \pm 358 \mu\text{m}$ (Fig. 4B), an average of 4 ± 3 branches per hypha (Fig. 4C), and a mean branching level of 2 ± 1 (Fig. 4D) during overnight incubation in IAC models. About 92% of all conidia applied to the epithelial side of these models gave rise to germlings or hyphae (Fig. 4E) 4-6h after seeding (Supplementary video 2).

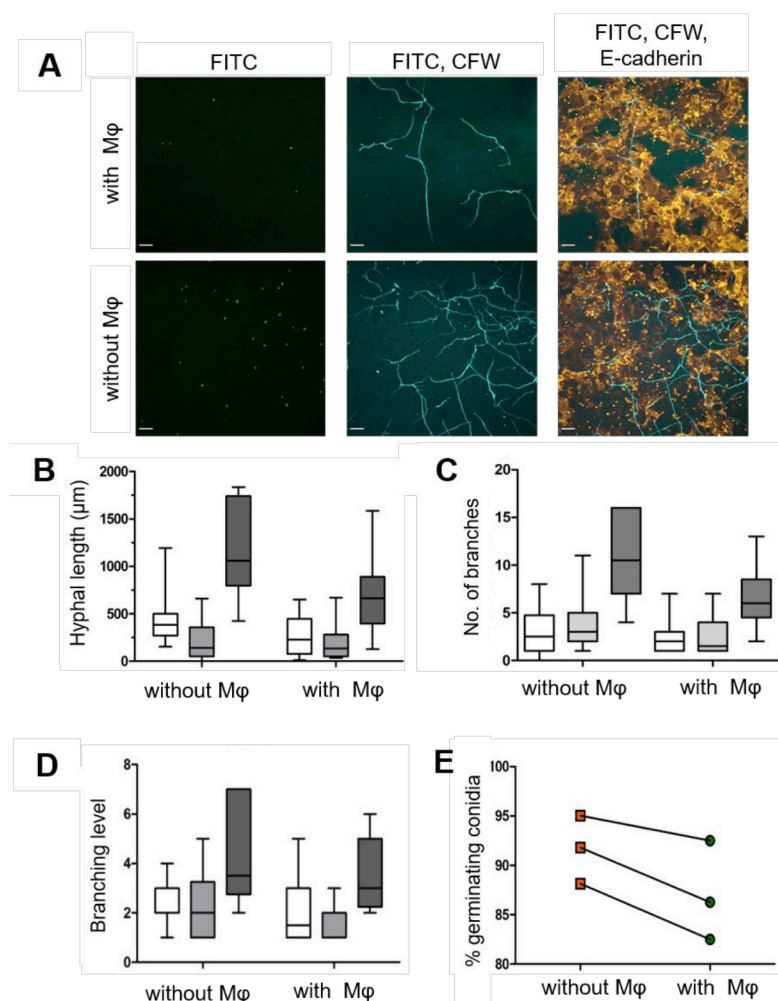


Figure 4: Partial inhibition of *A. fumigatus* growth by human macrophages. A) In IAC models, *A. fumigatus* growth was reduced in presence of macrophages. Conidia stained with FITC (green), hyphae stained with CFW (blue), epithelial cells stained with E-cadherin (orange). Nuclei stained with Hoechst 33258 (blue). Scale bar = 50 μm . B-D) Image analysis-based quantification of B) hyphal length, C) branching level and D) number of branches from IAC models without and with macrophages. Box and whiskers plot of three independent experiments with three different macrophage donors (shades of grey, 6-27 hyphae analysed per experiment). Boxes represent quartiles around median (line). Whiskers indicate minima and maxima. E) Percentage of germinated

conidia in IAC models with and without macrophages from three independent experiments with three different macrophage donors.

M ϕ : Macrophages

The outgrowth of *A. fumigatus* is altered by interaction with macrophages

When grown overnight in the presence of macrophages and under perfusion (Fig. 4A), *A. fumigatus* horizontal hyphal growth was limited (on average $329 \pm 319 \mu\text{m}$, Fig. 4B). In contrast, the mean number of branches (3 ± 3 , Fig. 4C), branching levels (2 ± 1 , Fig. 4D), and germination rate (Fig. 4E) changed only marginally. Macrophages had a further impact on the direction of hyphae formation. In the absence of macrophages, relatively long *A. fumigatus* hyphae were extending on the epithelial side of the IAC model (Fig. 5A, lateral (XY) view), with only occasional invasion through the membrane pores reaching the endothelial side (Fig. 5A, axial (XZ) view). Although fewer hyphae occurred in the presence of macrophages, we observed that about $37 \pm 7 \%$ of these hyphae became invasive (Fig. 5A and Fig. 5B), which is three times more than in the absence of macrophages (on average $12 \pm 5 \%$, $p < 0.01$, Fig. 5B).

Attempting to understand the discrepancy between the percentage of invasive hyphae in the presence or absence of macrophages, we next investigated the invasive behaviour of *A. fumigatus* in response to macrophages in more detail. Fig. 5C shows an example of lateral growth of a hypha above the epithelial cell layer, including branching points (blue arrows) and a turn (orange arrow) from which the branch grew straight towards a membrane pore. Tracking the hypha, we computed the confinement ratio C as a quantitative measure of straightness of invasive hyphal segments [24]. In particular, we evaluated invasive hyphae over a distance of $60 \mu\text{m}$ before the hyphal tips reached the middle point of the membrane. A matrix generated from each subset of points along each invasive hyphal segment is visualized as a heat map (Fig. 5D) and allows detecting hyphal subparts with a straight growth pattern [24]. The straightness of hyphal parts corresponds to high C values (red), whereas turns of the growth direction correspond to low C values (yellow / green). Employing this method in infection scenarios, we observed several turning points (orange arrows) and short distances of straight growth in between in the absence of macrophages.

In contrast, infection scenarios with macrophages exhibited longer straight growth of the invasive hyphal segments before entering the membrane. At around $20 \mu\text{m}$ from the membrane midpoint, *A. fumigatus* hyphae distinctly turned (orange arrow) to continue their fairly straight path through the membrane, arguing for a direct growth fashion of hyphae from the epithelial to the endothelial side. We therefore conclude that invasive hyphal segments grow in a directed manner into the endothelial side. This might occur upon a nutritional gradient. To rule out increased glucose consumption and / or lactate accumulation influencing the fungal growth in macrophage-containing infection scenarios, we analysed the medium used to perfuse the endothelial side during the overnight incubation. Here neither the glucose nor the lactate concentrations were different between samples with or without macrophages (Supplementary fig. 3).

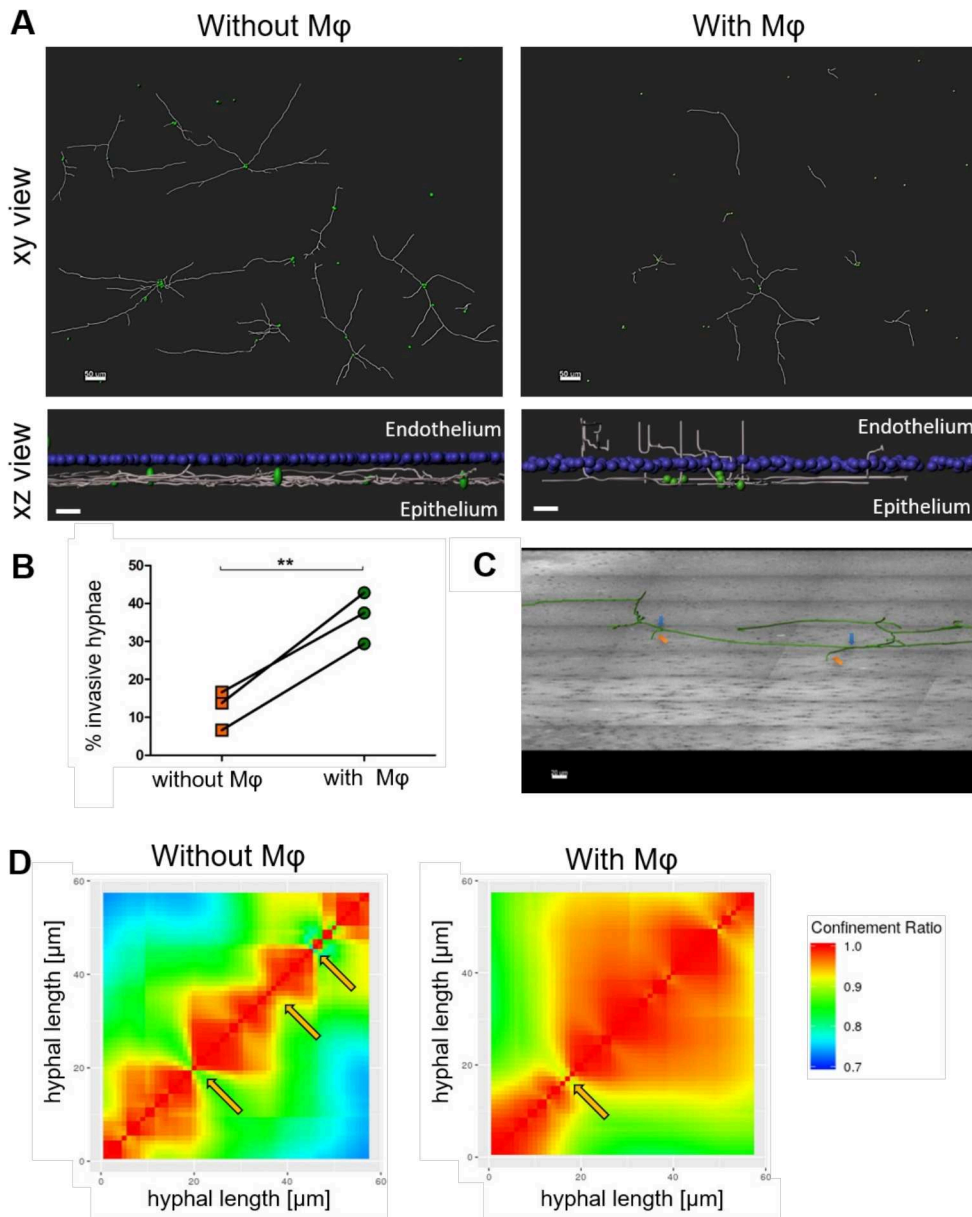


Figure 5: The Outgrowth of *A. fumigatus* is altered by interaction with macrophages A) Reconstructions of *A. fumigatus* hyphae from IAC models with and without macrophages presented as top view (xy view) and as lateral view (xz view) of the epithelial side showing length and direction of fungal growth. Grey lines represent hyphae, green spots represent conidia, blue spots in xz view represent membrane pores. Scale bars = 50 μm . B) Percentage of invasive hyphae in IAC models with and without macrophages from three independent experiments with three different macrophage donors. Unpaired two-tailed t-test, ** $p < 0.01$. C) 3D view of a reconstructed hypha on the epithelial side above the membrane (grey plane with dark spots indicating the pores) with blue arrows pointing to branching points and an orange arrow pointing to turning points of the invasive hypha. D) Heatmaps visualising undirected fungal growth in models without macrophages and models with macrophages showing a straighter growth towards the membrane. Heatmaps were generated from the average confinement ratios of all invasive hyphal segments, i.e. the last 60 μm of a membrane-piercing hyphal branch before reaching the membrane centre (lower left corner of the matrix). The orange arrows indicate turning points where hyphae start to grow straight towards the membrane centre.

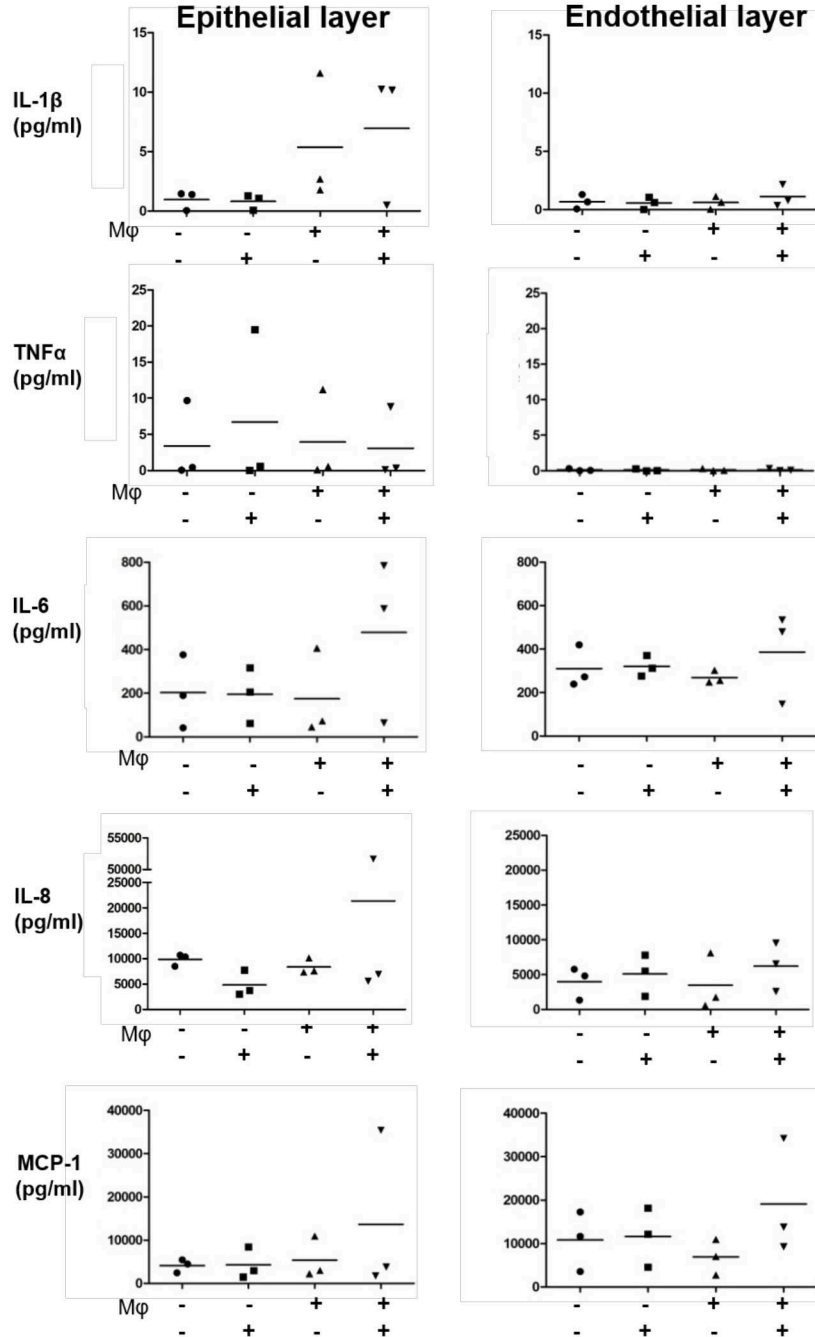
A. fumigatus elicits macrophage response in the IAC model

Figure 6: Cytokine release in IAC models upon *A. fumigatus* infection. Pro-inflammatory cytokines (IL-1 β , TNF α and IL-6) and chemokines (IL-8 and MCP-1) were detected separately on the epithelial and endothelial side of IAC models with and without macrophages in presence or absence of *A. fumigatus*. Each data point presents results obtained by multiplex-assays from three independent experiments (n=3) with three different macrophage donors. Lines represent means. One-way ANOVA with Bonferroni post-test.

Further characterisation of the macrophage response towards *A. fumigatus* in the IAC model was done by investigating cytokines release in the alveolus after overnight incubation, both in the presence and absence of macrophages (Fig. 6 and Supplementary tables 1 and 2). On the epithelial side, the release of the pro-inflammatory cytokines IL-1 β and IL-6 were elevated in the presence of macrophages (on average IL-1 β : 7.0 ± 5.6 pg/ml and IL-6: 195 ± 128 pg/ml compared to controls without macrophages IL-1 β : 0.8 ± 0.6 pg/ml and IL-6: 479 ± 372 pg/ml). Likewise, mean concentrations of IL-8 and MCP-1 increased from IL-8: 4838 ± 2539 pg/ml and MCP-1: 4292 ± 3640 pg/ml without macrophages to IL-8: 21360 ± 26240 pg/ml, MCP-1: 13649 ± 18853 pg/ml in presence of macrophages. IL-8 and MCP-1 are important chemotactic molecules for neutrophils and monocytes, respectively, thus helping to recruit additional immune cells to the site of infection. Because of large inter-individual variation, differences did not reach statistical significance. On the endothelial side, MCP-1 concentrations were elevated after addition of fungus (mean concentration 19071 ± 13283 pg/ml versus 6905 ± 4077 pg/ml without fungus). In contrast to proinflammatory cytokines, we have not observed the release of anti-inflammatory cytokines such as IL-10 (Supplementary fig. 4).

Our data demonstrate that macrophages are activated by conidia germination and affect hyphae formation in the alveolus. However, they are not sufficient for entirely eradicating fungal infection, supporting the hypothesis that additional immune cells, such as neutrophils, are required to mount a robust and efficient antifungal response [25].

The outgrowth of *A. fumigatus* is inhibited by therapeutic levels of voriconazole and amphotericin B

To explore the feasibility of the IAC model as a platform for antifungal drug testing, we mimicked *in vivo* scenarios of invasive aspergillosis in the presence of macrophages under treatment with antifungal agents. We first administered voriconazole or amphotericin B at therapeutic concentrations of $4 \mu\text{g/ml}$ and found that *A. fumigatus* hyphal growth was completely inhibited by both agents. In contrast, we observed extensive hyphal growth by most of the conidia in controls where antifungals were absent (Fig. 7A).

The outgrowth of *A. fumigatus* is modulated by therapeutic levels of caspofungin

In contrast to the observed hyphal growth inhibition by voriconazole or amphotericin B, application of caspofungin at concentrations of 0.05 or $0.5 \mu\text{g/ml}$ only resulted in stalled growth of hyphae (Fig. 7B and 7C). This effect was most pronounced at $0.5 \mu\text{g/ml}$ (mean hyphal length $222 \pm 156 \mu\text{m}$) compared to untreated controls (mean hyphal length $1775 \pm 1462 \mu\text{m}$, $p < 0.001$) and reversed at $5 \mu\text{g/ml}$ (mean hyphal length $741 \pm 659 \mu\text{m}$). This phenomenon is known as “paradoxical growth” and is common to *A. fumigatus* growing under echinocandin treatment (reviewed in [26]). Importantly, in line with previous studies on caspofungin-treated *A. fumigatus* [27-31], hyphae were found in colonies instead of the usually extended hyphal networks of untreated fungi (Fig. 7B), and we observed an altered morphology with relatively short and thick hyphae. In addition, compared to untreated controls (mean branching level 4 ± 2 , mean number of branches 9 ± 8 , see Fig. 7D and 7E), branching of *A. fumigatus* hyphae was

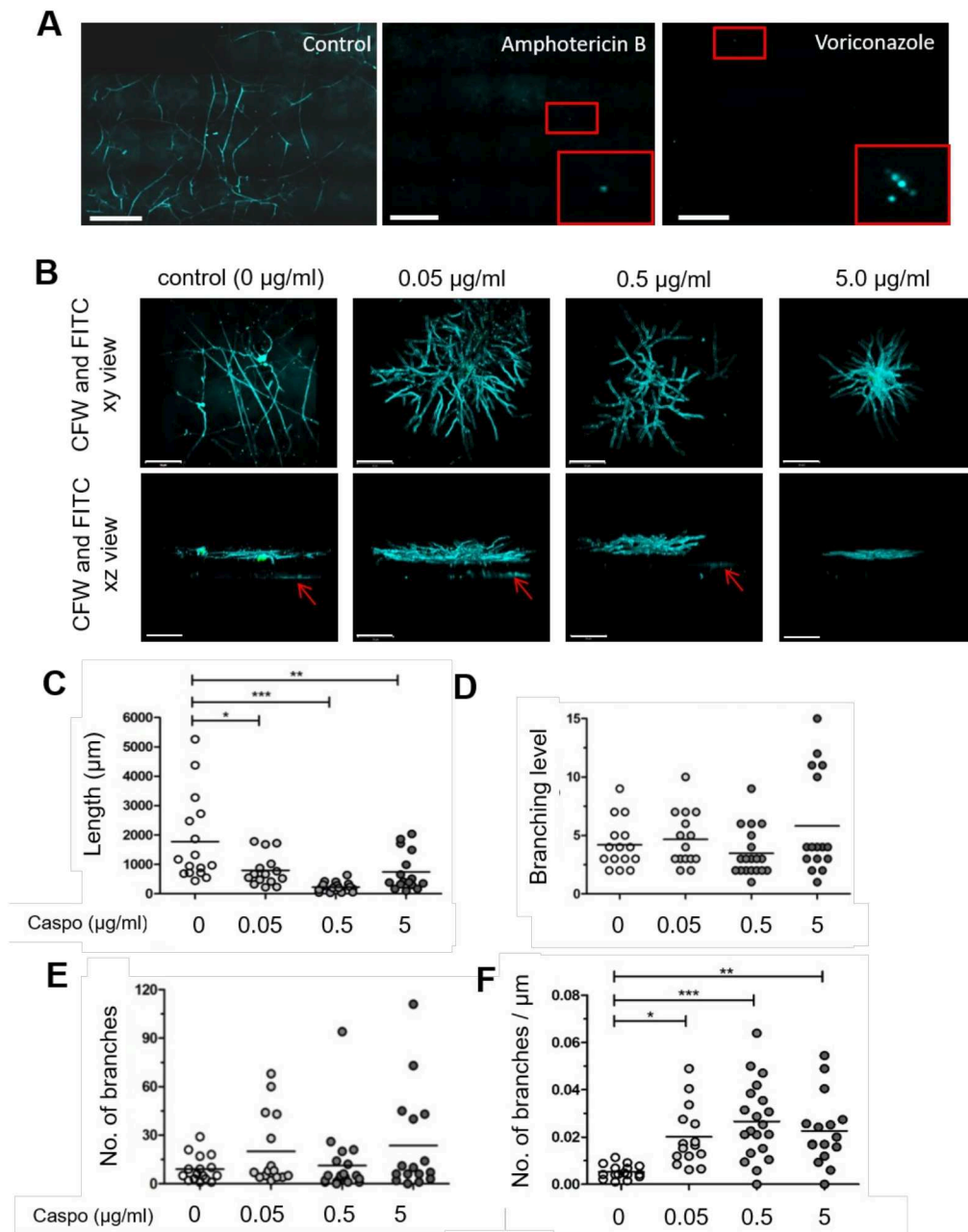


Figure 7: IAC model as a platform for drug testing. A) Fungicidal drugs amphotericin B (4 $\mu\text{g/ml}$) and voriconazole (4 $\mu\text{g/ml}$) completely eradicate *A. fumigatus* growth. Some not germinated conidia were still found (red insert). Hyphae and conidia stained by CFW. Scale bars = 200 μm . B) Application of caspofungin at increasing concentrations (0.05, 0.5 and 5 $\mu\text{g/ml}$) yielded known morphological changes in terms of filament length and clustering (top panel: xy plane, bottom panel: xz plane). Red arrows indicate invasive hyphae grown from the epithelial to the endothelial layer. Hyphae stained by CFW. Scale bars = 50 μm . C-F) Bioimage analysis of hyphae from untreated and caspofungin-treated IAC models revealed significant differences in filament length but neither in the number of branches, nor branching level. The number of branches per μm hyphal length was significantly increased upon caspofungin-treatment, however. Dot plots show results from three independent experiments with 5-8 hyphae analysed per condition and experiment, with the line indicating the mean. * $p<0.05$, ** $p<0.01$, *** $p<0.001$ (one-way ANOVA with Bonferroni post-test). CFW: Calcofluor White

increased by caspofungin and was most pronounced at 5 $\mu\text{g/ml}$ (mean branching level 6 ± 4 , mean number of branches 23 ± 31). Although the number of branches per hyphae and the branching levels analysed separately for caspofungin-treated samples did not yield statistically significant differences (Fig. 7D and 7E), we found a significantly increased number of branches per μm hypha in caspofungin-treated samples compared to untreated samples (Fig. 7F). Thus, caspofungin-treatment might not result in more branching but denser branching compared to untreated fungal hyphae.

Importantly, invasive growth was also observed in addition to the horizontal growth of *A. fumigatus* (Fig. 7B, red arrows, and Fig. 8A). Control infections in the absence of caspofungin produced the highest percentages of invasive hyphae. On average $53 \pm 50\%$ of all hyphae protruded into the endothelial side of the IAC model (Fig. 8B). Even though increasing concentrations of caspofungin reduced the number of invasive hyphae, the treatment was not sufficient to completely avoid hyphal invasion (mean percentages: $47 \pm 12\%$ at 0.05 $\mu\text{g/ml}$, $10 \pm 10\%$ at 0.5 $\mu\text{g/ml}$, and $18 \pm 17\%$ at 5 $\mu\text{g/ml}$ caspofungin).

We employed the confinement ratio analysis to characterize the growth of these invasive hyphal segments. In the absence of caspofungin (control condition), fungal hyphae grew as relatively straight filaments (Fig. 7B) corresponding to high confinement ratios C as represented by the extended red areas in the heat maps (Fig. 8C). The fairly straight growth of these invasive hyphal segments was interrupted by turns at distances of around 20 μm from the membrane midpoint. Compared to controls, caspofungin-treated samples showed more turns at different lengths along the invasive hyphal segments (Fig. 8C). This corresponds well to the images of a more clustered growth of the fungus as seen in the images (Fig. 7B and 8A).

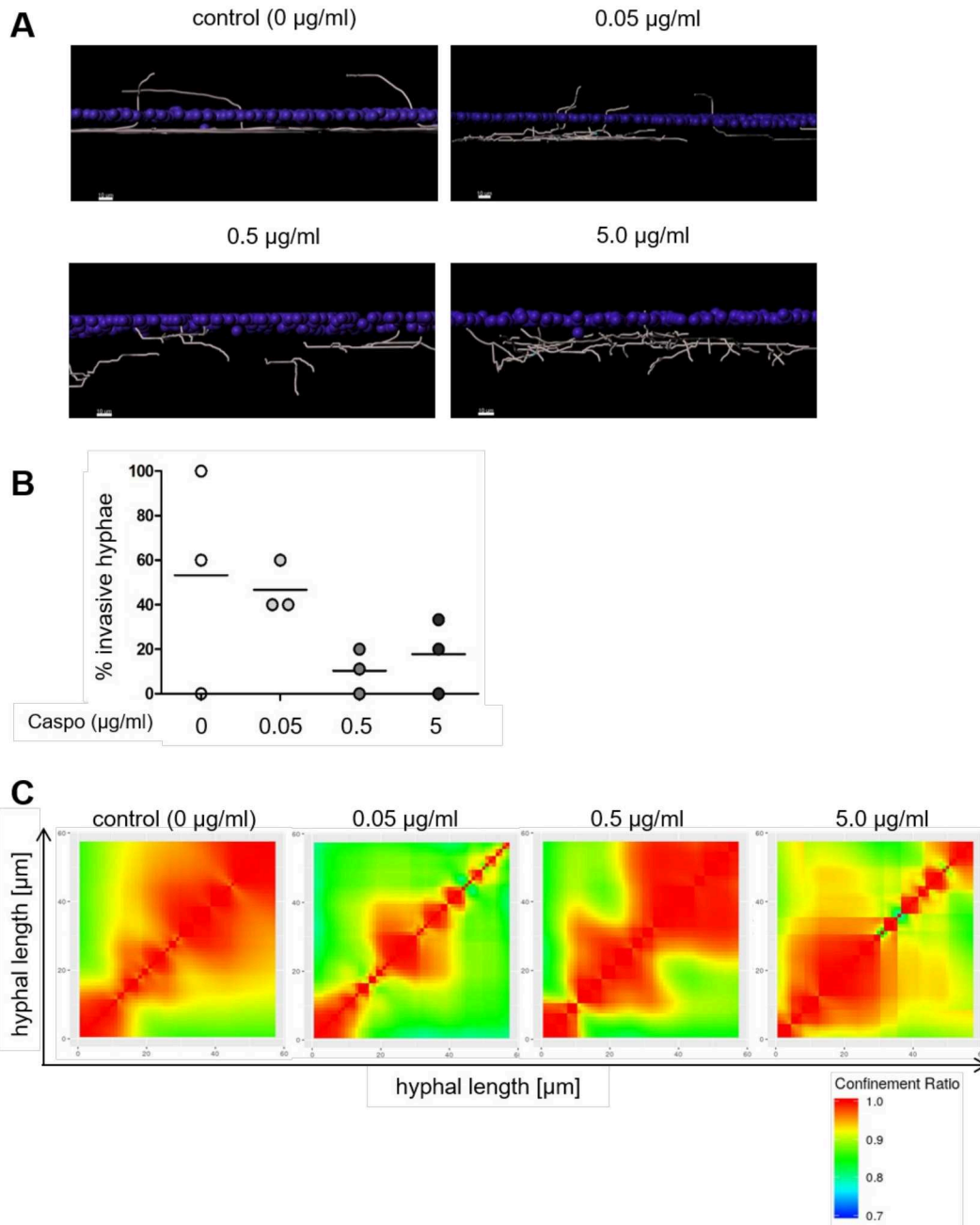


Figure 8: Modulation of invasive hyphal growth at therapeutic levels of caspofungin. A) Reconstructions of *A. fumigatus* hyphae from IAC models treated without (control, 0 $\mu\text{g/ml}$) or with increasing concentrations of caspofungin as lateral view (xz view) showing invasive fungal growth. Grey lines represent hyphae, blue spots represent membrane pores. Scale bars = 10 μm . B) Percentage of invasive hyphae in untreated models or caspofungin-treated models from three independent experiments. C) Changes in growth characteristics between untreated and caspofungin-treated hyphae visualised by heatmaps of the average confinement ratios of all invasive hyphal segments, i.e. the last 60 μm of a membrane-piercing hyphal branch before reaching the membrane midpoint (lower left corner). Heatmaps were constructed from 64 (control), 68 (0.05 $\mu\text{g/ml}$), 4 (0.5 $\mu\text{g/ml}$) and 12 (5 $\mu\text{g/ml}$) invasive hyphal segments from 15-19 reconstructed hyphae per condition obtained in three independent experiments.

Discussion

To overcome the classical limitations of cell culture, e.g., lack of organotypic structures or monolayer cultures of single-cell lines, we used a human immunocompetent, microfluidic perfused model of the alveolus to closely mimic the physiology of the human alveolus. The reconstruction of lung functions on a microfluidic chip has been used to model several human pulmonary diseases, including COPD [16, 19] or drug-induced pulmonary edema [32], as well as bacterial / viral co-infections [20]. The IAC model was applied to study *A. fumigatus* hyphal growth in all three spatial dimensions as well as in time using time-lapse 3D confocal microscopy. Image acquisition and subsequent image analysis provided quantitative data on morphology, including hyphal length or branching and germination and invasion behaviour. Recently, several studies used microscopy techniques to quantify the growth of filamentous fungi [33-35], but they were limited to the 2D lateral growth of mycelia. Thus, the 3D and 4D capability of our IAC model provides a more reliable way to quantify the growth of individual hyphae. Wurster et al. described a similarly effective but expensive time-lapse fluorescence microscopy-integrated incubation system [36]. Even though with the current setup, we cannot meet the 48h surveillance period presented in that report, the IAC model can be subjected to live-cell imaging for 24h, which is adequate for the infection process to be monitored, considering that hyphal growth already starts around 4-6h after the seeding of conidia on the epithelial cell layer.

The IAC model has the advantage of bearing a high structural resemblance to the human air-blood barrier, composed mainly of alveolar epithelial and endothelial cells. A major benefit of our study is the inclusion of primary human macrophages, the most abundant type of immune cells in the respiratory tract [37]. Although monocyte-derived macrophages should be considered surrogates for alveolar macrophages due to different origination during embryonic development and related functional differences in its immune response, they are suitable cells to study the first stages of *A. fumigatus* infection in the lung. Our IAC allowed us to track interactions between primary macrophages and *A. fumigatus* conidia in space and time by live-cell imaging, thus verifying that macrophages were able to capture and phagocytose conidia. Studies of the directionality of macrophage migration are of high importance because random movements alone would result in a very inefficient and slow process for the immune cells to find the intruding conidia before these may germinate [38, 39]. In our experiments, macrophages alone were not sufficient to completely inhibit hyphal growth from apically applied conidia. Similar phenomena were also previously observed in submerged 3D cell cultures [7]. Aside from the various mechanisms developed by *A. fumigatus* to escape conidial killing by macrophages (reviewed in [40]), the limited prevention of fungal growth may also reflect the need for recruitment of additional immune cells (especially neutrophils) to the site of infection, as was already suggested by Mircescu *et al.* from experiments in mice [41]. On the other hand, it has been reported that the impairment of alveolar macrophages is a risk factor for invasive mycoses [42]. This potential controversy may be resolved by comparing infection scenarios depending on the infection dose and combining these experiments with biophysical modeling [25]. The fungal infection dose typically used in mice experiments is orders of magnitude larger than the daily dose of *A. fumigatus* conidia inhaled by humans. Biophysical modeling has elucidated the difference of *A. fumigatus* infection between mice and humans and how it depends on the infection dose as well as on the morphometry of the lung [13, 43]. Since mathematical modelling necessarily involves the use of model parameters, the IAC model in combination with the image analysis can be exploited by an image-based systems biology approach [44-46]. In addition to macrophages, the IAC model allows the inclusion of additional immune cells and,

consequently, the observation and modelling of alterations in the immune system dynamics, e.g., the migration and interaction of cells [47, 48]. Therefore, the IAC model provides a unique tool to address unanswered questions regarding the directed movement of macrophages and other immune cells in the setting of fungal infection.

In our study, cytokines were measured at the epithelial and endothelial sides of the IAC model and displayed a distinct spatial profile emphasizing the physiological barrier integrity. Neither the epithelium nor the endothelium by themselves reacted significantly to the presence of *A. fumigatus* conidia. Still, in the presence of macrophages, we found significant expression and release of IL-1 β and IL-6 on the epithelial side and IL-8 and MCP-1 on the endothelial side. This is in line with reports demonstrating the central role of macrophages in mediating an inflammatory response to swollen or germinated conidia [6] and recruiting additional immune cells.

In the IAC model, we recapitulated the major steps in invasive aspergillosis, including the longitudinal fungal growth on the epithelium and the invasiveness. The membrane's pores in the alveolus models enable fungal hyphae to penetrate the air-liquid barrier and grow from the apical epithelium to the basal endothelium resulting in cell detachment. This is in agreement with several other studies that reported horizontal growth of *A. fumigatus* without significant damage to A549 cells [10, 49] or primary epithelial cells [7]. It was also shown that *A. fumigatus* was penetrating through primary human bronchial epithelial cells cultured at ALI by forming actin tubules without cell destruction [8]. In contrast, the endothelium was fundamentally disturbed by fungal growth. Invasive growth of *A. fumigatus* accompanied by massive vascular tissue damage is a hallmark of IPA [50, 51] and can thus be modelled in the IAC. Vascular tissue damage generally is a feature of severe infection, also by bacteria and viruses, and can be emulated by the alveolus model [20]. In addition to quantification of invasive hyphae, image-based identification of the pores and the hyphal reconstruction allowed us to address whether fungal growth has a specific direction. Confinement ratio analysis revealed that the invasive hyphal segments adjusted their behaviour according to the presence or absence of alveolar macrophages. In samples without macrophages, the hyphae grew horizontally on top of the epithelial cell layer but the growth pattern switched to an invasive mode in tissue models with macrophages, thus allowing the hyphae to escape by directly targeting the membrane pores. However, elucidation of the exact nature of this "guided" growth mechanism will require further in-depth experiments. Our results found no indication that the formation of nutritional gradients (e.g. glucose or lactate) alone could explain the observed growth behaviour. As invasive growth by *A. fumigatus* was observed more frequently in samples containing macrophages than in those without macrophages, transversal growth through a nearby pore could be considered evasive behaviour of hyphae from macrophages. A similar phenomenon was described by Ellet *et al.*, who confronted growing hyphae with neutrophils and found a *de novo* formation of hyphal branches to avoid contact and continue growth [52].

Caspofungin is a well-established drug in IPA treatment [2] with known fungistatic effects. Stalling of growth and an increase in branching as observed in the IAC model following caspofungin treatment are typical morphological changes of *A. fumigatus* also reported by others [26, 28-31]. Earlier reports hypothesise that these caspofungin-related responses are caused by the depletion of β -1,3 glucan, a major cell wall compound. We also recapitulated the "paradoxical growth" of hyphae with hyperbranched morphology at high caspofungin concentrations (>4 μ g/ml), a phenomenon that may be caused by redirection of Fks1, *i.e.*, the catalytic compound of β -1,3-glucan synthase, to the hyphal tips [29]. While these reports

exclusively relied on qualitative description, we were able to quantify these observations based on the analysis of microscopy images and the application of the confinement ratio approach.

The caspofungin concentrations used in this study were chosen to resemble drug susceptibility assays and represent clinical observations upon antifungal therapy. In patients, serum peak concentrations of up to 13 $\mu\text{g/ml}$ 1 hour after application [53-56], and serum trough levels between 1 and 4 $\mu\text{g/ml}$ after 24h have been reported [53-57]. For the first time, our analyses show the existence of invasive growth of hyphae treated with caspofungin in therapeutically relevant concentrations (0.5 $\mu\text{g/ml}$ and 5 $\mu\text{g/ml}$) from the epithelium towards the endothelium. On the one hand, this might raise concerns about the drug's efficacy as it cannot completely prevent fungal vascular invasion in the absence of neutrophils, in which case caspofungin may require the presence of neutrophils to be therapeutically effective as already suggested by clinical studies [58]. On the other hand, those IAC samples with therapeutic concentrations of caspofungin (0.5 and 5 $\mu\text{g/ml}$), as opposed to untreated controls, showed only a low number of invasive hyphae and a significantly reduced hyphal length. Thus, our IAC approach provides further quantitative evidence of how the fungistatic drug caspofungin is clinically effective against *A. fumigatus*.

Drug susceptibility testing by broth microdilution as standardised by the European Committee for Antimicrobial Susceptibility Testing [27] or the Clinical and Laboratory Standards Institute [59], is challenging for caspofungin as well as for other echinocandins because of the minimal effective concentration (MEC) is indicated by the appearance of short and branched fungal colonies (in contrast to long unbranched untreated hyphae). Thus, these assays rely on the manual macroscopic readout of fungal morphology and require training and experience from the experimenter. The significantly reduced hyphal length and lower number of invasive hyphae observed in 0.5 $\mu\text{g/ml}$ caspofungin-treated infection scenarios quantitatively underline publications by the CLSI naming 0.5 $\mu\text{g/ml}$ as MEC for caspofungin against *A. fumigatus* [59]. However, as with all susceptibility testing, a discrepancy may occur between results determined *in vitro* and the drug's clinical efficacy in the infected human due to the simplistic microdilution approach. In the future, the IAC may provide a more realistic platform for susceptibility testing, for example, by perfusion of patient-specific medication that might interfere with antifungal drug efficacy and/or co-perfusion of patient-derived immune cells. Such personalised settings would resemble the particular *in vivo* situation more closely and may therefore be clinically more relevant.

Taken together, this is the first report that applies a microfluidic model of the human alveolus to fungal infection research while also extending the model's possibilities to simultaneously study three and four-dimensional (3D plus time) behavioural patterns of fungal hyphae and human immune cells in high fidelity in a *in vivo*-like biological environment. Combining 3D infection scenarios with up-to-date methods of advanced image analysis allowed us to precisely dissect *A. fumigatus* hyphal growth as well as human host cell responses, which makes the model ideal for system biology approaches. The IAC model can be tailored to specific experimental needs with regard to a choice of cell lines or primary cells, the inclusion of human immune cells either statically on the epithelial side (e.g., macrophages, stromal cells, etc.) or perfused in the endothelial side (e.g., neutrophils or lymphocytes). The model allows testing of different strains of *A. fumigatus* and correlating *in vitro* data with clinical observations for virulent strains or antifungal resistance. Furthermore, the IAC model allows the description of immune cell dynamics upon infection as well as mimicry of specific, either

inherited or therapy-induced, immune defects. Thus, our versatile IAC model is a major step towards a better understanding of the pathophysiology in invasive aspergillosis.

Methods

Cell culture and lung-on-chip assembly

NCI-H441 cells (ATCC, USA) were maintained in RPMI 1640 (Gibco, Germany) + 10% FCS (ThermoFisher Scientific, Germany) and HUVECs isolated from human umbilical cord veins were maintained in endothelial cell growth medium + supplements (EC⁺, all Promocell, Germany), both at 37°C, 5%CO₂ in a humidified incubator. Biochip assembly is described in detail in [20]. Briefly, in microfluidic biochips ([60], microfluidic ChipShop, Germany), containing a polyethylene-terephthalate membrane of one cm² in size with randomly distributed pores (median density: 1 x 10⁵ cm⁻²) of 8 µm in diameter, HUVEC and H441 cells were seeded consecutively on opposite sides of the membrane, yielding the endothelial and epithelial side, respectively. Media used were: EC⁺ for HUVECs and RPMI 1640 + 10% FCS + 1µM dexamethasone (Sigma-Aldrich, Germany) for H441. After 7 days, human macrophages derived from monocytes obtained by PBMC isolation (detailed in [20]) were seeded onto the H441 cells. For H441 cells, the medium was changed to RPMI 1640 + 20% autologous serum from the macrophage donor + 10 ng/ml GM-CSF (PeproTech, Germany) + 1µM dexamethasone. Up to this point, the biochips were cultured under static conditions. The following day, perfusion of the endothelial side was initiated with a peristaltic pump (Reglo digital MS-CA-4/12-100, Ismatec, Germany) at a flow rate of 21 µl/min. A reservoir supplied the medium. On day 13, the ALI was initiated by the removal of media from the epithelial side. The perfused media was changed to endothelial cell growth medium without supplements + 20 % autologous serum + 10 ng/ml GM-CSF. Biochips were used for experiments after total cultivation of 14 days. All media were changed daily.

The study was approved by the ethics committee of the Jena University Hospital, Jena, Germany (3939-12/13). According to the Declaration of Helsinki, all individuals donating cells for the study gave their informed consent.

Fungal strains

Aspergillus fumigatus A1160 (wildtype) and GnoA-eGFP mutant [23] were cultured on *Aspergillus* minimal medium [61] (1,58 g/l K₂HPO₄; 0,52 g/l KCl; 30 g/l glucose, 0,5 g/l MgSO₄, 8 g/l agar and 1 ml/l Hutner's trace elements [62]) for 5-7 days at 37°C. Conidia were harvested in PBS (without Ca²⁺ and Mg²⁺, ThermoFisher Scientific, Germany) + 0.01% Tween 20 (Sigma-Aldrich, Germany), filtered through a 30µm strainer (MiltenyiBiotec, Germany), centrifuged for 5 minutes at 2600x g at room temperature and resuspended in PBS and stored at 4°C until use. If indicated, conidia were swollen in RPMI 1640 (Gibco, ThermoFisher Scientific, Germany) + 10% FCS (PAA, Germany) for 4 hours at 37°C in a rotator, washed three times with PBS + 0.01% Tween20 and filtered through a 30µm strainer. For fluorescent labelling conidia were incubated with FITC (Sigma-Aldrich, Germany) at a final concentration of 10 µg/ml in Na₂CO₃ (Sigma-Aldrich, Germany) for 20 minutes at 37°C in a rotator, afterwards washed three times in PBS + 0.01% Tween20 and centrifuged for 5 minutes at 2,600x g.

Infection and growth assay

Resting *A. fumigatus* conidia were FITC-labelled and resuspended in RPMI 1640 + 5% FCS; 1×10^5 conidia were injected onto the epithelial side. In the presence of macrophages, FCS was replaced by autologous serum of the macrophage donor, and the medium was supplemented with 10 ng/ml GM-CSF. Models were incubated for 90 minutes upside-down without perfusion to allow attachment of fungi to the lung epithelium. Afterwards, media were withdrawn from both sides of the chip, thereby re-establishing the ALI of the epithelial side. Additionally, the epithelial side was rinsed with 300 μ l of fresh medium to remove non-attached conidia. The endothelial side was then perfused with fresh endothelial cell medium (without supplements) + 5% autologous serum + 10 ng/ml GM-CSF overnight at 37°C and 5% CO₂. The following morning, media from the reservoirs of the endothelial chambers were collected. For epithelial chambers, 150 μ l of RPMI 1640 + 5% autologous serum was added to each chamber, incubated for 15 minutes, and collected. All supernatants were immediately stored at -80°C.

Antifungal drug testing

Voriconazole (Pfizer, Germany) and amphotericin B (European Directorate for Quality of Medicines, France) were tested at a concentration of 4.0 μ g/ml, caspofungin (MSD Sharp & Dohme, Germany) was tested at 0.05, 0.5, and 5.0 μ g/ml. As control 5 μ g/ml DMSO (Sigma Aldrich, Germany) was used. 1×10^5 FITC labelled, 4 hour-swollen *A. fumigatus* conidia in RPMI 1640 + 5% autologous serum + 10 ng/ml GM-CSF were injected into the lung chamber. The biochip was then incubated upside-down in a humidified incubator at 37°C and 5% CO₂ to allow attachment and germination of conidia for 4 hours. After the initial incubation in a static condition, the medium was retaken out of the lung chamber. The chamber was rinsed with 300 μ l of fresh medium to remove floating conidia. The blood chamber was perfused with fresh endothelial cell medium (without supplements) + 5% autologous serum + 10 ng/ml GM-CSF and the respective drug concentration at the flow rate of 21 μ l/min in an incubator at 37°C and 5% CO₂ for 20 hours.

Cytokine profiling

Supernatants were collected from the endothelial and the epithelial side of IAC models after overnight incubation, as detailed above. According to the manufacturer's instructions, high sensitivity ProcartaPlex (ThermoFisher Scientific, Germany) was used to determine IL-1 β , IL-6, and TNF α levels. The measurement was done using the BioPlex 200 device (Bio-Rad, Germany). IL-8 and MCP-1 were measured using Cytometric Bead Assay Flex Sets (BD Biosciences, Germany) according to the manufacturer's instructions.

Immunofluorescence

After overnight incubation, chambers were washed twice with cold D-PBS (with Ca²⁺ and Mg²⁺, Gibco, ThermoFisher Scientific) and fixed with 4% formaldehyde (Carl Roth, Germany) for 10 minutes. Next, membranes were removed from the chips and immediately blocked with D-PBS + 0.1% Saponin (Sigma-Aldrich, Germany) + 3% goat serum (Dianova, Germany) for one hour at RT. For immunofluorescent staining. The following primary antibodies were diluted in D-PBS + 0.1% Saponin + 0.3% goat serum and incubated overnight at 4°C: CD68 (Cat.no. 76437T, Cell Signaling, U.S.A.) and E-cadherin (Cat.no. 610181, BD Biosciences, Germany), VE-Cadherin (Cat.no. AF938-SP, R&D Systems, UK), von Willebrand factor (Cat.no. A0082, DAKO / Agilent, Germany). The next day, secondary goat anti-mouse antibodies Cy3 or Cy5 (Cat.no. ab97035 and ab97037, Abcam, UK), goat anti-rabbit Cy5 (Cat.no. A10523, ThermoFisher Scientific) or donkey anti-goat Dylight 488 (Cat.no. SA5-10086, ThermoFisher Scientific) were incubated in D-PBS + 0.1% Saponin + 0.3% goat serum for 45 minutes at room temperature (RT). For visualization of nuclei 0.5 µg/ml Hoechst 33258 (ThermoFisher Scientific, Germany) was used. Fungi were stained with 2 µg/ml Calcofluor White (CFW, Sigma Aldrich, Germany) for 7 minutes at RT. After washing, the membranes were mounted on glass slides with Roti®-Mount FluorCare (Carl Roth, Germany) and allowed to settle for 2 days in the dark at 4°C.

Microscopy

Three-dimensional imaging of the FITC and CFW-stained hyphae was performed using an LSM 780 Zeiss confocal laser scanning microscope (Carl Zeiss, Germany) with a 63x NA1.4 oil immersion objective lens. Tile scanning and z-stack acquisition with 0.7 µm axial distance increment between z layers were used simultaneously to obtain large area-of-view 3D images. The 3D dimensions of a single tile equalled 224.9 µm x 224.9 µm x 45-90 µm (at 16 bits per pixel), and a total of 1 to 64 (8x8) tiles (corresponding to 5x10⁴ µm² to 3,2x10⁶ µm²) were acquired, depending on the size of the hyphae structure that was to be imaged. Note that the thickness of the z-stacks varied depending on the vertical growth range of hyphae in the biochips. In addition, the membranes in the biochips were not completely flat but rather varied axially in several micrometres among tiles, thus requiring the Z range of the image stack to be adjusted to include the entire biochip volume of interest. For the subsequent quantitative analysis of individual hyphae, the dimensions of the 3D tile scan images were chosen to cover the entire hyphal structure were acquired. Similar to hyphae, 3D images of FITC-labelled conidia on the epithelial side were also acquired for quantitative analysis of conidial germination. For each sample, 3D images from various areas on the membrane were acquired, resulting in a total of 60 tiles covering an area of about 3x10⁶ µm² and 15-40 µm of axial depth.

The following excitation wavelengths and emission bandpass filters were applied: FITC: 488 nm, 479-533 nm; Cy3: 564 nm, 561-597 nm; Cy5: 633 nm, 658-709 nm; Hoechst 33258 and CFW: 405 nm, 419-526 nm. For the visualization of the membrane pores, reflected light microscopy was included in the acquisition settings, using laser illumination at 594 nm and epifluorescence detection at 570-605 nm, using the Zeiss microscope's reflected light settings.

Image analysis

The detected hyphae, conidia, and membrane pores in the 3D confocal images were analysed using IMARIS 9.2.1 and 9.5.1 (Bitplane, Switzerland).

A. fumigatus conidia were first analysed automatically, segmenting them as Spot objects in IMARIS. However, not all conidia present in an image could be analysed automatically even when adjusting the segmentation parameters (e.g., diameter, elongation, quality filter, signal intensity filter, etc.). This was due to the heterogeneity of conidial swelling and germination. Therefore, manual corrections were applied after the automated analysis in order to give a more precise number of FITC-labelled conidia in the image. The decision of whether a spot object represented a conidium was based on the conidial FITC signal, shape, size, and intactness (conidia that were optically cut in the 3D image were excluded from further analysis).

The 3D reconstruction of the pores was carried out as follows: The pores in the 3D images appeared as dark round dots (diameter of 8 μm) against a bright background in the reflected light channel. In order to reconstruct the pores automatically, the signal in the reflected light channel was inverted using the MATLAB-based built-in IMARIS XTension "Channel arithmetic" by subtracting each actual pixel value from the maximum value of the reflected light signal, applied to the entire reflected light image. The automated spot analysis of IMARIS with a spot diameter of 8 μm and background subtraction was then applied on a shallow subset of z-layers, using the Z-range where the pores were most clearly visible. The Z range of the most likely location of the PET membrane was judged visually and used to filter the spot locations, which were then stored in a newly generated channel. The thickness of this Z range filter varied amongst different samples, depending on the flatness of the PET membrane. A quality filter was then applied so that the pores were correctly recognized.

Hyphal 3D segmentation and subsequent characterization was done as follows. The automated analysis was performed using the Filament Tracker algorithm of IMARIS, which is optimized for the analysis of the dendritic arbor of neurons. Whilst the IMARIS algorithm was efficient and fast, the automated analysis alone could not entirely resolve the precise 3D spatial structure of CFW-stained hyphae. This was due to the relatively low signal-to-noise ratio of CFW-stained hyphae, especially problematic for images where neighboring hyphal branches came very close to each other. In this case, automated Filaments analysis of IMARIS often resulted in several erroneous connections, merging or cutting of the filaments. Consequently, semi-automated and manual filament tracing were routinely applied to the automatically pre-segmented hyphae. Here, three drawing modes of filament tracing of IMARIS were applied: AutoPath, AutoDepth and Manual. From the semi-manually and manually corrected 3D reconstructions of hyphae, numerous hyphal growth parameters were extracted; for example: hyphal length (total length of all branches within one hypha), number of branches (all branches that belong to one hypha), highest hyphal branching levels (or "branching levels" in short), etc. A higher branching level is assigned to a "segment" when it grows out from a previous branch and is further away from the starting point (the conidium) than the preceding branch (Supplementary figure 2).

Calculations used:

a) Percentage of germinated conidia (in the epithelial side) = (number of germinated conidia / total number of conidia on the epithelial side) x 100

b) Percentage of invasive hyphae = (number of invasive hyphae (hyphae going through a pore and entering the blood side) / total reconstructed hyphae in the epithelial side) x 100

Confinement ratio analysis

In order to trace the hyphae along the entire length of 60 μm , the precise distance between the hyphae and the membrane surface had to be determined at each position. Whilst the reflected light mode imaging was successfully applied to reveal the exact position of the membrane pores, it was not able to approximate the membrane surface in the necessary details, partially due to the uneven reflection of laser light from the membrane layer. Consequently, the exact position of the surface points of the membrane had to be interpolated using the very precise locations of membrane pores. In order to simplify and accelerate the analysis of the growth of hyphal structures, we performed a skeletonization procedure of the segmented hyphae (Supplementary video 4). Since the surface points, as reconstructed by IMARIS, are consecutively ordered along the hyphal growth direction, we were able to compute the spatial mean position of the surface points using a sliding window approach. This allowed the detection of structural points within the hyphal segmentation, thus providing a skeleton of the hyphal volume. During post-processing, the overlapping structures of hyphal segments were removed and interpolated to enhance the data quality and obtain a spatially uniform coverage of the entire hyphal growth. When a hypha pierced through the membrane, all side branches that did not belong to the piercing branch were removed and a growth analysis algorithm was executed as follows: for a hyphal skeleton of N points the confinement ratio " $C(1,N)$ " was computed, representing the ratio of displacement between the first point ($d(1,1)$) and the N th point ($d(1,N)$) over the total length of the hyphal branch $l(1,N)$ [24]. To characterize local growth patterns, the confinement ratio was calculated for each subset of the hypha $C(i,j)$ $1 \leq i \leq j \leq N$, resulting in a symmetric confinement ratio matrix with a diagonal of $C(i,i)=1$. A straight hyphal growth is represented by squares of high $C(i,j)$ values, whereas sharp turns of the growth direction are visualized by low $C(i,j)$ values, positioned near the diagonal of the matrix.

Statistical analysis

Statistical analysis was performed using Prism 5.0 (GraphPad, U.S.A.) using unpaired, two-tailed t-test to compare two groups and one-way ANOVA with Bonferroni post-tests to compare more than two groups. $P < 0.05$ was considered significant.

Acknowledgments

We thank Tobias Vogt and Ava Kieseletter for their excellent technical assistance. We also thank Dr. Grit Walther, National Reference Center for Invasive Mycoses, Jena, Germany for the gifts of voriconazole, amphotericin B and caspofungin. We thank the Department Molecular and Applied Microbiology, Leibniz Institute for Natural Product Research and Infection Biology, Jena, Germany for sharing the *A. fumigatus* GnoA-eGFP mutant. We also thank the team of the Placenta Laboratory of the Jena University Hospital for supplying umbilical cords for HUVEC isolation and all peripheral blood donors.

Funding

M.T.N.H. was supported by the Jena School for Microbial Communication, funded by the German Research Foundation (FKZ 214/2) and the Carl Zeiss Foundation. A.S.M and M.v.L-T. acknowledge financial support by the Center for Sepsis Control and Care, funded by the German Federal Ministry of Education and Research (FKZ 01EO1002). M.T.F. received funding by the Collaborative Research Center / Transregio 124 – FungiNet (project number 210879364, project B4) as well as by the Collaborative Research Center 1278 “PolyTarget” (project number 316213987; project Z01) both funded by the German Research Foundation (DFG).

Conflicts of Interest

A.S.M. is scientific advisor to Dynamic 42 GmbH and holds equity in the company. K.R. is CEO of Dynamic42 GmbH.

References

1. Brown, G.D., et al., *Hidden killers: human fungal infections*. Science translational medicine, 2012. **4**(165): p. 165rv13.
2. von Lilienfeld-Toal, M., et al., *Invasive Fungal Infection*. Dtsch Arztebl Int, 2019. **116**(16): p. 271-278.
3. Cseresnyes, Z., et al., *Quantitative Impact of Cell Membrane Fluorescence Labeling on Phagocytosis Measurements in Confrontation Assays*. Front Microbiol, 2020. **11**: p. 1193.
4. Hartung, S., et al., *Fast and Quantitative Evaluation of Human Leukocyte Interaction with Aspergillus fumigatus Conidia by Flow Cytometry*. Cytometry A, 2019. **95**(3): p. 332-338.
5. Hassan, M.I.A., et al., *The geographical region of origin determines the phagocytic vulnerability of Lichtheimia strains*. Environ Microbiol, 2019. **21**(12): p. 4563-4581.
6. Hellmann, A.M., et al., *Human and Murine Innate Immune Cell Populations Display Common and Distinct Response Patterns during Their In Vitro Interaction with the Pathogenic Mold Aspergillus fumigatus*. Frontiers in immunology, 2017. **8**: p. 1716.
7. Chandorkar, P., et al., *Fast-track development of an in vitro 3D lung/immune cell model to study Aspergillus infections*. Scientific reports, 2017. **7**(1): p. 11644.
8. Fernandes, J., et al., *Penetration of the Human Pulmonary Epithelium by Aspergillus fumigatus Hyphae*. J Infect Dis, 2018. **218**(8): p. 1306-1313.
9. Toor, A., et al., *Transcriptomic and proteomic host response to Aspergillus fumigatus conidia in an air-liquid interface model of human bronchial epithelium*. PLoS One, 2018. **13**(12): p. e0209652.
10. Belic, S., et al., *Comparative Analysis of Inflammatory Cytokine Release and Alveolar Epithelial Barrier Invasion in a Transwell((R)) Bilayer Model of Mucormycosis*. Frontiers in microbiology, 2018. **9**: p. 3204.
11. Morton, C.O., et al., *Gene expression profiles of human dendritic cells interacting with Aspergillus fumigatus in a bilayer model of the alveolar epithelium/endothelium interface*. PLoS One, 2014. **9**(5): p. e98279.
12. Desoubeaux, G. and C. Cray, *Animal Models of Aspergillosis*. Comp Med, 2018. **68**(2): p. 109-123.
13. Blickensdorf, M., S. Timme, and M.T. Figge, *Comparative Assessment of Aspergillosis by Virtual Infection Modeling in Murine and Human Lung*. Front Immunol, 2019. **10**: p. 142.
14. Mestas, J. and C.C. Hughes, *Of mice and not men: differences between mouse and human immunology*. J Immunol, 2004. **172**(5): p. 2731-8.
15. Seok, J., et al., *Genomic responses in mouse models poorly mimic human inflammatory diseases*. Proc Natl Acad Sci U S A, 2013. **110**(9): p. 3507-12.
16. Benam, K.H., et al., *Small airway-on-a-chip enables analysis of human lung inflammation and drug responses in vitro*. Nature methods, 2016. **13**(2): p. 151-7.
17. Huh, D., et al., *Reconstituting organ-level lung functions on a chip*. Science, 2010. **328**(5986): p. 1662-8.
18. Stucki, J.D., et al., *Medium throughput breathing human primary cell alveolus-on-chip model*. Scientific reports, 2018. **8**(1): p. 14359.
19. Benam, K.H., et al., *Matched-Comparative Modeling of Normal and Diseased Human Airway Responses Using a Microengineered Breathing Lung Chip*. Cell systems, 2016. **3**(5): p. 456-466 e4.
20. Deinhardt-Emmer, S., et al., *Co-infection with Staphylococcus aureus after primary influenza virus infection leads to damage of the endothelium in a human alveolus-on-a-chip model*. Biofabrication, 2020. **12**(2): p. 025012.
21. Schicke, E., et al., *Staphylococcus aureus Lung Infection Results in Down-Regulation of Surfactant Protein-A Mainly Caused by Pro-Inflammatory Macrophages*. Microorganisms, 2020. **8**(4).

22. Brakhage, A.A., et al., *Interaction of phagocytes with filamentous fungi*. Current opinion in microbiology, 2010. **13**(4): p. 409-15.
23. Lapp, K., et al., *Characterization of the Aspergillus fumigatus detoxification systems for reactive nitrogen intermediates and their impact on virulence*. Frontiers in microbiology, 2014. **5**: p. 469.
24. Mokhtari, Z., et al., *Automated characterization and parameter-free classification of cell tracks based on local migration behavior*. PLoS One, 2013. **8**(12): p. e80808.
25. Pollmacher, J., et al., *Deciphering the Counterplay of Aspergillus fumigatus Infection and Host Inflammation by Evolutionary Games on Graphs*. Sci Rep, 2016. **6**: p. 27807.
26. Steinbach, W.J., F. Lamoth, and P.R. Juvvadi, *Potential Microbiological Effects of Higher Dosing of Echinocandins*. Clin Infect Dis, 2015. **61 Suppl 6**: p. S669-77.
27. *EUCAST Technical Note on the method for the determination of broth dilution minimum inhibitory concentrations of antifungal agents for conidia-forming moulds*. Clinical microbiology and infection : the official publication of the European Society of Clinical Microbiology and Infectious Diseases, 2008. **14**(10): p. 982-4.
28. Loiko, V. and J. Wagener, *The Paradoxical Effect of Echinocandins in Aspergillus fumigatus Relies on Recovery of the beta-1,3-Glucan Synthase Fks1*. Antimicrob Agents Chemother, 2017. **61**(2).
29. Moreno-Velasquez, S.D., et al., *Caspofungin-Mediated Growth Inhibition and Paradoxical Growth in Aspergillus fumigatus Involve Fungicidal Hyphal Tip Lysis Coupled with Regenerative Intrahyphal Growth and Dynamic Changes in beta-1,3-Glucan Synthase Localization*. Antimicrob Agents Chemother, 2017. **61**(10).
30. Wagener, J. and V. Loiko, *Recent Insights into the Paradoxical Effect of Echinocandins*. J Fungi (Basel), 2017. **4**(1).
31. Walker, L.A., et al., *Caspofungin Treatment of Aspergillus fumigatus Results in ChsG-Dependent Upregulation of Chitin Synthesis and the Formation of Chitin-Rich Microcolonies*. Antimicrob Agents Chemother, 2015. **59**(10): p. 5932-41.
32. Huh, D., et al., *A human disease model of drug toxicity-induced pulmonary edema in a lung-on-a-chip microdevice*. Science translational medicine, 2012. **4**(159): p. 159ra147.
33. Barry, D.J. and G.A. Williams, *Microscopic characterisation of filamentous microbes: towards fully automated morphological quantification through image analysis*. J Microsc, 2011. **244**(1): p. 1-20.
34. Sanchez-Orellana, G., S. Casas-Flores, and B. Gutierrez-Medina, *Automated, continuous video microscopy tracking of hyphal growth*. Fungal Genet Biol, 2019. **123**: p. 25-32.
35. Vidal-Diez de Ulzurrun, G., et al., *Fungal feature tracker (FFT): A tool for quantitatively characterizing the morphology and growth of filamentous fungi*. PLoS Comput Biol, 2019. **15**(10): p. e1007428.
36. Wurster, S., et al., *Live Monitoring and Analysis of Fungal Growth, Viability, and Mycelial Morphology Using the IncuCyte NeuroTrack Processing Module*. mBio, 2019. **10**(3).
37. Philippe, B., et al., *Killing of Aspergillus fumigatus by alveolar macrophages is mediated by reactive oxidant intermediates*. Infect Immun, 2003. **71**(6): p. 3034-42.
38. Pollmacher, J. and M.T. Figge, *Agent-based model of human alveoli predicts chemotactic signaling by epithelial cells during early Aspergillus fumigatus infection*. PloS one, 2014. **9**(10): p. e111630.
39. Pollmacher, J. and M.T. Figge, *Deciphering chemokine properties by a hybrid agent-based model of Aspergillus fumigatus infection in human alveoli*. Front Microbiol, 2015. **6**: p. 503.
40. Heinekamp, T., et al., *Interference of Aspergillus fumigatus with the immune response*. Seminars in immunopathology, 2015. **37**(2): p. 141-52.
41. Mircescu, M.M., et al., *Essential role for neutrophils but not alveolar macrophages at early time points following Aspergillus fumigatus infection*. J Infect Dis, 2009. **200**(4): p. 647-56.

42. Roilides, E., H. Katsifa, and T.J. Walsh, *Pulmonary host defences against Aspergillus fumigatus*. Res Immunol, 1998. **149**(4-5): p. 454-65; discussion 523-4.
43. Blickensdorf, M., S. Timme, and M.T. Figge, *Hybrid Agent-Based Modeling of Aspergillus fumigatus Infection to Quantitatively Investigate the Role of Pores of Kohn in Human Alveoli*. Front Microbiol, 2020. **11**: p. 1951.
44. Medyukhina, A., et al., *Image-based systems biology of infection*. Cytometry A, 2015. **87**(6): p. 462-70.
45. Figge, M.T., *Quantitative bioimage analysis of cell characteristics*. Cytometry A, 2018. **93**(3): p. 278-280.
46. Figge, M.T. and R.F. Murphy, *Image-based systems biology*. Cytometry A, 2015. **87**(6): p. 459-61.
47. Figge, M.T., *Advances in Quantitative Bioimage Analysis for Proteins and Cells*. Cytometry A, 2020. **97**(4): p. 344-346.
48. Svensson, C.M., et al., *Untangling cell tracks: Quantifying cell migration by time lapse image data analysis*. Cytometry A, 2018. **93**(3): p. 357-370.
49. Escobar, N., et al., *Hide, Keep Quiet, and Keep Low: Properties That Make Aspergillus fumigatus a Successful Lung Pathogen*. Front Microbiol, 2016. **7**: p. 438.
50. Al-Bader, N. and D.C. Sheppard, *Aspergillosis and stem cell transplantation: An overview of experimental pathogenesis studies*. Virulence, 2016. **7**(8): p. 950-966.
51. Kosmidis, C. and D.W. Denning, *The clinical spectrum of pulmonary aspergillosis*. Thorax, 2015. **70**(3): p. 270-7.
52. Ellett, F., et al., *Neutrophil Interactions Stimulate Evasive Hyphal Branching by Aspergillus fumigatus*. PLoS Pathog, 2017. **13**(1): p. e1006154.
53. Spriet, I., et al., *Pharmacokinetics of caspofungin and voriconazole in critically ill patients during extracorporeal membrane oxygenation*. J Antimicrob Chemother, 2009. **63**(4): p. 767-70.
54. Stone, J.A., et al., *Single- and multiple-dose pharmacokinetics of caspofungin in healthy men*. Antimicrob Agents Chemother, 2002. **46**(3): p. 739-45.
55. Sinnollareddy, M.G., et al., *Pharmacokinetic variability and exposures of fluconazole, anidulafungin, and caspofungin in intensive care unit patients: Data from multinational Defining Antibiotic Levels in Intensive care unit (DALI) patients Study*. Crit Care, 2015. **19**: p. 33.
56. Wurthwein, G., et al., *Population pharmacokinetics of escalating doses of caspofungin in a phase II study of patients with invasive aspergillosis*. Antimicrob Agents Chemother, 2013. **57**(4): p. 1664-71.
57. Vena, A., et al., *Therapeutic Drug Monitoring of Antifungal Drugs: Another Tool to Improve Patient Outcome?* Infect Dis Ther, 2020. **9**(1): p. 137-149.
58. Betts, R., et al., *Efficacy of caspofungin against invasive Candida or invasive Aspergillus infections in neutropenic patients*. Cancer, 2006. **106**(2): p. 466-73.
59. Espinel-Ingroff, A., et al., *Wild-type MIC distributions and epidemiological cutoff values for caspofungin and Aspergillus spp. for the CLSI broth microdilution method (M38-A2 document)*. Antimicrob Agents Chemother, 2011. **55**(6): p. 2855-9.
60. Raasch, M., et al., *Microfluidically supported biochip design for culture of endothelial cell layers with improved perfusion conditions*. Biofabrication, 2015. **7**(1): p. 015013.
61. Pontecorvo, G., et al., *The genetics of Aspergillus nidulans*. Adv Genet, 1953. **5**: p. 141-238.
62. Hutner, S., et al., *Some approaches to the study of the role of metals in the metabolism of microorganisms*. Proc. Am. Phil. Soc., 1950. **94**: p. 152-170.

SPHARM SHAPE CLASSIFICATION OF MIGRATING CELLS

FORMULAR 1¹**Manuskript Nr. 4****Titel des Manuskriptes:** Dynamic spherical harmonics approach for shape classification of migrating cells**Autoren:** Medyukhina, A., Blickensdorf, M., Cseresnyés, Z., Ruef, N., Stein J.V., Figge, M.T.**Bibliographische Informationen :** *Scientific Reports* volume 10, Article number: 6072 (2020)**Der Kandidat / Die Kandidatin ist** Erstautor/-in, Ko-Erstautor/-in, Korresp. Autor/-in, Koautor/-in.**Status :** publiziert**Anteile (in %) der Autoren / der Autorinnen an der Publikation** (anzugeben ab 20%)

Autor/-in	Konzeptionell	Datenanalyse	Experimentell	Verfassen des Manuskriptes	Bereitstellung von Material
Medyukhina	50 %	40 %	30 %	40 %	
Blickensdorf		40 %	30 %	40 %	
Cseresnyés			20 %		
Ruef					
Stein					50 %
Figge	50 %				50 %

Unterschrift Kandidat/-in_____
Unterschrift Betreuer/-in (Mitglied der Fakultät)

¹ Die Unterschriften müssen nur im separat im Dekanat einzureichenden ausgefüllten Formular im Original vorliegen. In der in die Dissertation eingebundenen Fassung dürfen die Unterschriften und Unterschriftenfelder fehlen.

OPEN Dynamic spherical harmonics approach for shape classification of migrating cells

Anna Medyukhina^{1,5,6}, Marco Blickensdorf^{1,6}, Zoltán Cseresnyés¹, Nora Ruef³, Jens V. Stein³ & Marc Thilo Figge^{1,2,4*}

Cell migration involves dynamic changes in cell shape. Intricate patterns of cell shape can be analyzed and classified using advanced shape descriptors, including spherical harmonics (SPHARM). Though SPHARM have been used to analyze and classify migrating cells, such classification did not exploit SPHARM spectra in their dynamics. Here, we examine whether additional information from dynamic SPHARM improves classification of cell migration patterns. We combine the static and dynamic SPHARM approach with a support-vector-machine classifier and compare their classification accuracies. We demonstrate that the dynamic SPHARM analysis classifies cell migration patterns more accurately than the static one for both synthetic and experimental data. Furthermore, by comparing the computed accuracies with that of a naive classifier, we can identify the experimental conditions and model parameters that significantly affect cell shape. This capability should – in the future – help to pinpoint factors that play an essential role in cell migration.

A cell's migration behavior depends on the state of the cell, extracellular environment, and signals from other cells¹. We can study the mechanisms of cell migration by, e.g., knocking out a certain gene or altering the structure of the extracellular matrix (ECM) and testing whether these changes affect cell migration patterns, such as cell trajectory, shape, or shape dynamics (Fig. 1). To compare migration patterns in an objective and statistically sound way, they have to be automatically analyzed and quantified². Whereas both cell trajectories^{3,4} and cell shape^{5,6} can be quantified with a multitude of available methods, the analysis of shape dynamics – especially in 3D – received considerably less attention.

When analyzing cell shape in a static fashion, we look at just one snapshot of the cell's migration history. Depending on how we choose this snapshot, we may either miss important differences in cell shape – e.g., if cells transiently appear similar but have different migration patterns – or detect spurious differences – e.g., if cells occur in different phases of the same migration pattern. Even averaging cell shape descriptors over time⁷ may not always be sufficient to distinguish some migration patterns, for example when all cells evolve through similar phases of cell shape but different cells do this with different frequencies (Fig. S1)⁸. To distinguish such details of migration behavior we need dynamic shape analysis that takes into account relative changes in cell shape between consecutive time points.

While such dynamic shape analysis has been done in 2D^{8–11}, 3D shape descriptors have not been applied to characterize and compare the full dynamic migration patterns of cells. The ultimate goal, however, is to understand how cells migrate in living organisms¹². Due to advances in intravital microscopy^{13–15}, we have increasingly more 3D + time data of cells migrating *in vivo* and we should exploit the potential of 3D methods to analyze these data¹⁶.

Although there are many simple shape descriptors that can be applied in 3D (e.g., solidity, ellipticity, prolateness), only relatively complex ones can reveal the fine details of the cell shape and classify between relevant spatial patterns while ignoring random shape variations⁷. One especially popular and promising approach involves spherical harmonics (SPHARM)^{17–19}. SPHARM is a 3D extension of a Fourier analysis, where an arbitrary shape

¹Applied Systems Biology, Leibniz Institute for Natural Product Research and Infection Biology – Hans Knöll Institute (HKI), Jena, Germany. ²Institute of Microbiology, Faculty of Biological Sciences, Friedrich Schiller University Jena, Jena, Germany. ³Department of Oncology, Microbiology and Immunology, University of Fribourg, Fribourg, Switzerland. ⁴Center for Sepsis Control and Care (CSCC), Jena University Hospital, Jena, Germany. ⁵Present address: Center for Bioimage Informatics, St. Jude Children's Research Hospital, Memphis, TN, USA. ⁶These authors contributed equally: Anna Medyukhina and Marco Blickensdorf. *email: thilo.figge@leibniz-hki.de

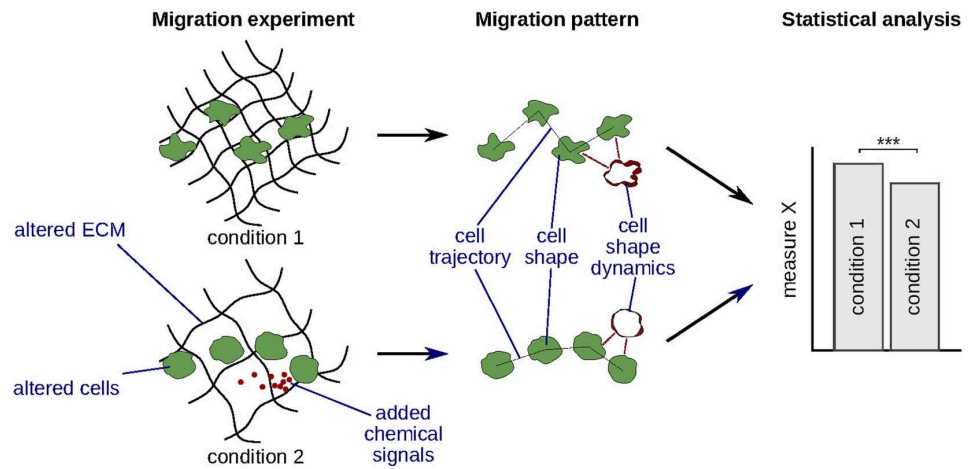


Figure 1. Analysis and quantification of migration patterns can help to study cell migration mechanisms. First, a migration experiment is performed, which involves altering the migrating cells (genetic or chemical modification, choosing cells of a different type), altering the extracellular matrix (ECM), or adding chemical signal to the extracellular environment. Next, cell migration patterns are analyzed and quantified. Finally, one or more quantitative measures derived from these patterns are statistically compared between conditions to detect significant differences.

function is expanded on a sphere using a set of orthogonal spherical functions as a basis. This approach was shown to be effective for characterizing the shape of proteins^{20,21}, red blood cells^{22,23}, brain structures^{19,24,25}, as well as migrating cells^{7,26–28}. In the contexts of cell migration analysis, SPHARM have been applied to identify phases of amoeboid cell motion^{26–28} and to classify shapes of migrating cells based on SPHARM spectra averaged over time⁷. Therefore, SPHARM descriptors represent an ideal first candidate to be extended for dynamic 3D shape analysis.

In this proof-of-principle study, we investigate, whether the use of dynamic shape descriptors can improve classification between migration patterns of cells. We extend the SPHARM analysis by computing dynamic SPHARM descriptors, combine both descriptors with a support-vector-machine classifier, and compare their ability to distinguish between migration patterns of cells in synthetic and experimental data.

Materials and Methods

To study the use of dynamic SPHARM for classifying migrating cells, we analyzed two types of input data: synthetic cells generated with an in-house developed cell migration simulator (CMS), and T cells visualized with intravital microscopy. For each cell, we extracted cell surfaces at various time points and transformed them into a static or dynamic SPHARM feature vector. We then used the computed feature vectors to classify cells according to their migration behavior.

Cell migration simulator. To generate synthetic migrating cells, we used our previously developed cell migration simulator (CMS)²⁹. In CMS, each cell consists of a set of grid-based spatial units (SU), and the cell migration in 3D is simulated by iteratively moving SU from the rear of the cell to the front (Fig. 2a).

The simulation starts with a spherical cell with the center of mass at position p_{mit} and a randomly chosen migration direction \vec{v}_D (Fig. 2a). Each SU of the cell receives a position vector \vec{v}_p , which is used to compute the relative SU position P as the dot product between the normal vectors \vec{v}_p and \vec{v}_D : $P = \vec{v}_D \cdot \vec{v}_p \in [-1, 1]$. The value of P defines whether the corresponding SU belongs to the cell's rear or front: for all front SU, P must be greater than a pre-defined front-rear threshold FR , whereas all SU with $P \leq FR$ belong to the cell's rear. The parameter FR defines the fraction of the cell volume considered as the front. Thus, for $FR = 0$ the front and the back have equal weights; for a negative FR the front is wider than the back, and for a positive FR the front is narrower than the back (Fig. S2a).

In addition to FR , the model has three further parameters: neighbor weight (NW), position weight (PW), and distance weight (DW), which define the probability of moving a specific SU from the rear to the front surface. In each iteration, an SU from the rear surface and a free position at the cell's front are chosen randomly using Monte Carlo acceptance-rejection sampling. The acceptance probability for each SU depends on the number of neighbors N , position P , and the distance to the center of mass D (Fig. S2b–d) and is computed based on the rear and front scores S_r and S_f : $S_r = |P|^{PW} \cdot (6 - N)^{NW} \cdot D^{DW}$, $S_f = |P|^{PW} \cdot N^{NW}$. Thus, those rear SU and free front positions have a higher probability of being selected that are closer to the cell's migration axis (large P). Additionally, those SU are more likely to be removed that are further away from the cells' center of mass (large D) and have fewer neighbors (small N), whereas the free positions at the front are preferred when they have more neighbors (large N).

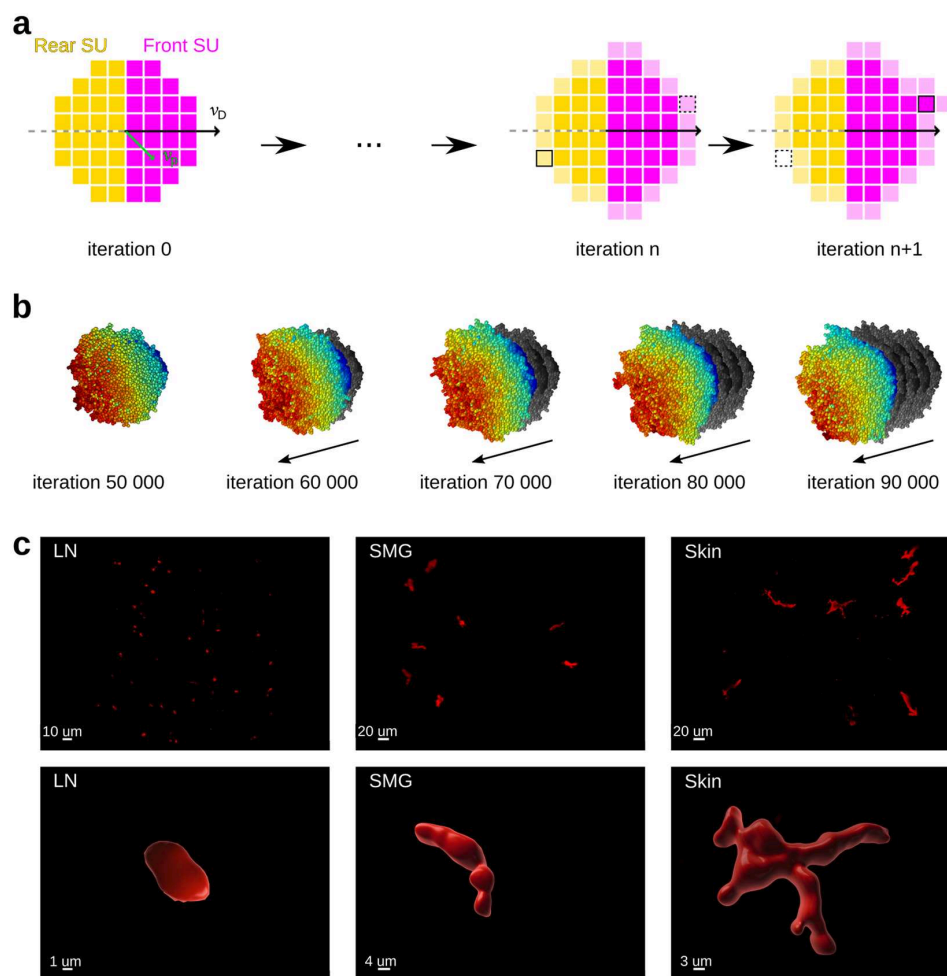


Figure 2. Synthetic and real migrating cells analyzed in this study. **(a)** Schematic overview of a 2D version of the cell migration simulator; the simulation starts with a spherical cell consisting of the pixel-based spatial units (SU); for each SU, we compute a position vector \vec{v}_p relative to the center of mass of the cell; we randomly choose the migration direction \vec{v}_D and define the cell's front and rear perpendicularly to \vec{v}_D ; at each iteration, we take one SU from the rear surface and move it to the front, which causes the cell to shift its center of mass; pale yellow SU indicate the candidates for removal, whereas pale purple SU indicate the free positions at the cell front. **(b)** Example of a cell generated with the 3D version of the cell migration simulator; gray shades designate the cell positions at previous time points. **(c)** Upper row: Deconvolved images of CD8⁺ T cells migrating in a lymph node (LN), submandibular salivary gland (SMG) and skin shown in Maximum Intensity Projection (MIP) mode; Lower row: individual representative cells in higher magnification zoom-in from the same groups as in the upper row in 3D Surface Rendering mode in Imaris.

In each iteration of the model, only one SU moves from the cell's rear to the front. Thus, the cell shape changes only slightly even after 1000 iterations, and the cell moves a fraction of its diameter (Fig. 2b, Supplement Video S1). This means that our cell migration simulator allows us to study the changes in cell shape with high spatio-temporal resolution. Therefore, we focused on resolving the changes in cell shape rather than on following the cells for extended time intervals. We simulated each cell for 100 000 iterations and saved the coordinates of all SU every 500 iterations. We analyzed the cells starting at iteration 60 000 when the cell shape appeared sufficiently different from its initial spherical shape; this resulted in 80 time points per cell. To investigate diverse patterns of cell migration, we generated four sets of cells – one for each parameter of the model. Each set consisted of three classes corresponding to three different values of the examined parameter, and each class contained 70 cells (see section 3.1).

Experimental data. Besides synthetic cells, we applied our analysis to intravital two-photon microscopy images of T cells migrating in the popliteal lymph node (LN), submandibular salivary gland (SMG), and skin (Fig. 2c, Supplementary Videos S2–S4). We isolated T cells from the spleen and the peripheral lymph nodes of

GFP⁺ or dsRed⁺ donor mice and transferred them to recipient mice, which were subsequently infected with a virus to generate memory T cells in various organs (see Supplementary Methods for details). We visualized the T cells migrating in the LN, SMG, and skin with two-photon microscopy, and acquired six time series for each condition. All experiments were approved by the Cantonal Committee for Animal Experimentation (License 2018_22_FR) and performed in accordance with federal guidelines.

Surface extraction. To obtain cell surfaces for SPHARM analysis, we reconstructed the surface of each cell as a triangular mesh and extracted the x, y, z coordinates of the mesh vertices. For synthetic cells, we converted the SU coordinates of each cell into a binary mask and reconstructed the cell surface using the marching cube algorithm implemented in the scikit-image library of Python³⁰. To reconstruct the surfaces of T cells, we first deconvolved the microscopy images using HuygensPro 19.04 (SVI, Hilversum, Netherlands) and then segmented and tracked them using Imaris 9.3.1 (Bitplane, Zürich, Switzerland; see Supplementary Methods for details). The resulting cell shapes were saved as VRML files for further analysis. To unify the different time intervals between frames (20 seconds for LN and SMG vs. 60 seconds for the skin), we analyzed only every third time point in the tracks from LN and SMG.

Feature extraction with spherical harmonics. To analyze the cell shape and its dynamics, we decomposed the cell surface at each time point into rotation-invariant spherical harmonics. The SPHARM transform was calculated using the Python library SHTools³¹, which requires a regular $N \times N$ spherical grid as input. Such grid was obtained by converting the surface coordinates from the Cartesian to the spherical coordinate system and then interpolating them onto a 120×120 grid of the polar angle θ and azimuthal angle φ (Fig. 3, left). The spherical grid was expanded into complex spherical harmonics using Driscoll and Healy's sampling theorem³² implemented within SHTools. In order to obtain a rotation-invariant shape feature $F(l)$, the power $A(l, m)^2$ of each complex harmonic was computed and summed up for all orders m of each degree l (Fig. 3, middle)³³. The first l_{max} degrees of each rotation-invariant spectrum were used to represent the shape of an individual cell at a single time point.

The rotation-invariant spectra $F(l)$ were either used to characterize the static cell shape or combined with spectra from other time points to characterize the shape dynamics (Fig. 3, middle). For both static and dynamic analysis, individual migrating cells – rather than individual time points of the same cell – served as independent observations. Thus, to obtain static shape features, we used $F(l)$ from the first time point of each cell and discarded the remaining time points. Information from different time points was combined by computing two types of dynamic features in the time and the frequency domain. To compute the features in the time domain (dynamic time features), we combined $F(l)$ from the first T time points of each cell into a time map $F(l, t)$. Being concatenated one after another, the time-ordered spectra served as an extended feature vector of size $l_{max} \cdot T$. The features in the frequency domain (dynamic frequency features) were revealed by a Fourier transform of $F(l, t)$ calculated for each l . This transform resulted in a frequency map $F(l, f)$ of the same size, whose values constituted another dynamic feature vector. The sizes of the three feature vectors were defined by the parameters l_{max} and T , which we adjusted to maximize the classification accuracy (Supplementary Methods, Fig. S3, S4).

Shape classification. After extracting static and dynamic shape features, we classified the cells using the linear-kernel support vector machine (SVM) classifier implemented in the scikit-learn library of Python³⁴ (Fig. 3, right). In order to compare the shape between different classes of cells and to identify significant shape differences, we computed the classifier accuracy between each pair of classes and compared it to the accuracy of a control classifier.

The classifier accuracy was evaluated for each pair of classes by performing 150 rounds of cross-validation with stratified shuffle split for synthetic cells and stratified group shuffle split for T cells. For synthetic data, 50 cells from each class were randomly chosen in each cross-validation round to serve as the training dataset, while the remaining cells (20 cells per class) were used to test the classifier performance (Fig. 4). For experimental data, we had to combine the cells into groups according to time series (six groups per class). In each cross-validation round, one time series from each class was left out for testing, while the cells from the remaining time series served to train the classifier (Fig. 5). In this way, T cells from the same time series were either in the training or testing dataset, but not in both.

After evaluating the classifier accuracy, we compared it to a naive control classifier, which was chosen depending on whether the classified dataset was balanced or unbalanced. We considered a dataset to be balanced if none of the classes contained more than 60% of all cells. In this case, we used a random classifier as the best naive classifier. As a control for unbalanced data – where more than 60% of cells belonged to one class – we used the majority classifier. This classifier assigns all cells to the class with the most observation and thus performs better than a random classifier.

Since the dataset of synthetic cells was balanced (70 cells per class), we used a random classifier as control (Fig. 4). To compute the accuracy of the random classifier, we randomly shuffled class labels and carried out ten rounds of cross-validation with stratified-shuffle-split with 20 cells from each class serving as test data. We repeated the shuffling of class labels five times for each pair of classes, which produced 50 control accuracy values for each pair. We combined the accuracy values from all three pairs into a single control set with 150 values.

In contrast to synthetic data, each class of T cells contained different cell numbers (though the number of time series was the same). Hence, for each pair of classes, we determined whether the data was balanced or unbalanced and computed the control accuracy with either a random or a majority classifier (Fig. 5). For balanced data, we randomly shuffled class labels (repeated 15 times) and carried out cross-validation with stratified group shuffle split (10 rounds). For unbalanced data, we randomly selected one time series from each class (repeated 150

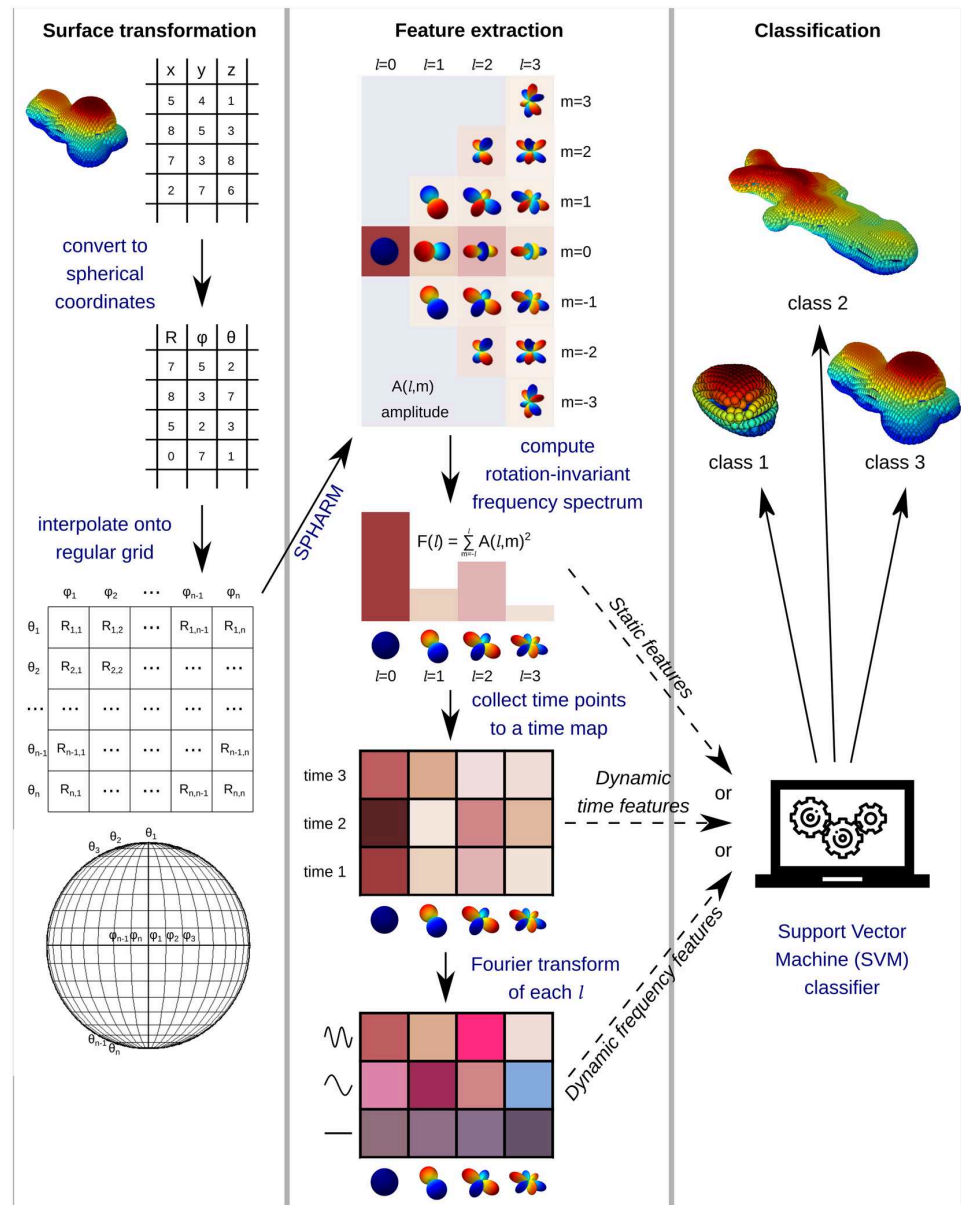


Figure 3. Schematic overview of the surface analysis and classification. We convert surface coordinates to a regular spherical grid, transform them with SPHARM, and compute a rotation-invariant spectrum. We use the spectrum of a single time point either as a feature vector by its own (static features) or combine it with other time points into a time map (dynamic time features). We can further convert the time map into a frequency map by Fourier transform of each degree l (dynamic frequency features). We then use one of the three feature vectors to classify cells according to their shape.

times), assigned all selected cells to the majority class, and computed the resulting accuracy. Thus, for each pair of classes, we used an individual control group with 150 accuracy values.

Results

We used the described cross-validation scheme to classify migration patterns in both synthetic cells and T cells. We examined how the applied feature vector (static, dynamic time-domain, or dynamic frequency-domain features) affected the accuracy of the classifier. The classifier accuracy was further compared to that of a control classifier (random or majority) to identify experimental conditions and model parameters that significantly change the cell migration patterns.

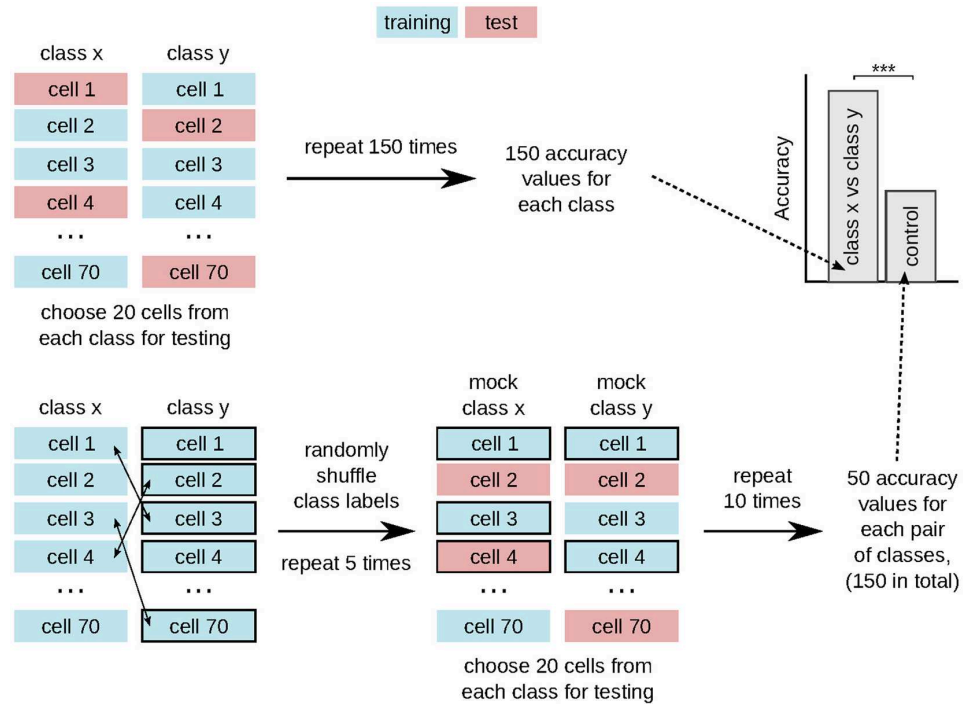


Figure 4. Schematic of the cross-validation scheme for synthetic data. We compute the classifier accuracy for each pair of classes using two-class classification with stratified shuffle split cross-validation. For the control group, we apply stratified shuffle split cross-validation after randomly shuffling class labels.

Dynamic SPHARM-based classification of synthetic cells. By detecting significant differences in migration patterns, our approach can be used to study how various parameters of the cell migration simulator (CMS) affect the shape of generated cells. To illustrate this use, we applied static and dynamic SPHARM-based classification to examine the behavior of the four parameters of the CMS. For each parameter, we examined three different values, while setting the other parameters to their default values. Thus, we tested the neighbor-weight parameter NW, which determines the cell surface roughness (default value NW = 4), the parameter for position weight PW, which affects the cell elongation (default value PW = 4), the distance weight parameter DW, which governs the size of cell protrusions (default value DW = 6), and the front-rear threshold FR, which is associated with the cell volume fraction considered as the front (default value FR = 0). We then quantified the classification accuracy between each pair of classes and compared it to a random control classifier to identify significant differences (Fig. 4).

Interestingly, different parameters affected cell shape to a different extent (Fig. 6). Thus, changing the value of the PW parameter from 1 to 2 to 4 resulted in visually distinct cells (Figs. 6a, S5a) and large quantitative differences between the cell shapes (Fig. 6b). Changing the value of NW from 1 to 2 to 4 resulted in a similarly large quantitative difference (Fig. 6d), but the cells' 3D surface reconstructions were hard to distinguish visually (Fig. 6c). Only looking at the cells' maximum projections revealed that – indeed – lower NW values resulted in a more structured cell surface (Fig. S5b). For the DW parameter, both 3D surfaces and maximum projections were similar (Figs. 6e, S5c) for different parameter values (2, 4, and 6), and no significant differences in cell shape could be identified by the static classifier (Fig. 6f). In contrast, when shape dynamics was included, the classifier accuracy was significantly higher than random, indicating that the visually similar cells might evolve their shape in different ways. Interestingly, different value ranges of the FR parameter had different effects on the cell shape, even though the parameter values were equally spaced. Thus, cell shape did not change when the value of FR increased from 0 to 0.3, which was both observed visually (Figs. 6g, S5d) and reflected by the close-to-random classifier accuracy (Fig. 6h). In contrast, cell shape for FR = 0.6 was significantly different from both other classes, which was confirmed by visual inspection and by the classifier accuracy for all three feature vectors (Fig. 6g,h).

Although we examined only three values for each parameter, our approach should bring the most benefit when many parameter values and their combinations have to be scanned and it is hard to visually control the outcome of every combinations. Adjusting parameter values of a model can be a daunting task, and our approach can facilitate this endeavor by quantifying the shape differences that result from different parameter values and thus support the identification of meaningful parameter ranges. For instance, for our CMS, it would probably make little sense to further examine FR values between 0 and 0.3, since these values result in very similar cell shape, and one should rather focus on the FR values between 0.3 and 0.6.

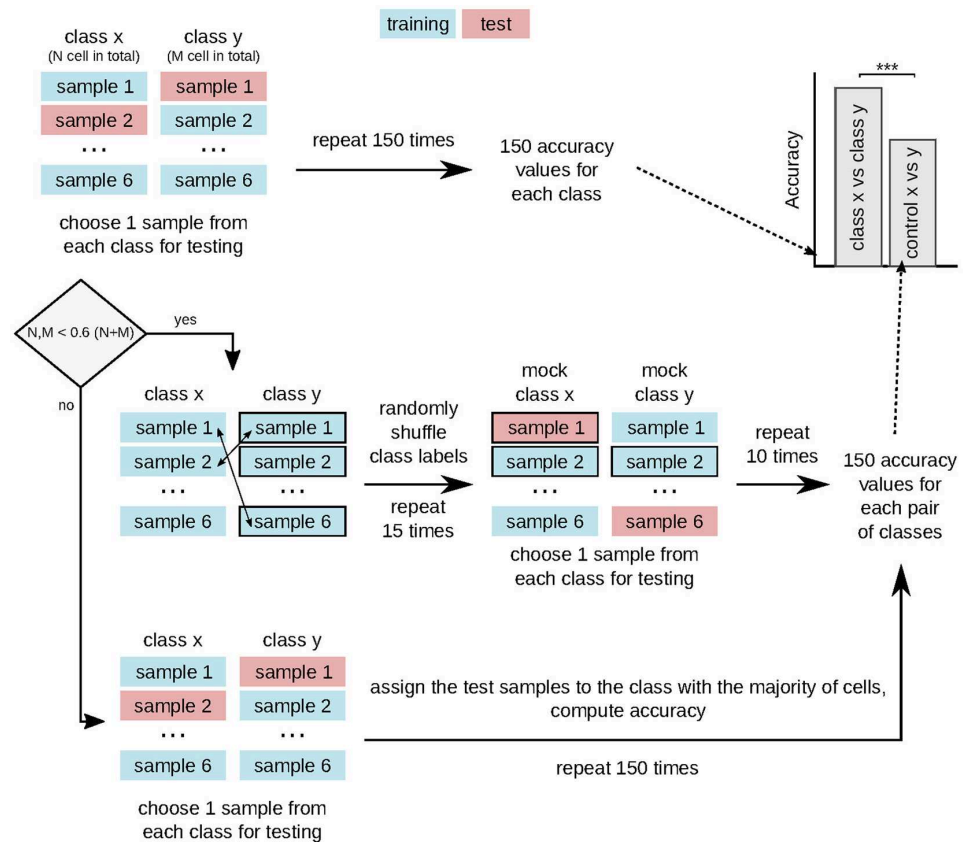


Figure 5. Schematic of the cross-validation scheme for experimental data. We compute the classifier accuracy for each pair of classes using two-class classification with stratified group shuffle split cross-validation. If the data is balanced (none of the classes contains more than 60% of cells), the control accuracy is computed by randomly shuffling the class labels and performing cross-validation with stratified group shuffle split. For unbalanced data, the majority classifier serves as a control.

When comparing the accuracy of the static and dynamic classifiers, dynamic features outperformed static features in nearly all comparisons (Fig. 6). No improvement was achieved only in those cases, where the static classifier accuracy was close to 100% (Fig. 6b,d), or the dynamic classifier detected no significant shape differences (Fig. 6h, $FR = 0.0$ vs. $FR = 0.3$). The use of dynamic frequency domain did not further improve classifier performance and resulted in similar accuracy values as for dynamic time domain (Fig. 6).

Importantly, the higher accuracy of the dynamic classifiers was not due to the larger dataset used to train them. As described in Materials and Methods, we used only the first time point for extracting static SPHARM features in order to keep the number of independent observations equal between the static and dynamic classifiers. Effectively, this resulted in a much larger feature vector for the dynamic classifiers while most of the information for the static classifier was discarded. Using all time points as independent observations, however, does not improve the performance of the static classifier because these data points are highly correlated. In fact, a static classifier based on all time points was inferior to the one based on just the first time point (Fig. S6). It also detected significant differences in cell shape where the actual classifier accuracy was only marginally higher than random (Fig. S6, $FR = 0$ vs. $FR = 0.3$). Thus, simply gathering cell shapes from all time points into a static classifier not only doesn't help to improve the classifier accuracy, but also can result in overfitting and misleading conclusions. Only a truly dynamic way to handle time information can boost the classifier performance by including the shapes at different time points into feature vectors of individual cells.

Dynamic SPHARM-based classification of T cells. We further examined whether our approach can also be used to classify migration patterns in experimental data. We analyzed the three groups of T cells migrating in various tissues (LN, skin, and SMG). As in synthetic data, we quantified the classification accuracy between each pair of tissues and compared it to a control classifier (Fig. 5).

The classifier accuracy significantly differed from control for each comparison and each feature vector (Fig. 7a–c). This difference was most apparent for the comparison of environments LN versus skin (Fig. 7b)

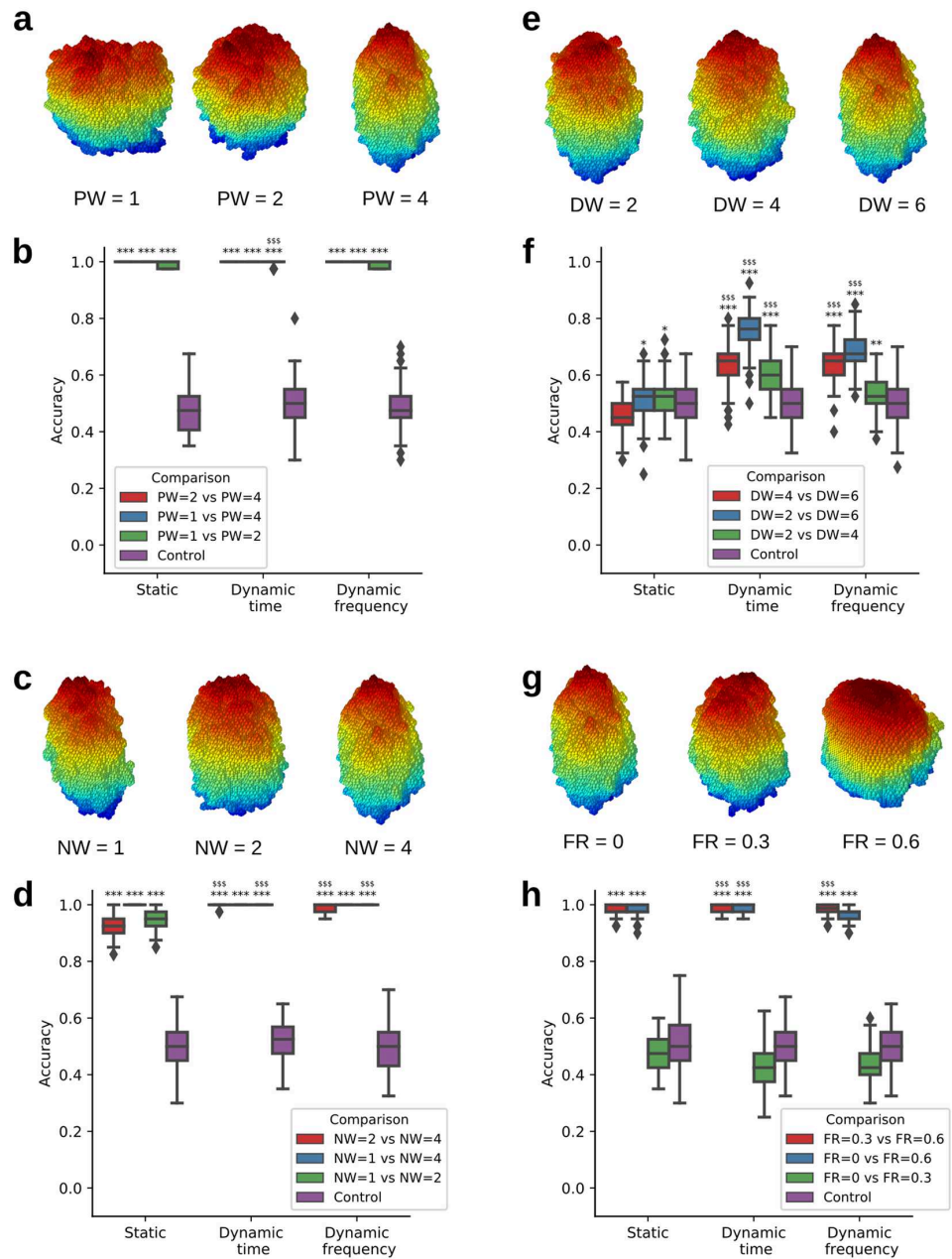


Figure 6. Classification of synthetic cells. Surfaces of representative cells generated with three different values of the position weight (PW) (a), neighbor weight (NW) (c), distance weight (DW) (e), and front-rear (FR) (g) parameters. Classifier accuracy for different pairs of classes relative to control for different values of the PW (b), NW (d), DW (f), and FR (h) parameters. Unless indicated, the default parameter values were used: FR = 0, NW = 4, PW = 4, DW = 6. Significantly higher than control: * $p < 0.05$, ** $p < 0.01$, *** $p < 0.001$; significantly higher than static features: sss $p < 0.001$; one-sided Mann-Whitney test, $n = 150$ per group.

because these tissues induce two extremes in the shape of T cells (Figs. 2c, 7d). The T cells migrating in LN had a more regular close-to-spherical shape, whereas the T cells from skin were irregular and made many protrusions. T cells migrating in SMG had an intermediate shape, which also strongly varied from time series to time series.

The relative accuracy of the static and dynamic classifiers differed for each comparison, but the dynamic classifiers generally performed better (Fig. 7a–c). Thus, the dynamic classifiers both in the time- and frequency-domain were superior when comparing LN to the other two environments, whereby in the LN vs. skin comparison, the accuracy further increased with the use of dynamic frequency features. When comparing SMG and skin, the use

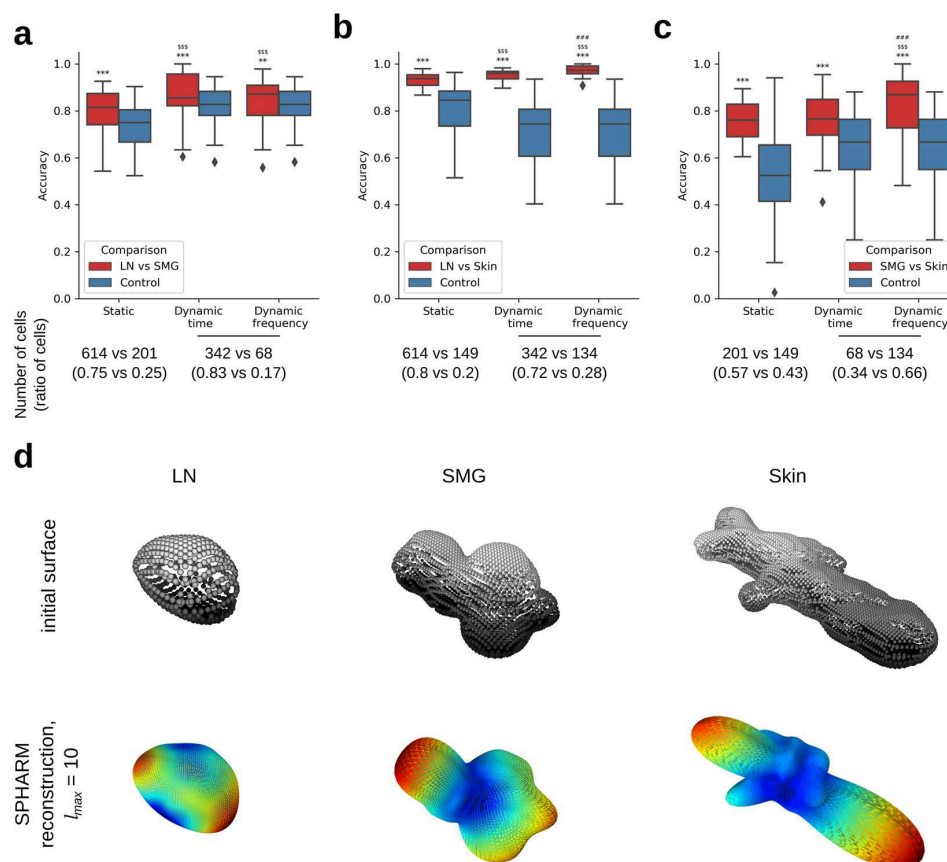


Figure 7. Classification of T cells for various pairs of classes relative to control. **(a)** LN vs SMG. **(b)** LN vs Skin. **(c)** SMG vs Skin. **(d)** Surfaces and SPHARM reconstructions of representative cells from the three analyzed classes. Significantly higher than control: ** $p < 0.01$, *** $p < 0.001$; significantly higher than static features: $^{SSS}p < 0.001$; significantly higher than dynamic time features: $^{###}p < 0.001$; one-sided Mann-Whitney test, $n = 150$ per group. Numbers below the box plots indicate the number (ratio) of cells in each class for the corresponding class pair. For ratios between 0.4 and 0.6, the random classifier was used as control. In all other cases, the majority classifier was used, whose accuracy is defined by the ratio of cells. In the dynamic classifiers, fewer cells were analyzed because not all cell tracks were sufficiently long (20 time points) to be included. This resulted in different ratios between cell numbers and hence different control accuracies for the static and dynamic classifiers.

of dynamic time features did not bring any benefit, whereas the dynamic frequency features outperformed both dynamic time and static features. As a common trend for all comparisons, the classifier accuracy with dynamic frequency features was always significantly higher than the accuracy of the static classifier. This trend confirms our hypothesis that not only static shape features but also the dynamic shape patterns play an essential role in defining unique modes of cell migration in different environments.

Comparison of SPHARM-based classification to 2D shape descriptors. We evaluated how SPHARM-based descriptors perform in comparison to 2D shape descriptors. As SPHARM is a 3D extension of a Fourier analysis, we applied a method that is based on the classification of a set of Fourier components produced by Discrete Fourier Transform (DFT) after carrying out a 3D-to-2D projection of surface-rendered cells³⁵. The advantage of the latter approach is two-fold: (i) the more complex 3D shape characterization by SPHARM is reduced to 2D DFT and (ii) the combination of various random 3D-to-2D projections allows a seamless transition from a pure 2D shape descriptor to a quasi-3D description of cell shapes. We combined these 2D descriptors obtained from various numbers of projections with the same classification scheme that we used for SPHARM and compared the classification accuracy to a static SPHARM classifier.

The results of this comparison for synthetic cells are summarized in Figs. S7–S10 and reveal that the SPHARM-based approach always outcompetes the 2D shape descriptors, except for variations in the DW parameter (see Fig. S9) and for a specific comparison of FR parameters (see Fig. S10a). This does not come as a surprise, because we noted before that for these parameters the SPHARM-based classifier does not perform better than

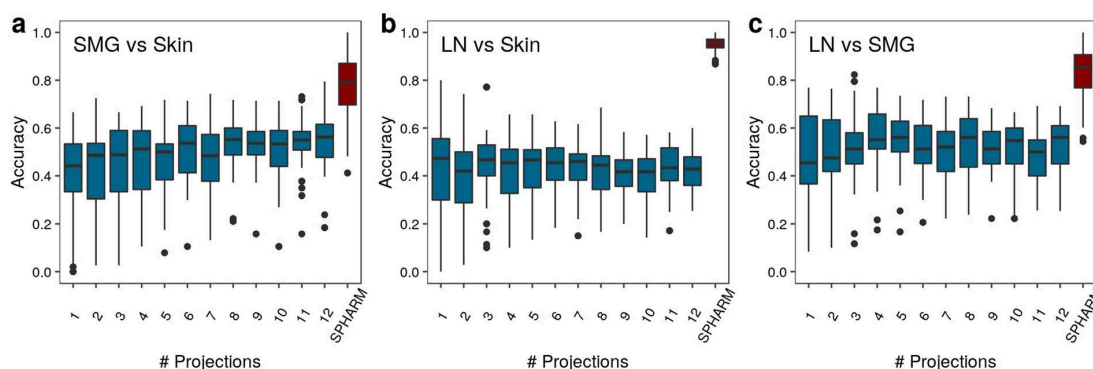


Figure 8. Static SPHARM-based classifier accuracy for T cells of different pairs of environments in comparison to the DFT-based with projection numbers between 1 and 12. The environments. (a) SMG versus Skin, (b) LN versus Skin, and (c) LN versus SMG are compared.

the random classifier in the static case (see Fig. 6f,h). These observations suggest that the DFT-based approach is more sensitive to details in the outline of the shape projections than the SPHARM-based approach. On the other hand, increasing the number of projections gives rise to a quasi-3D description of cell shapes that is approaching but not superseding the accuracy of the SPHARM-based classification for variations in the model parameters PW, NW and FR. For T cells, the performance of the static SPHARM-based classification compared with the DFT-based revealed that the accuracy of the former is always significantly higher, even if the latter approach includes numerous projections for a quasi-3D representation of the cell shapes. In fact, as can be seen in Fig. 8, the classification accuracy of the DFT-based approach is comparable to that of a random classifier. We conclude that the complexity of the T cell shape determines the minimum number of projections for which the DFT-based approach of T cell representation performs as well as the SPHARM-based approach does by 3D reconstruction.

We conclude from this comparison that the SPHARM-based approach is generally superior to using 2D shape descriptors.

Discussion

In our proof-of-principle study, we confirmed that adding dynamics to shape analysis can improve the classification of migration patterns of cells. We illustrated this improvement by combining the dynamic SPHARM approach with an SVM classifier to identify conditions with significantly different cell shapes. This approach, however, is not restricted to SPHARM and SVM. We believe that adding dynamics to other shape descriptors, such as Fourier-based descriptors³⁵ or wavelets^{36,37}, could also improve their classification accuracy. The performance of other classifiers – such as random forest or neural networks – should also be studied in the future.

Other implementations of the SPHARM analysis should also be tested, e.g. the SPHARM-MAT toolbox available in MATLAB. Here we focused on an open-source Python alternative SHTools³¹ making this analysis freely available to the community. The problem of the SHTools implementation, however, is that it is based on converting the cell shape to spherical coordinates and is therefore accurate only for cells with the center of mass inside the cell body. While this requirement was always met for synthetic cells, some T cells – especially those migrating in the skin – had a complex shape with the center of mass temporarily appearing outside the cell body. Such shape could not be accurately represented in spherical coordinates, which resulted in erroneous shape reconstructions after SPHARM transform (Fig. S11, bottom row). Since such complex-shaped cells constituted only a fraction of the total T cell number (9% LN, 7% in SMG, and 28% in the skin), we neglected this inaccuracy in the current study, but this problem will have to be addressed in the future. One solution to this could be to create open-source implementations of other SPHARM variants (like SPHARM-MAT) that calculate the SPHARM transform directly from the Cartesian coordinates of the surface and thus do not suffer from the center-of-mass problem.

Despite the limitations of our approach for cells with highly irregular shape, most of the cells analyzed in our study (all synthetic cells, as well as > 90% of LN and SMG T cells) had their center of mass inside the cell and thus could be accurately analyzed by our method. In all comparisons that involved these accurately represented cells (Figs. 6, 7a), dynamic SPHARM outperformed its static counterpart and – in one case – could even reveal shape differences not detected by the static SPHARM analysis (Fig. 6f). This suggests that including dynamic shape features is especially relevant when shape differences between the analyzed groups are small, whereas for visually distinct shapes, static analysis – or even simpler shape descriptors – may be sufficient.

When looking at dynamic SPHARM in the frequency domain, in most cases it did not bring any improvement relative to the time domain. Interestingly, the only comparisons where the dynamic frequency features were superior involved the T cells migrating in skin (Fig. 7b,c), which included a relatively high fraction (28%) of cells with center of mass transiently appearing outside the cell body. This event resulted in a dramatic change in shape representation for some of the time points (Fig. S11, bottom row) and apparently created a unique frequency pattern that was picked up by the dynamic frequency classifier and used as a feature to distinguish skin T cells from other T cells. This observation confirms that the use of frequency domain can indeed help to detect interesting frequency patterns⁸, either relevant for cell migration, or irrelevant artifacts as in our case.

By recognizing differences in dynamic cell shape, dynamic shape analysis methods like ours can be used to study how cell migration patterns change under various experimental conditions. Here we showed that the extracellular environment affects the dynamic shape of migrating T cells: even though we looked at the same type of cells, their migratory behavior dramatically changed depending on the surrounding tissue. In the future, a similar approach can be used to study other factors that affect cell migration¹ (Fig. 1), which could involve various cell types migrating in different intact or altered extracellular environments both *in vivo* and in 3D artificial matrices³⁸.

Dynamic SPHARM analysis can also be applied to study cell migration *in silico*. Classifying between cells generated with different parameters of migration models will help to better understand the meaning of these parameters both in our CMS and other models of cell migration. Furthermore, comparing the shape of synthetic migrating cells to that of real cells will enable the use of the image-based systems biology approach^{39,40} to create cell migration models that are realistic and data-driven. With these models, we can identify and interpret the meaning of the model parameters that induce cell shapes observed in a particular experiment⁴¹.

Taken together, dynamic SPHARM-based classification can contribute to our understanding of cell migration in two ways. On the one hand, it can help to investigate various experimental settings and their effect on cell migration patterns. On the other hand, it should enable identifying parameters of realistic migration models that produce specific experimentally observed cell shapes. Both of these applications can help to pinpoint the factors that affect the shape of migrating cells and thus bring us closer to understanding the mechanisms underlying cell migration.

Data and Code availability

The authors declare that all relevant data supporting the findings of this study are available within the paper (and its Supplementary Information file). Any raw data can be downloaded from https://asbdata.hki-jena.de/publdata/MedyukhinaEtAL_SPHARM/. The source code for the dynamic SPHARM analysis is available at https://github.com/applied-systems-biology/Dynamic_SPHARM. The source code for the cell migration simulator is available at <https://github.com/applied-systems-biology/cell-migration-simulator>.

Received: 19 September 2019; Accepted: 24 March 2020;

Published online: 08 April 2020

References

- Ridley, A. J. *et al.* Cell Migration: Integrating Signals from Front to Back. *Science* **302**, 1704–1709 (2003).
- Masuzzo, P., Van Troys, M., Ampe, C. & Martens, L. Taking Aim at Moving Targets in Computational Cell Migration. *Trends Cell Biol.* **26**, 88–110 (2016).
- Mokhtari, Z. *et al.* Automated Characterization and Parameter-Free Classification of Cell Tracks Based on Local Migration Behavior. *PLoS ONE* **8**, e80808 (2013).
- Svensson, C.-M., Medyukhina, A., Belyaev, I., Al-Zaben, N. & Figge, M. T. Untangling cell tracks: Quantifying cell migration by time lapse image data analysis. *Cytometry A* **93**, 357–370 (2018).
- Pincus, Z. & Theriot, J. A. Comparison of quantitative methods for cell-shape analysis. *J. Microsc.* **227**, 140–156 (2007).
- Tangelder, J. W. H. & Veltkamp, R. C. A survey of content based 3D shape retrieval methods. *Multimed. Tools Appl.* **39**, 441–471 (2008).
- Dufour, A. C. *et al.* Signal Processing Challenges in Quantitative 3-D Cell Morphology: More than meets the eye. *IEEE Signal Process. Mag.* **32**, 30–40 (2015).
- Maeda, Y. T., Inose, J., Matsuo, M. Y., Iwaya, S. & Sano, M. Ordered Patterns of Cell Shape and Orientational Correlation during Spontaneous Cell Migration. *PLoS ONE* **3**, e3734 (2008).
- Driscoll, M. K., Fourkas, J. T. & Losert, W. Local and global measures of shape dynamics. *Phys. Biol.* **8**, 055001 (2011).
- Li, H., Pang, F., Shi, Y. & Liu, Z. Cell dynamic morphology classification using deep convolutional neural networks. *Cytometry A* **93**, 628–638 (2018).
- Li, H., Liu, Z., Pang, F. & Shi, Y. Characterization of single cell dynamic morphology by local deformation pattern modeling. In *2017 39th Annual International Conference of the IEEE Engineering in Medicine and Biology Society (EMBC)* 329–332, <https://doi.org/10.1109/EMBC.2017.8036829> (2017).
- Mogilner, A. & Keren, K. The Shape of Motile Cells. *Curr. Biol.* **19**, R762–R771 (2009).
- Coombes, J. L. & Robey, E. A. Dynamic imaging of host–pathogen interactions *in vivo*. *Nat. Rev. Immunol.* **10**, 353–364 (2010).
- Konjufca, V. & Miller, M. J. Two-photon microscopy of host–pathogen interactions: acquiring a dynamic picture of infection *in vivo*. *Cell. Microbiol.* **11**, 551–559 (2009).
- Secklehner, J., Celso, C. L. & Carlin, L. M. Intravital microscopy in historic and contemporary immunology. *Immunol. Cell Biol.* **95**, 506–513 (2017).
- Driscoll, M. K. & Danuser, G. Quantifying Modes of 3D Cell Migration. *Trends Cell Biol.* **25**, 749–759 (2015).
- Brechbühler, C., Gerig, G. & Kübler, O. Parametrization of Closed Surfaces for 3-D Shape Description. *Comput. Vis. Image Underst.* **61**, 154–170 (1995).
- Shen, L., Kim, S. & Saykin, A. J. Fourier method for large-scale surface modeling and registration. *Comput. Graph.* **33**, 299–311 (2009).
- Styner, M. *et al.* Framework for the Statistical Shape Analysis of Brain Structures using SPHARM-PDM. *Insight J.* 242–250 (2006).
- Morris, R. J., Najmanovich, R. J., Kahraman, A. & Thornton, J. M. Real spherical harmonic expansion coefficients as 3D shape descriptors for protein binding pocket and ligand comparisons. *Bioinformatics* **21**, 2347–2355 (2005).
- Venkatraman, V., Sael, L. & Kihara, D. Potential for Protein Surface Shape Analysis Using Spherical Harmonics and 3D Zernike Descriptors. *Cell Biochem. Biophys.* **54**, 23–32 (2009).
- Khairy, K., Foo, J. & Howard, J. Shapes of Red Blood Cells: Comparison of 3D Confocal Images with the Bilayer-Couple Model. *Cell. Mol. Bioeng.* **1**, 173–181 (2008).
- Khairy, K. & Howard, J. Minimum-energy vesicle and cell shapes calculated using spherical harmonics parameterization. *Soft Matter* **7**, 2138 (2011).
- Gerig, G., Styner, M., Shenton, M. E. & Lieberman, J. A. Shape versus Size: Improved Understanding of the Morphology of Brain Structures. in *Medical Image Computing and Computer-Assisted Intervention – MICCAI 2001* (eds. Niessen, W. J. & Viergever, M. A.) 24–32 (Springer Berlin Heidelberg, 2001).
- Shen, L., Ford, J., Makedon, F. & Saykin, A. A surface-based approach for classification of 3D neuroanatomic structures. *Intell. Data Anal.* **8**, 519–542 (2004).

26. Du, C.-J., Hawkins, P. T., Stephens, L. R. & Bretschneider, T. 3D time series analysis of cell shape using Laplacian approaches. *BMC Bioinformatics* **14**, 296 (2013).
27. Ducroz, C., Olivo-Marín, J. & Dufour, A. Characterization of cell shape and deformation in 3D using Spherical Harmonics. In *2012 9th IEEE International Symposium on Biomedical Imaging (ISBI)* 848–851, <https://doi.org/10.1109/ISBI.2012.6235681> (2012).
28. Ducroz, C., Olivo-Marín, J.-C. & Dufour, A. Spherical Harmonics based extraction and annotation of cell shape in 3D time-lapse microscopy sequences. *Conf. Proc. Annu. Int. Conf. IEEE Eng. Med. Biol. Soc. IEEE Eng. Med. Biol. Soc. Annu. Conf.* **2011**, 6619–6622 (2011).
29. Blickensdorf, M. Agent based modeling of cell migration and shape analysis. (Friedrich Schiller University Jena, 2015).
30. Walt, Svander *et al.* scikit-image: image processing in Python. *PeerJ* **2**, e453 (2014).
31. Wiczorek, M. A. & Meschede, M. SHTools: Tools for Working with Spherical Harmonics. *Geochem. Geophys. Geosystems* **19**, 2574–2592 (2018).
32. Driscoll, J. R. & Healy, D. M. Computing Fourier Transforms and Convolutions on the 2-Sphere. *Adv. Appl. Math.* **15**, 202–250 (1994).
33. Kazhdan, M., Funkhouser, T. & Rusinkiewicz, S. Rotation Invariant Spherical Harmonic Representation of 3D Shape Descriptors. In *Proceedings of the 2003 Eurographics/ACM SIGGRAPH Symposium on Geometry Processing* 156–164 (Eurographics Association, 2003).
34. Pedregosa, F. *et al.* Scikit-learn: Machine Learning in Python. *J. Mach. Learn. Res.* **12**, 2825–2830 (2011).
35. Kriegel, F. L. *et al.* Cell shape characterization and classification with discrete Fourier transforms and self-organizing maps. *Cytometry A* **93**, 323–333 (2018).
36. Antoine, J.-P. & Vanderghyest, P. Wavelets on the 2-Sphere: A Group-Theoretical Approach. *Appl. Comput. Harmon. Anal.* **7**, 262–291 (1999).
37. Tournemenne, R., Ducroz, C., Olivo-Marín, J. & Dufour, A. 3D shape analysis using overcomplete spherical wavelets: Application to BLEB detection in cell biology. In *2014 IEEE 11th International Symposium on Biomedical Imaging (ISBI)* 365–368, <https://doi.org/10.1109/ISBI.2014.6867884> (2014).
38. Griffith, L. G. & Swartz, M. A. Capturing complex 3D tissue physiology *in vitro*. *Nat. Rev. Mol. Cell Biol.* **7**, 211–224 (2006).
39. Figge, M. T. & Murphy, R. F. Image-based systems biology. *Cytometry A* **87**, 459–461 (2015).
40. Medyukhina, A., Timme, S., Mokhtari, Z. & Figge, M. T. Image-based systems biology of infection. *Cytometry A* **87**, 462–470 (2015).
41. Figge, M. T. Quantitative bioimage analysis of cell characteristics. *Cytometry A* **93**, 278–280 (2018).

Acknowledgements

We want to thank Carl-Magnus Svensson for valuable hints on the choice of control classifiers. This work was financially supported by the International Leibniz Research School (ILRS) and by the Deutsche Forschungsgemeinschaft (DFG) through the Excellence Graduate School Jena School for Microbial Communication (JSMC) and CRC 1278 PolyTarget under DFG project number 316213987 (project Z01 to M.T.F.).

Author contributions

A.M. and M.T.F. conceived and designed the study. M.B. developed the migration model and generated synthetic cells. N.R. and J.S. performed microscopy experiments. Z.C. performed deconvolution and image analysis of the microscopy data, and carried out the 3D-to-2D projection-based DFT analysis. A.M. developed and performed the SPHARM-based shape analysis and classification. A.M., M.B., Z.C. and M.T.F. interpreted the analysis results. A.M., M.B. and Z.C. prepared the figures. All authors were involved in writing, critically revising, and approving the manuscript.

Competing interests

The authors declare no competing interests.

Additional information

Supplementary information is available for this paper at <https://doi.org/10.1038/s41598-020-62997-7>.

Correspondence and requests for materials should be addressed to M.T.F.

Reprints and permissions information is available at www.nature.com/reprints.

Publisher's note Springer Nature remains neutral with regard to jurisdictional claims in published maps and institutional affiliations.



Open Access This article is licensed under a Creative Commons Attribution 4.0 International License, which permits use, sharing, adaptation, distribution and reproduction in any medium or format, as long as you give appropriate credit to the original author(s) and the source, provide a link to the Creative Commons license, and indicate if changes were made. The images or other third party material in this article are included in the article's Creative Commons license, unless indicated otherwise in a credit line to the material. If material is not included in the article's Creative Commons license and your intended use is not permitted by statutory regulation or exceeds the permitted use, you will need to obtain permission directly from the copyright holder. To view a copy of this license, visit <http://creativecommons.org/licenses/by/4.0/>.

© The Author(s) 2020

Part III

DISCUSSION

DISCUSSION

Fungal infections impose a serious threat to mankind's health as the worldwide incidence has constantly increased over recent decades. This is caused by a larger share of immunocompromised patients like the elderly or chronically ill, prompted by improved medical care. The most important representative, *Aspergillus fumigatus*, is an airborne ubiquitous mould with worldwide abundance, which, upon inhalation, may manifest severe infections in the human lung with high mortality rates [32]. The constant exposure to conidia of *A. fumigatus* in combination with a manifestation in the human lung make it extremely difficult to capture the early dynamics of infection. Although experimental methods as mice models or *in vitro* methods exist, the infection dynamics cannot be examined *in vivo*, imposing a need for new methods of research. Hence, simulated computer models, as used in the manuscripts presented in this thesis, provide a valuable addition to the research methodology since they overcome ethical and methodical limitations in a controllable and flexible way.

In the following, the results of the publications presented in the previous chapter are summarized and critically discussed. The second section discusses possible steps for further development of the used hybrid agent-based alveolus model of research on *A. fumigatus* infections and presents new targets for *in silico* experiments.

7.1 DISCUSSION OF MAIN RESULTS

7.1.1 Modeling reveals infection dynamics in murine alveoli

Although many mammalian wet lab models for investigating of *A. fumigatus* infections exist, the murine model represents the most common and established animal model [115]. Despite the close evolutionary link, various alterations arise comparing the human and murine lung. These differences must be taken into account and evaluated to understand how a direct transfer of findings from the murine model to human infections can be achieved. Therefore, the established hybrid agent-based alveolus model of human *A. fumigatus* infections [116, 117] was adapted to a murine alveolus infection model, making it possible to quantify differences and evaluate their impact on the infection dynamics.

The simulations with the murine alveolus infection model revealed three morphological key aspects that influence the infection dynamics. First, the overall alveolar diameter is smaller in the mouse compared to the human by a factor of four, resulting in a larger surface area by a factor of 20. Consequently, the number of more than 100 AEC in the human alveolus is reduced to only eight in the murine alveolus, imposing alterations in the cellular signaling dynamics. Second, the relation of lung surface area to AMs available in the lung shows that the mean AM number to expect per alveolus is 4.38 in the human alveolus but 0.74 in the murine alveolus. Considering the aforementioned surface area differences, a human AM has to scan a six-times larger area compared to the murine AM. The third important difference of alveolar morphology concerns the interconnection of alveoli. Immune cells like AM can enter or leave the alveolus through either the alveolar entrance ring or through a pore of Kohn (PoK), which function as passageways between neighboring alveoli. An increased number of PoK in the murine alveolus results in a smaller surface-to-boundary ratio, allowing for smaller migration distances of macrophages entering the murine alveolus. In parallel, the increased number of PoK allows for more outflow of chemokines, which might distort the signaling, resulting in a loss of chemokine efficiency.

Our simulation results show that for a typical *A. fumigatus* daily exposition dosage, AM detect conidia with higher efficiency in the murine alveolus, resulting in a faster infection clearance compared to humans. This is predominantly governed by the smaller migration distance for AM, causing a fast detection of the conidium. We could demonstrate that quantitative differences in the chemokine signaling induced by the altered alveolar morphology are majorly outperformed by the smaller scanning area per AM. These results hold true as long as parameters like AM speed or chemokine secretion rate are assumed to be fairly similar in humans and mice. We could demonstrate that our results are robust in the way that a single conidium in the murine alveolus is cleared with higher efficiency as long as the chemokine parameters do not differ between the organisms by at least a factor of three.

7.1.2 Fungal burden governs infections in murine model

Besides assessing the impact of altered morphologies, a second important issue must be considered when comparing natural *A. fumigatus* infections in humans to experimental infections in murine models, namely different conidia exposures. Infections in humans are caused by air-soluted conidia, which are naturally inhaled during respiration. Studies show that humans typically inhale

thousands of conidia per day [21], whereas the number of administered conidia in experimental mice models is in the range of $10^6 - 10^8$ [118–120]. Water-soluted conidia are most commonly administered to the lung either intranasally or intratracheally to an anesthetized, immunocompromised mouse [121]. Already in 2004, Steinbach *et al.* demonstrated that this way of infection causes a highly heterogeneous conidia distribution in the lung, which could be resolved by the use of respiration chambers in which air-soluted conidia are naturally inhaled by the mouse [122]. Despite the obvious benefits of a naturally-inhaled infection, the intranasal or intraperitoneal administration of conidia remains widely in use [123–125]. An additional drawback of intranasal administration is that only an estimated fraction of $10^3 - 10^5$ of the administered conidia actually reach the lung, whereas the majority of conidia flow back out of the nose or into the gastrointestinal tract, limiting the exact quantification of fungal burden in the lung [126, 127]. Considering the smaller number of alveoli in the murine lung, the fungal burden per murine alveolus is much higher than in humans and must be taken into consideration.

Thus, a different number of conidia per alveolus and their respective clearance efficiency, as simulated by the hybrid agent-based alveolus model, must be considered when evaluating clearance efficiency for humans and mice for identical fungal burden of the whole lung. We could demonstrate that the human and murine model can clear the infection in more than 95% of all simulations given optimal parameters of chemokine signaling and a uniform distribution of conidia in the lung up to a fungal burden of 10^5 conidia. For higher fungal burden, as applied in the experimental murine model, the clearance efficiency in mice quickly declines, whereas we only see a slight decrease of efficiency in the human model. These differences in the dependence on fungal burden can be explained by inspecting the respective situation in the alveolus. For a fungal burden of $3 \cdot 10^5$, we consider a maximum of two conidia per alveolus in the human but four conidia in the murine alveolus. However, since in the murine alveolus four AEC of type I cover 95% of the surface, it becomes likely that all of these cells are associated with a conidium and thus simultaneously induce chemokine secretion. Consequently, almost the whole surface is covered by signaling type I AEC, triggering AM to migrate in each direction with a similar probability, resulting in a random walk and a loss of efficiency. This imposes a natural limit of efficient conidia detection in the murine alveolus but not in humans under the mentioned administration dosages.

Although the high fungal burden where this loss of efficiency occurs does not cover the stated range of fungal burden in mice models, it becomes relevant when assuming a heterogeneous conidia distribution and local accumulation of conidia, as shown by Steinbach *et al.* for the intranasal administration [122]. We

therefore conclude that the successful manifestation of *A. fumigatus* infections in the murine experimental model relies on a locally high number of conidia which cannot be cleared simultaneously rather than an inefficient clearance in the whole lung, supporting the air-soluted murine with a homogeneous distribution model as the more realistic infection model.

7.1.3 Pores of Kohn influence infection dynamics

Alveoli of the mammalian lung are interconnected by Pores of Kohn (PoK). These small connections between neighboring alveoli with a diameter of roughly $4\ \mu\text{m}$ were first described more than a century ago [128, 129]. Although a regulatory role within the cellular immune response was long postulated for PoK, their impact on infection dynamics is not understood [130]. Although early microscopy of PoK suggested passaging of immune cells, it took until 2020 for Neupane *et al.* to image AM migrating through PoK *in vivo* [131, 132]. Regardless, PoK are known to open and close during respiration, possibly contributing to collateral ventilation and an altered number of PoK is associated with a higher risk of atelectasis or emphysema [114, 133, 134]. This raised the question of how these two functions of ventilation and immune cell passaging can be joined. How can PoK frequently open and close while AM passage through them and how would this effect infection dynamics? To quantitatively assess this problem, the hybrid agent-based alveolus model was extended to simulate three different theories of AM passaging through PoK. A first model (POK+/+) allows for AM and chemokine to enter and exit the model through PoK. The second model (POK+/-) allows only for chemokine in/out flow. In the third model (POK-/-), PoK do not allow passaging of cells nor molecules.

PoK as passageways for AM would allow these to enter the alveolus through many positions instead of only through the alveolar entrance ring. This eases the scanning of the complete alveolar surface by AM and a faster infection clearance can be expected. Our simulations revealed that differences exist in the clearance efficiency of infections between the three PoK models. However, this effect is small and an efficient phagocytosis of conidia is possible without PoK passaging.

The simulations showed that the spatial distribution of AM is altered depending on the passaging through PoK. Where an entry to the alveolus is only possible at the alveolar entrance ring, like in the POK-/- model, AM tend to accumulate in proximity to the entrance ring due to the spatial dead-end constitution of the alveolus. In such a model, the alteration of model boundaries changes the spatial equilibrium of AM compared to the POK+/+ model. Conse-

quently, conidia at the alveolar pole, the spot most distanced from the entrance ring, are detected with a lower probability in the POK^{-/-} model. In our simulations, we assumed a spatially uniform distribution of the conidia. Nonetheless, if conidia tend to arrive in the alveolus with a spatial bias *e.g.* towards the alveolar entrance ring, as suggested by the particle deposition model of Xi and Talaat [135], the POK^{-/-} model might clear an infection faster and thus outperform the POK^{+/+} model.

Attraction of AM towards the site of infection typically causes a local accumulation of AM. This effect is increased in the POK^{+/-} model due to a stronger chemokine gradient, which is not distorted by outflow through PoK and even larger in the POK^{-/-} model due to the dead end constitution of the alveolus. Such an accumulation of AM increases their overall number within an alveolus up to a factor of 10. For the lung, an organ that is constantly exposed to pathogens and a homogeneous AM distribution is beneficial for efficient infection clearance and an accumulation may impose an unnecessary threat. Similar to the accumulation of AM, an accumulation of chemokines could be observed due to the impaired outflow through PoK in the POK^{-/-} model. This effect supersedes the chemokine secretion, and thus shifts the optimal parameters of chemokine secretion.

We conclude that a passing of AM through PoK would only influence *A. fumigatus* infections to a minor extent but imposes positive alterations on the cellular and molecular dynamics in the alveolus as a homogeneous spatial AM distribution. The remaining question is how such a mechanism can be reconciled with the theory of a regulation of collateral ventilation by PoK as argued by Namati *et al.* [114]. With a typical respiration frequency of 12 – 18 min^{-1} , AM migration would be frequently interrupted as AM would need around one minute to pass only a few micrometers considering a speed of 4 $\mu\text{m min}^{-1}$ [136, 137]. Akei *et al.* showed that the surface tension of the alveolus influences AM's shape [138]. Therefore, it seems possible that AM migrate through a PoK by flexible changes of their shape, despite frequent openings. Oldham and Moss brought up the idea that the surfactant covering the alveolar surface might burst during the opening of PoK [113]. In such a case, an AM within the surfactant might be accelerated through the PoK. This would allow for a new perspective on cellular migration in the alveolus.

7.1.4 Hyphal growth is affected by macrophage presence

The limited accessibility of alveolar tissue *in vivo* impedes research on *A. fumigatus* infections. Nevertheless, emerging microfluidic alveolus-on-chip devices

promise a new source for insights as they enable investigating alveolar tissues under more realistic settings that could not be studied before [139–141]. Such a device contains a centric porous membrane, which was equipped with alveolar epithelial cells (H441) on one “lung side” and a perfused “blood side” made of HUVECs to create an invasive aspergillosis-on-chip [142, 143]. This allows running confrontation assays with *A. fumigatus* conidia and macrophages (CD68+) to mimic a more realistic infection environment. Infection dynamics were investigated by live-cell confocal laser scanning microscopy, which allowed capturing spatial dynamics such as the hyphal growth. The images showed that *A. fumigatus* hyphae, similar to the invasive growth in alveoli, are able to penetrate the chip membrane’s pores but can also grow alongside the cell layer without destruction of epithelium. This raises the question of how these modes of growth can be distinguished, considering that the invasive growth of hyphae is crucial for *A. fumigatus* pathogenicity.

As the image data allows for a quantification of the hyphal growth, the confinement ratio, a method originating from cell track analysis, was applied, allowing to localize and distinguish regions of straight hyphal growth [144]. The results show that invasive hyphae do not attach to the membrane before pore penetration but rather change direction within the epithelial cell layer before migrating fairly straight into the pore. This behavior could be observed with higher frequency when macrophages were present within the aspergillosis-on-chip device. This suggests that the hyphal growth may be influenced by a signal. However, the nature of such a signal is not easy to determine as many potential molecules are present and tests for nutrients as glucose or lactate gradients did not explain the observed growth. Similarly, aspergillosis-on-chip devices with macrophages showed a higher number of pore-penetrating hyphae, suggesting that such growth may be an evasion mechanism against macrophages as similarly described in the presence of PMN [145]. Tissue invasion is an important mechanism for *A. fumigatus* virulence. Therefore, the use of invasive aspergillosis-on-chip devices represents an ideal environment for understanding hyphal growth, representing a valuable extension of the tool box against invasive aspergillosis.

The applied growth analysis is exemplary for a common strategy in systems biology: quantification. The transfer of a complex process as hyphal growth into a numerical representation of *e.g.* a matrix allows for a clear and non-subjective perspective on a problem. Moreover, distinct hyphae can be quantitatively compared by numbers and reveal differences or similarities. The search of such quantitative descriptors is a frequent problem in systems biology.

7.1.5 Dynamic SPHARM captures cell migration dynamics

Efficient migration of immune cells is important for host defense. For some immune cell types such as PMN or T cells, such migration is predominantly achieved by fluid changes of the cellular shape. In this amoeboid movement shape changes are caused by surface protrusions, leading to a shift of the center of mass and ultimately locomotion [146]. For a quantitative understanding of such a migration process, descriptors are needed that efficiently reflect and distinguish shape changes of different cells or different experimental environments [147]. The better that such descriptors can indicate differences in amoeboid motion, the better that they can be used to study intrinsic processes driving migration as well as the effects caused by migration. In the same way, cellular migration can be included into models with more realism, the higher the distinctive power of such descriptors. Two difficulties arise when constructing such descriptors. First, random alterations of the shape must be distinguished from those relevant for migration. Second, the frequent changes of shape only allow for a comprehensive assessment under a time-resolved and dynamic perspective.

In our study, we used dynamic spherical harmonics (SPHARM) as a descriptor of shape changes during cellular migration. SPHARM bases upon Fourier analysis and describes the surface of an object by a set of orthogonal spherical functions $F(l, m)$ of order l and degree m . It can be applied in two and three dimensions and has been shown to be a promising shape descriptor for cellular migration [148]. In our proof-of-principle study, we extend the static SPHARM analysis of one cell at a given time point to a dynamic analysis by computing SPHARM for consecutive time series of one cell. To test the descriptive power of dynamic SPHARM, we used 3D images of murine T cells migrating in the popliteal lymph node, the salivary gland and the skin as well as synthetic cells generated from an agent-based migration model. T cell surface data was acquired by two-photon microscopy with a time resolution of 20 to 60 s per image over one hour. The synthetic cells were generated with an adaption of a previously-developed agent-based migration model [149]. In this model, the synthetic 3D cell body is considered as a set of thousands of small cubic sub-units. Migration of the cell is realized by repetitive random movement of single sub-units from the cell rear to the cell front. The shape of the migrating cell can be controlled by parameters assigning different probabilities of sub-unit movement depending on its relation to the migration axis, the local surface environment and distance to the center of cell. Such a model allows generating many migrating cells with nearly arbitrary spatial and temporal resolution compared to the cost-intensive imaging of cells originating from wet lab experiments, thus representing a valuable extension of the data basis to test SPHARM.

Each cell was described by a rotation-invariant feature vector V of size $l_{max} \cdot T$ reflecting the time and shape domain, where T denotes the observed time points $t_1 \dots t_T$ and l_{max} the maximal order of the spherical basis function used. Each entry $V_{t,l}$ denotes the summed-up power over each degree m of order l at time point t . We trained a support vector machine to classify the cells depending on their cellular origin based on this feature vector. The results show that the accuracy of the dynamic SPHARM feature vector classifier outperforms a naive control classifier. This holds true not only for classification of T cells from different tissues but also for classification of synthetic cells generated by the agent-based model with different migration parameters. We could also show that the dynamic SPHARM classifier outperforms a classifier based on static cell shapes and that the dynamic 3D SPHARM classifier outperforms a SPHARM classifier based on multiple 2D projections of the cell shape of different angles.

Our workflow demonstrates how powerful models in systems biology can support research. The migration model used allows for inexpensive generation of data to test and evaluate methods under fast and controlled conditions. Furthermore, the migration model can be used in the future for *in silico* modeling of cell migration observed in wet lab experiments. This can be achieved by altering the migration model parameters so that their dynamic SPHARM feature vector fits those of the observed cells.

7.2 OPEN ISSUES, PERSPECTIVES AND FUTURE WORK

Research is an evolving process, that must constantly depict a far-sighted vision of the next steps. In the following, I want to raise a perspective on how the research presented in this thesis can be further developed and which next steps might help in answering open questions regarding the understanding of *A. fumigatus* infections. According to the presented cycle of systems biology, two general routes are available (see Figure 7.1). The first goes back to the wet lab and aims for validation as new experimental results may either allow critically revising the hypotheses raised in the presented publications or narrowing down the uncertainty in hitherto undetermined, and thus scanned, parameters. The second route integrates knowledge originating from either published or newly-performed experiments to achieve an extension of the hybrid alveolus model to allow for a more generalized perspective of the model or a higher degree of detail. Synergies are created when route one allows for a reduction of the parameter scanning space and thus simulation effort to allow for computation-intensive refinement of model detail of route two.

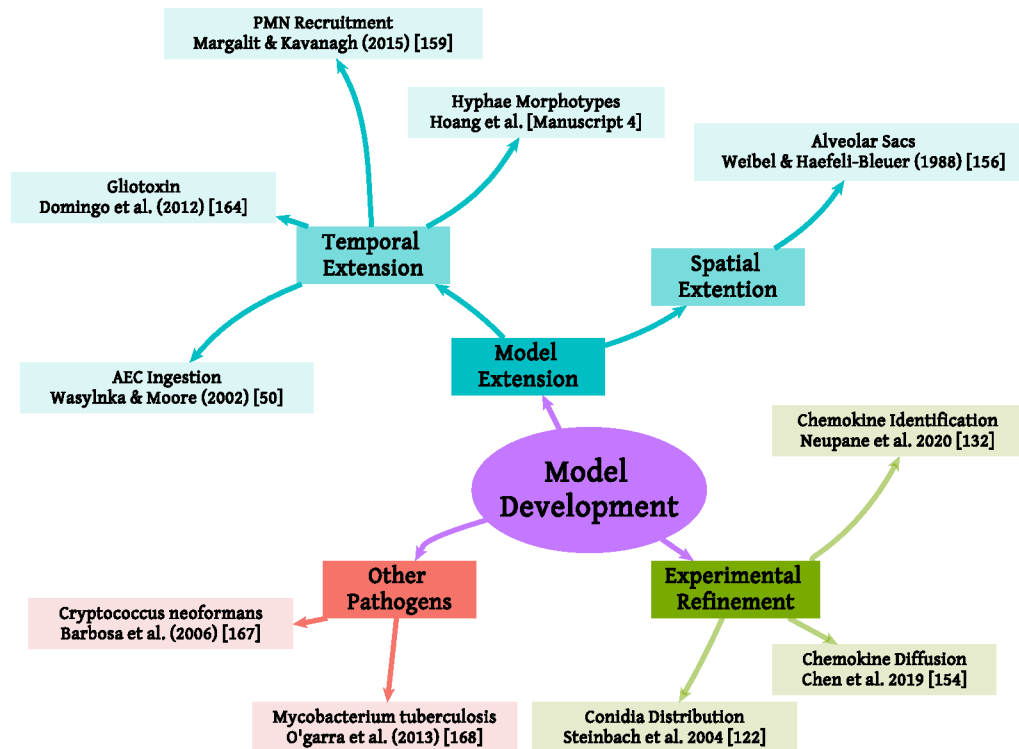


Figure 7.1: Model Development. The cycle of systems biology offers two routes for future development of the hybrid agent-based alveolus model. The first route (green) aims for wet lab experiments allowing to reduce parameter uncertainties. The second route (blue) stays in the dry lab and tries to enhance the model detail by including new dynamics or mechanisms. The third route (red) shows a possible application to other pathogens than *A. fumigatus*.

7.2.1 Perspectives on experimental validation

The most critical uncertainty in the mechanisms of the hybrid alveolus model may be the chemokine signaling. This mechanism was predicted by Pollmächer *et al.* after the observation that a random walk migration of AM would lack an efficient conidia detection [116]. In the following, the hybrid alveolus model was extended by a postulated chemokine, which guides AM towards the conidium, allowing for an efficient conidia detection [117]. However, the molecular identity of the chemokine is unknown including the secretion rate and the diffusion coefficient. Thus, simulations of the hybrid alveolus model must scan these parameters over a range of biologically reasonable values. This increases not only the simulation effort but also the complexity of the analysis of the simulation result. Although a set of chemokines *e.g.* IL-6 is known to be induced by the epithelial A_{549} cell line upon contact with *A. fumigatus*, a proper candidate has not been identified [150, 151]. For Example, IL-6 is produced by AM itself, limiting its efficiency to attract AM towards the conidium [152].

Of note, the recent publication of Neupane *et al.* might help to identify the chemokine mechanism [132]. In their study, they achieve *in vivo* imaging of alveolar dynamics in mice by spinning-disk confocal intravital microscopy. Although focusing on bacterial pathogens, they observe randomly migrating AM as well as directed migration towards the pathogen, which is in accordance with the signaling mechanism in the hybrid alveolus model. Moreover, they showed a dependency on the complement activation pathways, as C3 knock-out mice show an impaired directed migration of AM. By blocking of C5a-mediated chemotaxis, the bacterial clearance was limited, leading to the conclusion "...that AMs utilise rapidly generated C5a...". Thus, activation of the complement system, as induced by *A. fumigatus* [153], could cause rapid production of the C5a chemokine, making it a promising candidate for AM attraction. Its diffusion coefficient could be calculated by the Stokes-Einstein equation given the molecular radius of C5a and the lung surfactant layer viscosity. The latter has been investigated in various studies but the stated numbers remain in the range of multiple magnitudes which leaves a high uncertainty [154]. Additionally, these studies often relied on patients with pulmonary disease and the non-Newtonian nature of the surfactant layer may require investigations under realistic mechanical stress. Consequently, the diffusion coefficient of C5a in the alveolus remains uncertain.

It is worth noting that the publication of Neupane *et al.* supports important aspects of our model design as the important role of AM clearance in the early infection phase. They are the first to show passaging of AM through PoK *in vivo* and agreed with our hypothesis of a positive effect for spatial AM distribution of such passaging.

Regarding the study of murine *A. fumigatus* infection in the first manuscript [155], an assessment of the true spatial conidia distribution in the experimental murine lung would allow for a more detailed perspective. The first manuscript of this thesis concludes that the murine infection model relies on a locally high number of conidia which can not be cleared efficiently by AM due to a heterogeneous distribution of conidia after intranasal deposition. Although such a heterogeneous distribution of conidia in the murine lung has been demonstrated by Steinbach *et al.* [122], a quantification of the real distribution would allow determining the local increase of alveolar fungal burden compared to the uniform distribution, which was assumed in the hybrid alveolus model. Ultimately, this perspective would also hold value for human inhalation. Studies on the particle deposition in the alveoli demonstrate that the complex dynamics of air flow in the respiratory tract do not guarantee a uniform distribution of conidia on the alveolar surface [135]. Thus, significant alterations to the assumed uniform distribution seem possible also in humans.

7.2.2 Perspectives on model developments

The hybrid agent-based alveolus model used for the presented research comprises the most relevant actors in early *A. fumigatus* infections. However, it can be further developed by either increasing the level of detail applied or extending the spatial or temporal dimension. Both ways will allow for new *in silico* experiments but will also increase computational needs. Thus, promising ideas of model development should be attempted with care. In the following, these ideas are discussed regarding their relevance and the availability of data.

A spatial extension of the alveolus model would allow for more comprehensive studies of *A. fumigatus* infections, but it would also increase the computational needs and induce a redefinition of the boundary dynamics. The logical next organizational unit is the alveolar sac, which comprises on average 20 alveoli, interconnected by a shared alveolar duct leading to the bronchioles [156]. Such an alveolar sac could be simulated by a parallel simulation of 20 instances of the hybrid agent-based alveolus model extended by a management of cells and molecules shifting from one alveolus to another. This would allow investigating *e.g.* cellular dynamics such as the accumulation of AM or the impact of boundary conditions for model dynamics as found in the PoK study of the second manuscript [157]. Despite a small implementation effort and a broader perspective on cellular dynamics, this strategy leaves focus from the conidium towards distant alveoli, which may not influence infection dynamics eminently. However, it would allow studying the clearance of multiple distributed conidia. Considering a typical daily inhalation rate of a few thousand conidia, it

is unlikely to have one single alveolus with two present conidia in the whole lung ($p = 0.04$). When extending the model to an alveolar sac, it becomes likely ($p = 0.58$) that two conidia are present in such a sac. This would allow studying how AM have to detect and phagocytose two conidia in a complex spatial environment of a sac.

The hybrid agent-based alveolus model includes the first 6 hr of infection onset between inhalation of the conidium and the starting development of invasive hyphae. As the arms race between host and fungus is yet not decided at this time point, a temporal extension of the hybrid agent-based alveolus model would hold strong benefit. For this purpose, the passive role of the conidium must switch to an active role including swelling, development of hyphae or even tissue penetration and dissemination. Thus, depending on the applied level of detail, parameters for swelling, growth speed or direction and branching must be determined or scanned. The third manuscript on aspergillosis-on-chip devices [158] would serve as an ideal starting point to assess these parameters.

Increasing the temporal space of the hybrid agent-based alveolus model beyond the first six hours would allow including PMN or dendritic cells, which are recruited to the site of infection [159, 160]. For such an extension of the model, it has to be defined where, when and how many PMN arrive within the alveolus and how their migration is modeled. One difference to the fairly shape-preserving AM is that the amoeboid movement of PMN involves frequent shape alterations. This could be integrated by applying the migration model presented in the fourth manuscript [161]. Another question that similarly can be asked for AM is how phagocytosis of a conidium by PMN is modeled. The hybrid agent-based alveolus model finishes simulation when a contact between the macrophage and the conidium is established and assumes a successful phagocytosis within time. Although this is probable, phagocytosis may fail at all or require multiple contacts and depends on the conidial surface, which changes during morphological development of *A. fumigatus*. Thus, including a detailed phagocytosis model would allow for new insights into the infection dynamics.

Another mechanism of relevance during the infection is the impact of gliotoxin. This molecule is a known virulence factor of *A. fumigatus* and secreted by conidia during the infection [162, 163]. It may cause apoptosis of AEC and therefore might severely alter infection dynamics [164]. Consequently, gliotoxin might impair AEC chemokine secretion or maintenance of lung surfactant, both with unknown effects on the fungal clearance. Similarly, in 1986 Eichner *et al.* already showed that gliotoxin alters adhesion, metabolism and phagocytic activity of macrophages, again with unknown effects on the fungal clearance [165]. Although the exact role of gliotoxin has not yet been deciphered and exact pa-

rameters like its secretion rate are not available, its effects could be studied by *e.g.* including a time-dependent impairment of AEC secretion or AM phagocytosis.

Another mechanism worth discussing is the ingestion of conidia by AEC, as has been shown *in vitro* [166]. Up to 30% of present conidia are internalized by AEC [50]. This process might serve as an immune evasion mechanism by the fungus given that most, but not all, conidia are trafficked to the phagolysosome but the remaining manage to germinate [48, 49]. It would be interesting to investigate how infection clearance would be affected by this process. The model could be easily extended in such a way, as conidia are taken up in a time-dependent rate, and combined with the gliotoxin mechanism, revealing interesting dynamics.

Besides applications of the hybrid agent-based alveolus model to *A. fumigatus* infections, it is possible to adapt the model and investigate infections of different pathogens. The opportunistic fungus *Cryptococcus neoformans*, similarly to *A. fumigatus*, may be inhaled into the alveoli, infect immunosuppressed patients, disseminate and cause a fungal meningoencephalitis [167]. Another possible application is tuberculosis, caused by *Mycobacterium tuberculosis*. Although a bacterial infection, a successful manifestation may occur after inhalation into the alveoli and is tackled by phagocytosing cells as AM and PMN, similar to *A. fumigatus* infections [168].

BIBLIOGRAPHY

- [1] Corentin C. Loron, Camille François, Robert H. Rainbird, Elizabeth C. Turner, Stephan Borensztajn, and Emmanuelle J. Javaux. “Early fungi from the Proterozoic era in Arctic Canada.” In: *Nature* 570 (2019), pp. 232–235. DOI: [10.1038/s41586-019-1217-0](https://doi.org/10.1038/s41586-019-1217-0) (cit. on p. 5).
- [2] Jan De Vries, Bruce A. Curtis, Sven B. Gould, and John M. Archibald. “Embryophyte stress signaling evolved in the algal progenitors of land plants.” In: *Proceedings of the National Academy of Sciences of the United States of America* 115.15 (2018), E3471–E3480. DOI: [10.1073/pnas.1719230115](https://doi.org/10.1073/pnas.1719230115) (cit. on p. 5).
- [3] Philippe Janvier and Gaël Clément. “Muddy tetrapod origins.” In: *Nature* 463 (2010), pp. 40–41. DOI: [10.1038/463040a](https://doi.org/10.1038/463040a) (cit. on p. 5).
- [4] David L. Hawksworth. “The magnitude of fungal diversity: The 1.5 million species estimate revisited.” In: *Mycological Research* 105.12 (2001), pp. 1422–1432. DOI: [10.1017/S0953756201004725](https://doi.org/10.1017/S0953756201004725) (cit. on p. 5).
- [5] David L. Hawksworth and Robert Lücking. “Fungal Diversity Revisited: 2.2 to 3.8 Million Species.” In: *The Fungal Kingdom*. Ed. by Heitman J, Howlett B, P Crous, E Stukenbrock, T James, and N Gow. Washington, DC: ASM Press, 2017, pp. 79–95. DOI: [10.1128/microbiolspec.funk-0052-2016](https://doi.org/10.1128/microbiolspec.funk-0052-2016) (cit. on p. 5).
- [6] Christopher W. Schadt, Andrew P. Martin, David A. Lipson, and Steven K. Schmidt. “Seasonal dynamics of previously unknown fungal lineages in tundra soils.” In: *Science* 301.5638 (2003), pp. 1359–1361. DOI: [10.1126/science.1086940](https://doi.org/10.1126/science.1086940) (cit. on p. 5).
- [7] Lucie A. Malard and David A. Pearce. “Microbial diversity and biogeography in Arctic soils.” In: *Environmental Microbiology Reports* 10 (2018), pp. 611–625. DOI: [10.1111/1758-2229.12680](https://doi.org/10.1111/1758-2229.12680) (cit. on p. 5).
- [8] Manuela Murgia et al. “Biodiversity of fungi in hot desert sands.” In: *MicrobiologyOpen* 8 (2019), e595. DOI: [10.1002/mbo3.595](https://doi.org/10.1002/mbo3.595) (cit. on p. 5).
- [9] Heather E. Hallen-Adams and Mallory J. Suhr. “Fungi in the healthy human gastrointestinal tract.” In: *Virulence* 8.3 (2017), pp. 352–358. DOI: [10.1080/21505594.2016.1247140](https://doi.org/10.1080/21505594.2016.1247140) (cit. on p. 5).
- [10] Felix Bongomin, Sara Gago, Rita O. Oladele, and David W. Denning. “Global and multi-national prevalence of fungal diseases—estimate precision.” In: *Journal of Fungi* 3.4 (2017), p. 57. DOI: [10.3390/jof3040057](https://doi.org/10.3390/jof3040057) (cit. on p. 5).
- [11] R. A. Samson et al. “Phylogeny, identification and nomenclature of the genus *Aspergillus*.” In: *Studies in Mycology* 78 (2014), pp. 141–173. DOI: [10.1016/j.simyco.2014.07.004](https://doi.org/10.1016/j.simyco.2014.07.004) (cit. on p. 5).

- [12] Georg Fresenius. *Beiträge zur mykologie*. Frankfurt am Main: Bröner, 1863 (cit. on p. 5).
- [13] S Horne, P.D. & Redford. "Aspergillois and dracunculiasis in mummies from the Tomb of Parennefer." In: *Palaeopathology Newsletter* 92 (1995), pp. 10–12 (cit. on p. 5).
- [14] John Dighton and J.F. White. *The Fungal Community*. 4th. Boca Raton, FL, USA: CRC Press, 2005. DOI: [10.1201/9781420027891](https://doi.org/10.1201/9781420027891) (cit. on p. 5).
- [15] P. D. Millner, P. B. Marsh, R. B. Snowden, and J. F. Parr. "Occurrence of *Aspergillus fumigatus* during composting of sewage sludge." In: *Applied and Environmental Microbiology* 34.6 (1977), pp. 765–772. DOI: [10.1128/aem.34.6.765-772.1977](https://doi.org/10.1128/aem.34.6.765-772.1977) (cit. on p. 5).
- [16] R. A. Samson, J. Varga, and Paul. S. Dyer. "Morphology and Reproductive Mode of *Aspergillus fumigatus*." In: *Aspergillus fumigatus and Aspergillois*. Ed. by William J. Steinbach and Jean-Paul Latgé. 1st. Washington, DC: ASM Press, 2009. Chap. 2, p. 7 (cit. on p. 6).
- [17] Alexandra Brand. "Hyphal growth in human fungal pathogens and its role in virulence." In: *International Journal of Microbiology* 2012 (2012), pp. 517–529. DOI: [10.1155/2012/517529](https://doi.org/10.1155/2012/517529) (cit. on p. 6).
- [18] Richard L. Kradin and Eugene J. Mark. "The pathology of pulmonary disorders due to *Aspergillus* spp." In: *Archives of Pathology and Laboratory Medicine* 132.14 (2008), pp. 606–614. DOI: [10.1043/1543-2165\(2008\)132\[606:TPODD\]2.0.CO;2](https://doi.org/10.1043/1543-2165(2008)132[606:TPODD]2.0.CO;2) (cit. on p. 6).
- [19] Kyung J Kwon-Chung and Janyce A Sugui. "Aspergillus fumigatus - what makes the species a ubiquitous human fungal pathogen?" In: *PLoS pathogens* 9.12 (2013), e1003743. DOI: [10.1371/journal.ppat.1003743](https://doi.org/10.1371/journal.ppat.1003743) (cit. on p. 7).
- [20] M. Kousha, R. Tadi, and A. O. Soubani. "Pulmonary aspergillois: A clinical review." In: *European Respiratory Review* 20 (2011), pp. 156–174. DOI: [10.1183/09059180.00001011](https://doi.org/10.1183/09059180.00001011) (cit. on p. 6).
- [21] R. Codina, Roger W. Fox, R. F. Lockey, P. DeMarco, and A. Bagg. "Typical levels of airborne fungal spores in houses without obvious moisture problems during a rainy season in Florida, USA." In: *Journal of Investigational Allergology and Clinical Immunology* 18.3 (2008), pp. 156–162 (cit. on pp. 6, 95).
- [22] Gayatri Patel and Paul A. Greenberger. "Allergic bronchopulmonary aspergillois." In: *Allergy and Asthma Proceedings* 40.6 (2019), 421–424(4). DOI: [10.2500/aap.2019.40.4262](https://doi.org/10.2500/aap.2019.40.4262) (cit. on p. 6).
- [23] Paul A. Greenberger. "Allergic bronchopulmonary aspergillois." In: *Journal of Allergy and Clinical Immunology* 110.5 (2002), pp. 685–692. DOI: [10.1067/mai.2002.130179](https://doi.org/10.1067/mai.2002.130179) (cit. on p. 6).

- [24] David W. Denning, Alex Pleuvry, and Donald C. Cole. "Global burden of allergic bronchopulmonary aspergillosis with asthma and its complication chronic pulmonary aspergillosis in adults." In: *Medical Mycology* 3.4 (2013), p. 57. DOI: [10.3109/13693786.2012.738312](https://doi.org/10.3109/13693786.2012.738312) (cit. on p. 6).
- [25] Chandramani Panjabi and Ashok Shah. "Allergic Aspergillus sinusitis and its association with allergic bronchopulmonary aspergillosis." In: *Asia Pacific Allergy* 1.3 (2011), pp. 130–137. DOI: [10.5415/apallergy.2011.1.3.130](https://doi.org/10.5415/apallergy.2011.1.3.130) (cit. on p. 6).
- [26] David W. Denning, Jacques Cadranel, Catherine Beigelman-Aubry, Florence Ader, Arunaloke Chakrabarti, Stijn Blot, Andrew J. Ullmann, George Dimopoulos, and Christoph Lange. "Chronic pulmonary aspergillosis: Rationale and clinical guidelines for diagnosis and management." In: *European Respiratory Journal* 47 (2016), pp. 45–68. DOI: [10.1183/13993003.00583-2015](https://doi.org/10.1183/13993003.00583-2015) (cit. on p. 7).
- [27] Ashutossh Naaraayan, Ronak Kavian, Jeffrey Lederman, Prasanta Basak, and Stephen Jesmajian. "Invasive pulmonary aspergillosis – case report and review of literature." In: *Journal of Community Hospital Internal Medicine Perspectives* 5.1 (2015). DOI: [10.3402/jchimp.v5.26322](https://doi.org/10.3402/jchimp.v5.26322) (cit. on p. 7).
- [28] Arthur T Henrici. "An Endotoxin from *Aspergillus Fumigatus*." In: *The Journal of Immunology* 36.4 (1939), pp. 319–338. URL: <https://www.jimmunol.org/content/36/4/319> (cit. on p. 7).
- [29] A. H. Groll, P. M. Shah, C. Mentzel, M. Schneider, G. Just-Nuebling, and K. Huebner. "Trends in the postmortem epidemiology of invasive fungal infections at a University Hospital." In: *Journal of Infection* 33.1 (1996), pp. 23–32. DOI: [10.1016/S0163-4453\(96\)92700-0](https://doi.org/10.1016/S0163-4453(96)92700-0) (cit. on p. 7).
- [30] Erik J. Dasbach, Glenn M. Davies, and Steven M. Teutsch. "Burden of Aspergillosis-Related Hospitalizations in the United States." In: *Clinical Infectious Diseases* 31.6 (2000), pp. 1524–1528. DOI: [10.1086/317487](https://doi.org/10.1086/317487) (cit. on p. 8).
- [31] Kaitlin Benedict, Brendan R. Jackson, Tom Chiller, and Karlyn D. Beer. "Estimation of Direct Healthcare Costs of Fungal Diseases in the United States." In: *Clinical Infectious Diseases* 68.11 (2019), pp. 1791–1797. DOI: [10.1093/cid/ciy776](https://doi.org/10.1093/cid/ciy776) (cit. on p. 8).
- [32] S.-J. Lin, J. Schranz, and S. M. Teutsch. "Aspergillosis Case-Fatality Rate: Systematic Review of the Literature." In: *Clinical Infectious Diseases* 32.3 (2001), pp. 358–366. DOI: [10.1086/318483](https://doi.org/10.1086/318483) (cit. on pp. 8, 93).
- [33] Taylor R T Dagenais and Nancy P Keller. "Pathogenesis of *Aspergillus fumigatus* in Invasive Aspergillosis." In: *Clinical microbiology reviews* 22.3 (2009), pp. 447–65. DOI: [10.1128/CMR.00055-08](https://doi.org/10.1128/CMR.00055-08). (cit. on p. 8).
- [34] Thorsten Heinekamp, Hella Schmidt, Katrin Lapp, Vera Pähtz, Iordana Shopova, Nora Köster-Eiserfunke, Thomas Krüger, Olaf Kniemeyer, and Axel A. Brakhage. "Interference of *Aspergillus fumigatus* with the immune response." In: *Seminars in Immunopathology* 37 (2015), pp. 141–152. DOI: [10.1007/s00281-014-0465-1](https://doi.org/10.1007/s00281-014-0465-1) (cit. on p. 8).

- [35] Axel A. Brakhage, Sandra Bruns, Andreas Thywissen, Peter F. Zipfel, and Judith Behnsen. "Interaction of phagocytes with filamentous fungi." In: *Current Opinion in Microbiology* 13.4 (2010), pp. 409–415. DOI: [10.1016/j.mib.2010.04.009](https://doi.org/10.1016/j.mib.2010.04.009) (cit. on p. 8).
- [36] C Gernez-Rieux, C Voisin, C Aerts, F Wattel, and B Gosselin. "Experimental aspergillosis in the guinea pig. Dynamic study of the role of alveolar macrophages in the defense of the respiratory tract, after massive inhalation of *Aspergillus fumigatus* spores." In: *Revue de tuberculose et de pneumologie* 31.6 (1967), pp. 705–725 (cit. on p. 9).
- [37] Kathrin Luther, Antonella Torosantucci, Axel A. Brakhage, Jürgen Heesemann, and Frank Ebel. "Phagocytosis of *Aspergillus fumigatus* conidia by murine macrophages involves recognition by the dectin-1 beta-glucan receptor and Toll-like receptor 2." In: *Cellular Microbiology* 9.2 (2007), pp. 368–381. DOI: [10.1111/j.1462-5822.2006.00796.x](https://doi.org/10.1111/j.1462-5822.2006.00796.x) (cit. on p. 9).
- [38] Cecilia Garianda et al. "Non-redundant role of the long pentraxin PTX3 in anti-fungal innate immune response." In: *Nature* 420 (2002), pp. 182–186. DOI: [10.1038/nature01195](https://doi.org/10.1038/nature01195) (cit. on p. 9).
- [39] Fabrice N. Gravelat et al. "*Aspergillus* Galactosaminogalactan Mediates Adherence to Host Constituents and Conceals Hyphal β -Glucan from the Immune System." In: *PLoS Pathogens* 9.8 (2013), e1003575. DOI: [10.1371/journal.ppat.1003575](https://doi.org/10.1371/journal.ppat.1003575) (cit. on p. 9).
- [40] Christine Henry, Jean Paul Latgé, and Anne Beauvais. " α _{1,3} glucans are dispensable in *Aspergillus fumigatus*." In: *Eukaryotic Cell* 11.1 (2012), pp. 26–29. DOI: [10.1128/EC.05270-11](https://doi.org/10.1128/EC.05270-11) (cit. on p. 9).
- [41] Tobias M. Hohl, Heather L. Van Epps, Amariliz Rivera, Laura A. Morgan, Patrick L. Chen, Marta Feldmesser, and Eric G. Pamer. "*Aspergillus fumigatus* triggers inflammatory responses by stage-specific β -glucan display." In: *PLoS Pathogens* 1.3 (2005), e30. DOI: [10.1371/journal.ppat.0010030](https://doi.org/10.1371/journal.ppat.0010030) (cit. on p. 9).
- [42] Karoll J. Cortez, Caron A. Lyman, Shyam Kottlil, Hee Sup Kim, Emmanuel Roilides, Jun Yang, Brandie Fullmer, Richard Lempicki, and Thomas J. Walsh. "Functional genomics of innate host defense molecules in normal human monocytes in response to *Aspergillus fumigatus*." In: *Infection and Immunity* 74.4 (2006), pp. 2353–2365. DOI: [10.1128/IAI.74.4.2353-2365.2006](https://doi.org/10.1128/IAI.74.4.2353-2365.2006) (cit. on p. 9).
- [43] Scott D. Kobayashi, Jovanka M. Voyich, Christopher Burlak, and Frank R. DeLeo. "Neutrophils in the innate immune response." In: *Archivum Immunologiae et Therapiae Experimentalis* 53.6 (2005), pp. 505–517 (cit. on p. 9).
- [44] David C. Dale, Laurence Boxer, and W. Conrad Liles. "The phagocytes: Neutrophils and monocytes." In: *Blood* 112.4 (2008), pp. 935–945. DOI: [10.1182/blood-2007-12-077917](https://doi.org/10.1182/blood-2007-12-077917) (cit. on p. 9).

- [45] Anh N. Hoang, Caroline N. Jones, Laurie Dimisko, Bashar Hamza, Josef Martel, Nikola Kojic, and Daniel Irimia. "Measuring neutrophil speed and directionality during chemotaxis, directly from a droplet of whole blood." In: *Technology* 1.1 (2013), pp. 49–57. DOI: [10.1142/S2339547813500040](https://doi.org/10.1142/S2339547813500040) (cit. on p. 9).
- [46] John A. Smith. "Neutrophils, host defense, and inflammation: a double-edged sword." In: *Journal of Leukocyte Biology* 56.6 (1994), pp. 672–686. DOI: [10.1002/jlb.56.6.672](https://doi.org/10.1002/jlb.56.6.672) (cit. on p. 9).
- [47] Sandra Bruns, Olaf Knemeyer, Mike Hasenberg, Vishukumar Aimanianda, Sandor Nietzsche, Andreas Thywien, Andreas Jeron, Jean Paul Latgé, Axel A. Brakhage, and Matthias Gunzer. "Production of extracellular traps against *Aspergillus fumigatus* in vitro and in infected lung tissue is dependent on invading neutrophils and influenced by hydrophobin rods." In: *PLoS Pathogens* 6.4 (2010), e1000873. DOI: [10.1371/journal.ppat.1000873](https://doi.org/10.1371/journal.ppat.1000873) (cit. on p. 9).
- [48] Carys A. Croft, Luka Culibrk, Margo M. Moore, and Scott J. Tebbutt. "Interactions of *Aspergillus fumigatus* Conidia with Airway Epithelial Cells: A Critical Review." In: *Frontiers in Microbiology* 7.472 (2016). DOI: [10.3389/fmicb.2016.00472](https://doi.org/10.3389/fmicb.2016.00472) (cit. on pp. 9, 105).
- [49] Julie A. Wasylnka and Margo M. Moore. "*Aspergillus fumigatus* conidia survive and germinate in acidic organelles of A549 epithelial cells." In: *Journal of Cell Science* 116.8 (2003), pp. 1579–1587. DOI: [10.1242/jcs.00329](https://doi.org/10.1242/jcs.00329) (cit. on pp. 9, 105).
- [50] Julie A. Wasylnka and Margo M. Moore. "Uptake of *Aspergillus fumigatus* conidia by phagocytic and nonphagocytic cells in vitro: Quantitation using strains expressing green fluorescent protein." In: *Infection and Immunity* 70.6 (2002), pp. 3156–3163. DOI: [10.1128/IAI.70.6.3156-3163.2002](https://doi.org/10.1128/IAI.70.6.3156-3163.2002) (cit. on pp. 9, 105).
- [51] Fangyan Chen, Changjian Zhang, Xiaodong Jia, Shuo Wang, Jing Wang, Yong Chen, Jingya Zhao, Shuguang Tian, Xuelin Han, and Li Han. "Transcriptome Profiles of Human Lung Epithelial Cells A549 Interacting with *Aspergillus fumigatus* by RNA-Seq." In: *PloS one* 10.8 (2015), e0135720. DOI: [10.1371/journal.pone.0135720](https://doi.org/10.1371/journal.pone.0135720) (cit. on p. 9).
- [52] Jean L. Oosthuizen, Pol Gomez, Jian Ruan, Tillie L. Hackett, Margo M. Moore, Darryl A. Knight, and Scott J. Tebbutt. "Dual Organism Transcriptomics of Airway Epithelial Cells Interacting with Conidia of *Aspergillus fumigatus*." In: *PLoS ONE* 6.5 (2011), e20527. DOI: [10.1371/journal.pone.0020527](https://doi.org/10.1371/journal.pone.0020527) (cit. on p. 9).
- [53] Anna H.T. Hissen, Adrian N.C. Wan, Mark L. Warwas, Linda J. Pinto, and Margo M. Moore. "The *Aspergillus fumigatus* siderophore biosynthetic gene *sidA*, encoding L-ornithine N⁵-oxygenase, is required for virulence." In: *Infection and Immunity* 73.9 (2005), pp. 5493–5503. DOI: [10.1128/IAI.73.9.5493-5503.2005](https://doi.org/10.1128/IAI.73.9.5493-5503.2005) (cit. on p. 9).

- [54] Hiroaki Kitano. "Computational systems biology." In: *Nature* 420 (2002), pp. 206–210. DOI: [10.1038/nature01254](https://doi.org/10.1038/nature01254) (cit. on pp. 10–12).
- [55] Aleksandra Barac, Christos Kosmidis, Ana Alastruey-Izquierdo, and Helmut Salzer. "Chronic pulmonary aspergillosis update: A year in review." In: *Medical mycology* 57 (2019), pp. 104–109. DOI: [10.1093/mmy/myy070](https://doi.org/10.1093/mmy/myy070) (cit. on p. 10).
- [56] Bernhard Palsson. *Systems biology: Properties of reconstructed networks*. 1st. San Diego: Cambridge University Press, 2006. DOI: [10.1017/CB09780.511790515](https://doi.org/10.1017/CB09780.511790515) (cit. on p. 10).
- [57] Uwe Sauer, Matthias Heinemann, and Nicola Zamboni. "Getting closer to the whole picture." In: *Science* 316.5824 (2007), pp. 550–551. DOI: [10.1126/science.1142502](https://doi.org/10.1126/science.1142502) (cit. on p. 10).
- [58] Alan Aderem. "Systems biology: its practice and challenges." In: *Cell* 121.4 (2005), pp. 511–513. DOI: [10.1016/j.cell.2005.04.020](https://doi.org/10.1016/j.cell.2005.04.020) (cit. on p. 10).
- [59] Anthony King, Sabine Louet, Claire O'Connell, and Sheridan Cormac. "Success stories in systems biology." In: *Systems Biology Ireland*, University College Dublin, 2014, p. 36 (cit. on p. 10).
- [60] Charles E. Cook, Mary Todd Bergman, Robert D. Finn, Guy Cochrane, Ewan Birney, and Rolf Apweiler. "The European Bioinformatics Institute in 2016: Data growth and integration." In: *Nucleic Acids Research* 44.D1 (2016), pp. D20–D26. DOI: [10.1093/nar/gkv1352](https://doi.org/10.1093/nar/gkv1352) (cit. on p. 10).
- [61] A Konopka. "Basic Concepts of Systems Biology." In: *Systems Biology: Principles, Methods, and Concepts*. Boca Raton, FL, USA: Taylor & Francis / CRC Press, 2006. Chap. Basic Conc, pp. 1–26. DOI: [10.13140/RG.2.1.4615.7923](https://doi.org/10.13140/RG.2.1.4615.7923) (cit. on p. 10).
- [62] Marc W. Kirschner. "The meaning of systems biology." In: *Cell* 121.4 (2005), pp. 503–504. DOI: [10.1016/j.cell.2005.05.005](https://doi.org/10.1016/j.cell.2005.05.005) (cit. on p. 11).
- [63] Fumiaki Katagiri. "Attacking complex problems with the power of systems biology." In: *Plant Physiology* 132.2 (2003), pp. 417–419. DOI: [10.1104/pp.103.021774](https://doi.org/10.1104/pp.103.021774) (cit. on p. 11).
- [64] Walter Karplus. "The Spectrum of Mathematical Models." In: *Perspectives in Computing* V3.N2 (1983), p4–13. DOI: [10.1007/978-1-4615-0235-7_7](https://doi.org/10.1007/978-1-4615-0235-7_7) (cit. on pp. 11, 15).
- [65] D. G. Bates and C. Cosentino. "Validation and invalidation of systems biology models using robustness analysis." In: *IET Systems Biology* 5.4 (2011), pp. 229–244. DOI: [10.1049/iet-syb.2010.0072](https://doi.org/10.1049/iet-syb.2010.0072) (cit. on p. 11).
- [66] Eugene C. Butcher, Ellen L. Berg, and Eric J. Kunkel. "Systems biology in drug discovery." In: *Nature Biotechnology* (2004), pages 1253–1259. DOI: [10.1038/nbt1017](https://doi.org/10.1038/nbt1017) (cit. on p. 11).

- [67] Frank J. Bruggeman, Jorrit J. Hornberg, Fred C. Boogerd, and Hans V. Westerhoff. "Introduction to systems biology." In: *Experientia Supplementum* 97. Plant Systems Biology (2007), pp. 1–19. DOI: [10.1007/978-3-7643-7439-6_1](https://doi.org/10.1007/978-3-7643-7439-6_1) (cit. on p. 11).
- [68] Abdallah Derbalah, Hesham Al-Sallami, Chihiro Hasegawa, Gulati Abhishek, and Stephen B. Duffull. "A framework for simplification of quantitative systems pharmacology models in clinical pharmacology." In: *British Journal of Clinical Pharmacology Landmarks in pharmacometrics* (2020), pp. 1–11. DOI: [10.1111/bcp.14451](https://doi.org/10.1111/bcp.14451) (cit. on p. 12).
- [69] Andreas V.M. Herz, Tim Gollisch, Christian K. Machens, and Dieter Jaeger. "Modeling single-neuron dynamics and computations: A balance of detail and abstraction." In: *Science* 314.5796 (2006), pp. 80–85. DOI: [10.1126/science.1127240](https://doi.org/10.1126/science.1127240) (cit. on p. 12).
- [70] Martin Meier-Schellersheim, Iain D.C. Fraser, and Frederick Klauschen. "Multiscale modeling for biologists." In: *Wiley Interdisciplinary Reviews: Systems Biology and Medicine* (2009). DOI: [10.1002/wsbm.33](https://doi.org/10.1002/wsbm.33) (cit. on p. 12).
- [71] Fulvio Mazzocchi. "Complexity in biology. Exceeding the limits of reductionism and determinism using complexity theory." In: *EMBO Reports* 9.1 (2008), pp. 10–14. DOI: [10.1038/sj.embor.7401147](https://doi.org/10.1038/sj.embor.7401147) (cit. on p. 12).
- [72] Wolf Singer. "Understanding the brain. How can our intuition fail so fundamentally when it comes to studying the organ to which it owes its existence?" In: *EMBO Reports* 8.S1 (2007), S16–S19. DOI: [10.1038/sj.embor.7400994](https://doi.org/10.1038/sj.embor.7400994) (cit. on p. 12).
- [73] Steven Rose. "Precis of lifelines: Biology, freedom, determinism." In: *Behavioral and Brain Sciences* 22.5 (1999), pp. 871–885. DOI: [10.1017/S0140525X99002204](https://doi.org/10.1017/S0140525X99002204) (cit. on p. 12).
- [74] Lev S. Tsimring. "Noise in biology." In: *Reports on Progress in Physics* 77 (2014), p. 026601. DOI: [10.1088/0034-4885/77/2/026601](https://doi.org/10.1088/0034-4885/77/2/026601) (cit. on p. 12).
- [75] Edda Klipp, Wolfram Liebermeister, Christoph Wierling, and Axel Kowald. "Systems Biology: A Textbook." In: 2nd ed. Weinheim, Germany: John Wiley & Sons, 2016. Chap. Coupled Sy, p. 504 (cit. on p. 13).
- [76] Alexander H.D. Cheng and Daisy T. Cheng. "Heritage and early history of the boundary element method." In: *Engineering Analysis with Boundary Elements* 29.3 (2005), pp. 268–302. DOI: [10.1016/j.enganabound.2004.12.001](https://doi.org/10.1016/j.enganabound.2004.12.001) (cit. on p. 13).
- [77] Richard M. Venable, Helgi I. Ingólfsson, Michael G. Lerner, B. Scott Perrin, Brian A. Camley, Siewert J. Marrink, Frank L.H. Brown, and Richard W. Pastor. "Lipid and Peptide Diffusion in Bilayers: The Saffman-Delbrück Model and Periodic Boundary Conditions." In: *Journal of Physical Chemistry B* 121.15 (2017), pp. 3443–3457. DOI: [10.1021/acs.jpccb.6b09111](https://doi.org/10.1021/acs.jpccb.6b09111) (cit. on p. 13).
- [78] Holger Perfahl et al. "Multiscale modelling of vascular tumour growth in 3D: The roles of domain size and boundary conditions." In: *PLoS ONE* 6.4 (2011), e14790. DOI: [10.1371/journal.pone.0014790](https://doi.org/10.1371/journal.pone.0014790) (cit. on p. 13).

- [79] Richard M. Burian, Robert C. Richardson, and Wim J. Van Der Steen. "Against generality: Meaning in genetics and philosophy." In: *Studies in History and Philosophy of Science Part A* 27.1 (1996), pp. 1–29. DOI: [10.1016/0039-3681\(95\)00034-8](https://doi.org/10.1016/0039-3681(95)00034-8) (cit. on p. 13).
- [80] Sara Green. "Revisiting generality in biology: systems biology and the quest for design principles." In: *Biology and Philosophy* 30 (2015), pp. 629–652. DOI: [10.1007/s10539-015-9496-9](https://doi.org/10.1007/s10539-015-9496-9) (cit. on p. 13).
- [81] Ira S. Lowry. "A short course in model design." In: *Journal of the American Planning Association* 31.158-165 (1965). DOI: [10.1080/01944366508978159](https://doi.org/10.1080/01944366508978159) (cit. on p. 14).
- [82] Per Nilsen. "Making sense of implementation theories, models and frameworks." In: *Implementation Science* 10.53 (2015). DOI: [10.1186/s13012-015-0242-0](https://doi.org/10.1186/s13012-015-0242-0) (cit. on p. 14).
- [83] Aneil Mallavarapu, Matthew Thomson, Benjamin Ullian, and Jeremy Gunawardena. "Programming with models: Modularity and abstraction provide powerful capabilities for systems biology." In: *Journal of the Royal Society Interface* 6.32 (2009), pp. 257–270. DOI: [10.1098/rsif.2008.0205](https://doi.org/10.1098/rsif.2008.0205) (cit. on p. 14).
- [84] Brian P. Ingalls. *Mathematical Modeling in Systems Biology: An Introduction*. 1st. Cambridge, USA: MIT Press, 2013, p. 424 (cit. on p. 14).
- [85] Manfred Gilli and Peter Winker. "Indirect Estimation of the Parameters of Agent Based Models of Financial Markets." In: *Computing in Economics and Finance 2001, Society for Computational Economics*, 59 (2001). DOI: [10.2139/ssrn.300220](https://doi.org/10.2139/ssrn.300220) (cit. on p. 14).
- [86] Hoshin V Gupta, Keith J Beven, and Thorsten Wagener. "Model Calibration and Uncertainty Estimation." In: *Encyclopedia of Hydrological Sciences*. Ed. by Malcolm G. Anderson. 1st. Hoboken, New Jersey: John Wiley & Sons, 2005. Chap. 11 - Rainf. DOI: [10.1002/0470848944.hsa138](https://doi.org/10.1002/0470848944.hsa138) (cit. on p. 15).
- [87] Maksat Ashyraliyev, Yves Fomekong-Nanfack, Jaap A. Kaandorp, and Joke G. Blom. "Systems biology: Parameter estimation for biochemical models." In: *FEBS Journal* 276.4 (2009), pp. 886–902. DOI: [10.1111/j.1742-4658.2008.06844.x](https://doi.org/10.1111/j.1742-4658.2008.06844.x) (cit. on p. 15).
- [88] Yaman Barlas. "Formal aspects of model validity and validation in system dynamics." In: *System Dynamics Review* 12 (1996), pp. 183–210. DOI: [10.1002/\(sici\)1099-1727\(199623\)12:3<183::aid-sdr103>3.0.co;2-4](https://doi.org/10.1002/(sici)1099-1727(199623)12:3<183::aid-sdr103>3.0.co;2-4) (cit. on p. 15).
- [89] G.E.P. Box. "Robustness in the Strategy of Scientific Model Building." In: *Robustness in Statistics*. Ed. by ROBERT L. LAUNER and GRAHAM N. WILKINSON. 1st. New York: Academic Press, 1979. Chap. Robustness. DOI: [10.1016/b978-0-12-438150-6.50018-2](https://doi.org/10.1016/b978-0-12-438150-6.50018-2) (cit. on p. 15).

- [90] Byron Cook, Jasmin Fisher, Benjamin A. Hall, Samin Ishtiaq, Garvit Junwal, and Nir Piterman. "Finding instability in biological models." In: *Computer Aided Verification. CAV 2014. Lecture Notes in Computer Science*. Vienna: Springer, 2014, vol 8559. DOI: [10.1007/978-3-319-08867-9_24](https://doi.org/10.1007/978-3-319-08867-9_24) (cit. on p. 15).
- [91] Laurence Loewe and Jane Hillston. "Computational models in systems biology." In: *Genome Biol* 9.328 (2008). DOI: [10.1186/gb-2008-9-12-328](https://doi.org/10.1186/gb-2008-9-12-328) (cit. on p. 16).
- [92] Reiko J. Tanaka, Neville J. Boon, Katarina Vrcelj, Anita Nguyen, Carmelina Vinci, Darius Armstrong-James, and Elaine Bignell. "In silico modeling of spore inhalation reveals fungal persistence following low dose exposure." en. In: *Scientific reports* 5 (2015), p. 13958. DOI: [10.1038/srep13958](https://doi.org/10.1038/srep13958) (cit. on p. 16).
- [93] Robert M.M. Mattheij and Jaap Molenaar. "Ordinary differential equations in theory and practice." In: *Classics in Applied Mathematics*. 1st. Philadelphia, PA: Society for Industrial and Applied Mathematics, 2002. Chap. 12. Mathem. DOI: [10.1109/mcse.1997.641611](https://doi.org/10.1109/mcse.1997.641611) (cit. on p. 16).
- [94] Lu Tang, Yiwang Zhou, Lili Wang, Soumik Purkayastha, Leyao Zhang, Jie He, Fei Wang, and Peter X.K. Song. "A Review of Multi-Compartment Infectious Disease Models." In: *International Statistical Review* 88.2 (2020), pp. 462–513. DOI: [10.1111/insr.12402](https://doi.org/10.1111/insr.12402) (cit. on p. 16).
- [95] Silvia Daun, Jonathan Rubin, Yoram Vodovotz, and Gilles Clermont. "Equation-based models of dynamic biological systems." In: *Journal of Critical Care* 23.4 (2008), pp. 585–594. DOI: [10.1016/j.jcrc.2008.02.003](https://doi.org/10.1016/j.jcrc.2008.02.003) (cit. on p. 16).
- [96] J. Maynard Smith and G. R. Price. "The logic of animal conflict." In: *Nature* 246 (1973), pp. 15–18. DOI: [10.1038/246015a0](https://doi.org/10.1038/246015a0) (cit. on p. 16).
- [97] Johannes Pollmächer, Sandra Timme, Stefan Schuster, Axel A. Brakhage, Peter F. Zipfel, and Marc Thilo Figge. "Deciphering the counterplay of aspergillus fumigatus infection and host inflammation by evolutionary games on graphs." In: *Scientific Reports* 6 (2016), p. 27807. DOI: [10.1038/srep27807](https://doi.org/10.1038/srep27807) (cit. on p. 17).
- [98] Cristina Bicchieri. "Rationality and Game Theory." In: *The Oxford Handbook of Rationality*. 1st. New York: Oxford University Press, 2004. Chap. 10. DOI: [10.1093/0195145399.003.0010](https://doi.org/10.1093/0195145399.003.0010) (cit. on p. 17).
- [99] Jörgen W. Weibull. *Evolutionary Game Theory*. 1st. Cambridge, USA; London, UK: MIT Press, 1995, p. 265 (cit. on p. 17).
- [100] Mohammad Soheilypour and Mohammad R.K. Mofrad. "Agent-Based Modeling in Molecular Systems Biology." In: *BioEssays* 40.7 (2018), e1800020. DOI: [10.1002/bies.201800020](https://doi.org/10.1002/bies.201800020) (cit. on p. 17).
- [101] U Wilensky. "NetLogo. <http://ccl.northwestern.edu/netlogo/>." In: *Center for Connected Learning and ComputerBased Modeling Northwestern University Evanston IL* (1999) (cit. on p. 17).

- [102] Michael J. North, Nicholson T. Collier, Jonathan Ozik, Eric R. Tataru, Charles M. Macal, Mark Bragen, and Pam Sydelko. "Complex adaptive systems modeling with Repast Symphony." In: *Complex Adaptive Systems Modeling* 1.3 (2013). DOI: [10.1186/2194-3206-1-3](https://doi.org/10.1186/2194-3206-1-3) (cit. on p. 17).
- [103] Yoram Vodovotz and Gary An. "Agent-based models of inflammation in translational systems biology: A decade later." In: *Wiley Interdisciplinary Reviews: Systems Biology and Medicine* 11.6 (2019), e1460. DOI: [10.1002/wsbm.1460](https://doi.org/10.1002/wsbm.1460) (cit. on p. 17).
- [104] A Stéphanou and Vitaly Volpert. "Hybrid Modelling in Biology: a Classification Review." In: *Mathematical Modelling of Natural Phenomena* 11 (2016), pp. 37–48. DOI: [10.1051/mmnp/2016111103](https://doi.org/10.1051/mmnp/2016111103) (cit. on p. 18).
- [105] Ewald R. Weibel. *Morphometry of the Human Lung*. 1st. Berlin Heidelberg: Springer, 1963, p. 164 (cit. on p. 18).
- [106] C. Desplechain, B. Foliguet, E. Barrat, G. Grignon, and F. Touati. "The Pores of Kohn in Pulmonary Alveoli." In: *Clinical Respiratory Physiology* 19.1 (1983), pp. 59–68 (cit. on p. 18).
- [107] Imre Balásházy, Werner Hofmann, Árpád Farkas, and Balázs G. Madas. "Three-Dimensional Model for Aerosol Transport and Deposition in Expanding and Contracting Alveoli." en. In: *Inhalation Toxicology* 20.6 (2008), pp. 611–621. DOI: [10.3314/jjmm.43.203](https://doi.org/10.3314/jjmm.43.203) (cit. on p. 18).
- [108] Mike Hasenberg, Sabine Stegemann-Koniszewski, and Matthias Gunzer. "Cellular immune reactions in the lung." In: *Immunological Reviews* 251.1 (2013), pp. 189–214. DOI: [10.1111/imr.12020](https://doi.org/10.1111/imr.12020) (cit. on p. 18).
- [109] Viviane Balloy and Michel Chignard. "The innate immune response to *Aspergillus fumigatus*." In: *Microbes and Infection* 11.12 (2009), pp. 919–927. DOI: [10.1016/j.micinf.2009.07.002](https://doi.org/10.1016/j.micinf.2009.07.002) (cit. on p. 18).
- [110] Nir Osherov. "Interaction of the pathogenic mold *Aspergillus fumigatus* with lung epithelial cells." In: *Frontiers in Microbiology* 3.346 (2012). DOI: [10.3389/fmicb.2012.00346](https://doi.org/10.3389/fmicb.2012.00346) (cit. on p. 18).
- [111] Monica M. Mircescu, Lauren Lipuma, Nico Van Rooijen, Eric G. Pamer, and Tobias M. Hohl. "Essential role for neutrophils but not alveolar macrophages at early time points following *aspergillus fumigatus* infection." In: *Journal of Infectious Diseases* 200.4 (2009), pp. 647–656. DOI: [10.1086/600380](https://doi.org/10.1086/600380) (cit. on p. 18).
- [112] J. Ferin. "Pulmonary alveolar pores and alveolar macrophage-mediated particle clearance." In: *The Anatomical Record* 203.2 (1982), pp. 265–272. DOI: [10.1002/ar.1092030208](https://doi.org/10.1002/ar.1092030208) (cit. on p. 19).
- [113] Michael J. Oldham and Owen R. Moss. "Pores of Kohn: Forgotten alveolar structures and potential source of aerosols in exhaled breath." In: *Journal of Breath Research* 13.2 (2019), p. 021003. DOI: [10.1088/1752-7163/ab0524](https://doi.org/10.1088/1752-7163/ab0524) (cit. on pp. 19, 97).

- [114] Eman Namati, Jacqueline Thiesse, Jessica De Ryk, and Geoffrey McLennan. "Alveolar dynamics during respiration: Are the pores of Kohn a pathway to recruitment?" In: *American Journal of Respiratory Cell and Molecular Biology* 38.5 (2008), pp. 572–578. DOI: [10.1165/rcmb.2007-01200C](https://doi.org/10.1165/rcmb.2007-01200C) (cit. on pp. 96, 97).
- [115] K. V. Clemons and D. A. Stevens. "The contribution of animal models of aspergillosis to understanding pathogenesis, therapy and virulence." In: *Medical Mycology* 43.SUPPL.1 (2005), S101–S110. DOI: [10.1080/13693780500051919](https://doi.org/10.1080/13693780500051919) (cit. on p. 93).
- [116] Johannes Pollmacher and Marc Thilo Figge. "Agent-based model of human alveoli predicts chemotactic signaling by epithelial cells during early *Aspergillus fumigatus* infection." In: *PloS one* 9.10 (2014), e111630. DOI: [10.1371/journal.pone.0111630](https://doi.org/10.1371/journal.pone.0111630) (cit. on pp. 93, 102).
- [117] Johannes Pollmacher and Marc Thilo Figge. "Deciphering chemokine properties by a hybrid agent-based model of *Aspergillus fumigatus* infection in human alveoli." In: *Frontiers in microbiology* 6.503 (2015). DOI: [10.3389/fmicb.2015.00503](https://doi.org/10.3389/fmicb.2015.00503) (cit. on pp. 93, 102).
- [118] J. Sarfati, M. Diaquin, J. P. Debeaupuis, A. Schmidt, D. Lecaue, A. Beauvais, and J. P. Latge. "A new experimental murine aspergillosis model to identify strains of *Aspergillus fumigatus* with reduced virulence." In: *Nihon Ishinkin Gakkai zasshi = Japanese journal of medical mycology* 43.4 (2002), pp. 203–213. DOI: [10.3314/jjmm.43.203](https://doi.org/10.3314/jjmm.43.203) (cit. on p. 95).
- [119] Alexander J Lepak, Karen Marchillo, Jaimie Vanhecker, and David R Andes. "Posaconazole pharmacodynamic target determination against wild-type and Cyp51 mutant isolates of *Aspergillus fumigatus* in an in vivo model of invasive pulmonary aspergillosis." In: *Antimicrobial agents and chemotherapy* 57.1 (2013), pp. 579–585. DOI: [10.1128/AAC.01279-12](https://doi.org/10.1128/AAC.01279-12) (cit. on p. 95).
- [120] Sarah Sze Wah Wong, Orhan Rasid, Paris Laskaris, Arnaud Fekkar, Jean-Marc Cavaillon, William J. Steinbach, and Oumaima Ibrahim-Granet. "Treatment of Cyclosporin A retains host defense against invasive pulmonary aspergillosis in a non-immunosuppressive murine model by preserving the myeloid cell population." In: *Virulence* 8.8 (2017), pp. 1744–1752. DOI: [10.1080/21505594.2017.1339007](https://doi.org/10.1080/21505594.2017.1339007) (cit. on p. 95).
- [121] Guillaume Desoubieux and Carolyn Cray. "Rodent models of invasive aspergillosis due to *aspergillus fumigatus*: Still a long path toward standardization." In: *Frontiers in Microbiology* 8.841 (2017). DOI: [10.3389/fmicb.2017.00841](https://doi.org/10.3389/fmicb.2017.00841) (cit. on p. 95).
- [122] William J Steinbach, Daniel K Benjamin, Scott a Trasi, Jackie L Miller, Wiley a Schell, Aimee K Zaas, W Michael Foster, and John R Perfect. "Value of an inhalational model of invasive aspergillosis." In: *Medical mycology : official publication of the International Society for Human and Animal Mycology* 42.5 (2004), pp. 417–425. DOI: [10.1080/13693780410001712034](https://doi.org/10.1080/13693780410001712034) (cit. on pp. 95, 103).

- [123] Isabella Luísa da Silva Gurgel, Karina Talita de Oliveira Santana Jorge, Nathália Luísa Sousa de Oliveira Malacco, Jéssica Amanda Marques Souza, Marina Campos Rocha, Marina Faria Fernandes, Flávia Rayssa Braga Martins, Iran Malavazi, Mauro Martins Teixeira, and Frederico Marianetti Soriani. "The *Aspergillus fumigatus* Mucin MsbA Regulates the Cell Wall Integrity Pathway and Controls Recognition of the Fungus by the Immune System." In: *mSphere* 4.3 (2019), e00350–19. DOI: [10.1128/msphere.00350-19](https://doi.org/10.1128/msphere.00350-19) (cit. on p. 95).
- [124] Joe L. Hsu et al. "Microhemorrhage-associated tissue iron enhances the risk for *Aspergillus fumigatus* invasion in a mouse model of airway transplantation." In: *Science Translational Medicine* 10.429 (2018), eaag2616. DOI: [10.1126/scitranslmed.aag2616](https://doi.org/10.1126/scitranslmed.aag2616) (cit. on p. 95).
- [125] James I.P. Stewart, Vinicius M. Fava, Joshua D. Kerkaert, Adithya S. Subramanian, Fabrice N. Gravelat, Melanie Lehoux, P. Lynne Howell, Robert A. Cramer, and Donald C. Sheppard. "Reducing *Aspergillus fumigatus* virulence through targeted dysregulation of the conidiation pathway." In: *mBio* (2020). DOI: [10.1128/mBio.03202-19](https://doi.org/10.1128/mBio.03202-19) (cit. on p. 95).
- [126] J. C. Bowman, G. K. Abruzzo, J. W. Anderson, A. M. Flattery, C. J. Gill, V. B. Pikounis, D. M. Schmatz, A. Liberator, and C. M. Douglas. "Quantitative PCR assay to measure *Aspergillus fumigatus* burden in a murine model of disseminated aspergillosis: Demonstration of efficacy of caspofungin acetate." In: *Antimicrobial Agents and Chemotherapy* 45.12 (2001), pp. 3474–3481. DOI: [10.1128/AAC.45.12.3474-3481.2001](https://doi.org/10.1128/AAC.45.12.3474-3481.2001) (cit. on p. 95).
- [127] Donald C. Sheppard, K. A. Marr, D. N. Fredricks, L. Y. Chiang, T. Doedt, and S. G. Filler. "Comparison of three methodologies for the determination of pulmonary fungal burden in experimental murine aspergillosis." In: *Clinical Microbiology and Infection* 12.4 (2006), pp. 376–380. DOI: [10.1111/j.1469-0691.2005.01349.x](https://doi.org/10.1111/j.1469-0691.2005.01349.x) (cit. on p. 95).
- [128] H. N. (1893). Kohn. "Zur Histologie der indurirenden fibrinösen Pneumonie." In: *Munch. med. Wschr.* 40 (1893), p. 42 (cit. on p. 96).
- [129] M Kawakami and T Takizawa. "Distribution of pores within alveoli in the human lung." In: *Journal of applied physiology* 63.5 (1987), pp. 1866–70. DOI: [10.1152/jappl.1987.63.5.1866](https://doi.org/10.1152/jappl.1987.63.5.1866). (cit. on p. 96).
- [130] H. M. Adams, W. E., and Livingstone. "Obstructive pulmonary atelectasis." In: *Arch. Surg.* 23 (1931), p. 500 (cit. on p. 96).
- [131] J. L. Cordingley. "Pores of Kohn." In: *Thorax* 27.4 (1972), pp. 433–441. DOI: [10.1136/thx.27.4.433](https://doi.org/10.1136/thx.27.4.433) (cit. on p. 96).
- [132] Arpan Sharma Neupane et al. "Patrolling Alveolar Macrophages Conceal Bacteria from the Immune System to Maintain Homeostasis." In: *Cell* 183.1 (2020), 110–125.e11. DOI: [10.1016/j.cell.2020.08.020](https://doi.org/10.1016/j.cell.2020.08.020) (cit. on pp. 96, 102).
- [133] R. Paul Guillerman. "Imaging of childhood interstitial lung disease." In: *Pediatric, Allergy, Immunology, and Pulmonology* 23.1 (2010), pp. 43–68. DOI: [10.1089/ped.2010.0010](https://doi.org/10.1089/ped.2010.0010) (cit. on p. 96).

- [134] Akira Yoshikawa, Shuntaro Sato, Tomonori Tanaka, Mikiko Hashisako, Yukio Kashima, Tomoshi Tsuchiya, Naoya Yamasaki, Takeshi Nagayasu, Hiroshi Yamamoto, and Junya Fukuoka. "Breakdown of lung framework and an increase in pores of kohn as initial events of emphysema and a cause of reduction in diffusing capacity." In: *International Journal of COPD* 16.11 (2016), pp. 2287–2294. DOI: [10.2147/COPD.S114281](https://doi.org/10.2147/COPD.S114281) (cit. on p. 96).
- [135] Jinxiang Xi and Mohamed Talaat. "Nanoparticle deposition in rhythmically moving acinar models with interalveolar septal apertures." In: *Nanomaterials* 9.8 (2019), p. 1126. DOI: [10.3390/nano9081126](https://doi.org/10.3390/nano9081126) (cit. on pp. 97, 103).
- [136] J. E. Glasgow, B. E. Farrell, E. S. Fisher, D. A. Lauffenburger, and R. P. Daniele. "The motile response of alveolar macrophages. An experimental study using single-cell and cell population approaches." In: *American Review of Respiratory Disease* (1989). DOI: [10.1164/ajrccm/139.2.320](https://doi.org/10.1164/ajrccm/139.2.320) (cit. on p. 97).
- [137] KE Barrett, SM Barman, S Boitano, and HL Brooks. *Ganong's Review of Medical Physiology*, 24. 24th. London: New York : McGraw-Hill Medical, 2012 (cit. on p. 97).
- [138] Hiroko Akei, Jeffrey A. Whitsett, Michelle Buroker, Takafumi Ninomiya, Haruyuki Tatsumi, Timothy E. Weaver, and Machiko Ikegami. "Surface tension influences cell shape and phagocytosis in alveolar macrophages." In: *American Journal of Physiology - Lung Cellular and Molecular Physiology* 291.4 (2006), pp. L572–9. DOI: [10.1152/ajplung.00060.2006](https://doi.org/10.1152/ajplung.00060.2006) (cit. on p. 97).
- [139] Dongeun Huh, Benjamin D. Matthews, Akiko Mammoto, Martin Montoya-Zavala, Hong Yuan Hsin, and Donald E. Ingber. "Reconstituting organ-level lung functions on a chip." In: *Science* 328.5986 (2010), pp. 1662–1668. DOI: [10.1126/science.1188302](https://doi.org/10.1126/science.1188302) (cit. on p. 98).
- [140] Janick D. Stucki et al. "Medium throughput breathing human primary cell alveolus-on-chip model." In: *Scientific Reports* 8 (2018), p. 14359. DOI: [10.1038/s41598-018-32523-x](https://doi.org/10.1038/s41598-018-32523-x) (cit. on p. 98).
- [141] Kambez H. Benam et al. "Matched-Comparative Modeling of Normal and Diseased Human Airway Responses Using a Microengineered Breathing Lung Chip." In: *Cell Systems* 3.5 (2016), pp. 456–466. DOI: [10.1016/j.cels.2016.10.003](https://doi.org/10.1016/j.cels.2016.10.003) (cit. on p. 98).
- [142] Hui Ren, Nigel P. Birch, and Vinod Suresh. "An optimised human cell culture model for alveolar epithelial transport." In: *PLoS ONE* 11.10 (2016), e0165225. DOI: [10.1371/journal.pone.0165225](https://doi.org/10.1371/journal.pone.0165225) (cit. on p. 98).
- [143] Ho Jin Park, Yali Zhang, Serban P. Georgescu, Kristin L. Johnson, Dequon Kong, and Jonas B. Galper. "Human umbilical vein endothelial cells and human dermal microvascular endothelial cells offer new insights into the relationship between lipid metabolism and angiogenesis."

- In: *Stem Cell Reviews* 2.2 (2006), pp. 93–102. DOI: [10.1385/SCR:2:2:93](https://doi.org/10.1385/SCR:2:2:93) (cit. on p. 98).
- [144] Zeinab Mokhtari, Franziska Mech, Carolin Zitzmann, Mike Hasenberg, Matthias Gunzer, and Marc Thilo Figge. “Automated characterization and parameter-free classification of Cell tracks based on local migration behavior.” In: *PLoS ONE* 8.12 (2013), e80808. DOI: [10.1371/journal.pone.0080808](https://doi.org/10.1371/journal.pone.0080808) (cit. on p. 98).
- [145] Felix Ellett, Julianne Jorgensen, Galit H. Frydman, Caroline N. Jones, and Daniel Irimia. “Neutrophil Interactions Stimulate Evasive Hyphal Branching by *Aspergillus fumigatus*.” In: *PLoS Pathogens* 13.1 (2017), e1006154. DOI: [10.1371/journal.ppat.1006154](https://doi.org/10.1371/journal.ppat.1006154) (cit. on p. 98).
- [146] Kunito Yoshida and Thierry Soldati. “Dissection of amoeboid movement into two mechanically distinct modes.” In: *Journal of Cell Science* 119.18 (2006), pp. 3833–3844. DOI: [10.1242/jcs.03152](https://doi.org/10.1242/jcs.03152) (cit. on p. 99).
- [147] Alex Mogilner and Kinneret Keren. “The Shape of Motile Cells.” In: *Current Biology* 19.17 (2009), R762–R771. DOI: [10.1016/j.cub.2009.06.053](https://doi.org/10.1016/j.cub.2009.06.053) (cit. on p. 99).
- [148] Christel Ducroz, Jean Christophe Olivo-Marin, and Alexandre Dufour. “Characterization of cell shape and deformation in 3D using Spherical Harmonics.” In: *2012 9th IEEE International Symposium on Biomedical Imaging (ISBI)*. 2012, pp. 848–851. DOI: [10.1109/ISBI.2012.6235681](https://doi.org/10.1109/ISBI.2012.6235681) (cit. on p. 99).
- [149] Marco Blickensdorf. “Agent based Simulation of Cell Migration and Shape Dynamics.” In: *Master Thesis* (2015), pp. 1–11 (cit. on p. 99).
- [150] Nir Osherov. “The top three areas of basic research on *Aspergillus fumigatus* in 2011.” In: *Annals of the New York Academy of Sciences* 1273.1 (2012), pp. 74–77. DOI: [10.1111/j.1749-6632.2012.06798.x](https://doi.org/10.1111/j.1749-6632.2012.06798.x) (cit. on p. 102).
- [151] Michael Lieber, George Todaro, Barry Smith, Andras Szakal, and Walter Nelson-Rees. “A continuous tumor-cell line from a human lung carcinoma with properties of type II alveolar epithelial cells.” In: *International Journal of Cancer* 17.1 (1976), pp. 62–70. DOI: [10.1002/ijc.2910170110](https://doi.org/10.1002/ijc.2910170110) (cit. on p. 102).
- [152] Rachael Zoe Murray and Jennifer Lea Stow. “Cytokine secretion in macrophages: SNAREs, Rabs, and membrane trafficking.” In: *Frontiers in Immunology* 5.538 (2014). DOI: [10.3389/fimmu.2014.00538](https://doi.org/10.3389/fimmu.2014.00538) (cit. on p. 102).
- [153] Thomas R. Kozel. “Activation of the complement system by pathogenic fungi.” In: *Clinical Microbiology Reviews* 9.1 (1996), pp. 34–46. DOI: [10.1128/cmr.9.1.34-46.1996](https://doi.org/10.1128/cmr.9.1.34-46.1996) (cit. on p. 102).
- [154] Zhenglong Chen, Ming Zhong, Yuzhou Luo, Linhong Deng, Zhaoyan Hu, and Yuanlin Song. “Determination of rheology and surface tension of airway surface liquid: A review of clinical relevance and measurement techniques.” In: *Respiratory Research* 20.274 (2019). DOI: [10.1186/s12931-019-1229-1](https://doi.org/10.1186/s12931-019-1229-1) (cit. on p. 102).

- [155] Marco Blickensdorf, Sandra Timme, and Marc Thilo Figge. "Comparative assessment of aspergillosis by virtual infection modeling in murine and human lung." In: *Frontiers in Immunology* 10.142 (2019). DOI: [10.3389/fimmu.2019.00142](https://doi.org/10.3389/fimmu.2019.00142) (cit. on p. 103).
- [156] Beatrice Haefeli-Bleuer and Ewald R. Weibel. "Morphometry of the human pulmonary acinus." In: *The Anatomical Record* (1988). DOI: [10.1002/ar.1092200410](https://doi.org/10.1002/ar.1092200410) (cit. on p. 103).
- [157] Marco Blickensdorf, Sandra Timme, and Marc Thilo Figge. "Hybrid Agent-Based Modeling of *Aspergillus fumigatus* Infection to Quantitatively Investigate the Role of Pores of Kohn in Human Alveoli." In: *Frontiers in Microbiology* (2020). DOI: [10.3389/fmicb.2020.01951](https://doi.org/10.3389/fmicb.2020.01951) (cit. on p. 103).
- [158] M.T.N. Hoang, Z. Cseresnyés, S. Hartung, M. Blickensdorf, C. Saffer, K. Rennert, A.S. Mosig, M. von Lilienfeld-Toal, and M.T. Figge. "Invasive aspergillosis-on-chip: A quantitative treatment study of human *Aspergillus fumigatus* infection." In: *submitted to Biomaterials* (2021) (cit. on p. 104).
- [159] Anatte Margalit and Kevin Kavanagh. "The innate immune response to *Aspergillus fumigatus* at the alveolar surface." In: *FEMS Microbiology Reviews* 39.5 (2015), pp. 670–687. DOI: [10.1093/femsre/fuv018](https://doi.org/10.1093/femsre/fuv018) (cit. on p. 104).
- [160] Silvia Bozza, Roberta Gaziano, Antonio Spreca, Angela Bacci, Claudia Montagnoli, Paolo di Francesco, and Luigina Romani. "Dendritic Cells Transport Conidia and Hyphae of *Aspergillus fumigatus* from the Airways to the Draining Lymph Nodes and Initiate Disparate Th Responses to the Fungus." In: *The Journal of Immunology* 168.3 (2002), pp. 1362–1371. DOI: [10.4049/jimmunol.168.3.1362](https://doi.org/10.4049/jimmunol.168.3.1362) (cit. on p. 104).
- [161] Anna Medyukhina, Marco Blickensdorf, Zoltán Cseresnyés, Nora Ruef, Jens V. Stein, and Marc Thilo Figge. "Dynamic spherical harmonics approach for shape classification of migrating cells." In: *Scientific Reports* 10.6072 (2020). DOI: [10.1038/s41598-020-62997-7](https://doi.org/10.1038/s41598-020-62997-7) (cit. on p. 104).
- [162] Emer P. Reeves, C. G.M. Messina, S. Doyle, and K. Kavanagh. "Correlation between gliotoxin production and virulence of *Aspergillus fumigatus* in *Galleria mellonella*." In: *Mycopathologia* 158.7 (2004), pp. 73–79. DOI: [10.1023/B:MYCO.0000038434.55764.16](https://doi.org/10.1023/B:MYCO.0000038434.55764.16) (cit. on p. 104).
- [163] Russell E. Lewis, Nathan P. Wiederhold, Jingduan Chi, Xiang Y. Han, Krishna V. Komanduri, Dimitrios P. Kontoyiannis, and Randall A. Prince. "Detection of gliotoxin in experimental and human aspergillosis." In: *Infection and Immunity* 73.1 (2005), pp. 635–637. DOI: [10.1128/IAI.73.1.635-637.2005](https://doi.org/10.1128/IAI.73.1.635-637.2005) (cit. on p. 104).
- [164] Maria P. Domingo et al. "Bis(methyl)gliotoxin proves to be a more stable and reliable marker for invasive aspergillosis than gliotoxin and suitable for use in diagnosis." In: *Diagnostic Microbiology and Infectious Disease* 73.1 (2012), pp. 57–64. DOI: [10.1016/j.diagmicrobio.2012.01.012](https://doi.org/10.1016/j.diagmicrobio.2012.01.012) (cit. on p. 104).

- [165] R. D. Eichner, M. Al Salami, P. R. Wood, and A. Müllbacher. "The effect of gliotoxin upon macrophage function." In: *International Journal of Immunopharmacology* 8.7 (1986), pp. 789–797. DOI: [10.1016/0192-0561\(86\)90016-0](https://doi.org/10.1016/0192-0561(86)90016-0) (cit. on p. 104).
- [166] S. Paris, E. Boisvieux-Ulrich, B. Crestani, O. Houcine, D. Taramelli, L. Lombardi, and J. P. Latge. "Internalization of *Aspergillus fumigatus* conidia by epithelial and endothelial cells." In: *Infection and Immunity* 65.4 (1997), pp. 1510–4. DOI: [10.1128/iai.65.4.1510-1514.1997](https://doi.org/10.1128/iai.65.4.1510-1514.1997) (cit. on p. 105).
- [167] Fabiane M. Barbosa, Fernanda L. Fonseca, Carla Holandino, Celuta S. Alviano, Leonardo Nimrichter, and Marcio L. Rodrigues. "Glucuronoxylomannan-mediated interaction of *Cryptococcus neoformans* with human alveolar cells results in fungal internalization and host cell damage." In: *Microbes and Infection* 8.2 (2006), pp. 493–502. DOI: [10.1016/j.micinf.2005.07.027](https://doi.org/10.1016/j.micinf.2005.07.027) (cit. on p. 105).
- [168] A. O'garra, Paul S. Redford, Finlay W. McNab, C. Bloom, R. Wilkinson, and M. Berry. "The Immune Response in Tuberculosis." In: *Annu Rev Immunol* . 31 (2013), pp. 475–527. DOI: [10.1146/annurev-immunol-032712-095939](https://doi.org/10.1146/annurev-immunol-032712-095939) (cit. on p. 105).

“Somewhere, something incredible is waiting to be known.” — Carl Sagan

POSTFACE

As the reader reminds this thesis’ preface, I started writing at the beginning of the COVID-19 pandemic and the, we now call it first, lockdown. Although the global perspective has brightened, I will not forget to be at the mercy of such a dangerous disease, sitting at home and making the best out of it. Strangely, as happy as it makes me to finish my thesis with these lines, I see it will always remind me, when I occasionally browse through this document in years, of a critical time. Despite the pandemic is not over by now, the scientific community has achieved remarkable success. Thousands of papers were published, many about co-infections of *A. fumigatus* with COVID-19, and vaccines have been developed, tested and approved in short time, depicting a positive future and demonstrating how powerful research can influence the world.

For me, it remains to say thank you to all scientists putting their energy into research but especially to the people supporting me during the last years. First to the applied systems biology research group, in particular Prof. Marc Thilo Figge, Sandra Timme and Zoltán Cseresnyés, but also the whole Hans Köll Institute, the Friedrich Schiller University, all Collaborators and of course my beloved ones supporting me outside the office who all made this possible.

Thank you for reading

Marco Blickensdorf

EHRENWÖRTLICHE ERKLÄRUNG

Hiermit erkläre ich, dass mir die geltende Promotionsordnung der biologisch-pharmazeutischen Fakultät bekannt ist und ich mich mit bestem Wissen an diese Ordnung gehalten habe. Die vorliegende Dissertation habe ich selbständig und nur unter Verwendung der angegebenen Hilfsmittel, Daten und Quellen angefertigt. Unterstützung während meiner wissenschaftlichen Arbeit und zur Erstellung des vorliegenden Dissertationstextes habe ich nur von den genannten Co-Autoren und in der Danksagung genannten Personen erhalten. Ich habe keine Hilfe von externen Vermittlungs- oder Beratungsdiensten in Anspruch genommen. Niemand hat mittelbare oder unmittelbare geldwerte Leistungen erhalten, für Arbeiten die im Zusammenhang mit dem Inhalt der vorgelegten Dissertation stehen. Die vorgelegte Dissertation wurde bisher nicht als Prüfungsarbeit für eine andere wissenschaftliche Prüfung eingereicht. Im Speziellen habe ich sie an keiner anderen Hochschule eingereicht, um einen akademischen Grad zu erhalten.

Jena, August 2021

Marco Blickensdorf

Part IV

APPENDIX

FORMULAR 2²**Manuskript Nr. 1****Kurzreferenz** Blickensdorf et al. *Front. Immunol.* 2019**Beitrag des Doktoranden / der Doktorandin**

Beitrag des Doktoranden / der Doktorandin zu Abbildungen, die experimentelle Daten wiedergeben (nur für Originalartikel):

Abbildung(en) # alle*	<input type="checkbox"/>	100% (die in dieser Abbildung wiedergegebenen Daten entstammen vollständig experimentellen Arbeiten, die der Kandidat/die Kandidatin durchgeführt hat)
	<input type="checkbox"/>	0% (die in dieser Abbildung wiedergegebenen Daten basieren ausschließlich auf Arbeiten anderer Koautoren)
	<input checked="" type="checkbox"/>	Etwaiger Beitrag des Doktoranden / der Doktorandin zur Abbildung: 95 % Kurzbeschreibung des Beitrages: (z. B. „Abbildungsteile a, d und f“ oder „Auswertung der Daten“ etc)
*Kann sich auf mehrere Abb. beziehen, wenn die Antwort dieselbe ist		

(Anfügen weiterer Tabellenkästen je nach Zahl der Abbildungen)

Unterschrift Kandidat/-in_____
Unterschrift Betreuer/-in (Mitglied der Fakultät)

² Die Unterschriften müssen nur im separat im Dekanat einzureichenden ausgefüllten Formular im Original vorliegen. In der in die Dissertation eingebundenen Fassung dürfen die Unterschriften und Unterschriftenfelder fehlen.

FORMULAR 2²**Manuskript Nr. 2****Kurzreferenz** Blickensdorf et al. *Front Microbiol.* 2020**Beitrag des Doktoranden / der Doktorandin**

Beitrag des Doktoranden / der Doktorandin zu Abbildungen, die experimentelle Daten wiedergeben (nur für Originalartikel):

Abbildung(en) # alle*	<input type="checkbox"/>	100% (die in dieser Abbildung wiedergegebenen Daten entstammen vollständig experimentellen Arbeiten, die der Kandidat/die Kandidatin durchgeführt hat)
	<input type="checkbox"/>	0% (die in dieser Abbildung wiedergegebenen Daten basieren ausschließlich auf Arbeiten anderer Koautoren)
	<input checked="" type="checkbox"/>	Etwaiger Beitrag des Doktoranden / der Doktorandin zur Abbildung: 95 % Kurzbeschreibung des Beitrages: (z. B. „Abbildungsteile a, d und f“ oder „Auswertung der Daten“ etc)
*Kann sich auf mehrere Abb. beziehen, wenn die Antwort dieselbe ist		

(Anfügen weiterer Tabellenkästen je nach Zahl der Abbildungen)

Unterschrift Kandidat/-in_____
Unterschrift Betreuer/-in (Mitglied der Fakultät)

² Die Unterschriften müssen nur im separat im Dekanat einzureichenden ausgefüllten Formular im Original vorliegen. In der in die Dissertation eingebundenen Fassung dürfen die Unterschriften und Unterschriftenfelder fehlen.

FORMULAR 2²**Manuskript Nr. 3****Kurzreferenz Submitted to *Biomaterials*****Beitrag des Doktoranden / der Doktorandin**

Beitrag des Doktoranden / der Doktorandin zu Abbildungen, die experimentelle Daten wiedergeben (nur für Originalartikel):

Abbildung(en) # alle*	<input type="checkbox"/>	100% (die in dieser Abbildung wiedergegebenen Daten entstammen vollständig experimentellen Arbeiten, die der Kandidat/die Kandidatin durchgeführt hat)
	<input type="checkbox"/>	0% (die in dieser Abbildung wiedergegebenen Daten basieren ausschließlich auf Arbeiten anderer Koautoren)
	<input checked="" type="checkbox"/>	Etwaiger Beitrag des Doktoranden / der Doktorandin zur Abbildung: 5 % Kurzbeschreibung des Beitrages: (z. B. „Abbildungsteile a, d und f“ oder „Auswertung der Daten“ etc)
*Kann sich auf mehrere Abb. beziehen, wenn die Antwort dieselbe ist		

(Anfügen weiterer Tabellenkästen je nach Zahl der Abbildungen)

Unterschrift Kandidat/-in

Unterschrift Betreuer/-in (Mitglied der Fakultät)

² Die Unterschriften müssen nur im separat im Dekanat einzureichenden ausgefüllten Formular im Original vorliegen. In der in die Dissertation eingebundenen Fassung dürfen die Unterschriften und Unterschriftenfelder fehlen.

FORMULAR 2²**Manuskript Nr. 4****Kurzreferenz** Medyukhina, A., Blickensdorf, M., Cseresnyés, Z. et al. *Sci Rep* (2020)**Beitrag des Doktoranden / der Doktorandin**

Beitrag des Doktoranden / der Doktorandin zu Abbildungen, die experimentelle Daten wiedergeben (nur für Originalartikel):

Abbildung(en) # alle*	<input type="checkbox"/>	100% (die in dieser Abbildung wiedergegebenen Daten entstammen vollständig experimentellen Arbeiten, die der Kandidat/die Kandidatin durchgeführt hat)
	<input type="checkbox"/>	0% (die in dieser Abbildung wiedergegebenen Daten basieren ausschließlich auf Arbeiten anderer Koautoren)
	<input checked="" type="checkbox"/>	Etwaiger Beitrag des Doktoranden / der Doktorandin zur Abbildung: 25 % Kurzbeschreibung des Beitrages: (z. B. „Abbildungsteile a, d und f“ oder „Auswertung der Daten“ etc)
*Kann sich auf mehrere Abb. beziehen, wenn die Antwort dieselbe ist		

(Anfügen weiterer Tabellenkästen je nach Zahl der Abbildungen)

Unterschrift Kandidat/-in_____
Unterschrift Betreuer/-in (Mitglied der Fakultät)

² Die Unterschriften müssen nur im separat im Dekanat einzureichenden ausgefüllten Formular im Original vorliegen. In der in die Dissertation eingebundenen Fassung dürfen die Unterschriften und Unterschriftenfelder fehlen.